Synthesis and Defect Structure Analysis of Complex Oxides for Li-Ion Battery Electrodes

By

Xiaoguang Hao

A dissertation submitted in partial fulfillment
of the requirements for the degree of
Doctor of Philosophy
(Chemistry)
in the University of Michigan
2014

Doctoral Committee

Assistant Professor Bart M. Bartlett
Professor Wei Lu
Professor Adam J. Matzger
Professor Mark E. Meyerhoff
Professor Anton Van der ven

DEDICATION

This thesis is dedicated to my family.

ACKNOWLEDGEMENTS

First, I would like to thank my research advisor, my boss man, Prof. Bart Bartlett. I admire his critical and scientific thinking of research questions. He is a fantastic tutor. I appreciate your encouragement during my inorganic chemistry study. I still recall what you said to me after my small progress. I can't be more grateful for Bart's kind support of my study, life in his group and my future career. I enjoyed my research in our lab. Many thanks, boss.

Thanks a ton to my committee members, Prof. Matzger, Prof. Van der ven, Prof. Meyerhoff, and Prof. Lu. Adam, thanks for allowing me using the equipments and disturbing your lab thousands of times. I really appreciate that. Thanks for all the support from Prof. Lu and all the ABCD members.

I really appreciate the friendship and supports from all the Bartlett members. Thanks to Brendan Liddle for your very kind help when I first joined the group. Thanks Emily and Tanya for helping me with so many small things for past five years. Thank you Joe and Jimmy for chatting with me about the wired stuff. Thanks for Yenting and Vinod's company during the battery research life. Thanks for my undergrad Mark and Scott working with me and making fun of each other. Thanks to all the other members in Bart's lab, Kayla for driving me with her manual car, Ben for Amy's homemade Jello shots, Charlie for his broken arm reminding us never do crazy things. I wish you all the best.

I thank all the people who have helped me during my PhD research outside the Bartlett lab. I thank two of my best friends. Junsi, thanks for all the arguing, helping and

everything. Linjie, thanks for all the sharing and listening. I wish you both the best for your research career. Thanks for all the help and discussion from Antek. Thank you to Prof. Maldonado for letting me borrow great minds and gadgets from your lab. Many thanks to research scientist Dr. Ashfia Huq and Dr. Olivier Gourdon for their research assistance when I was in ORNL.

I also want to specially acknowledge my two friends, Xianke Lin, Dr. Lin Liu who is now a professor at Kansas University. Thank you all for the great conversations. I appreciate all fun with you guys. Let's fight for our new future together.

I thank my friend Zhao Liu at Northwestern University. Although we only stayed together for two weeks, I appreciate your friendship and support.

I thank my friend and current colleague Dr. Kan Huang at Nissan. I wish you the best and looking forward to our future working together. I specially thank my supervisor Dr. Taehee Han who has offered me the great chance in my career. I appreciate all the understanding and support from my current boss Dr. Kenzo Oshihara. Thank you all for the help before I left graduate school.

I thank one of my best friends Yun Wang. Without your support and help, I couldn't gone this far. I appreciate your patience and kindness.

Thanks to Shuai for being very supportive during the past years.

Thank you to my parents. I apologize I didn't accompany you when you need me. I hope to see you folks everyday in the future. Grandfather, I wish you the best in heaven. I did it.

Life is hard, but I never stopped moving forward!

TABLE OF CONTENTS

LIST OF SCHEMES

LIST OF FIGURES

LIST OF TABLES

LIST OF APPENDICES

LIST OF ABBREVIATIONS

CV	cyclic voltammetry
DSC	differential scanning calorimetry
E_g	thermal dynamic window of electrolyte
E^O	standard electromotive force
G^O	Gibbs energy
EIS	electrochemical impedance spectroscopy
EDX	energy dispersive X-ray spectroscopy
EPR	electron paramagnetic resonance spectroscopy
HOMO	highest occupied molecular orbital
ICP-AES	inductively coupled plasmas atomic emission spectroscopy
IR	infra-red
LMO	lithium manganese oxide/$LiMn_2O_4$
LNMO	lithium nickel manganese oxide/$LiNi_{0.5}Mn_{1.5}O_4$
LTO	lithium titanium oxide/$Li_4Ti_5O_{12}$
LUMO	lowest unoccupied molecular orbital
NMR	nuclear magnetic resonance
NPD/ND	neutron powder diffraction
SAED	selected area electron diffraction
SEM	scanning electron microscopy
TEM	transmission electron microscopy
TGA	thermal gravimetric analysis
XPS	X-ray photoelectron spectroscopy
XRD	X-ray diffraction
Φ_A	anode work funtion
Φ_B	cathode work function
μA	anode electrochemical potential
μC	cathode electrochemical potential

ABSTRACT

Lithium-ion batteries have attracted increased attention for energy storage development due to the vast demand from portable electronics, (hybrid) electric vehicles and future power grids. The research in this dissertation is focused on the development of oxide electrodes for lithium-ion batteries with high power density and improved stability.

One of the promising cathodes for lithium-ion batteries is lithium manganospinel ($LiMn_2O_4$). However, this compound suffers from manganese dissolution and a Jahn-Teller distortion due to Mn^{3+}, especially in oxygen deficient $LiMn_2O_{4-\delta}$. Hydrothermal based synthesis methods were developed to eliminate oxygen vacancies to enable high power in cathodes composed of nano-sized spinel particles. The relationship between oxygen defects and the capacity fading mechanism was demonstrated, and collapse of the mechanical structure was identified in defect-rich $LiMn_2O_{4-\delta}$.

Next, the nickel substituted manganospinel, $LiNi_{0.5}Mn_{1.5}O_4$ shows unexpected high voltage side reactions. To overcome this drawback, a thin and chemically inert titanate was used as an artificial SEI (solid electrolyte interface) coating to prohibit transition-metal dissolution and parasitic side reactions, which led to a 200% improvement of the capacity retention at 55 ℃ and negligible polarization losses.

Finally, the spinel-structured lithium titanate ($Li_4Ti_5O_{12}$) is introduced as an anode material for lithium-ion batteries due to its higher operating potential and excellent structural stability compared to current graphite anodes. However, the poor electronic conductivity and low lithium diffusion coefficient hinder its wide application. Given these advantages, a facile, low-cost solution method is explored to synthesize nano-sized titanates. Rapid charge/ discharge was achieved up to rates of 100 *C* (36 second charge/ discharge) due to a shorter lithium mean-free path and better contact between the active material and conductive agents.

CHAPTER 1
Introduction

1.1 Energy storage in batteries

More than 85% of the energy consumption of the world is dominated by non-renewable energy sources, such as, petroleum, natural gas and coal.[1] The depletion of those fossil fuels is accompanied by the inevitable discharge of environmental pollutants and associated climate changes. The current development of advanced technology enhanced the application of renewable energy conversion processes, such as wind and solar power.[2,3] However, lack of highly efficient and cost effective energy storage method hinders the wide application of such renewable energies.[4]

Batteries show the highest potential for efficient electrical storage.[5] Rechargeable battery systems are more practical since they reduce environmental impacts.[6] A rechargeable battery reversibly supplies and restores energy by means of an electrochemical redox reaction.[7] The energy stored is defined as the potential difference between two electrodes (cathode and anode).[8] Notable is that current efficiency of a battery is not limited by the Carnot cycle compared to heat engines, which enables higher efficiencies.[9,10]

Another important component in battery is the electrolyte, which supports mass transfer between the cathode and anode. In addition to electrons flowing through the external circuit, ions in the electrolyte balance the charge internally.[11] The design principle of a rechargeable battery is to select electrodes that offer the highest voltage (energy) and

charge (capacity), while maintaining chemical stability when in contact with the electrolyte. The main challenge is to improve this stability to increase the lifetime of the battery.[12]

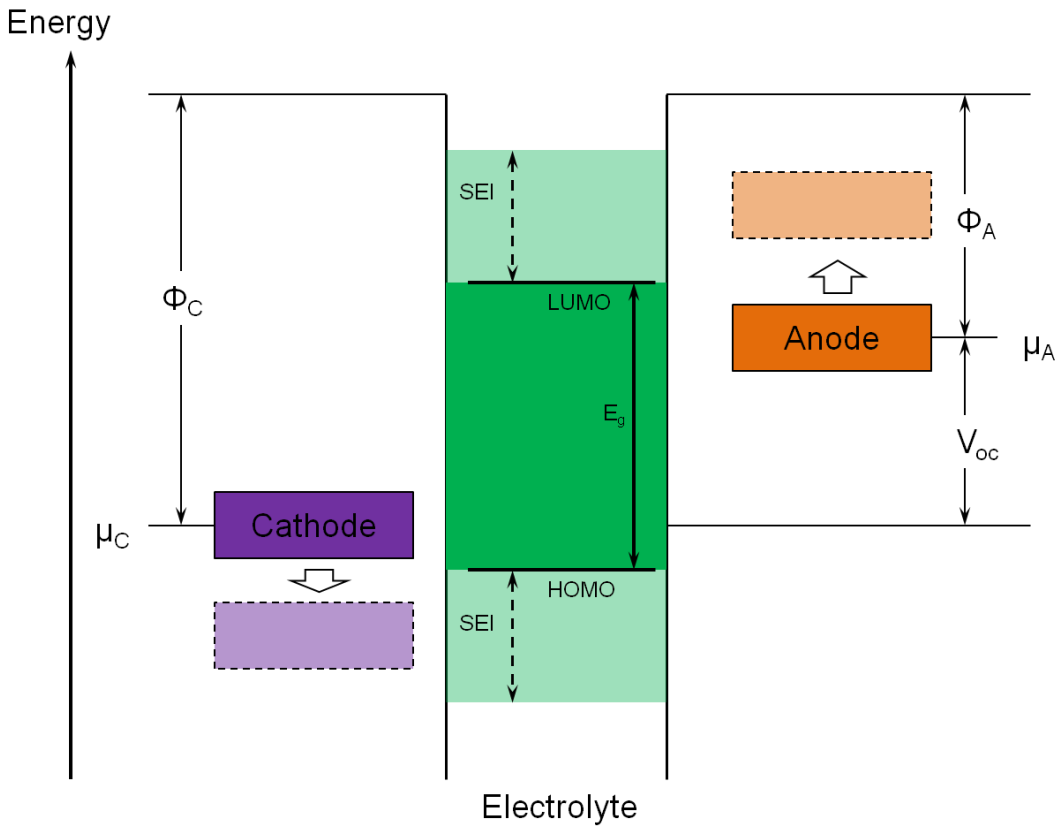

Figure 1.1 Schematic open-circuit energy diagram of electrodes in contact with a liquid electrolyte (adapted from ref. 12). Φ_A and Φ_C are the anode and cathode work functions. Eg is the window of the electrolyte for thermodynamic stability. A $\mu_A >$ LUMO and/or a $\mu_C <$ HOMO requires a kinetic stability by the formation of an SEI layer.

1.2 General consideration of a battery

A battery performs a chemical reaction to convert chemical energy into electrical energy, and vice versa. The battery potential is determined by the Gibbs free energy of the battery reaction,[13,14] which can be expressed as:

$$\Delta G^{O}=-nFE^{O}$$

In this equation, E^{O} is the (standard) electromotive force or open circuit potential of the battery, which is the difference between the anode and cathode's electrochemical potential μ_A and μ_C (when n equals 1). From Figure 1.1, the potential of the battery is limited by the electrolyte and solvent stability window E_g, which is defined by the HOMO (the highest occupied molecular orbital) and LUMO (the lowest unoccupied molecular orbital) of the most reactive species. It's important to match the chemistry of the anode or cathode with the electrolyte. In occasions of mismatch, a solid electrolyte interface (SEI) layer can impart slight kinetic stability to the system.[15,16] The ion mobility within electrodes and electrolyte is small compared to the carrier mobility, which leads to internal resistance. This also hints that the SEI layers should offer good ionic permeability. To improve the stability of the battery, both the bulk and surface properties must considered.[17,18]

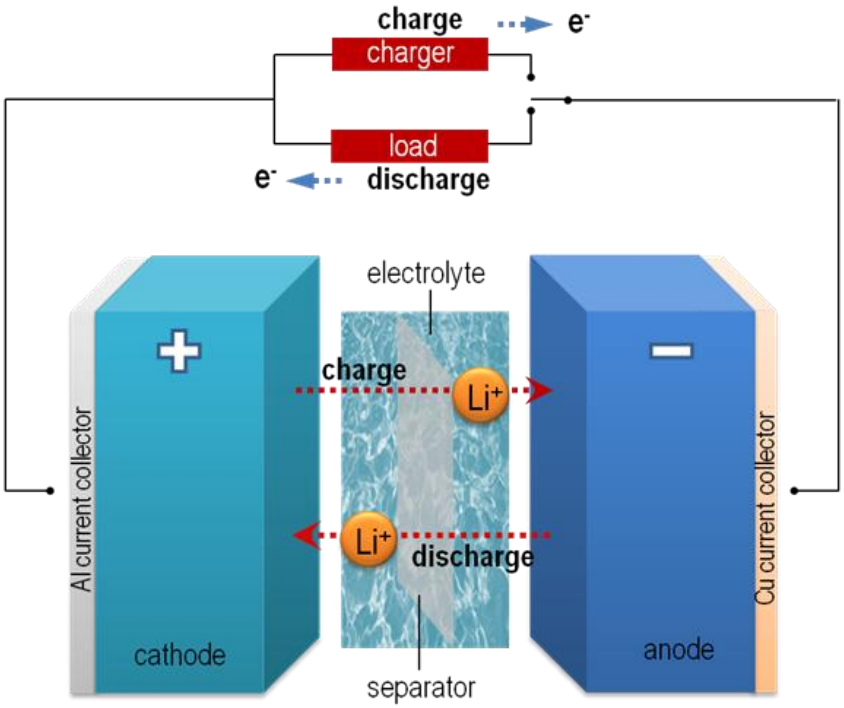

Scheme 1.1 Scheme of lithium ion battery

1.3 Lithium ion battery

Li/Li^+ has low standard potential of -3.04 V versus the standard hydrogen electrode, which suggests that the battery with the highest voltage would be configured with a metallic lithium anode. At the beginning of the lithium battery history, there have been a few systems, such as MoS_3//Li,[19] TiS_2//Li,[20] MnO_2//Li,[21] in which intercalation materials were used as cathodes and pure lithium metal was the anode. However, due to uneven lithium plating and lithium dendrite growth, potential safety concerns have lead to the secondary (Li-ion) concept for lithium battery research.[22,23]

Lithium-ion batteries apply a lithium-ion intercalation material for *both* electrodes.[24] Scheme 1 demonstrates the simplified system of a lithium-ion battery. Lithium ions move between cathode and anode during cycling. The lithium-ion battery has also been known as a "rocking chair" battery based on lithium ion's rocking back and forth.[25] The cathode

material is typically a transition-metal oxide with a layered or tunneled structure.[8] In the 1980s, John Goodenough conceived of using $LiCoO_2$ with a layered structure as the cathode material, which is still the dominant cathode material in lithium-ion batteries.[26] To replace pure lithium as the anode, graphitic carbon was introduced since it shows lithium-ion intercalation ability (Li_xC_6, $0 \le x \le 1$) within its layered sp^2 carbon structure.[27,28] Carbonate based organic solvents and $LiPF_6$ are mostly used to prepare liquid-phase electrolytes for lithium ion batteries.[29,30] To minimize the mass transfer distance between the cathode and anode and maintain electrical isolation, a polymer membrane with microporous structures is used as the separator, which offers a perfect carrier for the electrolyte and pathways for lithium shuttles.[31] Two half reactions are involved during charge or discharge of the battery. Typical charge/discharge reactions could be described by the following equations, in which $LiCoO_2$ and carbon are the cathode and anode, respectively:

$$\text{Cathode: } LiCoO_2 \leftrightarrow Li_{1-x}CoO_2 + xLi^+ + xe^-$$

$$\text{Anode: } 6C + xLi^+ + xe^- \leftrightarrow Li_xC_6$$

$$\text{Overall: } LiCoO_2 + 6C \leftrightarrow Li_{1-x}CoO_2 + Li_xC_6$$

In spite of the wide application, the gradual increase in the cost of $LiCoO_2$ as well as growing safety concerns require the development of other cheaper and greener candidates for its replacement,[32] such as manganese oxide based cathodes with cubic spinel structures.[33,34] Meanwhile, the capacity of $LiCoO_2$ is limited by the instability of $Li_{0.5}CoO_2$ after half of the theoretical capacity has been charged.[35,36,37] In addition, high voltage (i.e. the high oxidation state of cobalt) is catalytic for the thermal runaway of the

battery.[38,39] An energy burst in the form of an explosion results in the case of a battery short-circuit. On the anode side, the potential of lithium intercalation into graphite anode is only 0.2 V vs. Li^+/Li. At relatively low temperature (i.e.—room temperature), lithium dendrite plating can occur even without a lithium metal substrate, which increases the probability of internal short-circuit.[40] The low operating potential stays out of the stability window of the common carbonate electrolyte. Such side reactions cause the SEI layer to grow constantly,which consumes electrolyte and Li^+ ions, and leads to increases in the battery internal resistance.[41] To overcome these issues, more chemically stable intercalation anodes with a higher operation voltage are desired.[12]

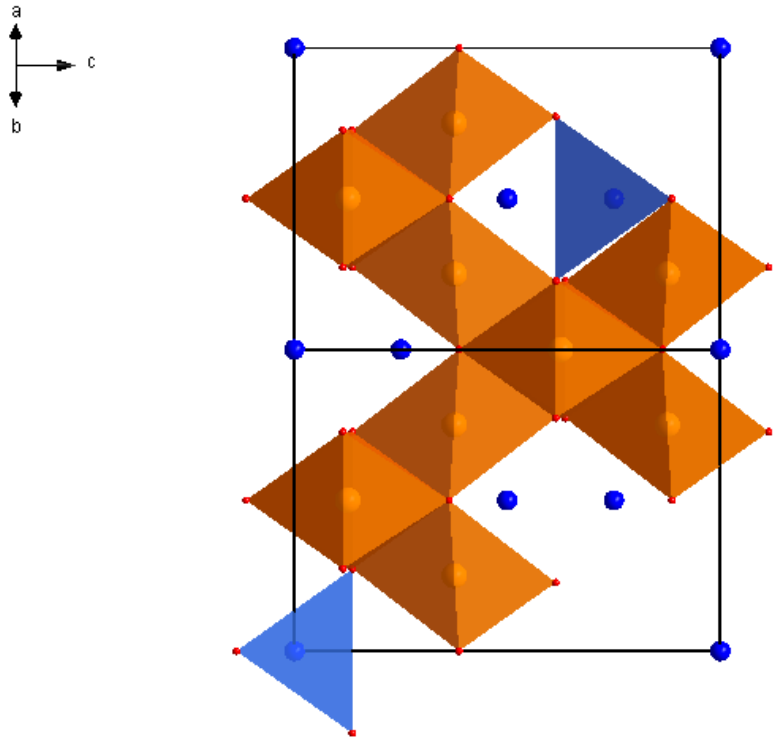

Figure 1.2 Crystal structure of cubic spinel $LiMn_2O_4$, $Li_4Ti_5O_{12}$ or $LiNi_{0.5}Mn_{1.5}O_{4-\delta}$ with space group of *Fd*-3*m*

1.4 $LiMn_2O_4$ and its oxygen defects structure

Stoichiometric $LiMn_2O_4$ has a cubic spinel structure with the space group of *Fd*-3*m*,[42,43] illustrated in Figure 1.2. The lattice parameter, *a* is ~ 8.24 Å. In the structure, lithium ions reside at the 8a tetrahedral Wyckoff sites. During charging delithiation, $LiMn_2O_4$ will be converted to λ-MnO_2, maintaining the cubic oxide anion-close packed array, but with empty lithium sites. This reaction was first discovered through chemical delithiation by mild acid.[33] Later on, Goodenough applied the lithium reversible intercalation chemistry of $LiMn_2O_4$ to a lithium-ion battery.[34,44] Although the one-electron redox reaction is formally between Mn^{3+} and Mn^{4+}, there is only one chemical environment for manganese atoms can be identified in $LiMn_2O_4$. Manganese stays at 16*d* octahedral sites. The formal oxidation state of manganese is then +3.5. and the close packed oxygen anions are located at the 32e octahedral sites with half of the spots filled.

Other than being oxidized or delithiated in the form of $LiMn_2O_4$, lithium insertion can also be accompanied by significant crystal structural rearrangement.[45,46] As lithium insert, all lithium ions will both be located at 16*c* sites, resulting a chemical formula of $Li_2Mn_2O_4$. All the manganese will be reduced to Mn^{3+} during the lithiation. It is known that the ionic radii of Mn^{3+} is slightly larger than Mn^{4+} (0.654 Å *vs* 0.53 Å), which results in an increase of the lattice. More importantly, the MnO_6 octahedral unit distorts from octahedral to tetragonal symmetry, due to the Jahn-Teller effect. Such an effect leads to a 16% increase of the lattice along *c* axis with accompanied structure failure and crystal fracture. The desired lithium insertion chemistry is reversible and occurs at ~4.1 V (vs. Li^+/Li). The second lithium's insertion chemistry occurs at ~ 2.8 V (vs. Li^+/Li), and leads to rapid mechanical degradation. In addition to the Jahn-Teller effect,[47,48] Mn^{3+} has strong tendency to disproportionate according to the following reaction:[49]

$$2\ Mn^{3+} \rightarrow Mn^{2+} + Mn^{4+}$$

This dispropotionation reaction will consume manganese active material and produce the electrolyte soluble species, Mn^{2+}.[50] This corrosion reaction is observable in the SEM image of $LiMn_2O_4$ after long cycling. Therefore, it is important to control the oxidation state of manganese and minimize the side reactions.

Oxygen vacancies can be easily introduced into the cubic spinel structure during traditional high temperature solid state synthesis.[50] The oxygen deficient sample can be written as $LiMn_2O_{4-\delta}$, in which δ is the vacancy factor. To maintain charge neutrality, the oxidation state of manganese is forced to be lower than +3.5, which leads to a higher risk of corrosion based on the arguments presented above. Just below room temperature (~10 ℃), oxygen-deficient $LiMn_2O_{4-\delta}$ suffers a phase change from a cubic structure to a tetragonal or orthorhombic one, leading to a structural stability issue at low temperatures.[51] During electrochemical cycling, cation mixing and an unwanted phase change from cubic spinel to double-hexagonal also contribute to the stability issue of the cathode material, although the detailed failure mechanism of $LiMn_2O_4$ related to the oxygen defects is still unclear.[52] The challenge lies in how to control the oxygen content and improve the stability of $LiMn_2O_4$. This work is discussed in Chapter 2 and 3.

1.5 High voltage cathode $LiNi_{0.5}Mn_{1.5}O_4$

$LiMn_2O_4$ has a theoretical capacity A of 148 mAh/g based on one lithium ion's intercalation chemistry. The average redox potential E of manganese is ~ 4.0 V. The theoretical gravimetric (specific) energy density as the product of AE is ~ 600 Wh/kg. One effective way to improve the gravimetric energy density of lithium manganospinel is to raise the reaction potential of the cathode material by introducing new redox active

element, such as nickel.[53] In $LiNi_{0.5}Mn_{1.5}O_4$, Ni possesses an ionic valence of +2. By 25% substitution to lower valence Ni, all the Mn stays at the uniform oxidation state of +4. Ni will be oxidized during charging from +2 to +4, maintaining one lithium deintercalation process. The reversible cycling reaction of $LiNi_{0.5}Mn_{1.5}O_4$ occurs with an average potential of 4.7 V. Although $LiNi_{0.5}Mn_{1.5}O_4$ and $LiMn_2O_4$ show similar theoretical capacities based on the lithium cation, the gravimetric energy density of $LiNi_{0.5}Mn_{1.5}O_4$ is ~ 15% larger than $LiMn_2O_4$ due to higher voltage, which enables it as a good cathode material candidate.

The stoichiometric $LiNi_{0.5}Mn_{1.5}O_4$ adapts a primitive simple cubic structure with space group of $P4_332$.[54,55] Figure 6 shows the structure of $LiNi_{0.5}Mn_{1.5}O_4$. Ni and Mn cations locate at different octahedral sites as 4*a* and 12*d*, respectively. In this structure, Li stays at tetrahedral 8*a* sites. Oxygen can be found at either 24*e* or 8*c* sites. Similar to $LiMn_2O_{4-\delta}$, oxygen vacancies can also be introduced into the structure which can be noted as $LiNi_{0.5}Mn_{1.5}O_{4-\delta}$. In the oxygen deficient $LiNi_{0.5}Mn_{1.5}O_{4-\delta}$, Ni maintains the oxidation state of +2. On the other hand, the average oxidation state of Mn will be dropped to lower than +4. During cycling, the $Mn^{3+/4+}$ redox couple will be activated compared to purely functional $Ni^{2+/4+}$ in $LiNi_{0.5}Mn_{1.5}O_4$. Furthermore, $LiNi_{0.5}Mn_{1.5}O_{4-\delta}$ is isostructural with $LiMn_2O_4$ (space group of *Fd*-3*m*). Ni and Mn are randomly distributed at 16*d* sites. Li stays at 8*a* sites with oxygen at 32*e* sites.

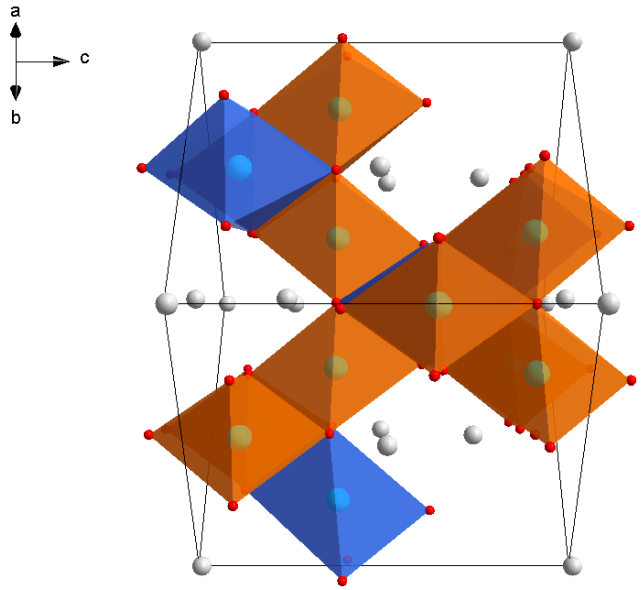

Figure 1.3 Crystal structure of stoichiometric $LiNi_{0.5}Mn_{1.5}O_4$ with space group of $P4_332$

An optimized charge-transfer mechanism is important to improve the rate capacity of the battery. Materials with small particle sizes have a larger surface-volume ratio, which enables better contact between the active electrode material and the electrolyte and conductive agent.[56] The electron transfer is more facile at the surface of the compound. Meanwhile, Li cations stay in the 3D tunnels of the spinel structure composed of closed-packed oxide anions. The charge transfer inside the bulk material occurs through lithium diffusion along those channels. Materials with open tunnels facing toward the electrolyte enable faster charge transfer at the electrode/electrolyte interface.[57] Compared to $LiNi_{0.5}Mn_{1.5}O_4$, oxygen deficient $LiNi_{0.5}Mn_{1.5}O_{4-\delta}$ shows better electrochemical

performance and structural stability, due to the higher electrical conductivity.[58] Other than artificially introducing controlled oxygen defects, small sized particles with preferred orientation are necessary to assist the charge transfer and lithium diffusion during cycling. This research is discussed in Chapter 4.

1.6 Artificial SEI layer on $LiNi_{0.5}Mn_{1.5}O_{4-\delta}$

The electrochemical performance of the electrode material is significantly influenced by the interface between the electrode and the electrolyte. Current liquid electrolyte systems employ carbonates as solvents as discussed above. However, the stability window of these solvents limits the operation potential of the battery to be lower than 4.7 V in the presence of fluorine contained salt. Reactions such as electrolyte decomposition will happen during cycling and cause battery failure. Such side reactions at high voltage could lead to accumulation of reaction products and corrosion of the electrode material's surface.

There have been reports of studying protection layers on the surface of the electrodes to improve the electrochemical stability of the battery.[59,60] In this case, the protection layers need to be thin or porous, which still support lithium permeability. And it should also be more chemically inert compared to the electrode material itself. This study has been applied to tatina coatings on $LiNi_{0.5}Mn_{1.5}O_4$, and discussed in Chapter 5.

1.7 $Li_4Ti_5O_{12}$ anode

Graphitic carbon is used as the dominant anode material for current lithium-ion batteries. However, due to the low lithium intercalation potential, SEI growth and lithium dendrite formation, the developing of new anode materials is necessary because of the safety concerns. Titanium oxide-based anodes have drawn more attention recently due to their low cost, low toxicity, and higher intercalation potential. TiO_2 with either the

anatase or rutile structure shows a high theoretical capacity of 337 mAh/g, and the electrochemical reaction toggles the $Ti^{4+/3+}$ redox couple. However, this material suffers from a structural stability issue as a lithium intercalation material.[61,62] Recently, TiO_2-(B) with a nano morphology has been studied with high potential to be the next generation anode material.[63,64] This material shows high capacity and excellent structural stability during cycling. However, due to the typical low temperature synthesis route, water molecules are often found in the structure, which function to stabilize the structure of the compound.[65] This lattice water may prohibit future practical application of this material.

$Li_4Ti_5O_{12}$ is another cubic spinel material and it shows better potential as anode candidate for lithium ion batteries.[66] The chemical formula of the compound could be written as $Li_{4/3}Ti_{5/3}O_4$. In the cubic unit cell, oxygen and titanium take the 32*e* and 16*d* sites, respectively.[67] 25% of the lithium stays at 16*d* sites with the rest occupying 8*a* sites. During charging of this material, one lithium can insert into $Li_{4/3}Ti_{5/3}O_4$ at ~ 1.5 V corresponding to theoretical capacity of 175 mAh/g. There is a 0.2% volume change detected between $Li_{4/3}Ti_{5/3}O_4$ and $Li_{7/3}Ti_{5/3}O_4$, resulting in a "zero strain" material with excellent cyclability. Meanwhile, the operating potential of the anode prohibits dendrites formation and fast accumulation of the SEI layer during cycling.

The redox active species in $Li_4Ti_5O_{12}$ is Ti^{4+} with a valence electron configuration of $3d^0$, which gives an electrical conductivity as low as 10^{-13} S/cm.[68] Meanwhile, the lithium diffusion rate is limited by the two phase reaction at 1.5 V between $Li_7Ti_5O_{12}$ and $Li_4Ti_5O_{12}$. There has been reports of the lithium diffusion coefficient as 10^{-14} to 10^{-17} cm^2/s. Both of these factors significantly influence the rate capability of the compound. To improve conductivity, there have been reports of applying dopants to narrow the

original wide band gap.[69,70] In addition, surface coatings, typically by conductive carbon, are favored by researchers to increase conductivity.[71,72] An effective way to facilitate lithium diffusion is to shrink the particle size to the nano scale. Nevertheless, this material still suffers from serious aggregation due to high surface energy of the nano-sized materials.[73,74] The big challenge is to synthesize nano-sized materials with minimized aggregation; in this case, much better contact between active $Li_4Ti_5O_{12}$ and conductive agents will help to improve the charge transfer during battery operation.

1.8 Outline

This thesis is focused on synthesis, structural analysis and optimization of electrochemical properties of electrode materials for lithium-ion batteries. Chapters 2 to 5 will present manganese-based cathode materials with cubic spinel structures. Chapter 6 will focus on the novel synthesis of $Li_4Ti_5O_{12}$ as a lithium-ion battery anode.

In Chapter 2, a hydrothermal synthesis method is discussed for preparing nano-sized $LiMn_2O_4$ with controllable oxygen content. The comparison of stoichiometric and oxygen deficient structures will be discussed (both physical and chemical differences), defect structure analysis using advance neutron diffraction.

Next, the failure mechanism of $LiMn_2O_4$ with oxygen vacancies will be discussed in Chapter 3. From the view of structural analysis, a commercially available oxygen-deficient sample has been studied. A structural failure related mechanism based on detailed diffraction and microscopy experiments has been carried out. In the end, the proposed mechanism of microstructural failure is expanded to lab synthesized materials.

Chapter 4 will introduce a two-step synthesis of high voltage $LiNi_{0.5}Mn_{1.5}O_{4-\delta}$ with controlled particle size and designed crystal growth directions. The final products show

optimized rate capability and excellent electrochemical stability within set potential limits.

To improve the stability of the high voltage cathode $LiNi_{0.5}Mn_{1.5}O_{4-\delta}$, Chapter 5 presents the development of novel artificial SEI layer coatings on the cathode material. Both the coating layer and cathode after coating has been characterized to achieve optimized properties of the products. The electrochemical performance of surface-protected materials is compared with the "bare" cathode to highlight the significance of the artificial SEI.

Chapter 6 will be focused on novel synthesis of nano-sized anode $Li_4Ti_5O_{12}$. In this chapter, the importance of preparing nano-sized material with minimal particle aggregation is emphasized. The synthesis mechanism is presented, which could be applied to future studies of analogous materials. The electrochemical performance of this anode has been tested in batteries to demonstrate its superior high rate capability.

In Chapter 7, I will offer conclusions and perspective on future directions in structural analysis of electrode materials, *in-situ* analysis,and the function mechanism of artificial SEI layers.

Following the main thesis, there are appendices containing supporting data pertinent to certain chapters. The appendix figures are appropriately referenced in each chapter.

CHAPTER 2

Identifying and Eliminating Oxygen Vacancies: a Case Study of Lithium Manganospinel Oxide Prepared by Hydrothermal Method

Portions of this chapter have been published:

Hao, X.; Gourdon, O.; Liddle, B. J.; Bartlett, B. M. *J. Mater. Chem.* **2012**, *22*, 1578-1591.

2.1 Introduction

Lithium-ion batteries have emerged as the preeminent technology for electrical energy storage in commercial application such as portable electronics, cellular communication, and even vehicle electrification. A battery is graded on three criteria: energy density, power density, and lifetime; all three need to be as large as possible. In developing chemistry for batteries, new electrode materials or alternative synthesis methods for existing electrode materials are only welcome if they result in improvements based upon these criteria. Accordingly, for any well-established battery material, the race is on to develop synthesis methods that optimize particle size and morphology in such a way that high energy density, high rate capability, and negligible capacity fade distinguish the electrochemistry of the resulting product from similar compositions prepared by tried and true conventional solid-state methods.

In this realm, the spinel structure of lithium manganese oxide, $LiMn_2O_4$, is one of the most well-studied battery materials because, in theory, two lithium ions (and therefore two electrons) can reside in the unit cell giving a range of compositions from $Li_2Mn_2O_4$ to Mn_2O_4 (= λ-MnO_2).[75,76] As synthesized, $LiMn_2O_4$ is formally mixed-valent Mn^{4+} and Mn^{3+}. However, all manganese ions in the cubic structure are crystallographically equivalent, residing on the 16d Wyckoff site of the $Fd\bar{3}m$ space group.[77] Therefore, it is more appropriate to describe manganese as having an oxidation state of +3.5. In the full range of compositions, this gives an overall gravimetric energy storage capacity of ~285 mAh/g. In practice however, only ~½ of this capacity is used; as the oxidation state of Mn drops below +3.5, the compound undergoes a symmetry-lowering phase transition that corresponds directly with the irreversible Jahn-Teller distortion of Mn^{3+}.[78,79] In fact, even if the material is cycled only between the end members Mn_2O_4 and $LiMn_2O_4$ at a potential of ~4.1 V vs. Li^+/Li (where the average oxidation state of manganese remains greater than or equal to +3.5), fracture of micron-sized crystallites occurs as the local lithium-ion concentration at the surface increases. The accumulation of Li^+ promotes Mn^{3+} disproportionation into Mn^{4+} and electrolyte-soluble Mn^{2+}.[80] Dissolution of manganese into the electrolyte results in severe and rapid capacity fade. In order to mitigate this surface chemistry and maintain sufficient lithium-ion diffusivity for reasonable kinetics, submicron to micron-sized particles are thought to be ideal.[81]

From a historical perspective, it was almost immediately recognized that the mere presence of the Jahn-Teller active Mn^{3+} ion may render the cubic spinel structure too unstable with respect to other structures and compositions for practical application.[82] However, the many open sites on the spinel lattice (only 1/8 of all tetrahedral sites and

only ½ of all octahedral sites are filled) and the possibility of non-stoichiometric compositions in the forms of both cation substitution and oxygen vacancies give it a rich chemistry that can be exploited to maintain the cubic structure during electrochemical cycling.[80–86] Moreover, if nanoscale particles can be stabilized such that energy density is not sacrificed due to the aforementioned surface reactions, high power density in lithium manganospinel cells can be realized.[87] There are many reports on using hydrothermal synthesis to prepare nanoscale lithium manganospinel.[88–102]Most of these methods yield materials with some substitution of lithium for manganese on the 16d sites and also have oxygen vacancies, a well established property of spinels.[103] Substituting lithium on the octahedral sites is beneficial for preventing surface fracture by increasing the manganese oxidation state,[104] but this comes at the expense of some capacity since lithium residing on the 16d sites cannot be extracted. However, oxygen vacancies lower the manganese oxidation state, and the detrimental effects of oxygen vacancies have been well documented in the lithium manganospinel literature.[82,105–109] Our group recently reported a hydrothermal method for preparing Li-rich spinel nanoparticles by the permanganate oxidation of acetone in an aqueous solution of lithium hydroxide.[110] Here, we report the structural chemistry and battery performance of our hydrothermally synthesized materials.

2.2 Experimental

2.2.1 General Considerations

Potassium permanganate 99.0% was purchased from J. T. Baker. Lithium hydroxide 98%, lithium hexfluorphosphate 99.99%, ethylene carbonate and diethyl carbonate solvents were purchased from Aldrich. The solvents were dried over P_2O_5 prior to storing a Vacuum Atmospheres OmniLab glove box under an argon atmosphere.

Lithium foil was obtained from Strem Chemicals. Iron (II) chloride (99.5%, argon packed) was purchased from Alfa Aesar. N_2 and O_2 gases (99.99+%) were purchased from Metro Cyrogenics. HPLC-grade acetone was purchased from EMD Chemicals and distilled prior to use.

Powder X-ray diffraction patterns were obtained with a Brüker D8 Advance diffractometer equipped with a Lynx-Eye detector and parallel beam optics using Cu-Kα radiation (λ= 1.54184 Å). XRD patterns were indexed and refined using the TOPAS program from Brüker AXS. Scanning electron microscopy images were obtained using a FEI Nova Nanolab SEM/FIB with an accelerating voltage of 10 kV. Infrared spectra were obtained with a Nicolet 6700 FT-IR spectrometer from Thermo Scientific with a MCT-B detector. All the spectra were collected as an average of 5000 scans with 4 cm^{-1} resolution. The BET surface area measurements were obtained from nitrogen sorption isotherms with a NOVA 4200e. All samples were heated in a standard laboratory Fisher vacuum oven 120 ºC prior to the measurement. Thermal analysis was obtained with a TGA7 Thermogravimetric Analyzer (Perkin Elmer) at a heating rate of 10 ºC under air or nitrogen flow, and differential scanning calorimetry was obtained with a DSC Q10 (TA instruments) at a heating rate of 10 ºC. DSC data were analyzed by the Universal Analysis 2000 software package.

2.2.2 Hydrothermal Synthesis and Annealing

All of the spinel-structured compounds in this study were prepared by hydrothermal treatment of 0.158 g (1.00 mmol) $KMnO_4$ in 12 mL 0.1 M LiOH(*aq*) with 1.00 mmol of acetone. Reactions were carried out in 23 mL PTFE-lined, stainless-steel Parr autoclaves which were sealed in a Plas-Lab wet box. The lithium hydroxide solution was purged

with N_2 gas or O_2 gas prior to sealing in the wet box under the same N_2 or O_2 atmosphere where appropriate. Autoclaves were heated to 200 ºC at a rate of 10 ºC/min. After a dwell time of five hours, reactions were cooled to room temperature at a rate of 5 ºC/min. Dark green microcrystalline powders were collected by centrifugation, washed several times with deionized water, and dried overnight in a vacuum oven at 120 ºC. Subsequent annealing was performed in an MTI compact muffle furnace at 500 ºC for 4h under ambient room atmosphere.

2.2.3 Elemental Analysis

ICP-AES elemental analysis for Li and Mn was obtained using a Perkin-Elmer Optima 2000DV. Samples were digested in 3-5 mL conc. HNO_3 with a few drops of H_2O_2. Samples were references to an yttrium internal standard and concentrations of lithium and manganese were determined from the maximum intensity lines (610.632 nm for Li; 257.610 nm for Mn) compared to those of standard reference solutions. The average oxidation states of manganese were determined by a potentiometric titration using $FeCl_2$/$KMnO_4$. 20 mg samples were digested in 0.020 M $FeCl_2$ solutions of 10% H_2SO_4 that were titrated against 4.68 mM $KMnO_4$ according to the balanced equation:

$$5Fe^{2+}(aq) + MnO_4^-(aq) + 8H^+(aq) \rightarrow 5Fe^{3+}(aq) + Mn^{2+}(aq) + 4H_2O(l)$$

2.2.4 Electrochemical Measurements

Active cathode mixtures were prepared by mixing the synthesized spinel material, carbon black and poly(vinylidene) fluoride (PVDF) using a mass ratio of 75:15:10 with a Thinky AR-100 rotation/revolution super mixer. *N*-methyl-2-pyrrolidone (NMP) was added to dissolve the PVDF and to maintain appropriate viscosity of the black slurry. This material was coated onto a de-oiled aluminum foil using the doctor blade method.

Then, the foil was dried in the vacuum oven overnight at 120 ºC prior to assembling the cell. The cathode and Celgard™ poly(propylene) film were cut and fit into a ¼″ Swagelok™ PTFE union under ambient room atmosphere. The partially assembled cell was then pumped into a Vacuum Atmospheres OmniLab glove box under argon, where cell assembly was completed. The electrolyte solution was composed of 1 M $LiPF_6$ in 2:1 (v/v) ethylene carbonate and diethyl carbonate, and lithium foil was used as the anode.

Cyclic voltammetry measurements were performed on an eight-channel CH Instruments 1000 Electrochemical Workstation at a scan rate of 0.1 mV/s. Gavlanostatic charge/ discharge measurements at the rate *C*/10 were recorded with CH Instruments 660C Electrochemical Workstation. Higher current charge/ discharge curves were recorded on a custom-designed Vencon UBA5 battery analyzer. Cycling at 55 ºC was accomplished by submerging the Swagelok cell into a heated sand bath maintained at constant temperature using a Variac transformer.

Electrochemical impedance spectra (EIS) were recorded on an Autolab PGSTAT302N with a FRA (frequency response analysis) module. Prior to EIS measurements, the cells were cycled 3 times between 3.4 and 4.45 V at current *C*/3. Then the EIS were recorded at various requested potentials from 4.00 to 4.40 V with a 1 hour equilibrium time such that the current flow declined to less than 5 nA. The AC perturbation was ±10 mV, and the frequency range was from 10^5 to 10^{-2} Hz. Data were fit using the Zview™ software package.

2.2.5 Powder Neutron Diffraction

Time-of-flight neutron diffraction experiments for air synthesized and air annealed samples were performed on a powder diffractometer (POWGEN) in a vanadium can

sample holder by applying a spallation neutron source (SNS) at ORNL (Oak Ridge National Lab). Differing from nearly all other time-of-flight (TOF) neutron powder diffractometers, the design of POWGEN is based on combining the diffracted neutrons collected at all angles into a single profile rather than assigning them to series of different profiles that traditionally were based on grouping detectors according to scattering angle. Such a unique approach yields to a high count rate while preserving good resolution $\Delta d/d = 0.0015$ at $d = 1$ Å. The diffraction data were collected at 293 K using incident neutron beam wavelengths centered at 1.066 Å and 3.198 Å for *d*-spacing ranges of 0.29–3.09 Å and 1.47–7.21 Å, respectively. The collected diffraction patterns were calibrated using a LaB_6 standard before Rietveld refinement using the software Jana2006.

2.3 Results

2.3.1 Establishing composition by ICP-AES, and potentiometric titration

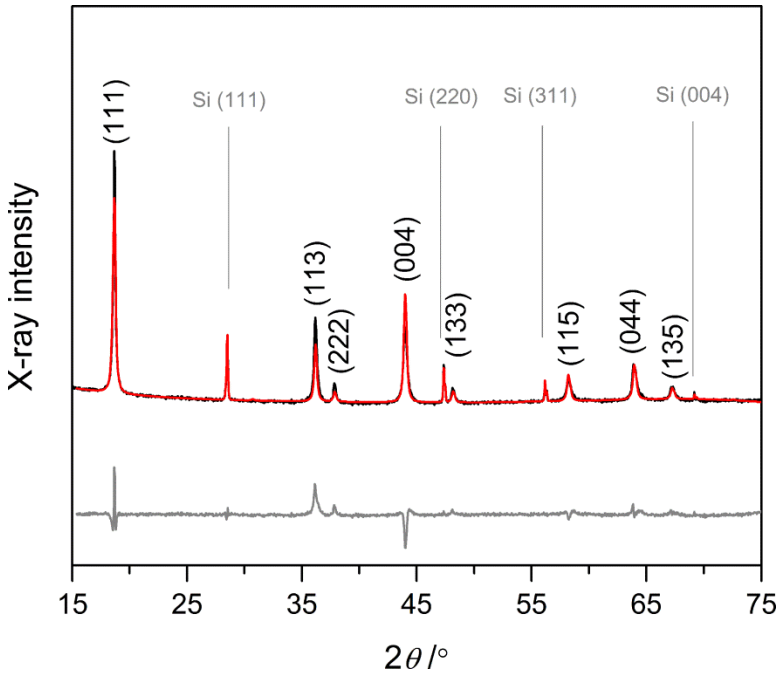

Figure 2.1 X-ray diffraction pattern of lithium manganospinel synthesized in air under hydrothermal conditions. The black, red, and gray traces represent the experimental pattern, the Rietveld refinement, and the difference pattern respectively. Miller indices for lithium manganospinel are shown in black. 10% silicon was added as an internal reference and its Miller indices are shown in gray.

The lithium manganese oxide spinel compounds in this study were prepared by hydrothermal synthesis starting from potassium permanganate, lithium hydroxide, and acetone according to the balanced equation:

$$4\mathrm{LiOH}(aq) + 8\mathrm{KMnO_4}(aq) + 6(\mathrm{CH_3})_2\mathrm{CO}(l) \rightarrow$$

$$4\mathrm{LiMn_2O_4}(s) + 6\mathrm{CH_3COCHO}(l) + 8\mathrm{KOH}(aq) + 4\mathrm{H_2O}(l) + \mathrm{O_2}(g) \quad (1)$$

In order to form spinel as the only solid-state product of the reaction (i.e.—without the common Mn_3O_4 haussmanite impurity present), we have discovered that reactions performed in a total volume of 12 mL of 0.1 M LiOH (1.20 mmol) with 1.00 mmol $KMnO_4$ and 1.00 mmol $(CH_3)_2CO$ heated to 200 ºC for 5 h are ideal. We have previously shown that pyruvaldehyde can be isolated from reaction mixture once the vessels have

cooled. Moreover, when considering the excess base added to the reaction, the ratio of LiOH to $KMnO_4$ remains 1:2 in the balanced equation even for the complete 16-electron oxidation of acetone to carbon dioxide:

$$16LiOH(aq) + 32KMnO_4(aq) + 7(CH_3)_2CO(l) \rightarrow$$
$$16LiMn_2O_4(s) + 21CO_2(g) + 32KOH(aq) + 13H_2O(l) \qquad (2)$$

The solid product in the balanced equations above is written as stoichiometric $LiMn_2O_4$. Figure 2.1 shows the X-ray diffraction pattern of lithium manganospinel synthesized using the hydrothermal conditions described above, noting that the vessels are sealed under the ambient room atmosphere. The lattice parameter is slightly smaller for this compound compared to that of stoichiometric $LiMn_2O_4$, (8.242 *vs*. 8.248 Å). The compound $LiMn_2O_4$ is formally mixed-valent with an average manganese valence, Z_{Mn}, of exactly 3.5. However, in the structure, manganese resides on a special position (16*d* octahedral sites) such that all manganese ions are symmetrically equivalent, related by a three-fold inversion axis and a mirror plane. A smaller lattice constant implies that the average manganese valence is greater than 3.5, and one way to accomplish this is the aliovalent substitution of lithium for manganese on the octahedral sites, where the average oxidation state of manganese must increase to maintain electroneutrality:

$$Li_{1+x}Mn_{2-x}O_4 \equiv [Li]_{8a}[Li_x,Mn_{2-x}]_{16d}[O_4]_{32e} \qquad (3)$$

where the subscripts outside brackets denote Wyckoff positions on the spinel lattice. Mn^{4+} is smaller (6-coordinate, high spin ionic radius = 0.67 Å) than is Mn^{3+} (0.72 Å), and the average oxidation state of manganese, Z_{Mn}, is related to the degree of ion substitution by $\frac{7-x}{2-x}$. The compound is still considered to be stoichiometric because the total number of cations in the formula unit remains 3 and the number of anions is 4.

ICP-AES analysis confirms that compounds prepared by our hydrothermal synthesis have a Li:Mn ratio greater than 0.5. However, potentiometric titration of manganese against ferrous iron gives a surprisingly smaller Z_{Mn} of +3.47. This hints that cation substitution alone does not tell the full story of spinel synthesized by hydrothermal methods. Rather, vacancies in the oxygen sublattice, a nonstoichiometric defect in the spinel structure, must also be considered. To demonstrate further the presence of oxygen vacancies that result from hydrothermal synthesis, we observe that the lattice parameter gets smaller still (8.228 Å) and Z_{Mn} increases (+3.57) after annealing the sample in air at 500 ºC for 4 h. Importantly, ICP-AES shows that the Li:Mn ratio is unchanged after annealing. We can understand our diffraction and titration results by considering first the formula for spinel with no cation substitution but with oxygen vacancies, $LiMn_2O_{4-\delta}$. Here, Z_{Mn} is given by $\frac{7-2\delta}{2}$, where the presence of oxygen vacancies lowers Z_{Mn}. By annealing in air, atmospheric oxygen is reduced at the surface and fills in these vacancies according to the reactions:

$$\delta/2\ O_2(g) \rightarrow \delta(O_{ads}) \quad (4)$$

$$\delta(\square_O^{\bullet\bullet}) + \delta(O_{ads}) + 2\delta e' \rightarrow \delta(O_O^{\times}) \quad (5)$$

in the standard Kröger-Vink notation. Notably, the electrons in the equation 5 are transferred from manganese; thus filling in oxygen vacancies increases Z_{Mn}.

Therefore, in compounds prepared by hydrothermal methods, the overall formula is best represented as having both cation substitution and oxygen vacancies, $Li_{1+x}Mn_{2-x}O_{4-\delta}$. Now, Z_{Mn} is determined by the formula $\frac{7-x-2\delta}{2-x}$. The mole fraction of lithium that substitutes on the 16*d* sites, *x*, can be measured directly from the Li:Mn ratio from ICP-AES analysis. We cannot analyze directly for oxygen using this technique, but we can

couple x with Z_{Mn} from our titration data to estimate δ, the oxygen non-stoichiometry. Table 2.1 compares elemental analysis data and X-ray data for all synthesized and annealed samples. The monikers "air," "N_2" and "O_2" in the text, table, and figure captions refer only to the atmosphere under which the hydrothermal reaction was carried out. Then, the terms "synthesized" and "annealed" refer to those compounds studied directly upon filtering the products under ambient conditions and those compounds that were subsequently annealed in air at 500 ºC for 4h, respectively.

Table 2.1 Characterization and electrochemistry of lithium manganospinels compared in this study.

	Air synthesized	Air annealed	N_2 synthesized	N_2 annealed	O_2 synthesized	O_2 annealed
a (Å)	8.242	8.228	8.244	8.230	8.230	8.221
Li:Mn	0.508	0.508	0.504	0.504	0.506	0.506
Z_{Mn}	3.47	3.57	3.45	3.55	3.47	3.58
Empirical Formula	$Li_{1.01}Mn_{1.99}O_{3.95}$	$Li_{1.01}Mn_{1.99}O_{4.06}$	$Li_{1.01}Mn_{1.99}O_{3.94}$	$Li_{1.01}Mn_{1.99}O_{4.04}$	$Li_{1.01}Mn_{1.99}O_{3.96}$	$Li_{1.01}Mn_{1.99}O_{4.07}$
SA (m^2/g)	65.5	54.6	61.7	68.1	56.0	59.5
Initial capacity at C/10 (mAh/g)	138	137	127	132	144	118
Initial discharge at C/10 (mAh/g)	117	106	116	124	116	112
Discharge capacity at C/3 (mAh/g)	114–86	122–101	116–87	116–91	120–108	115–108
% Capacity fade after 100 cycles at C/3	25.0	17.2	25.0	21.6	10.0	6.1

2.3.2 Altering the oxygen stoichiometry through synthesis

Hydrothermal synthesis is performed under constant volume, and we have prepared spinel-structured compounds in vessels sealed under ambient room atmosphere, under a pure nitrogen atmosphere, and under a pure oxygen atmosphere (99.99% gas purity) in order to compare the degree of cation substitution and oxygen vacancies that result. To ensure a pure atmosphere, the aqueous lithium hydroxide solution was thoroughly purged (at least 2 h) with the gas of interest prior to starting the reaction. Table 1 shows that as we increase the partial pressure of oxygen in the reaction vessel, we observe fewer oxygen vacancies in the synthesized spinel product (determined from ICP and titration data). Rietveld refinement of XRD data shows that as the oxygen content of the synthesis atmosphere increases from 0% (N_2) to 100% (O_2), the lattice parameter, a, indeed decreases from 8.244 Å to 8.223 Å when assigned to the space group $Fd\bar{3}m$. After annealing these samples at 500 ºC for 4 h in air, we observe the same trend: a decreases and Z_{Mn} increases. X-ray diffraction patterns with for all compounds is presented in Figure A.1. In a control experiment, we find that heat alone does not result in a smaller unit cell or increased Z_{Mn}; in fact, annealing lithium mangnospinels in pure N_2 at 500 ºC results in a slight increase of a to 8.250 Å (Figure A.2), and Z_{Mn} is +3.31.

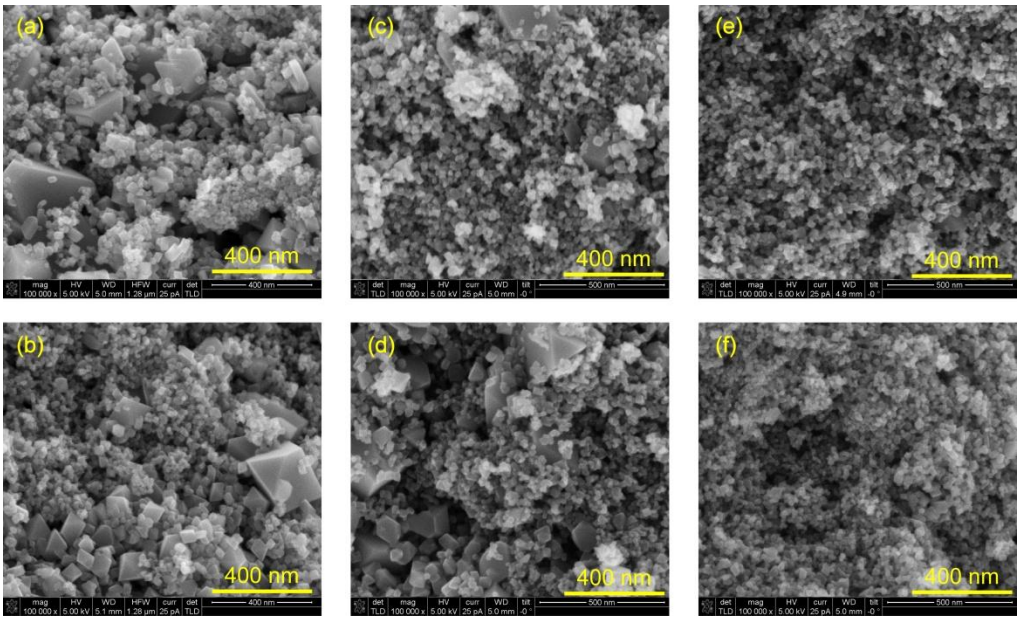

Figure 2.2 SEM images of lithium manganospinels synthesized by hydrothermal methods: a) airsynthesized; b) air annealed; c) N_2 synthesized; d) N_2 annealed; e) O_2 synthesized; f) O_2 annealed.

All of the spinel compounds prepared in this study crystallize as nanoparticles with a mean size of ~30 nm, illustrated in the SEM image of Figure 2.2. Interspersed in these nanoparticles are some larger 100–300 nm particles. Important to our work, particle size is conserved upon annealing—that is, no interfacial crystal growth occurs at 500 ºC. In addition, nitrogen sorption isotherms in Figure A.3 show that hydrothermally synthesized lithium manganospinels have surface areas (determined by the BET method) on the order of 60 m^2/g, but show type-II (non-porous) behavior. These areas are similar to those observed in materials prepared by calcination of lithium salts and electrolytic grade manganese oxide at temperatures below 500 ºC.

2.3.3 Observing lattice distortion by PND

The X-ray scattering factor for lithium is small as it scales with atomic number ($Z = 3$). Therefore, we turned to powder neutron diffraction to determine the structure and site occupancy factors for lithium manganospinel. $LiMn_2O_4$ known from the literature adopts

the cubic $Fd\bar{3}m$ structure, therefore, as a first attempt such cubic symmetry was used to refined the data collected on the $LiMn_2O_4$ synthesized in the air. However, such refinement leads to a poor reliability factor and the difference curves on the refinement showed poor agreement, particularly with the (004) reflection. As shown in the inset of the Figure 3a, this $(004)_c$ reflection, could be better described by the three independent reflections {(004), (040) and (400)}. Therefore, refinement using a *Fddd* orthorhombic symmetry (a subgroup of $Fd\bar{3}m$) was performed, leading to a noticeable improvement of the refinement to a satisfactory R = 7.3%. The pattern is shown in Figure 2.3, and the cell parameters refined as a = 8.2808(3) Å, b = 8.2133(3) Å and c = 8.24006(3) Å.

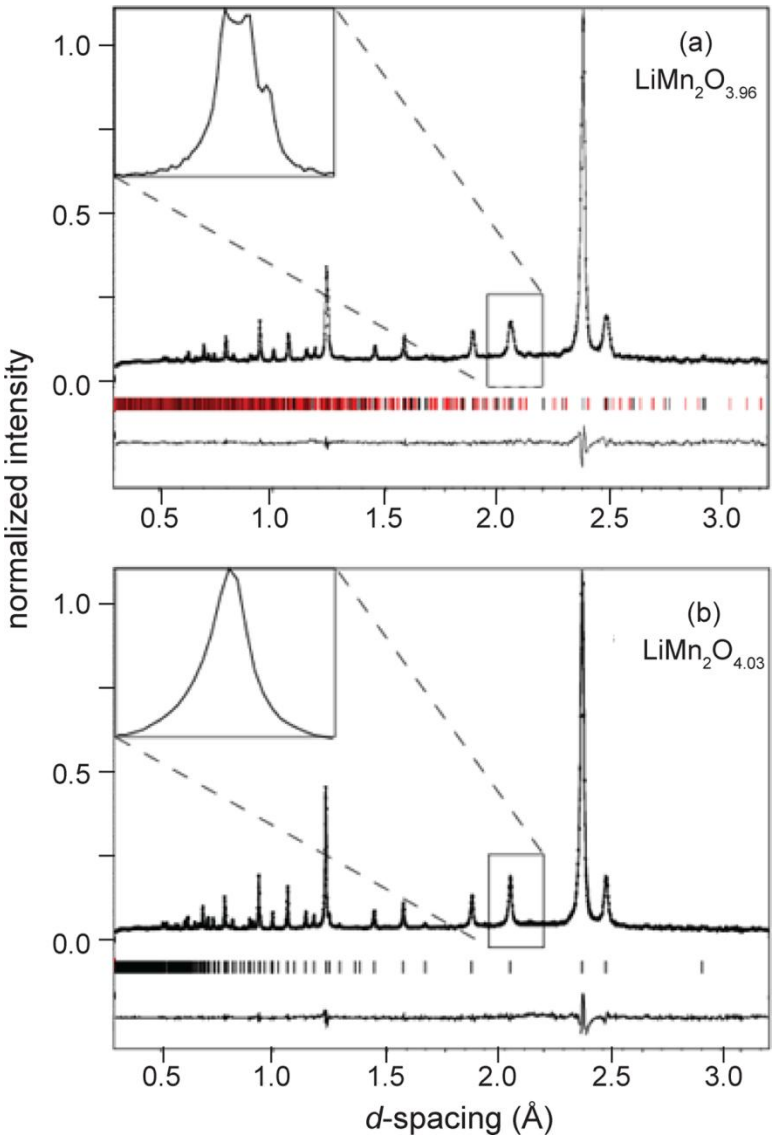

Figure 2.3 Neutron powder pattern obtained on POWGEN at 300 K on (a) $LiMn_2O_{3.96}$ synthesized in air and (b) the annealed $LiMn_2O_{4.03}$ sample. Dots indicate the normalized profile, the solid line is the calculated profile, tick marks below profile indicate the positions of all allowed reflections, and the difference curve is show below the tick marks on the same scale (*d*-spacing range 0.30 – 3.2 Å). In the case of $LiMn_2O_{3.96}$, black and red tick marks indicate main and satellite reflections, respectively (see Text for details). The insets present an expanded region around the $(004)_c$ reflection.

At this stage of refinement, we note an unusually large atomic displacement parameter (ADP) on the oxygen site. Since such behavior is characteristic of non-stoichiometry in oxides, the oxygen occupancy was refined and converged to 96(1)% with a significant

improvement of the refinement (R = 6.7% for a *G.o.F.* = 2.3). Table 2.2 lists the atomic positions, ADP and occupation parameters for $LiMn_2O_{3.96}$ synthesized in the air. PND cannot differentiate 1% substitution of Li for Mn on the 16*d* sites (surmised from our ICP results), but we note that the unit cell parameters support this formulation. For the last step of the refinement, some weak reflections, still non-indexed, are noticeable. These reflections could be indexed as first-order satellites of a commensurate tripling along the *a* direction of the average unit cell. As the number of parameters to refine will drastically increase, a superspace approach of the commensurate modulation has been preferred to a supercell one. Therefore the superspace group F*ddd(α00)* with α= 1/3 *a** was used to refine the structure fully. (For a comprehensive description of (3 + *n*)-dimensional crystallography, see, for instance, works by Janssen et al.[111] and van Smaalen[112] and references within.) The superspace model of this crystal structure has been obtained by subsequent introduction of modulation parameters on atomic positions and site occupancies. Such an approach has led to introducing one modulation wave on the Mn atomic position and one modulation wave on the oxygen occupancy. These modulations are presented in Figure 4 and red tick marks on the Figure 3a illustrate the position of these satellite reflections. The modulations parameters are classically written as:

$$\mathbf{u}\left(\bar{x}_4^{\nu}\right) = \sum_{n=1}^{k} s_n \sin\left(2\pi n \bar{x}_4^{\nu}\right) + \sum_{n=1}^{k} c_n \cos\left(2\pi n \bar{x}_4^{\nu}\right),$$

with s_n and c_n being the *refined* coefficients of the n^{th} order harmonic. Using this formalism, the modulation wave on the oxygen occupancy imply s_1=0.16(4) and c_1=0.13(3). For the Mn atomic displacement only sine terms have been used with s_1=-0.0118(15), 0.002(4) and 0.011(2) to express the deviation along the *x*, *y*, and *z*

crystallographic direction, respectively. The modulations show clearly than the oxygen vacancies are not randomly distributed, but with a frequency of every three average unit cells, the two other ones being fully occupied (Figure 2.4). Simultaneously, the Mn atoms present a small displacement along the *a* and *c* direction which implies a variation of the Mn–O distances. Therefore modulation waves could be associated in that class of materials with a variation of the covalence charge on the Mn site. Such types of modulation waves have already been observed for $LiMn_2O_4$ during delithiation.[113]

Table 2.2 Atomic Parameters, occupancies and Equivalent Displacement Parameters ($Å^2$) for $LiMn_2O_{3.96}$ synthesized in air.

Atom	Wyckoff Site	Occupation	*x*	*y*	*z*	U_{eq}
Li	8*a*	1	0.125	0.125	0.125	0.0061(10)
Mn	16*d*	1	0.5	0.5	0.5	0.0042(7)
O	32*e*	0.96(1)	0.7387(4)	0.7378(5)	0.7353(6)	0.0082(9)

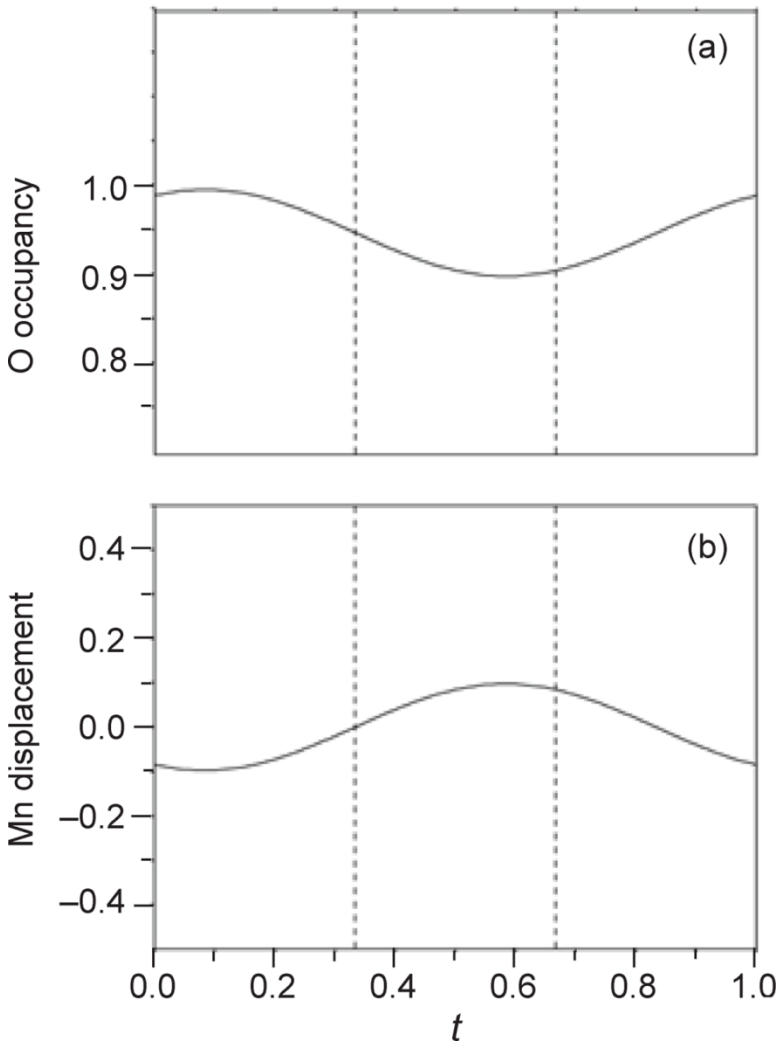

Figure 2.4 Representation of the atomic modulations on (a) the oxygen occupancy and (b) the manganese displacement along the *a* direction. The dashed lines represent the commensurate sections.

As presented in Figure 2.3b, annealing the $LiMn_2O_4$ sample introduces major modifications on the crystal structure of the material. First, the inset of the Figure 3b shows that splitting of the $(004)_c$ reflection is no longer observed, and therefore the final refinement was carried out using $Fd\bar{3}m$ symmetry. Notice that the asymmetry of the peak associated with a strong Lorentzian component in the profile shape indicates some degree

of defects in the crystal structure. The final refinement converge smoothly to a satisfactory R = 3.40% for a *G.o.F.* = 2.1. The cell parameters, atomic positions and equivalent atomic displacement are listed in Table 2.3. Importantly, the oxygen position is fully occupied, and additional residues localized near (0, 0.26, 0.73) could be eventually associated with some excess oxygen atoms (0.03 oxygen).

Table 2.3 Atomic Parameters, occupancies and Equivalent Displacement Parameters ($Å^2$) for air annealed $LiMn_2O_{4.03}$ (cell parameter: a = 8.2304(5) Å).

Atom	Wyckoff Site	Occupation	x	y	z	U_{eq}
Li	8*a*	1	0.125	0.125	0.125	0.0134(11)
Mn	16*d*	1	0.5	0.5	0.5	0.0081(3)
O	32*e*	1	0.26324(6)	0.26324(6)	0.26324(6)	0.0140(3)

The hypothesis developed from our structural and elemental analyses is that although cation substitution and oxygen non-stoichiometry are prevalent in materials prepared via hydrothermal synthesis, annealing the samples eliminates (at least minimizes beyond all detection, *vide infra*) oxygen vacancies. The distinct advantage of this approach compared to solid-state preparative methods is that soft chemical routes give rise to nanoparticles that will show much greater rate capability. The remainder of the results section details the experimental data supporting this hypothesis. We will illustrate the impact of synthesis conditions, which dictate structure and composition, on the electrochemical performance of these materials as cathodes for lithium-ion batteries.

Specific attention is given to the initial capacity, the capacity retention, and rate capability of the resulting cells.

2.3.4 Substantiating the presence of oxygen vacancies by TGA, DSC, and CV

Thermogravimetric analysis, differential scanning calorimetry, and cyclic voltammetry verify the qualitative presence of oxygen vacancies, as has been well discussed in the lithium manganospinel literature.[82,108,114,115] Figure 2.5 shows that all hydrothermally synthesized spinel samples as well as their annealed analogues lose up to 1% mass upon heating to 200 ºC by TGA, attributed to the loss of surface water from the nanocrystalline material. This assignment is corroborated by FTIR spectroscopy (Figure A.4); materials stored in the ambient room atmosphere show prominent ν(O–H) vibration and δ(H–O–H) bending modes at 3300 and 1630 cm^{-1} respectively.

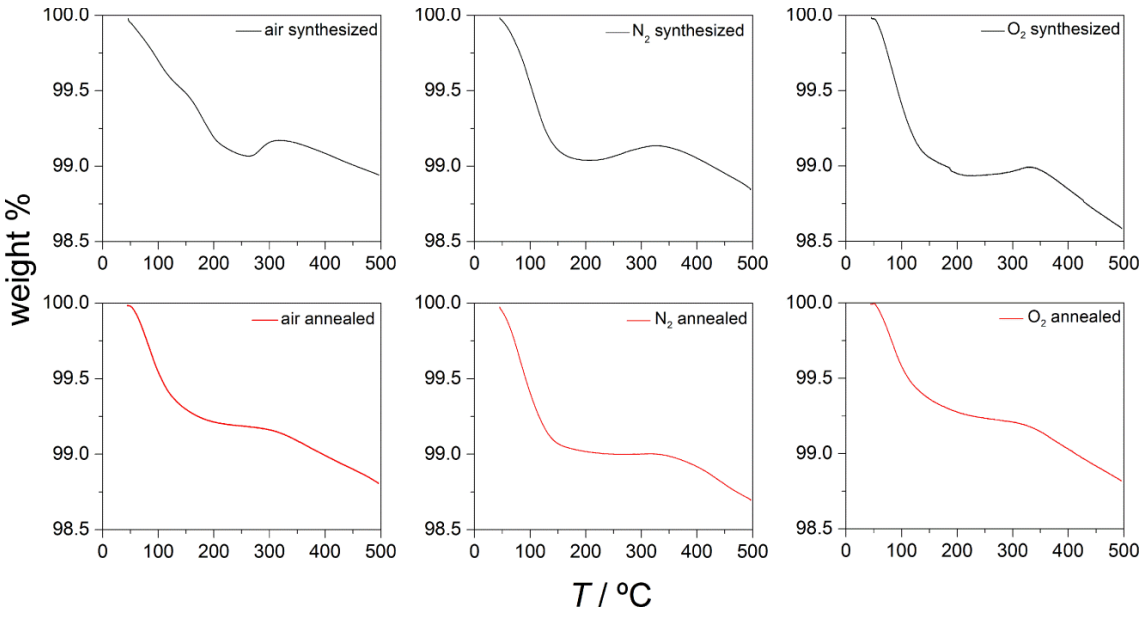

Figure 2.5 TGA traces of lithium manganospinels synthesized by hydrothermal methods.

First, we focus on the air- and N_2-synthesized samples. The TGA in Figure 2.5 a–b shows a mass gain between 200–300 ºC: 0.11% for the sample synthesized in air, 0.10%

for the sample prepared under N_2. However, TGA of the corresponding annealed samples in Figure 2.5 c–d shows no such gain in mass. This observation is understood by equations 4 and 5 from the first section of the results: oxygen vacancies are already filled by annealing, therefore no additional mass increase can occur. Important to this interpretation, a control experiment in which the TGA of the compound synthesized in air was performed under a nitrogen purge shows no such mass increase (Figure A.5). Above ~330 ºC, all samples show a mass decrease, as has been described in the chemistry of materials prepared at high temperature.[104,106] In our samples, this indicates that perhaps our hydrothermally synthesized compounds absorb excess oxygen at these low annealing temperatures. We will return to this point in the next section.

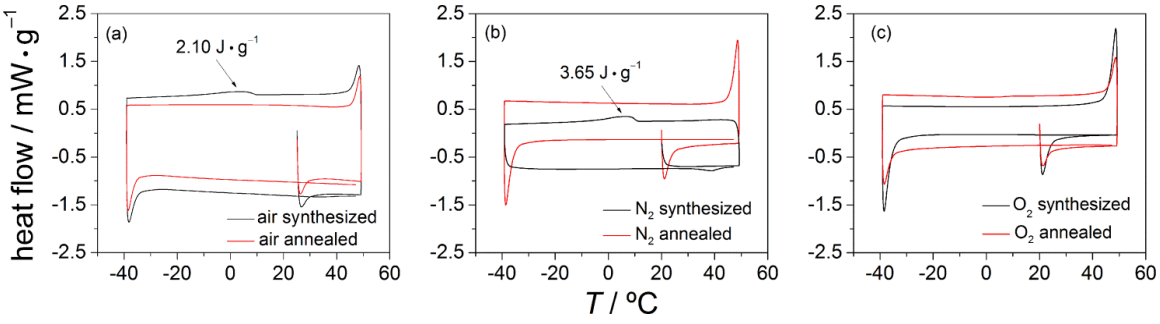

Figure 2.6 DSC traces for lithium manganospinels synthesized in a) air; b) N_2; c) O_2. Black and redcurves represent the synthesized and annealed samples, respectively.

Next, DSC measurements further support a change in the oxygen stoichiometry of hydrothermally synthesized samples. At ~280 K, lithium manganospinel undergoes a phase transition from the cubic structure ($Fd\,\bar{3}\,m$) to what was originally identified as a phase having tetragonal symmetry ($I4_1/amd$),[116] though later shown to be orthorhombic ($Fddd$) by synchrotron X-ray diffraction.[117] This first-order phase change is attributed to

partial columnar charge ordering,[118] and can be observed in the DSC. Figure 2.6 a–b shows that prior to annealing, the material synthesized in either ambient air or under a pure N_2 atmosphere shows the transition as an exotherm at 8.7 and 7.7 ºC, respectively with an enthalpy change of 2.10 and 3.65 J/g, respectively . This phase transition no longer appears after annealing the samples since Z_{Mn} increases to 3.57 and 3.55 for air and N_2 samples, sufficient to suppress the symmetry-lowering distortion.[119]

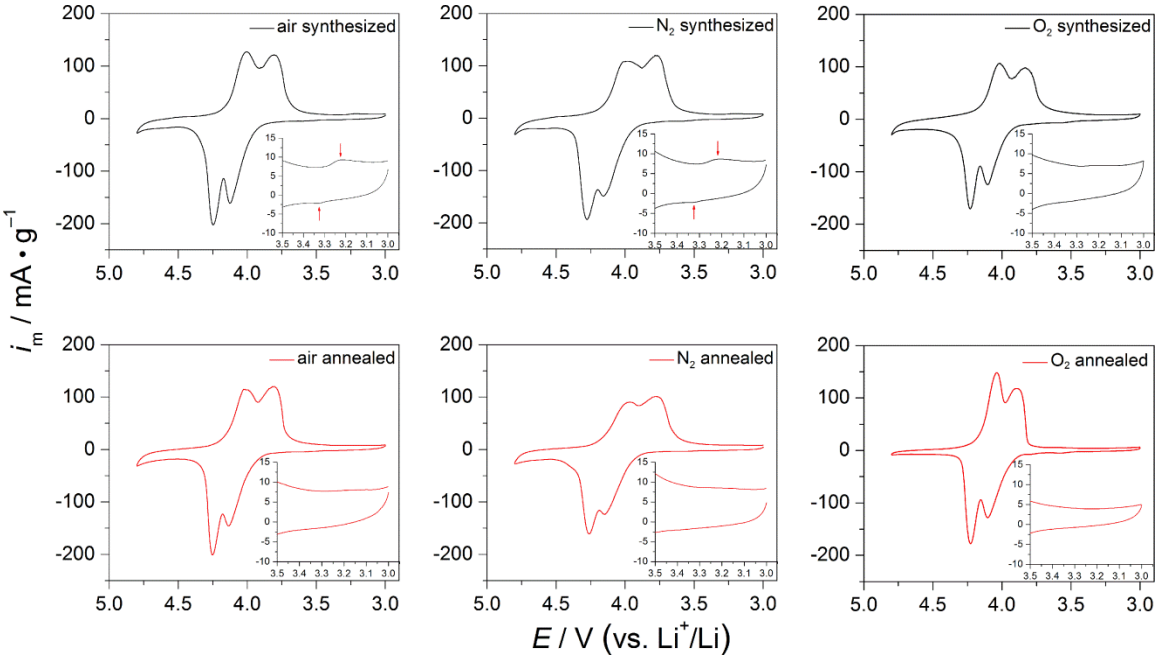

Figure 2.7 Cyclic voltammograms of lithium manganospinels. Black traces in the top panel are for the synthesized samples. Red traces in the bottom panels are for the corresponding annealed samples. The inset blows up the region between 3.5 and 3.0 V where an additional wave can be observed for the air and N_2 synthesized samples (noted by the red arrows).

Then, cyclic voltammetry points to the presence of oxygen vacancies within hydrothermally synthesized materials. Figure 2.7 shows the voltammograms of spinel materials prepared by hydrothermal synthesis. Upon charging, all materials show two

oxidation waves at 4.13 V and 4.26 V (vs. Li^+/Li) with corresponding reduction waves at 3.81 V and 4.02 V upon discharge. These correspond to the one-electron oxidation of Mn^{3+} to Mn^{4+} with lattice contraction/ expansion at ½ charge/ discharge. The change in lattice parameter and resultant shift in chemical potential was described in the first report of lithium manganospinel.79 Interestingly, the as-prepared hydrothermal samples synthesized under air and under N_2 display an additional wave at $E_{1/2}$ of ~3.25 V, previously shown to be attributed to oxygen vacancies formed in the structure as electrons are transferred to the electrolyte.[106,120] This results in a phase transition to a double hexagonal structure, as has been shown in previous HR-TEM studies.[52] Once annealed, the disappearance of this wave suggests that such a mechanism is no longer operable in these samples.

Finally, we consider together the data for lithium manganospinel synthesized under a pure O_2 atmosphere. TGA shows a small mass gain of 0.05% between 200–300 ºC, and it disappears after annealing, just as was the case for the air and N_2 samples. In the DSC, no exotherm near 280 K is observed in either the synthesized or the annealed sample, despite Z_{Mn} being slightly less than +3.5 in the synthesized compound (3.47). Finally, the compound prepared under an O_2 atmosphere shows no discernable wave at $E_{1/2}$ of ~3.25 V in its cyclic voltammogram. Together, the DSC and CV results hint that the oxygen mole fraction of 3.96 in the synthesized sample is sufficient to prevent charge ordering. Furthermore, the lack of oxygen vacancies in the O_2 annealed sample indicates that this material will result in superior electrochemical performance.

2.3.5 Measuring the capacity and reversibility as a function of oxygen vacancies

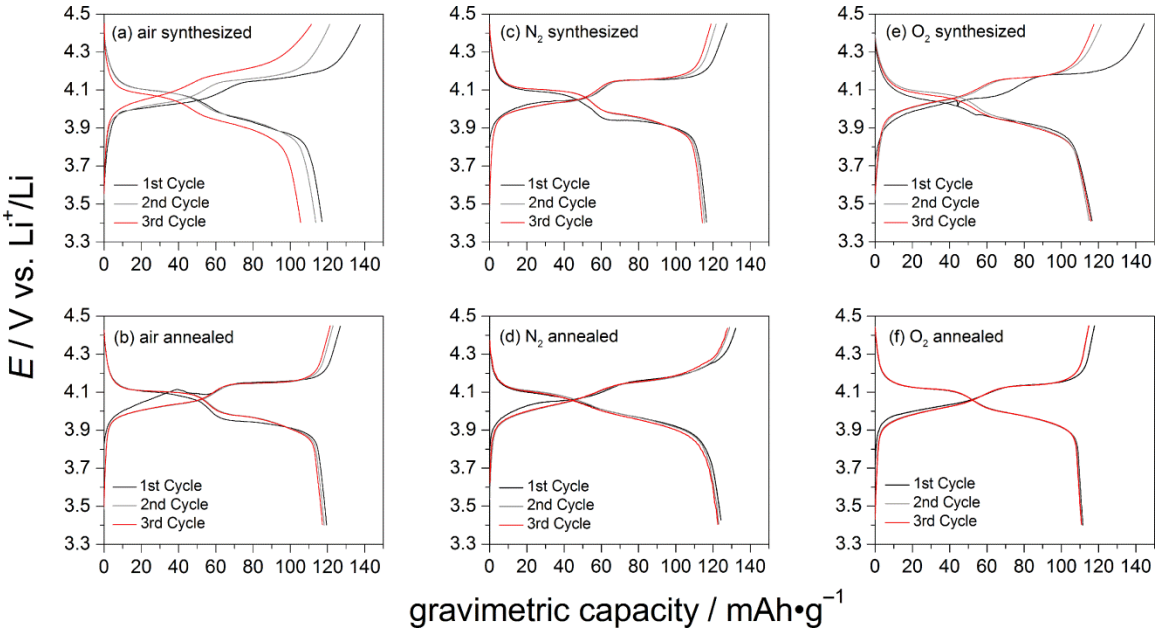

Figure 2.8 First three charge-discharge curves recorded at rate *C*/10 for lithium manganospinels. Black, gray, and red curves represents cycles one, two, and three respectively.

In order to assess the promise of hydrothermally synthesized materials as practical electrodes, we performed galvanostatic cycling under three sets of conditions. First, we recorded three charge-discharge cycles at a rate of *C*/10. Here, the initial capacities were determined as well any changes in the voltage profile as the solid-electrolyte interface (SEI) layer is forming. As shown in Figure 2.8, all spinel compounds show an initial discharge capacity between 115 and 120 mAh/g. For the air synthesized sample, the capacity fades to 106 mAh/g with the third cycle. The annealed compound still has a capacity of 117 mAh/g on the third cycle. Slow cycling gives the best measure of total available capacity as lithium in the core of the material has sufficient time to diffuse to the surface and allows us to determine the cycle-to-cycle Coulombic efficiency, q_{out}/q_{in}. For the third charge/discharge cycle, the measured Coulombic efficiency of

hydrothermally synthesized materials ranges from 94.83% (air synthesized sample) to 98.60% (O_2 synthesized sample). Of course, three slow cycles do not translate directly into the practical utility of an electrode, so we then constructed a second set of cells that were charged and discharged at the faster rate *C*/3, and the first one hundred cycles were recorded. The data are shown in Figure 2.9 and summarized in Table 2.1, with the individual charge-discharge curves for every 20th cycle available in Figure A.6. Upon discharge from 4.4 V, a flat plateau is observed at 4.1 V through ½ discharge, followed by a gently sloping voltage profile centered about 3.9 V to complete discharge. This suggests a two-phase region upon initial discharge, followed by alloyed region. The fade in capacity is least for the samples prepared under O_2, 10.0 and 6.1% for the as synthesized and annealed compounds respectively.

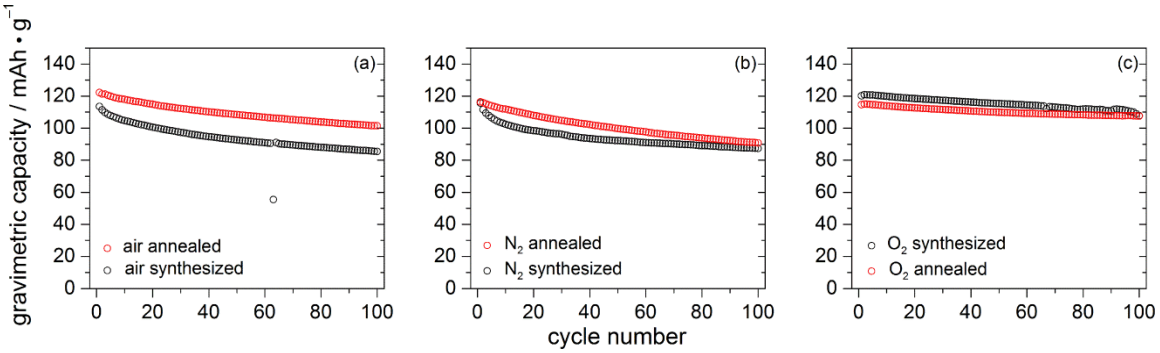

Figure 2.9 Galvanostatic cycling at current *C*/3 for lithium manganospinel synthesized hydrothermally in a) air; b) nitrogen; and c) oxygen. Black and red circles represent the synthesized and annealed samples, respectively. The anomalous data point at cycle 63 for the air synthesized sample arises because the computer had to be restarted during that measurement.

Here, we must address why we anneal at 500 Cº given our TGA results where maximum oxygen uptake occurs between 310 and 330 ºC. Experimentally, we performed two experiments summarized here with data presented in Figure A.7. First, we annealed

the air synthesized compound at 310 ºC and observe that over the first ten cycles, the capacity is stable, but significantly lower, only 81 mAh/g. We annealed a second sample at the weight-loss threshold, 270 ºC and observe a similar result—the capacity is nearly constant over the first ten cycles, but is only 73 mAh/g. X-ray diffraction performed on these compounds shows that the lattice parameters of these compounds are 8.219 and 8.216 Å respectively. In addition, potentiometric titration shows that Z_{Mn} significantly greater than 3.5 for these compounds (3.68 and 3.66 respectively), which explains the low gravimetric capacities. This is supported further by the lack of a constant voltage plateau in the galvanostatic cycling, shown for the 10^{th} cycle of these two samples in Figure A.7. This indicates that upon discharge from 4.4 V, Z_{Mn} is suffiently high such that Li insertion occurs in a single phase, not the typical two-phase mixture.[121] By annealing at 500 ºC, both the composition changes (from oxygen deficient to a slight excess of oxygen), and the structure changes (no orthorhombic superspace group is observed by PND) to give lithium manganospinel with high capacity.

Returning to the best sample with respect to capacity retention, the O_2 sample annealed at 500 ºC, cycling was performed at varying rate to demonstrate its utility in high power applications. Figure 2.10 illustrates that at a charge/ discharge rate of 3*C*, the O_2 annealed sample demonstrates an initial discharge capacity of 112 mAh/g with 95.6% rentention (108 mAh/g) after 100 cycles. This is nearly identical to the observed capacity and retention of at the slower rate of *C*/3. When the material is cycled at the even faster rate of 5*C*, the capacity is slightly lower, 99 mAh/g. Again, however, 95.6% of this capacity is retained (95 mAh/g) after 100 cycles.

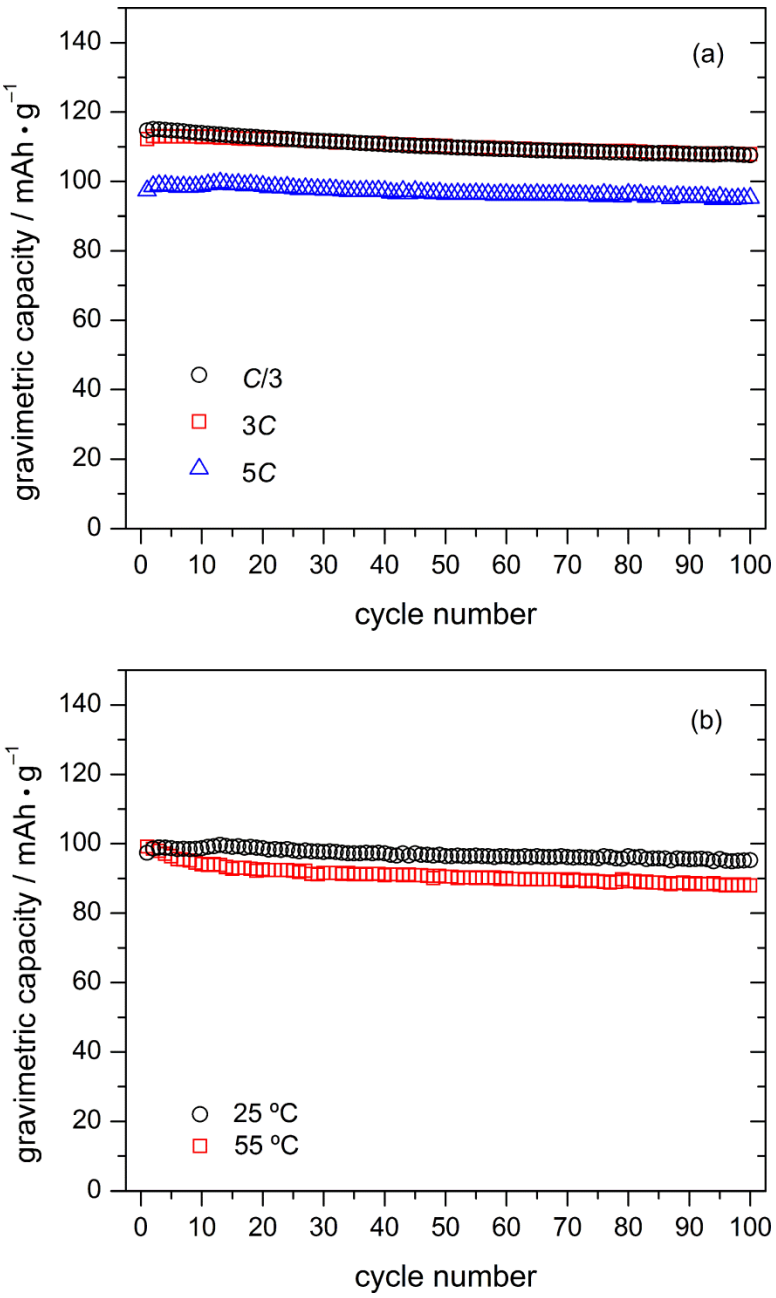

Figure 2.10 a) Rate capability of lithium manganospinel synthesized under O_2 followed by annealing in air. Black circles, red squares, and blue triangles represent cycling at currents corresponding to the rates *C*/3, 3*C*, and 5*C* respectively; b) Temperature-dependence of galvanostatic cycling at 5*C*.

Moreover, the O_2 annealed sample shows excellent cycling behavior at elevated temperature. This is important because the detrimental surface disproportionation of Mn^{3+} becomes more facile as temperature increases, and the majority of capacity fade is

observed within the first 15 cycles.[122] In the case of our lithium manganospinel nanoparticles, cycling the material with constant current of 5*C* at 55 ºC shows an initial capacity of 99 mAh/g that fades to only 88 mAh/g after 100 cycles (88.9% capacity retention).

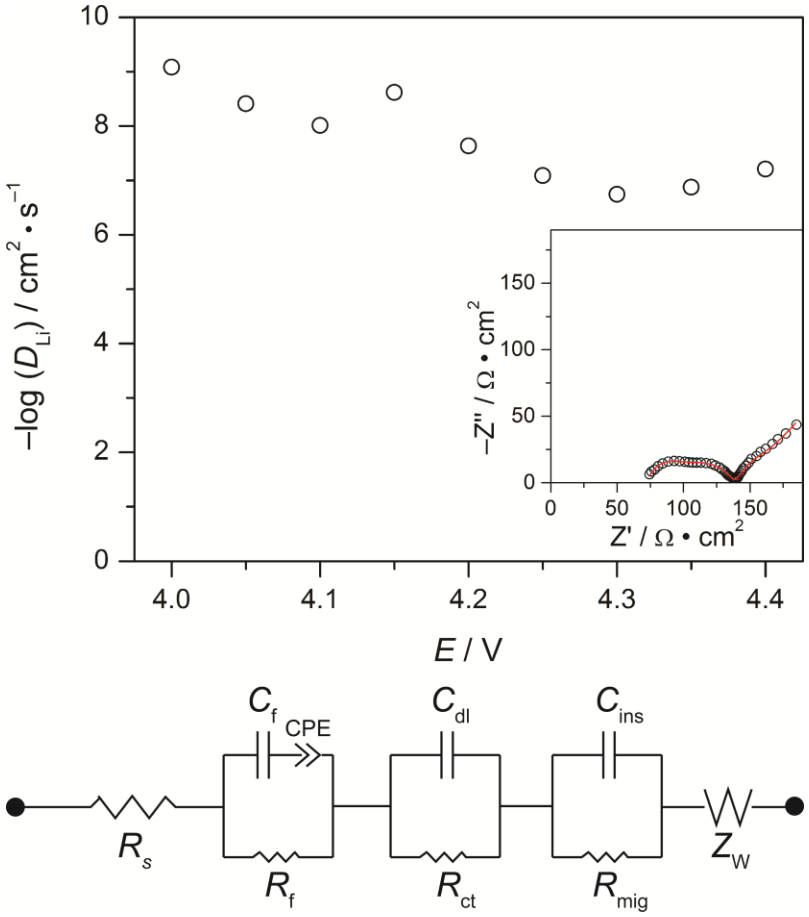

Figure 2.11 Lithium-ion diffusion constant as a function of potential determined by EIS. Inset. Nyquist plot for the 4.15 V data. The data (black circles) are fit (red line) to the quivalent circuit is illustrated below the main plot.

Together, these data suggest that lithium-ion diffusion is rapid in the sample. To verify that lithium-ion diffusion is indeed rapid, we performed electrochemical impedance spectroscopy. Figure 2.11 shows the voltage-dependence of the lithium-ion diffusion constant with Nyquist plot and fit of the data collected at 4.15 V to the equivalent circuit

illustrated. [123] The Nyquist plot shows three discernable semicircles corresponding physically to transport through the SEI layer, electronic reorganization associated with localized $Mn^{3+/4+}$ charge hopping, and charge transfer, as has been recently described.[124] Then, the low frequency Warburg impedance (Z_W) is related to the lithium-ion diffusion constant (D_{Li}) by the equation[125]

$$Z_W = \frac{V_m\left(\frac{dE}{dx}\right)}{FA(2D_{Li})^{1/2}} \qquad (6)$$

where V_m is the molar volume of lithium manganospinel (140 cm^3/mol), dE/dx, the slope of coulometric titration, is determined from cyclic voltammetry at 0.1 mV/s, F is Faraday's constant and A is the electrode surface 500 cm^2. The Nyquist plots for the compound cycled to other potentials are included as Figure A.8. For the O_2 annealed sample, D_{Li} is on the order of 10^{-7} to 10^{-9} cm^2/s, rapid indeed, but on par with has been determined by EIS for lithium manganospinel prepared by sol-gel methods.[126] This rapid Li-ion diffusion supports the conclusion that our nanoscale material prepared under O_2 followed by annealing shows a rate capability and gravimetric energy density that is at least on par with, if not exceeds even the best material prepared by solid-state synthesis.

2.4 Discussion

Oxygen vacancies in the Li–Mn–O spinel system have been long recognized in the solid-state literature,[127] predating the concept of energy storage by electrochemical Li^+ insertion and extraction. In this original study, it is shown that the lithiated cubic spinel phase reacts with hausmannite, Mn_3O_4 according to the reaction:

$$LiMn_2O_4 + Mn_3O_4 \rightarrow LiMn_2O_{3.5} + \tfrac{1}{2}O_2 \qquad (7)$$

Hausmannite also belongs to the spinel group ($Mn^{2+}Mn^{3+}{}_2O_4$), and is a common impurity phase encountered during lithium manganospinel synthesis. In addition to reaction with

hausmannite, oxygen vacancies are introduced into lithium manganospinel synthesized under reducing conditions such as ammonia reduction[105] or rapid quenching of solid-state reactions performed in air82,[108] Beyond the preparation of oxygen non-stoichiometric materials, there are several proposed thermodynamic models for vacancy formation on the surface.[128 – 130] Notably, after our annealing treatment, we do not observe any secondary phases by PND such as Mn_3O_4 or Li_2MnO_3 that frequenly result from high-temperature processing.[131]

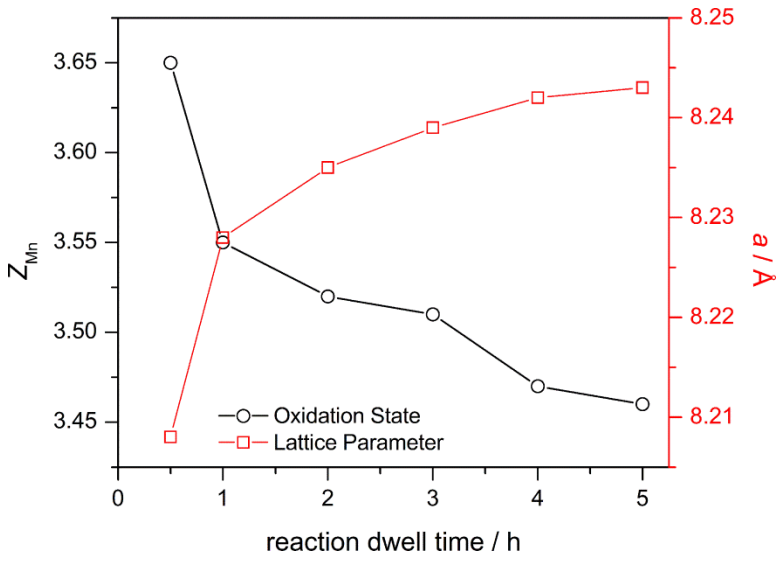

Figure 2.12 Average manganese oxidation state (black) and lattice parameter (red) or lithium manganospinel synthesized by hydrothermal methods in air as a function of dwell time.

Crystal distortions that arise from the presence of Mn^{3+} in the spinel structure were also recognized long before the electrochemistry was studied.[132] As mentioned in the introduction, oxygen vacancies result in materials with poor electrochemical performance, and an empirical set of guidelines for optimizing the performance of lithium manganospinel has been published.[133] Our work is aimed at the first principle: to

establish stoichiometry resulting from synthesis and any treatments applied prior to cell assembly. The hydrothermal reaction employed in our lab provides the most oxidized product when carried out under an oxygen atmosphere. The role of reaction atmosphere is not unique to hydrothermal synthesis, however. In preparing stoichiometric spinel from lithium hydroxide and either chemically prepared manganese dioxide[84] or γ-MnOOH[85] in a muffle furnace, the reaction proceeds most cleanly under a reducing nitrogen atmosphere to prevent the decomposition reaction to form Li_2MnO_3. In this reaction, the culprit is oxidation of Mn^{3+} in $LiMn_2O_4$ by atmospheric O_2. In stark contrast, hydrothermal conditions do not yield stoichiometric lithium manganospinel, rather material with oxygen vacancies. These oxygen vacancies suggest that our hydrothermal reaction conditions are reducing from the standpoint of the solid oxide product. Figure 2.12 shows the lattice parameter and the average manganese valence of the solid products obtained *ex situ* at varying reaction times. We observe an increase in the lattice parameter and decrease in the average manganese valence as the reaction proceeds, *even in an O_2 atmosphere*. This hints at the need to anneal our materials in an oxidizing environment after hydrothermal synthesis. Empirically, maximum weight uptake occurs at ~310 ºC, but we find that Z_{Mn} is large, 3.66, leading to low overall capacity. Notable is that the particle size and cation composition are conserved in our annealing procedure, which is different from what is observed in reference 95, where annealing at 800 ºC results in consumption of nanoparticles to form micron-sized particles.

The unique aspect of our synthesis work is discovering the structural complexity of compounds synthesized by hydrothermal methods. The results from our neutron diffraction data show that Mn^{3+} and/or oxygen vacancies lead to symmetry lowering,

which has large implications on the electrochemistry of the material, particularly the capacity retention. The *Fddd* orthorhombic structure that we observe has been previously reported for both stoichiometric $LiMn_2O_4$[134] as well as for non-stoichiometric $LiMn_2O_{4-\delta}$ prepared by calcination at temperatures above 800 ºC.[135] We note that this superstructure is not discernible using standard laboratory Cu-Kα radiation at room temperature. However, after annealing the sample, this superstructure is no longer observable in the room-temperature powder neutron diffraction; the only observable reflections are the Bragg peaks from the cubic $Fd\bar{3}m$ space group, similar to what has been observed for other stoichiometric spinels synthesized by ceramic routes.[136] The cubic structure cycles with greater capacity retention.

Then, from the perspective of power, our synthesis of small particles is advantageous because they are less susceptible to fracture. Volume changes in nanoparticles are more readily accommodated, giving rise to the excellent rate capability and capacity retention in the compound. Although there are several examples of using hydrothermal methods to prepare lithium manganospinel nanoparticles, Table 2.4 shows that the capacity retention from these preparations is often quite poor. Our work here suggests that preparing nanoparticles is not an inherent problem with lithium manganospinel. Rather, it is the composition (and perhaps the concomitant structural implications) that results in poor performance—namely the presence of oxygen vacancies. Although this fact is recognized in several of the references in Table 2.4, we have addressed the matter experimentally. The closest comparison in the table is reference 97, however there is no specific mention of nonstoichiometric composition therein. There, the increase in lattice parameter as a function of time suggests that oxygen vacancies may be present, and we note that only

after three days is highly electroactive spinel isolated in the absence of an organic reducing agent. Our materials, attainable in less than a day, show exceptional stability even at elevated temperatures and relatively rapid rates.

Table 2.4 Electrochemical Properties of Spinels Synthesized by Hydrothermal Conditions.

Nominal Composition	Capacity at 4 V Plateau (mAh/g)	Capacity Retention / # cycles	Reference
$Li_{0.96}Mn_{2.04}O_{4.05}$	107[a]	75% / 10	89
$Li_{1.08}Mn_{1.92}O_{3.97}$	92[a]	91% / 10	89
$Li_{1.23}Mn_{1.77}O_{3.87}$	66[a]	95% / 10	89
$Li_{0.90}Mn_2O_{3.95}$	~92 unstated	data not presented	93
$Li_{1.25}Mn_{1.75}O_{3.98}$	110 at *C*/2	82% / 10	92
$LiMn_2O_4$	130 at *C*/10	>95% / 60	95
$Li_{0.92}Mn_2O_4$	107 at *C*/3	84% / 50	96
$LiMn_2O_4$	91 at 8*C*	96% / 100	97
$LiMn_2O_4$	113 at *C*/5	93% / 20	98
$LiMn_2O_4$ nanorods	100 at 1 *C*	85% / 100	99
$LiMn_2O_4$	95 at 1.6 *C*	79% / 30	100
$LiMn_2O_4$	87 at *C*/10	85% / 25	101
$LiMn_2O_4$	98 at *C*/2	88% / 50	102
$Li_{1.01}Mn_{1.99}O_{4.07}$	115 at *C*/3 113 at 3*C* 99 at 5*C*	94% / 100 96% / 100 94% / 100	this work

a 200 μA/cm^2 current using a 10 mm diameter electrode

From the perspective of the Li–Mn–O phase diagram, we cannot yet say where these compositions fall, although current efforts in are group are focused on elucidating the

phase relationships. The phase diagram in air at elevated temperature has been well established [137 – 139] and a Pourbaix-like pH-stoichiometry diagram for lithium manganospinels in acid has been recently determined,[140] but relatively little is known regarding the phase equilibria present under hydrothermal conditions. Here, we can only conclude that our results of having both cation mixing and oxygen vacancies are consistent with the phase relationships of lithium manganospinels prepared from ceramic/calcination methods above 900 ºC, where $Li_{1+x}Mn_{2-x}O_{4-\delta}$ is proposed to be thermodynamically stable. Electrochemically, we observe superior capacity retention in compounds stoichiometric in oxygen, more akin to what is observed in the cation-deficient, Li-rich spinels.[141]

Here, we must discuss the potential technological advances initiated by the nanomaterials materials we have prepared. It has been suggested in the literature that the loss of cyclability in lithium manganospinel at both room temperature and elevated temperature does not originate from structural transformations per se, rather with the composition: the greater the mole fraction of Mn^{3+} in the compound, the greater the degradation.[142] We find that hydrothermal synthesis gives material that is deficient in oxygen and has an orthorhombic superstructure. These two features are not mutually exclusive, so it remains undetermined which factor is more important. That is, we cannot answer here the question: is electrochemical performance is enhanced simply by filling in vacancies or is it due to the loss of orthorhombic superstructure after annealing? At best, our results show that the Mn^{3+} concentration in the hydrothermally synthesized orthorhombic product is larger and there is oxygen nonstoichiometry. After annealing, electrons are transferred from Mn^{3+} to surface oxygen, giving cubic compounds with Z_{Mn}

larger than 3.5. At this point, the new chemistry stimulated in this well-studied material is that annealing nanoparticles synthesized hydrothermally using organic reducing agents such as acetone affords high rate capability. The novel aspect here is that it is simply structure and composition that results in high performance electrodes, not nano-architecture.

Finally, we have largely focused on power, but must also comment on the energy density of nanomaterials. In order to achieve a large *volumetric* energy density, the tap density is critical.[143] We have crudely measured the tap density of our nanoparticles (using a balance, a graduated cylinder, and a No. 2 pencil), and find that it is 1.2 g/cm^3, on par with lithium manganospinel prepared by other low temperature routes,[144] despite a significantly larger surface area according to our N_2 isotherms. As observed in the SEM images, our nanoparticles agglomerate readily and EIS shows that Li^+ diffusion is rapid. Further exploration is needed to optimize the carbon-coating levels to determine the packing density required for a practical battery. However, our results here are promising: the same gravimetric capacity attainable at the rate *C*/3 and 3*C* hints that a battery composed of our lithium manganospinel can be charged completely in 20 minutes. As a benchmark for the rate capability of our materials, the measured reversible capacity of 99 mAh/g at 5*C* (0.67 mol Li extracted) is greater than the literature-reported capacity at 2.5*C* for micron-sized particles, ~81 mAh/g (0.55 mol of Li extracted).[145] At present, we are exploring the generality of using organic oxidation reactions under hydrothermal conditions followed by annealing to prepare other manganese-containing oxide nanomaterials for high power electrical energy storage.

2.5 Conclusion

Lithium manganospinel nanoparticles prepared by hydrothermal methods has been shown to contain oxygen vacancies by the combination of TGA, DSC, CV, and PND characterization regardless of the environment under which the reaction is performed. However, these vacancies can be eliminated beyond the detection limits of all analytical methods by annealing the synthesized compounds at 500 ℃ in air for 4 h. In addition, the hydrothermally synthesized sample shows an orthorhombic *Fddd*(α00) supergroup that disappears upon annealing. As a result, the material prepared under the most oxidizing conditions (synthesized under an autogenous pressure of O_2, followed by annealing) shows the highest reversibility under various cycling conditions—*C*/3, 3*C*, 5*C*, and 5*C* at 55 ℃. This behavior is observed without having to coat our particles (beyond the typical use of carbon to enhance electrical conductivity) or insert compositional complexity in the form of nickel and/or cobalt on the octahedral lattice sites. Li-ion diffusion, measured by EIS, is found to be rapid, which explains the high rate capability. Current efforts are aimed at elucidating phase relationships within materials prepared by hydrothermal methods in order to examine the influence of cation stoichiometry and composition on the rate capability of nanoparticles, building on the larger body of lithium manganospinel literature.

CHAPTER 3

Oxygen Vacancies Lead to Loss of Domain Order, Particle Fracture, and Rapid Capacity Fade in Lithium Manganospinel ($LiMn_2O_4$) Batteries

Portions of this chapter have been submitted:
Hao, X.; Lin, X.; Lu, W.; Bartlett, B. M. *ACS App. Mater. Inter. Accepted.*

3.1 Introduction

Lithium ion batteries have drawn much attention as energy storage device for portable electronics, (hybrid) electric vehicles and next generation power grids due to their high volumetric and gravimetric energy densities.[146] The current research focus in lithium ion batteries system is developing high voltage electrode materials with long term reversible electrochemical stability. The rich lithium intercalation chemistry of transition metal oxides and polyanion complexes have enabled technological adoption of many candidates for cathode materials, such as $LiCoO_2$ [147], $LiNiO_2$ [148], $LiFePO_4$ [149], and the spinel-structured manganese oxides including $LiMn_2O_4$[150] and $LiNi_{0.5}Mn_{1.5}O_4$.[151] Carbon in the form of graphite[152] is the anode employed in current lithium-ion batteries. However, the wide adoption of high voltage cathodes is limited by the stability, in particular, mechanical degradation of the electrode active cathodes.[153,154] Microfractures in cathodes

composed of $LiCoO_2$[155,156] and $LiFePO_4$[157] powders have been observed in electron microscopy studies. Moreover, single-particle fracture during electrochemical cycling of $LiNiO_2$[158] is noticeable by optical microscopy. Acoustic techniques have been employed to monitor fracture in $LiCoO_2$[159] and MnO_2[160] during cycling. Finally, atomic probe tomography has also been applied to unveil the fracture mechanism of $LiCoO_2$ cathodes.[161, 162] Mechanical fractures arise as stress builds during lithium insertion/extraction.[163] Although volume expansion is more pronounced at the anode materials due to larger lattice change,[164–168] cathodes have received less attention. In graphite, there is 12.8% volume expansion during charging. TEM experiments confirm the presence of cracks on the meso-scale during graphene layer exfoliation.[169] As a result, the internal resistance increases with a concomitant drastic capacity fade. Based on these experimental observations, theoretical calculations have been dedicated to simulate mechanical failure, which also provide insights into related capacity fading mechanisms.[170–172]

This manuscript is devoted to the cathode, lithium manganese oxide, $LiMn_2O_4$ with a cubic symmetry spinel structure (Fd-3m) that delivers considerable capacity of 148 mAh/g at voltage of 4.1 V (*vs.* $Li^{+/0}$). The electrochemical potential is derived from the $Mn^{3+/4+}$ redox couple. Meanwhile, $LiMn_2O_4$ has the advantages of using a low-cost metal that is non-toxic. However, the cyclability of $LiMn_2O_4$ is limited by the oxygen vacancies, as we have previously reported.[174]Our work builds a connection between trace defects, structural changes and electrochemical performance. In this study, we substantiate the capacity fading mechanism by conducting structural analysis to show that electrochemical instability results from mechanical failure in $LiMn_2O_4$. Furthermore,

based on our previous findings, we demonstrate that chemical composition can be controlled to minimize the capacity fade.

3.2 Experimental

3.2.1 General Consideration

Lithium carbonate (99%), lithium metal foil (99.9%, metal basis) were purchased from Alfa Aesar. Manganese carbonate (99.9%, trace metal basis), Lithium hexafluorophosphate (99.9%, battery grade), lithium hexafluoroarsenate (99%), lithium manganese oxide (electrochemical grade) and nitronium tetrafluoroborate (95%) were purchased from Sigma Aldrich. *N*-methyl-2-pyrrolidone (99%) and poly(vinylidene difluoride) (battery grade) were purchased from Alfa Aesar. were used as received. Ethylene carbonate and diethyl carbonate were purchased from Sigma Aldrich and were distilled prior to storing in an argon-filled glove box (Vacuum Atmospheres). HPLC-grade acetonitrile was purchased from Fisher and dried in a solvent purification system (Vacuum Atmospheres) then stored in a nitrogen-filled glove box (Vacuum Atmospheres). Extra dry oxygen gas was supplied by Cryogenic Gases.

Powder X-ray diffraction patterns were collected on a Bruker D8 Advanced diffractometer with a Lynx-Eye detector and parallel beam optics using Cu-Kα radiation (λ = 1.542 Å). The patterns were refined using the Bruker TOPAS software. Time-of-flight neutron diffraction experiments were performed on a powder diffractometer (POWGEN) at the Spallation Neutron Source of ORNL (Oak Ridge National Lab). The experimental resolution $\Delta d/d$ = 0.0015 at d = 1 Å. The data were collected at room temperature using incident neutron beam wavelengths centered at 1.066 and 3.198 Å. Scanning electron microscopy (SEM) images were collected using an FEI Nova Nanolab

SEM/FIB. High resolution transmission electron microscopy (HR-TEM) was performed using a JEOL 3011 TEM with a LaB_6 electron beam source. The samples were dispersed in methanol and drop cast onto a copper grid with an ultra-thin holey carbon film (Ted Pella). ICP-AES elemental analysis for lithium and manganese was obtained using a Perkin-Elmer Optima 2000DV analyzer. Typically, ~10 mg samples were dissolved in 2 – 5 mL 12 M HCl (Fisher Scientific) with a few drops of H_2O_2 (Fisher Scientific, 30 wt%) for quick digestion. The average oxidation states of manganese were determined by a potentiometric titration using $FeCl_2$/$KMnO_4$ (Alfa Aesar, 99.9% metal basis/98%). All samples were digested using dilute H_2SO_4 prior to titration. Differential scanning calorimetry was obtained with a DSC Q10 (TA instruments) at a ramping rate of 10 ℃.

3.2.2 Materials Preparation

Commercial lithium manganese oxide (C-LMO) from Sigma Aldrich was directly used as an active cathode material in this study. Chemical delithiation was performed by reacting lithium manganese oxide with nitronium tetrafluoroborate in acetonitrile. Typically, 1 gram of lithium manganese oxide reacted with 2 equivalents of nitronium tetrafluoroborate. The reaction was kept under vigorous stirring for at least 96 h. The final products were collected by vacuum filtration and washed with fresh acetonitrile in the N_2 glove box.

Lithium manganese oxide samples with controlled oxygen content were also synthesized by a solid-state method. Lithium carbonate and manganese carbonate with the molar ratio 1.03 : 2 was ball milled overnight. The extra 3% lithium content was used to compensate for potential lithium evaporation during the synthesis. Acetone was used for milling assistance. The acetone was then evaporated under reduced pressure with a

rotary evaporator (Buchii). The carbonates were then calcined at 600 ℃ under pure oxygen flow (100 mL/min) with heating and cooling rates of 5 ℃ /min. The product was then ground and annealed at 750 ℃ under oxygen, again with heating and cooling rates of 5 ℃ /min. This sample was noted as S-LMO for synthesized LMO. The reaction yields on a ~25 gram scale. To create oxygen vacancies in S-LMO, 5 grams of S-LMO was heated to 800 ℃ with a ramping rate of 10 ℃ /min. After 30 min, the sample was removed from the furnace and directly quenched in liquid nitrogen. The sample noted as D-LMO for defect-LMO was then collected.

3.2.3 Electrochemical Measurements

Long term electrochemical cycling tests were performed using coin cells or two-electrode Swagelok^{TM} PTFE cells. For neutron diffraction sample preparation, the material was cycled in pouch cells. Pure lithium metal was used as the counter- and pseudoreference electrode for the measurements. To prepare the working electrode, Sigma-Aldrich lithium manganese oxide, carbon black (TIMCAL Super P) and poly(vinylidene) difluoride (PVDF) (mass ratio of 85:10:5) were mixed in a Thinky AR-100 mixer. *N*-Methyl-2-pyrrolidone (NMP) was added to dissolve the PVDF binder. The composite was then cast onto a de-greased aluminum foil by the doctor blade method. The foil was then dried in a vacuum oven (Fisher Scientific) at 120 ℃ overnight prior to assembling the electrochemical cells. The active material loading is approximately 11 mg/cm^2. The electrode masses were measured using a Sartorius ME36S microbalance. Celgard^{TM} separator (model 3401) was used in the electrochemical tests. Lab-prepared electrolytes (1 M) were prepared using $LiPF_6$ and $LiAsF_6$ with ethylene carbonate and diethyl carbonate with volume ratio of 2:1. Commercial electrolyte of 1 M $LiPF_6$ in ethylene

carbonate, dimethyl carbonate and diethyl carbonate (v/v/v, 1:1:1) was also used as control from MTI. All cells were assembled in the argon glove box.

Galvonostatic charge/ discharge experiments were performed on a NEWARE BTS-5V1MA or a Maccor 64 channel cycler in the voltage window 3.40 to 4.45 V (*vs.* $Li^{+/0}$). The constant current applied in the charge/ discharge test is 0.2 *C* (where *C* is the current required to discharge the theoretical capacity of the cell in one hour). Cyclic voltammetry (CV) was recorded on a CH Instruments 660 C electrochemical workstation. Electrochemical impedance spectra (EIS) were collected on an Autolab PGSTAT302N with a FRA module. Prior to EIS measurements, the cells were equilibrated at 3.40 V until the current dropped below 10 nA. The AC perturbation was ±10 mV, and the frequency range was from 10^5 to 10^{-2} Hz.

Electrochemical delithitation was applied for neutron sample preparation. The electrochemical cells were charged to the desired potential at 0.2 *C* current; then the cell potential was held until the current dropped below 1 μA. Then the cell was disassembled, the cathode was washed with diethyl carbonate solvent and kept under vacuum at room temperature. The active material was then carefully removed from the aluminum current collector by a razor blade. A similar treatment was used to collect the cathode material after 100 galvanostatic cycles at 0.2 *C* current for the neutron diffraction study.

3.3 Results

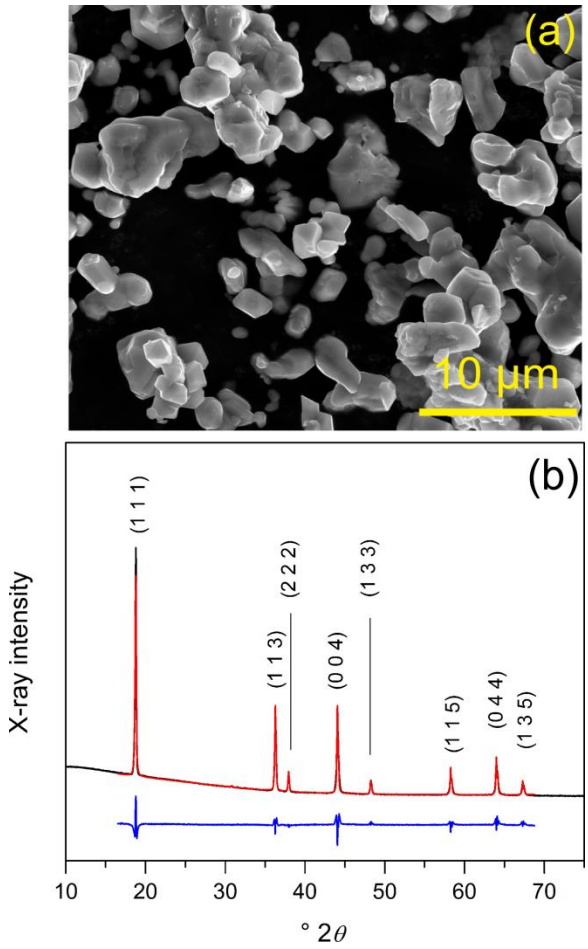

Figure 3.1 a. SEM image of fresh C-LMO; b. Powder X-ray diffraction pattern (black), Rietveld refinement (red), and difference pattern (blue) for C-LMO.

Lithium manganese oxide ($LiMn_2O_4$) has a cubic spinel structure with a space group of *Fd*–3*m* and a unique lattice parameter, *a*; in this structure, lithium, manganese and oxygen reside on the 8*a* (tetrahedral), 16*d* (octahedral) and 32*e* Wyckoff sites, respectively. Conventional solid-state synthesis requires high-temperature annealing to form products with suitable crystallinity. However, oxygen vacancies can be easily introduced during the calcination reaction. In a previous study,错误！未定义书签。 we

used neutron diffraction to quantify the oxygen defects in hydrothermally synthesized $Li_{1+x}Mn_{2-x}O_{4-\delta}$, in which δ is the vacancy factor. In the present study, commercial $LiMn_2O_4$ (C-LMO) from Sigma-Aldrich was used due to its wide availability. The scanning electron microscopy (SEM) image in Figure 3.1a shows that particles range from 2 – 10 μm in size. Figure 3.1b shows the X-ray diffraction pattern of C-LMO with the corresponding Rietveld refinement (Tables B.1 and B.2). Based on the XRD result, C-LMO shows very high crystallinity without any detectable impurities. The structural refinement result gives a lattice parameter a = 8.254 Å. The lattice parameter of stoichiometric $LiMn_2O_4$ is 8.248 Å.[175] We note that although the observed value is close to the literature value, the compound may be oxygen deficient.

Cyclic voltammetry (CV) and differential scanning calorimetry (DSC) indirectly provide evidence for oxygen vacancies in $LiMn_2O_4$. Figure B.1a shows the CV trace collected at 0.1 mV/s of C-LMO. The redox waves centered about 4.0 V are indicative of lithium insertion and extraction chemistry. However, we also observe electrochemical reactions at ~3.2 V and 4.5 V, which are attributed to a phase change from a cubic cell to a double hexagonal cell that arises due to oxygen deficiency.[176] In addition, Figure S1b shows the DSC profile recorded during the cooling process. The exotherm at ~10 ℃ suggests a phase change, which has also been shown to occur due to oxygen vacancies.[177, 178] Finally, elemental analysis (Table B.3) by ICP-AES analysis and potentiometric titration shows that C-LMO is best represented as the formula $LiMn_2O_{3.88}$, which confirms the oxygen non-stoichiometry in the material.

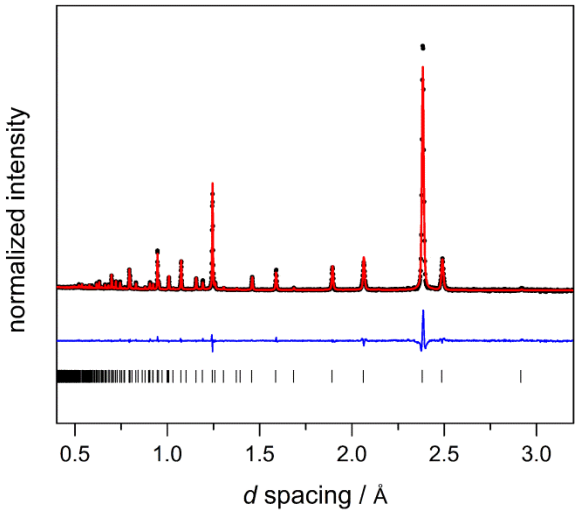

Figure 3.2 Neutron diffraction pattern obtained on POWGEN at 300 K of C-LMO: black dots represent the observed intensities, the red line is the fit, the blue line is the difference pattern, and the tick marks below the profiles indicate positions of all allowed Bragg reflections.

Figure 3.2 shows the neutron diffraction pattern of the fresh, uncycled C-LMO. As we expected, the site occupancies determined in the Rietveld refinement (Table B.4) show evidence of oxygen deficiencies, and the formula unit is best represented as $LiMn_2O_{3.88}$. This formula is in excellent agreement with the elemental analysis. The oxygen atoms located on the 32*e* Wyckoff sites are calculated to be 97.1% filled, which confirms the oxygen deficient structures of C-LMO. Meanwhile, the lattice parameter is 8.2530 Å, which corroborates the powder X-ray study.

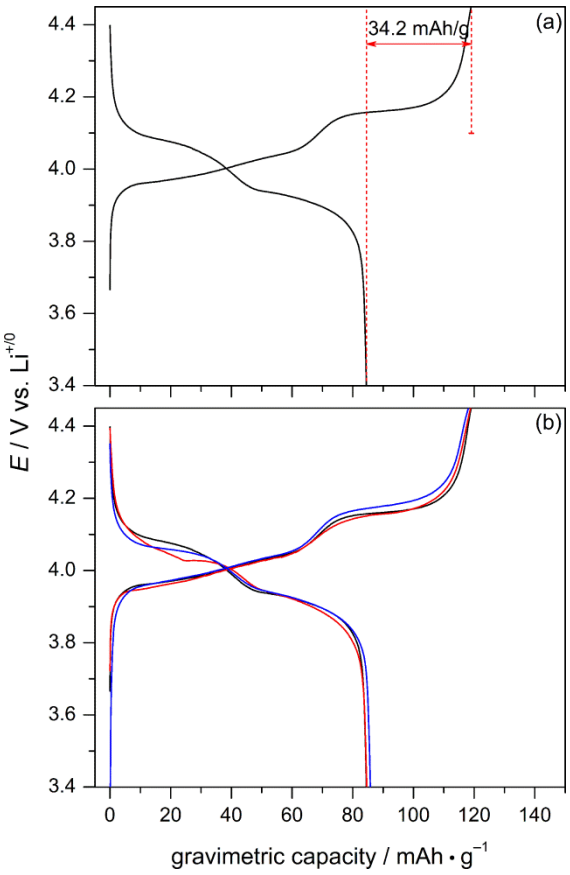

Figure 3.3 a. First electrochemical charge/discharge cycle of C-LMO collected at 0.2 *C* current within the potential window of 3.40 – 4.45 V; b. First electrochemical charge/ discharge cycle of C-LMO collected at 0.2 *C* current within potential window of 3.40 – 4.45 V in different solvents: black, 1 M $LiPF_6$ in EC:DEC mixture with v/v of 2:1 at room temperature; red, 1 M LiPF6 in EC:DEC mixture with v/v of 2:1 at 55 ℃; blue, 1 M LiAsF6 in EC:DEC mixture with v/v of 2:1 at room temperature.

We next carried out charge/discharge tests of a C-LMO battery between 3.40 to 4.45 V *vs.* $Li^{+/0}$ lithium foil in a lab-prepared electrolyte containing 1 M $LiPF_6$ in the typical carbonate solvents. To achieve detailed electrochemical behavior and to minimize energy losses due to polarization, a slow cycling rate of 0.2 *C* was used for all of the

galvanostatic charge/ discharge experiments in this work. The first charge/ discharge cycling profile of C-LMO is plotted in Figure 3.3a. A sloping region and a pseudo-plateau are observed in both charging and discharging curves, corresponding to the single phase and two phase insertion/extraction, respectively. During the charging process of C-LMO, ~120 mAh/g is stored, which corresponds to 81% of the theoretical capacity of $LiMn_2O_4$. However, only 84.5 mAh/g can be extracted during the first discharge process. That is, there is an ~30% irreversible capacity loss during the first electrochemical cycle.

There are at least two reasons that explain this observation: active material loss due to acid corrosion and side reactions between C-LMO and the electrolyte that blocks lithium channels. For the first possibility, it is well documented that trace moisture in the cell leads to HF formation from $LiPF_6$.[11] To test this possible degradation mechanism, we repeated the cycling experiment using the more hydrolytically stable $LiAsF_6$ electrolyte. Meanwhile, we also cycled the C-LMO cathode in a half-cell configuration at elevated temperature (55 ℃) to study electrolyte degradation and capacity loss during the first cycle, noting that detrimental HF formation should be faster at higher temperature. Figure 3b shows the first charge/ discharge profiles of C-LMO cycled under these different conditions. From this data, we conclude that *the capacity fade is the same regardless of temperature and electrolyte formulation, and is an inherent property of C-LMO cathode material.*

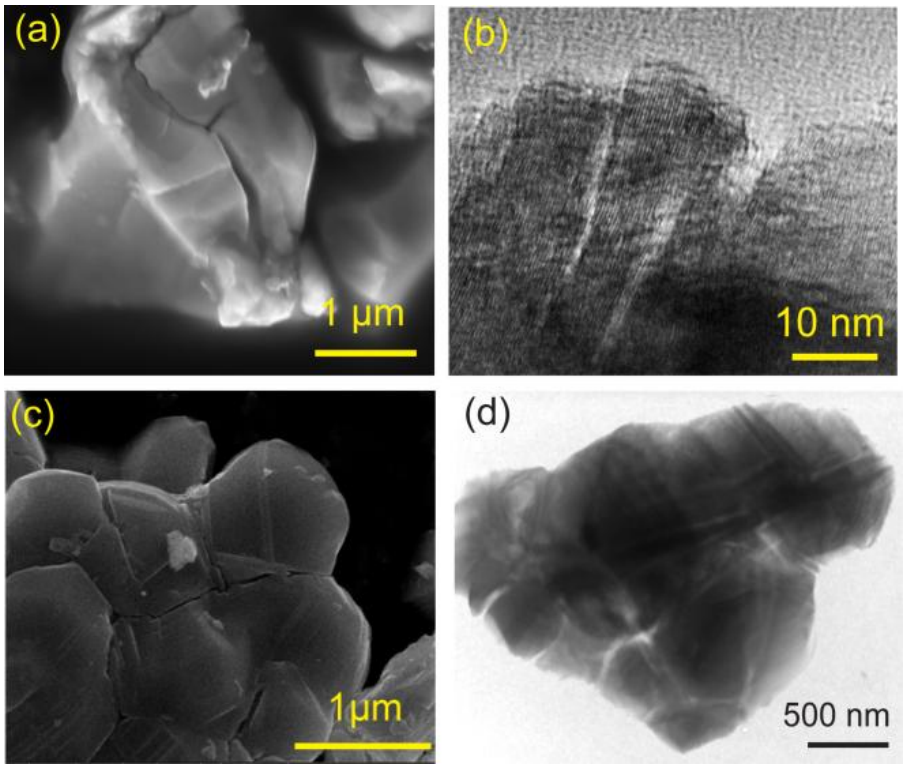

Figure 3.4 a. SEM image of C-LMO after first charge at SOC of 4.45 V; b. TEM image of C-LMO after first charge with SOC of 4.45 V; c. SEM image of C-LMO after 96 h chemical delithiation; d. TEM image of C-LMO after 96 h chemical delithiation in NO_2BF_4.

The 3.40 – 4.45 V electrochemical window does not include the irreversible phase transitions that occur at potentials < 3.2 and > 4.5 V. To determine whether detrimental changes occur at higher potential or if they occur throughout the entire electrochemical window, we collected the cathode material at a state-of-charge of 4.45 V to investigate possible microstructural variation after the first delithiation. The SEM image in Figure 3.4a shows unequivocal particle microfracture after the first charge. Meanwhile, transmission electron microscopy (TEM) in Figure 3.4b corroborates particle fracture through electrochemical shock during the first Li^+ extraction. In order to reproduce the electrochemical delithiation, we carried out chemical delithiation using the strong oxidant NO_2^+ to mimic the first charging process. Figure 3.4c and d shows the SEM and TEM

images of the delithiated C-LMO after its reaction with NO_2BF_4 for 96 h. A large frequency of cracks occurs over the samples, similar to what is observed in the electrochemically charged C-LMO.

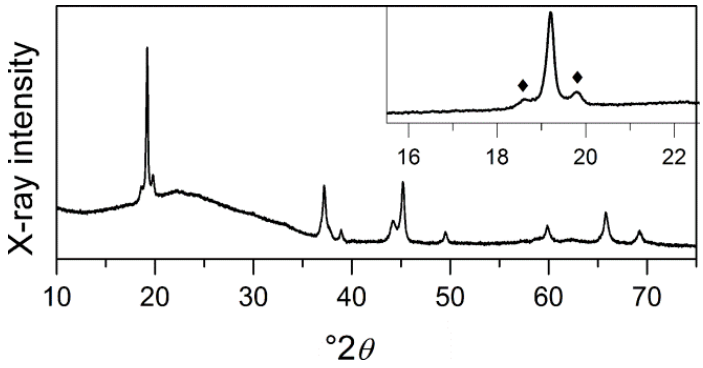

Figure 3.5 Powder X-ray diffraction pattern of C-LMO after first charge with SOC of 4.45 V. Newly evolved peaks are highlighted by the black diamonds.

We have shown that particle fracture occurs during the first delithiation process, similar to what has been observed in $LiCoO_2$ cathode material during the first charge by an acoustic study.[14] Meanwhile, in the study of charge and discharge behaviors of Li/MnO_2 cells, Ohzuku also noticed microfractures by monitoring acoustic counts during the first electrochemical cycle.[15] Sastry and coworkers have also shown possible $LiMn_2O_4$ fractures in a combined AFM and simulation study.[179] We next studied X-ray diffraction to look for the structural changes associated with cracking. Figure 3.5 shows the XRD pattern of C-LMO cathode at SOC of 4.45 V. The original (111) Bragg reflection at 18.8 ° splits into three new peaks: one major peak at 19.2 °and two small peaks at 18.6 ° and 19.8 °, which are highlighted in the inset. Those peaks can still be indexed to represent the (1 1 1) Miller plane. It is known that the cubic unit cell contracts during delithiation, which leads to the higher angle (right) shifts in the peaks that emerge at 19.2 and 19.8 °.

However, the peak at 18.6 ° hints a small lattice parameter *expansion* instead. This expansion has been observed by Aurbach's in previous work.[180] We surmise that expansion occurs because of possible manganese migration into adjacent lithium tetrahedral sites during the electrochemical oxidation. Nevertheless, multiple phases were identified after the first charge, which could lead to the accumulation of strain in the active material that ultimately results in particle fracture.[181] Figure 3.6 shows the powder neutron diffraction (PND) pattern before and after the first charge. There is a drastic decrease in the diffraction intensity after lithium extraction, demonstrating the loss of long-range crystalline order. The diffraction pattern of the C-LMO with a SOC of 4.45 V is blown up in the inset for a detailed comparison. Peak splitting and broadening are observed after the first charge. The SOC potential of 4.45 V is above the delithiation two phase region as shown in the charging profiles. A single phase was expected at cell potential of ~4.45 V. However, the lack of crystallinity after delithiation hinders precise indexing of solid phases.

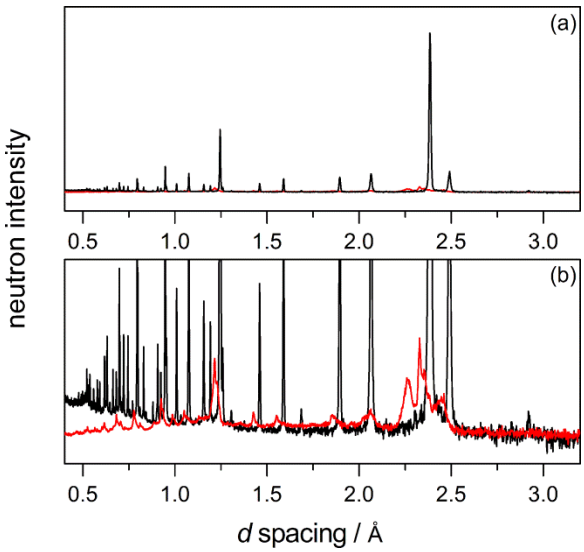

Figure 3.6 a. PND pattern of fresh C-LMO (black) and the sample after first charge with SOC of 4.45 V (red); b. Close-up of the region near the baseline to show that new Bragg reflections emerge.

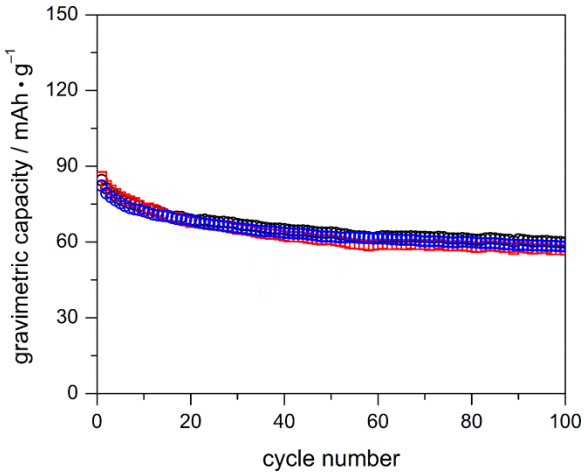

Figure 3.7 Comparison of the first 100 cycles of C-LMO in different solvents at room temperature: black circles, 1 M $LiPF_6$ in EC:DEC mixture with v/v of 2:1; red squares, 1 M $LiPF_6$ in EC:DEC mixture with v/v of 2:1; blue triangles, 1 M $LiPF_6$ in DMC:EC:DEC with v/v/v of 1:1:1.

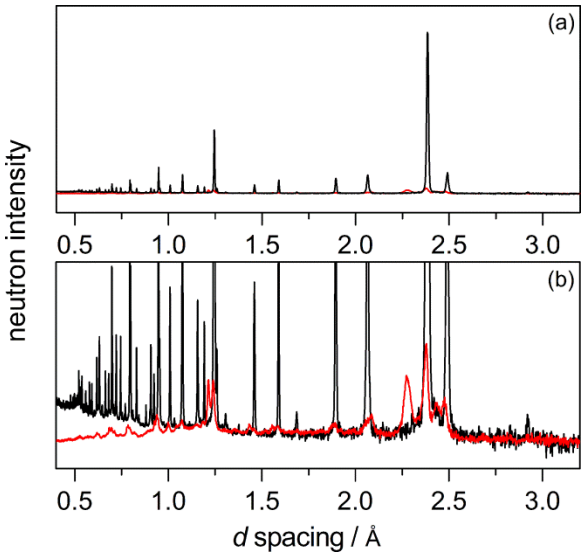

Figure 3.8 a. PND pattern of fresh C-LMO (black) and the sample after 100 electrochemical cycles in 1 M $LiPF_6$ within EC:DEC mixture with v/v of 2:1 with SOC of 3.40 V (red); b. Close-up of the region near the baseline.

We have shown in Figure 3.3 that the electrolyte and temperature-induced surface side reactions do not play significant role in influencing the irreversible capacity loss during the first cycle. Figure 3.7 shows that the first 100 cycles of the C-LMO in a different solvent system are unchanged; they too fade at a similar rate. In Figure 8, the neutron diffraction pattern is plotted for C-LMO at SOC of 3.40 V after 100 cycles in a lab-prepared $LiPF_6$ electrolyte. This pattern also shows multiple phases. Furthermore, the similarity between the neutron diffraction patterns of the firstly charged C-LMO with SOC of 4.45 V and the pattern collected after 100 cycles with SOC of 3.40 V demonstrates that the loss of crystallinity upon the first charge is irreversible. This results matches that observed in Woodford's study on $LiCoO_2$ cathodes.[45]

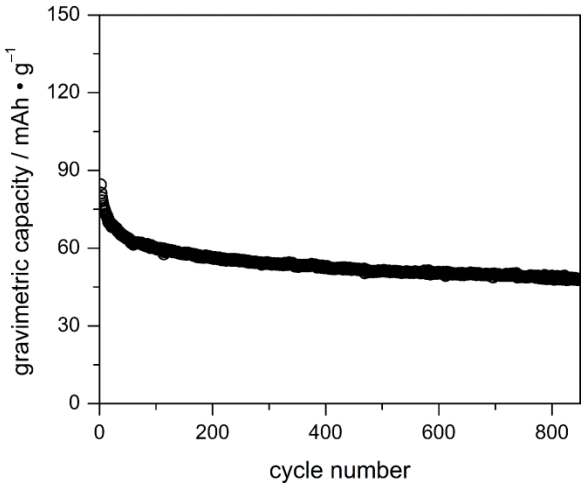

Figure 3.9 Cyclability of C-LMO over 850 cycles at 0.2 *C* current in 1 M $LiPF_6$ in 2:1 v/v EC:DEC at room temperature.

Longer term cycling of C-LMO is presented in Figure 3.9, showing ~43% capacity fade of lithium manganese oxide cathode over 850 cycles at 0.2 *C* current. The largest drop in capacity occurs over the roughly first 200 cycles, followed by more gradual capacity fade over the next ~ 650 cycles. The charge/ discharge profiles of the 1st, 200th and 800th cycle are plotted in Figure 3.10a. As we observed in the first cycle, there exist two distinct features corresponding to a single phase- and two phase regions,[182] which can also be observed in d*Q*/d*V* profile of Figure 3.10b from 3.9 to 4.2 V. The sharp features observed for the first cycle are smoothed in the 200th and 800th cycling data. In addition, there is a significant drop in peak intensity. Although there is still capacity fade observed from 200th cycle to 800th cycle in Figure 3.10a, their d*Q*/dV curves nearly overlap, and the electrochemical features do not change significantly over the remaining 600 cycles. The phenomenon described above corroborates the crystallinity loss observed in the diffraction study. The reduced crystalline domain size suggests indistinguishable phase change boundaries, which is supported by diminished d*Q*/d*V* peak intensities.[183] There

have been similar discussions regarding the electrochemical behaviors TiO_2, $LiCoO_2$ and $LiNi_{0.5}Mn_{1.5}O_4$, with different crystalline sizes.[184–186]

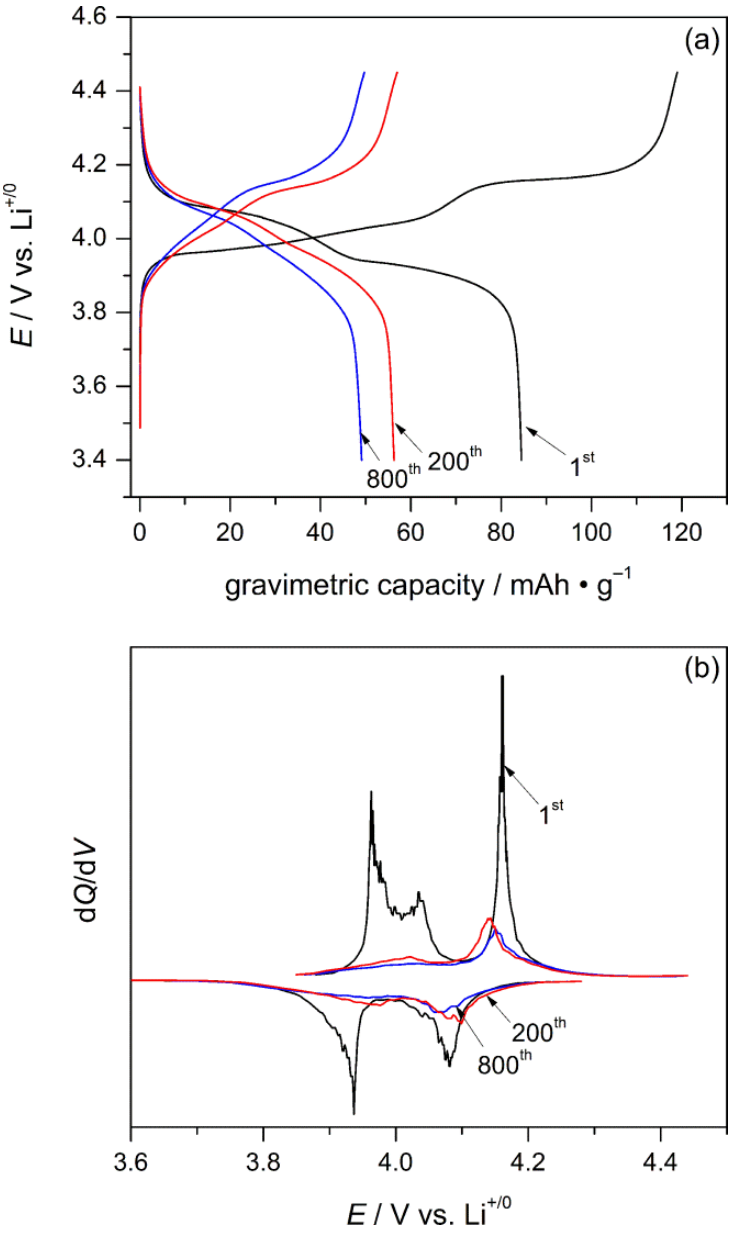

Figure 3.10 a. Charge/ discharge profiles of C-LMO at 1st, 200th and 800th cycles obtained at 0.2 *C* current; b. corresponding d*Q*/d*V* curves of 1st, 200th and 800th cycles.

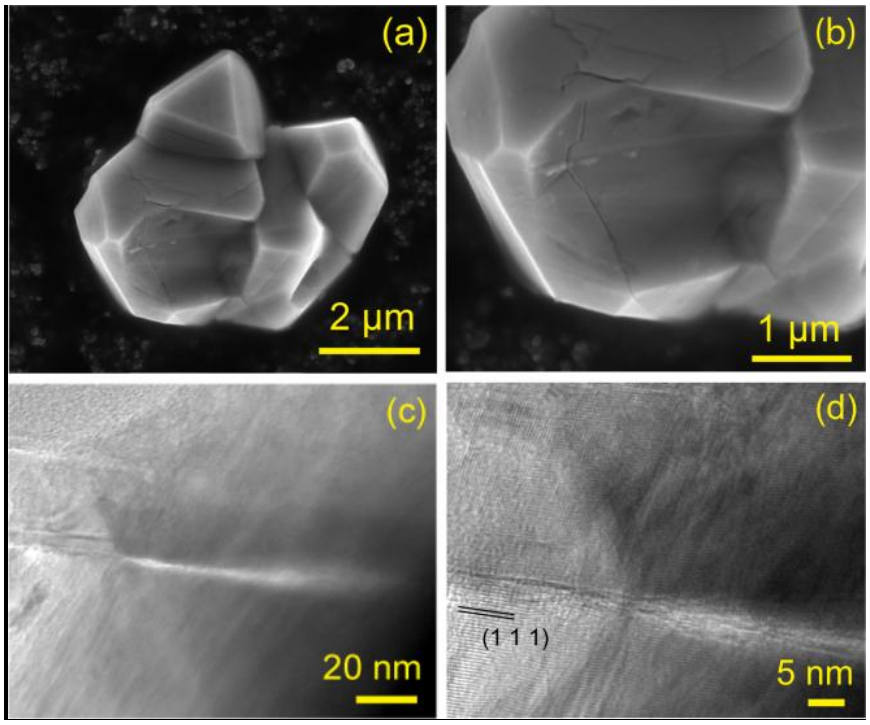

Figure 3.11 a. SEM image of C-LMO after 850 electrochemical cycles; b. enlarged SEM image showing cracks; c. TEM image of C-LMO after 850 electrochemicals; d. enlarged area showing the (111) family of planes.

Microstructural analysis after long-term cycling is presented in Figure 3.11. SEM imaging reveals that micron-sized active material with clearly defined crystal facets are maintained after 850 cycles. Several particles aggregate during cycling, and we initially suspected that fracture would occur at those interfaces between aggregated particles due to the higher surface energy at boundaries. However, we observe that cracks are well distributed all over surfaces as shown in Figures 3.11a and b, which was not observed after the first cycle. This behavior hints that structural failure is more pronounced after prolonged electrochemical cycling; more microfractures are generated by repeated delithiation and lithiation. Figure 3.11c shows the typical TEM image of the cathode after long term cycling with micro-scaled fracture identified. With higher magnification in

Figure 3.11d, we see that fracture occurs along the (1 1 1) planes. In addtion, the twisted fringes suggest significant internal stress that results in structural collapse on the microscale.

3.4 Discussion

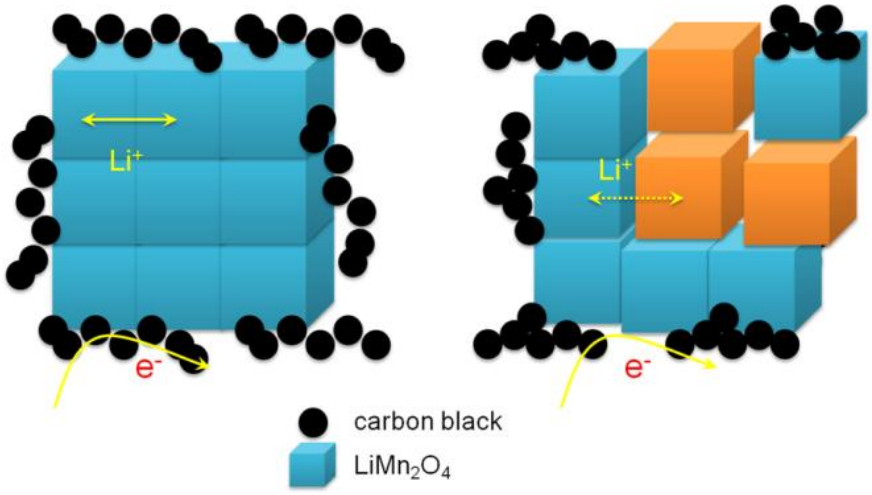

Scheme 3.1 Structural changes and interparticle shearing of C-LMO cathode material during electrochemical cycling: freshly prepared electrode (left); electrode after micro-fracturing occurs (right).

Capacity fade in $LiMn_2O_4$ is closely related to mechanical grinding, illustrated in Scheme 3.1. In a freshly prepared $LiMn_2O_4$ electrode, the bulk particles of active material are surrounded by the conductive carbon black network to enhance the electronic conductivity. Charge transfer occurs by lithium diffusion within an LMO particle, electron transfer at the LMO/carbon black interface, and also at LMO grain boundaries. However, after numerous charge/discharge cycles, fractures within active material propagate to increase the number of LMO/electrolyte interfaces. The smaller domains of the ruptured particles are electronically isolated due to the lack of contact with conductive additives or other LMO grains. Then, less access to the active cathode

material leads to capacity loss as we observed. Meanwhile, it is noteworthy that this fracture does not result from one electrochemical cycle. Rather, structural collapse occurs with continuous lithium insertion/extraction. Interestingly, from the long term cyclability study, the majority of the capacity fade occurs during the first 200 cycles, and the true active cathode is a best described as a multi-phase mixture of nano-scale domains.

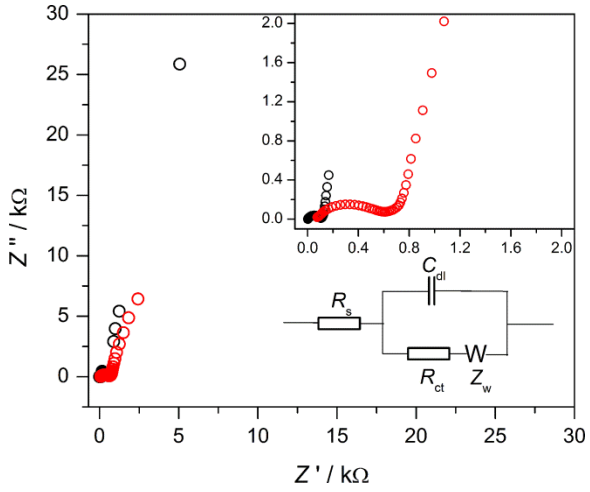

Figure 3.12 Electrochemical impedance spectra of a freshly prepared C-LMO half cell (black) and the cell after 850 electrochemical cycles with SOC of 3.40 V (red). The equivalent circuit is included in the plot.

The isolated domains should lead to an increase in the battery's internal resistance. Figure 3.12 shows the electrochemical impedance spectrum of C-LMO half cells both before and after long-term cycling (850 cycles). A modified Randle's circuit was applied to describe the profiles. R_s represents the solution resistance which matches the intersection at Z' axis. The diameter of the semi-circle gives the charge transfer resistance as R_{ct}. In comparison with the freshly prepared cell, there is a large increase in both R_s and R_{ct} values which is consistent with Scheme 3.1.

The composition of C-LMO in this study shows an oxygen deficient structure that has been confirmed by elemental analysis and the neutron structural refinements. In our

previous work, we have shown the electrochemical instability of oxygen-deficient $LiMn_2O_4$ compared to the stoichiometric spinel. Therefore, to bridge the cathode's composition and structural properties with the failure mechanism we found, we introduced two lab synthesized $LiMn_2O_4$ compounds with a controlled structure and oxygen level. Based on elemental analysis, the two compounds are represented by the formulas $LiMn_2O_{4.03}$ and $LiMn_2O_{3.87}$, with manganese oxidation states of +3.53 and +3.37, respectively. We use these samples as representative examples of oxygen-stoichiometric (S-LMO) and oxygen-deficient (D-LMO) materials, respectively. The number of oxygen vacancies was selected to match that found in C-LMO.; details of the characterization are presented in the appendix. We recognize that crystal plane/surface morphology of the cathode materials could also contribute to the electrochemical performance of the battery, [187 – 189] but note that we control for these effects by synthesizing these compounds using the same solid-state method. Consequently, similar morphologies are expected, as illustrated in the SEM images as Figure B.2. Due to the oxygen vacancies in D-LMO, the lattice parameter of 8.253 Å is larger compared to 8.233 Å in S-LMO.

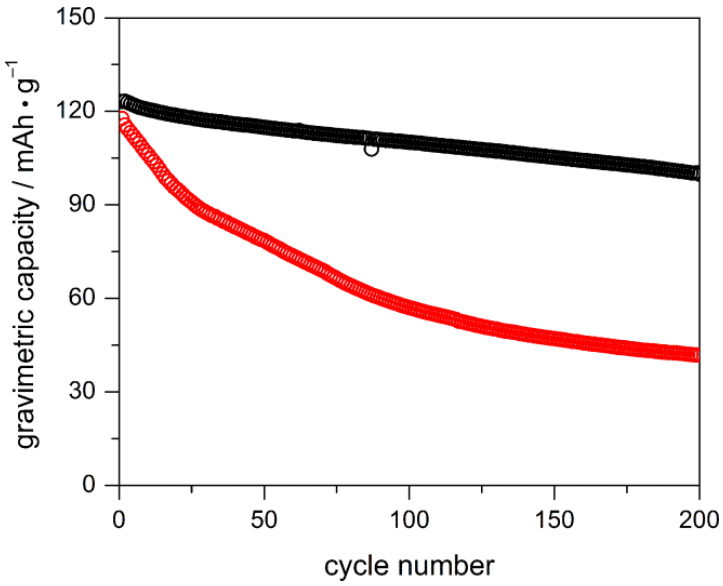

Figure 3.13 First 200 electrochemical cycles of S-LMO (black) and D-LMO (red) at 0.2 *C* current within potential window of 3.40-4.45 V.

In order to validate the comparison, both of the materials were cycled under the same electrochemical conditions in lab-prepared $LiPF_6$ electrolyte as the C-LMO. The cyclability is plotted in Figure 3.13. Half cells prepared from both synthesized compounds show a similar initial discharge capacity of ~120 mAh/g. However, there is a faster rate of capacity fade observed for the D-LMO. Over the first 200 cycles, the capacity of the S-LMO sample decreases to 98 mAh/g (81.6 % capacity retention), whereas, D-LMO decreases to only 64.2% of its initial capacity. We cycled the D-LMO for a longer period to achieve a better comparison with C-LMO, as shown in Figure B.3. Although the D-LMO sample is able to deliver higher capacity during the initial discharge, it shows a similar trend in capacity fade as that of C-LMO. Again, capacity fade occurs most markedly over the first 200 cycles, followed by relatively stable capacity retention over hundreds of cycles. Such a phenomenon indicates that the oxygen-deficient D-LMO sample might suffer a similar capacity fading mechanism as

discussed earlier. An EIS study was performed on S-LMO and D-LMO cells after 100 cycles at 1*C* current. The data presented in Figure B.8 show a significantly larger charge-transfer resistance for D-LMO after cycling, compared to S-LMO, which supports the deleterious effect of oxygen vacancies.

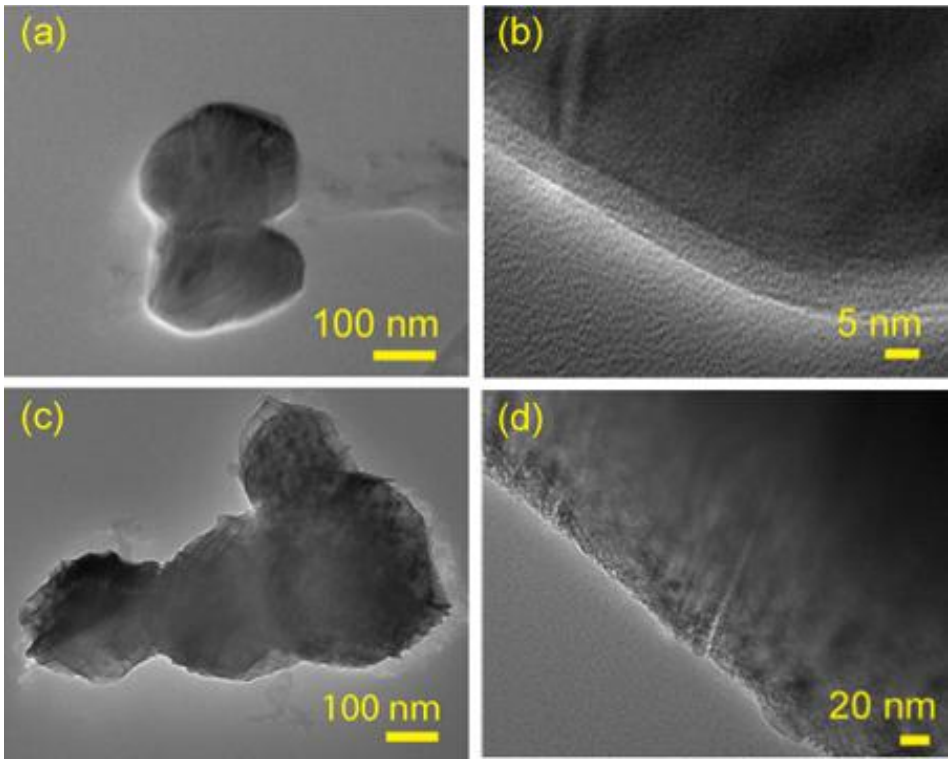

Figure 3.14 TEM images of lab prepared LMO after 200 cycles: a, b. S-LMO; c,d. D-LMO.

To confirm the capacity retention trend related to the oxygen content in LMO, we studied the microstructural properties of the lab prepared $LiMn_2O_4$ after 200 cycles as shown in Figure 3.14. Figure 3.14a shows that particles are largely intact, without noticeable microfractures, which leads to better cyclability and structural stability. The enlarged image in Figure 3.14b conveys the same information. On the other hand, Figure

3.14c shows fractures and grain dislocations in cycled D-LMO. Microfractures can be identified at higher resolution Figure 3.14d. The results link the microstructure, capacity fade, and oxygen nonstoichiometry in $LiMn_2O_4$. These defects are detrimental to long-term capacity retention and structural integrity of spinel electrodes.

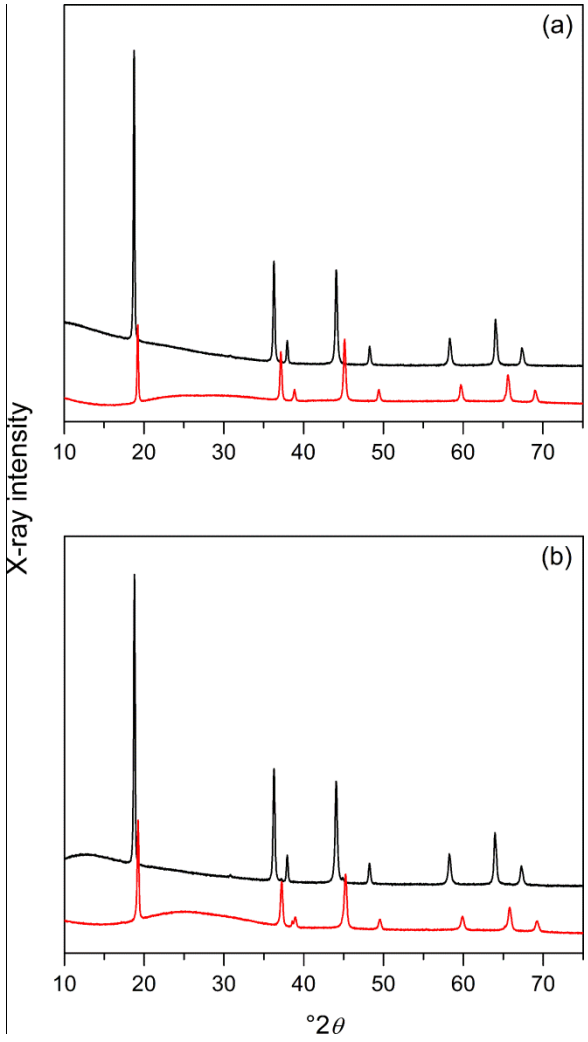

Figure 3.15 PXRD patterns of a. as prepared S-LMO (black) and its first charge delithiated sample (red) at SOC of 4.45 V; b. as prepared D-LMO (black) and its first charge delithiated sample (red) at SOC of 4.45 V.

In Figure 3.15, we plot the XRD patterns of both lab-prepared LMO samples and their structural profiles after charging to 4.45 V SOC. Neither material shows the appearance

of new phases although the peaks shift based on predicted lattice parameter changes. Moreover, slight peak broadening was observed for the both samples after the first charge. Based on the Rietveld refinement results, the crystalline domain size shrinks from 102.4 to 51.9 nm for S-LMO and 85.5 to 36 nm for D-LMO after the first electrochemical delithiation. All the structural patterns and refinement results are collected in Figures B.4-7 and Tables B.5-12, from which we can calculate the lattice displacement based on isotropic volume change assumption. The lithium extraction from S-LMO results in a 0.161 Å lattice shrinkage; in the contrast, a 0.203 Å decrease in lattice parameter results from the oxygen-deficient sample. The 25% larger lattice expansion could result in more strain, which accounts for the difference in capacity retention.

3.5 Conclusion

We have observed long term capacity fade in commercially available $LiMn_2O_4$, which is shown to be oxygen deficient. Powder diffraction and microstructural analysis have been carefully employed to observe account for structural failure. Surface side reactions and temperature do not play a significant role toward influencing the capacity retention. In contrast, we have shown that capacity fade arises due to structural collapse along the (1 1 1) planes. These microcracks lead to mechanical pulverization during electrochemical cycling of the cathodes, and leads to increased charge-transfer resistance within the cell.

This capacity fading mechanism is dependent on chemical composition. Similar fracture phenomena were illustrated in lab-prepared oxygen-deficient LMO. However, near stoichiometric oxygen content gives rise to prolonged structural integrity and stable electrochemical cycling. Lattice strain is suggested to be one of the main reasons causing

structural failures due to large volume changes. Current efforts focus on possible cation mixing during electrochemical cycling.

CHAPTER 4

Two Step Hydrothermal Synthesis of Submicron $Li_{1+x}Ni_{0.5}Mn_{1.5}O_{4-\delta}$ for Lithium-Ion Battery Cathodes ($x = 0.02$, $\delta = 0.12$)

Portions of this chapter have been published:

Hao, X.; Austin, M. H.; Bartlett, B. M. *Dalton Trans.* **2012**, *41*, 8067-8076. (New Talent: Americas themed issue)

4.1 Introduction

Lithium manganese oxide ($LiMn_2O_4$, LMO) with a cubic spinel structure (space group $Fd\bar{3}m$) has gained much interest because of its huge potential application as an environmental friendly and low-cost lithium-ion battery cathode.[190, 191] $LiMn_2O_4$ is formally mixed-valent Mn^{4+} and Mn^{3+} with a average oxidation state of manganese of 3.5. The compound experiences a symmetry-lowering phase transition that corresponds directly with the irreversible Jahn-Teller distortion of Mn^{3+},[192] which causes capacity fade during battery operation. To alleviate these structural distortions, a new group of 5 V (*vs* $Li^{+/0}$) spinel cathodes have been introduced in which the redox couple of low valent late transition metals such as Co, Ni, Cu, etc.[193–195] can be accessed at higher potential. The candidate $LiNi_{0.5}Mn_{1.5}O_4$ (LNMO), first prepared in 1996, offers a theoretical gravimetric capacity of 147 mAh/g.[196] In this compound, all manganese is present in its +4 formal oxidation state, and capacity is stored in the $Ni^{4+/2+}$ redox couple; Ni substitution of Mn greatly improves the structural stability of spinel.[197,198] A full cell using this high voltage cathode with a titanate anode is thought to be an excellent

candidate for future applications.[199–204]

The interplay between the structural chemistry of LNMO and its electrode behavior is rich. Original work in the area began with the discovery that Ni can substitute for Mn in $LiMn_2O_4$.[205] However, with less than 25% substitution, the electrochemistry is similar to that observed in $LiMn_2O_4$. $LiNi_{0.5}Mn_{1.5}O_4$ spinel crystallizes in two structures: one in which Ni and Mn reside on 4*a* and 12*d* Wyckoff sites respectively, giving an ordered $P4_332$ structure,[206–210] or one in which both ions reside on the 16*d* site, the disordered $Fd\bar{3}m$ structure.[211–214] Electrochemically, the distorted structure shows better performance, presumably due to superior electronic conductivity afforded by charge transfer between Ni and Mn that share the same lattice site.[12,215] Most of the reported syntheses rely on high-temperature methods to prepare the disordered phase selectively. However, this frequently results in forming $Li_xNi_{1-x}O$ as an impurity phase.[216–218]

To circumvent the formation of impurities, we have developed a facile two-step hydrothermal synthesis route for the large-scale preparation of LNMO. From previous work in our group, we know that low temperature synthesis routes force us to consider oxygen vacancies in the spinel lattice. The ordered and disordered structures for this compound adopt the approximate compositions $LiNi_{0.5}Mn_{1.5}O_4$ and $LiNi_{0.5}Mn_{1.5}O_{4-\delta}$, respectively. Our methods select for the latter at temperatures of 240 ℃ and a 10 hour total reaction *without* the need for annealing.

4.2 Experimental

4.2.1 General consideration

Potassium permanganate 99% was purchased from J. T. Baker. Nickel (II) chloride hexahydrate 98% was purchased from Acros. Lithium hydroxide 98%, lithium hexfluorphosphate 99.99%, ethylene carbonate and diethyl carbonate solvents were

purchased from Aldrich. The solvents were dried over P_2O_5 prior to storing a Vacuum Atmoshperes OmniLab glove box under an argon atmosphere. Lithium foil was obtained from Strem Chemicals. HPLC-grade acetone was purchased from EMD Chemicals and distilled prior to use.

Powder X-ray diffraction patterns were obtained with a Bruker D8 Advance diffractometer equipped with Lynx-Eye detector and parallel beam optics using Cu-Kα radiation (λ = 1.54184 Å). XRD patterns were indexed and refined using the TOPAS program from Bruker AXS. Scanning electron microscopy images were obtained using a FEI Nova Nanolab SEM/FIB with an accelerating voltage of 10kV. High resolution transmission electron microscopy was performed with a JEOL 3011 TEM operated at 300 kV equipped with a LaB_6 electron source. TEM samples were prepared by sonicating a dispersion of LNMO powder in acetone and drop casting the suspension onto a Cu grid with an ultra-thin holy carbon film (Ted Pella^{TM}). All samples were heated in a standard laboratory Fisher vacuum oven 120 ℃ prior to the measurement. Raman spectra were obtained using a Renishaw Ramascope Raman spectrometer equipped with a Leica microscope, a Nikon LU Plan 20× objective (numerical aperture = 0.40), and a 1200 lines/mm grating. All spectra were taken under 785 nm laser excitation with 1.1 mW incident power. Spectral analysis was performed using the fitting routines included in the WiRE 3.2 software package. XP spectra were collected with a Krato Axis Ultra spectrometer using a monochromatic Al Kα source. The Kratos charge neutralizer system was used for all the analyses. The data collected were fitted by Casa^{TM} XPS software package 2.3.15.

4.2.2 Hydrothermal synthesis and annealing

The birnessite-structured precursor, $K_{0.39}MnO_{2.04}$•$1.25H_2O$ was initially precipitated from reacting 0.158 g $KMnO_4$ with 1.00 mmol of acetone in 12 mL 0.1 M KOH(aq) at room temperature. The resulting dark brown slurry was collected by centrifugation and washed several times with deionized water. The two-step hydrothermal reactions were performed in 23 mL PTFE-lined, stainless-steel Parr autoclaves. Autoclaves were heated to 240 ℃ and cooled to room temperature at a rate of 10 ℃/min. First, the initial precursor was reacted with 12 mL 0.027 M $NiCl_2$ (*aq*) for 5 h to produce the intermediate; then the intermediate was collected and washed before reacting with 12 mL 0.1 M LiOH (*aq*) in a second hydrothermal step. After a dwell time of five hours, dark red microcrystalline powders were collected and dried overnight in a vacuum oven at 120 ℃. For the one-pot reaction, 1.00 mmol $K_{0.39}MnO_{2.04}$•$1.25H_2O$ and 0.33 mmol $NiCl_2$ were added to 12 mL 0.1 M LiOH (aq). The product was collected after a dwell time of 10 hours at 240 ℃.

4.2.3 Elemental analysis

ICP-AES elemental analysis for Li, Ni and Mn was obtained using a Perkin-Elmer Optima 2000DV. Samples were digested in 3-5 mL conc. HNO_3 with a few drops of H_2O_2. Samples were references to an yttrium internal standard and concentrations of lithium and manganese were determined from the maximum intensity lines (610.632 nm for Li; 257.610 nm for Mn; 341.476 nm for Ni) compared to those of standard reference solutions. The average oxidation state of manganese (Z_{Mn}) was determined by a potentiometric titration using $FeCl_2$/$KMnO_4$. 20 mg samples were digested in 0.020 M $FeCl_2$ solutions of 10% H_2SO_4 that were titrated against 4.68 mM $KMnO_4$ according to

the balanced equation:

$$5Fe^{2+}(aq) + MnO_4^-(aq) + 8H^+(aq) \rightarrow 5Fe^{3+}(aq) + Mn^{2+}(aq) + 4H_2O(l)$$

4.2.4 Electrochemical measurements

Active cathode mixtures were prepared by mixing the synthesized material, carbon black and poly(vinylidene) difluoride (PVDF) using a mass ratio of 75:15:10 with a Thinky AR-100 rotation/ revolution super mixer. *N*-methyl-2-pyrrolidone (NMP) was added to dissolve the PVDF and to maintain the appropriate viscosity of the black slurry. This material was coated onto a deoiled aluminum foil using the doctor blade method. The foil was then dried in the vacuum oven overnight at 120 ℃ prior to assembling the cell in order to minimize surface-bound water as best as possible. The cathode and Celgard™ poly(propylene) film were cut and fit into a 1/4" Swagelok™ PTFE union under ambient room atmosphere. Final cell assembly was performed in a Vacuum Atmospheres OmniLab glove box under an argon atmosphere. The active material mass is approximately 1 mg, with an electrode area of 0.32 cm^2. The electrolyte solution was composed of 1 M $LiPF_6$ in 2:1 (v/v) ethylene carbonate and diethyl carbonate, and lithium foil was used as the anode.

Cyclic voltammetry measurements were performed on an eight-channel CH Instruments 1000 Electrochemical Workstation at a scan rate of 0.1 mV/s. Gavlanostatic charge/ discharge measurements at the rate 0.1 *C* was recorded on a CH Instruments 660C Electrochemical Workstation. Those for rates 1–10 *C* were recorded on a custom-designed Vencon UBA5 battery analyzer.

Electrochemical impedance spectra were recorded on an Autolab PGSTAT302N with a FRA (frequency response analysis) module. Prior to EIS measurements, the cells were

cycled 3 times between 4.0 and 5 V at 1 *C* current. Then the EIS were recorded at various requested potentials from 4.0 to 5.0 V with a 1 hour equilibrium time such that the current flow declined to less than 5 nA. The AC perturbation was ±10 mV, and the frequency range was from 10^5 to 10^{-2} Hz. Data were fit using the Zview™ software package.

4.3 Results and discussion

4.3.1 Synthetic chemistry

Our two-step hydrothermal synthesis proceeds according to the reactions outlined in Scheme 4.1. Note that the initial reaction in gray is nearly instantaneous, and begins immediately under ambient conditions prior to employing any hydrothermal conditions. In this reaction, $KMnO_4$ is used as the manganese source to produce a $K_{0.39}MnO_{2.04}$•1.25 H_2O precursor by a rapid redox reaction in which acetone is oxidized in a 0.1 M KOH aqueous solution. We know from previous work in our group that this material has the layered birnessite structure, similar to that of the phase δ-MnO_2, and that the manganese valence in this precursor is less than 4 due to the combination of oxygen nonstoichiometry and K^+ intercalation.[175] In the present LNMO study, potentiometric titration combined with ICP-AES analysis show that the decreased manganese valence persists in the final product (Z_{Mn} = 3.82), corresponding to an ultimate composition $Li_{1.02}Ni_{0.5}Mn_{1.5}O_{3.875}$. Full data are presented *vide infra* and in the ESI.

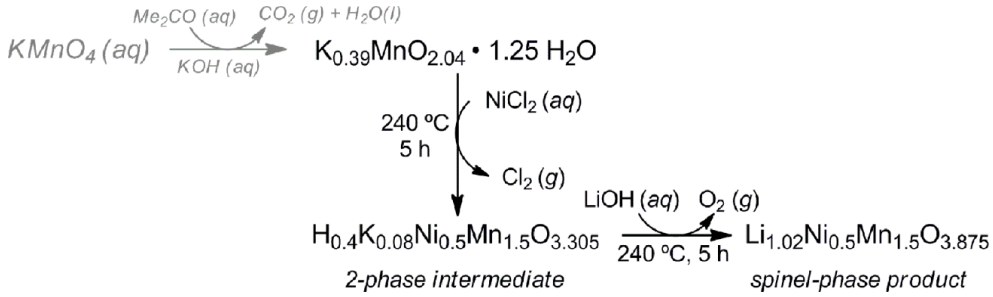

Scheme 4.1 Reaction scheme

In the first hydrothermal step, nickel reacts with this layered birnessite-type intermediate, $K_{0.39}MnO_{2.04}$•1.25 H_2O, in the absence of lithium at neutral pH. After a 5 h dwell time at 240 ℃, we isolate a dark brown crystalline product composed of a two-phase mixture having the α-MnO_2 and MnOOH structures, illustrated in Figure C.1. It is undetermined from X-ray diffraction experiments whether nickel intercalates directly into one or either of these structures or if it remains amorphous after this reaction. Although only sensitive to the surface, X-ray photoelectron spectroscopy indicates that nickel remains divalent and that manganese is mixed valent Mn^{4+} and Mn^{3+}; details follow in the next section. In addition, the EDX map in Figure C.2 indicates that nickel is evenly dispersed throughout the material. Previous work has shown that Cl^-(*aq*) can be used as an effective reductant toward $KMnO_4/MnO_2$, and gives access to low-dimensional morphologies.[219,220] α-MnO_2 adopts a tunnelled structure, into which alkali cations can insert hydrothermally[221] and under high temperature annealing.[222] Similarly, it has been shown that the oxyhydroxide MnOOH structure converts to spinel under hydro-thermal treatments.[223,224]

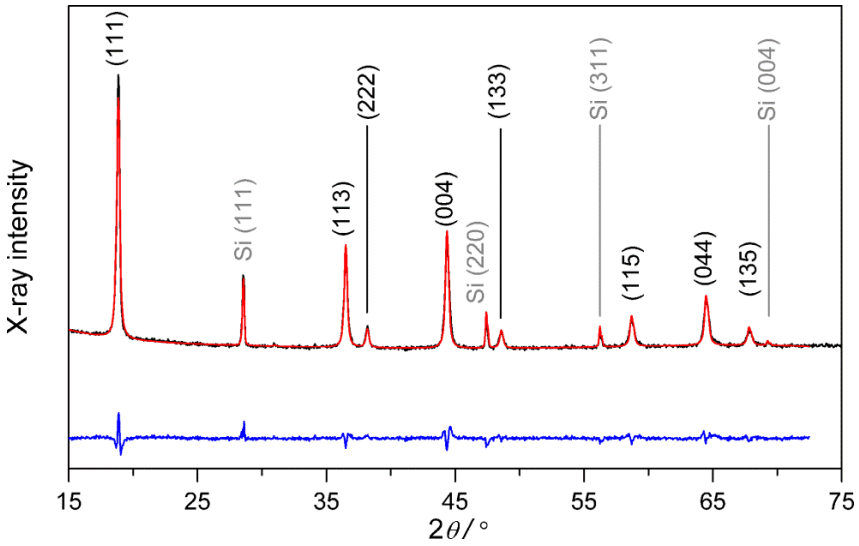

Figure 4.1 Powder X-ray diffraction pattern of $Li_{1.02}Ni_{0.5}Mn_{1.5}O_{3.88}$ spinel prepared by the two-step hydrothermal method of Scheme 1. Si was added as an internal reference.

Then, in a second reaction, the isolated initial product mixture above was transferred into a clean hydrothermal reaction vessel, and 12 mL of 0.1 M LiOH was added. After an additional 5 hour dwell time at 240 ℃, a dark red microcrystalline product is isolated. In this second step, lithium inserts by an ion-exchange reaction under basic conditions. Ion exchange between monovalent Li^+ and divalent Ni^{2+} does not occur to any appreciable extent during the phase transition to spinel structure; the EDX map in Figure C.3 shows that nickel remains evenly disbursed in the final LNMO product. Then, the powder X-ray diffraction pattern of the target compound is presented in Figure 4.1. The final product shows a diffraction pattern of $Fd\bar{3}m$ symmetry, in excellent agreement with previously reported LNMO material.[12,19,27] The lattice parameter of hydrothermally synthesized product is 8.183 Å, in good agreement with oxygen-deficient disordered structures observed by other groups.[4,8,226] Additional refinement parameters and atomic coordinates are presented in Tables C.1-2. An advantage of our wet chemical technique is that no

NiO or $LiNiO_2$ impurities are observed in the XRD pattern in our final compounds.

In previous work, lithium manganospinel ($Li_{1+x}Mn_{2-x}O_{4-\delta}$) has been successfully prepared in our group by introducing Li^+ directly through ion-exchange from the birnessite structure using a one-step hydrothermal synthesis.[227] Repeating this reaction with the simple modification of introducing $NiCl_2$ was explored, and Figure C.4 shows the X-ray diffraction pattern of the product and its resulting refinement. Although this material can be indexed as spinel, it shows very poor crystallinity after the same synthesis dwell period compared to the two-step synthesis procedure detailed above. The apparent crystalline domain size (determined by the Scherrer equation, $\tau = k\lambda/\beta \cos\theta$) is significantly smaller, only 9.4 nm, which matches the SEM images shown in Figure C.5. Simple solubility rules readily explain the small particle size resulting from the one-step reaction. Directly mixing the synthons LiOH, $NiCl_2$ and $K_{0.39}MnO_{2.04}\bullet 1.25$ leads to instant precipitation of the insoluble salt $Ni(OH)_2$ ($K_{sp} \sim 10^{-15}$). In this case, crystal growth of the product is limited by the reaction kinetics at the solid-solid interface or by dissolution at the surface. Nevertheless, the reaction does demonstrate that under basic conditions, Ni^{2+} can intercalate into the birnessite structure, and agrees with previous literature in which the spinel structure results after a 3- day hydrothermal treatment.[228] This results agrees with the conclusion that the dissolution-precipitation equilibrium of $Ni(OH)_2$ under hydrothermal conditions slows down Ni^{2+} intercalation.

Potentiometric titration of Mn against Fe^{2+} gives Z_{Mn} in NMO and LNMO of 3.42 and 3.82 respectively. We surmise that manganese oxidation in this second reaction step is accompanied by the reduction of oxygen vacancies according to the reaction:

$$2Mn^{3+} + \square_O^{\bullet\bullet} + \tfrac{1}{2} O_2(g) \rightarrow 2Mn^{4+} + O_O^{\times} \qquad (1)$$

as described in our previous LMO work. Meanwhile, the reaction sequence proposed in Scheme 4.1 presents a reducing environment for the second step. Therefore, these two reactions are in direct competition. To understand better the influence of oxygen partial pressure on product formation, we performed the second hydrothermal step under a pure oxygen atmosphere, but find that α-MnO_2 is formed as an impurity phase (Figure C.6). Notably, however, when the second hydrothermal reaction peformed in the strict absence of oxygen (under an N_2 atmosphere), we observe a larger lattice parameter (8.196 Å, XRD pattern in Figure C.7), which suggests a higher concentration of Mn^{3+} in the structure. Therefore, we conclude in our synthesis that oxygen partial pressure is critical in preparing phase-pure, high performing material, and that hydrothermal synthesis is therefore advantageous for generating high-performing electrodes.

The elemental composition of Li, K, Mn and Ni are determined from ICP data. Then, the manganese valence is determined from titration against Fe^{2+}. Nickel is assumed to be in its +2 formal oxidation state, consistent with the observed XP spectra. To derive an overall formula then, the negative charge is balanced by oxygen only, and the mass difference between the calculated formula and true mass of the compound is compensated by adding neutral H_2O. All data are presented in Table 4.1. The presence of lattice water in the NMO intermediate is corroborated by an IR stretch at 3300 cm^{-1}, illustrated in Figure C.8.

Table 4.1 Elemental analysis for compounds presented in this study.

compound	ppm Li	ppm K	ppm Mn	ppm Ni	Z_{Mn}	calculated formula mass/ mg	sample mass/ mg	H_2O	composition
δ-MnO_2	0	1.281 (12.16%)	4.620 (43.83%)	0	3.69	8.647	10.5	~17.9%	$K_{0.39}MnO_{2.04}$•$1.25H_2O$
NMO [a]	0	0.224 (1.86%)	5.918 (49.01%)	2.107 (17.45)%	3.42	11.82	12.1	~2%	$H_{0.4}K_{0.08}Ni_{0.5}Mn_{1.5}O_{3.305}$
LNMO	0.466 (3.91%)	0	5.432 (45.57%)	1.933 (16.22%)	3.82	11.92	11.9	0	$Li_{1.02}Ni_{0.5}Mn_{1.5}O_{3.875}$

4.3.2 Morphology, Photoelectron Spectroscopy, and Raman Spectroscopy

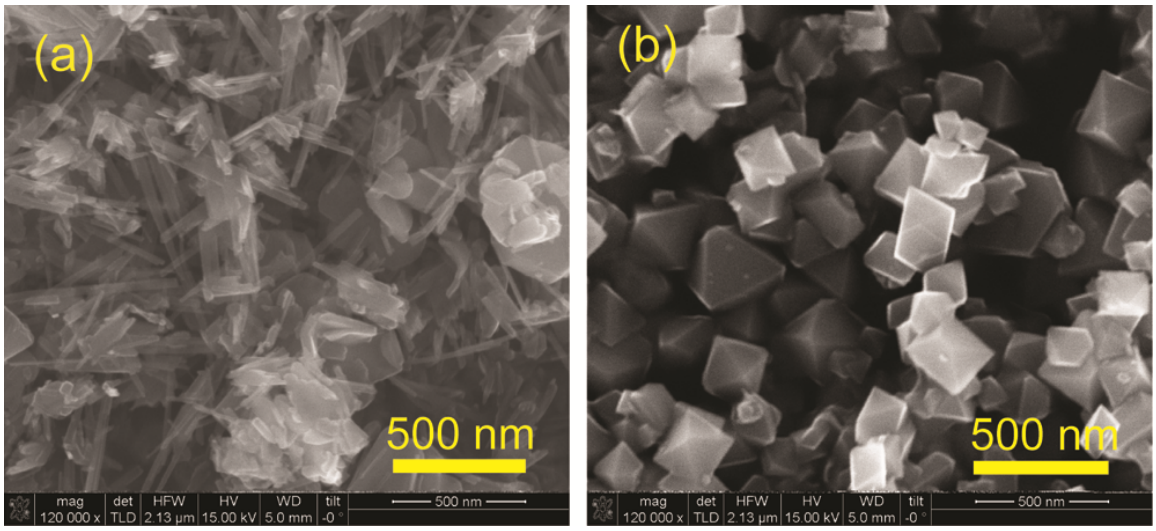

Figure 4.2 SEM images of a) the NMO two-phase intermediate; b) the LNMO spinel-phase product resulting from the two-step hydrothermal synthesis.

The morphology of the reaction intermediates and product is presented in the SEM images of Figure 4.2. Figure 4.2a shows that the isolated intermediates appear as a blend of nanowires and plates, consistent with the presence of two distinct phases in the X-ray diffraction pattern. Then, Figure 4.2b shows the morphology of the final LNMO product, which appears as regular octahedra with an edge length of ~200 nm, consistent with the cubic spinel structure. Then, using the BET method, the surface area of the product was determined to be 45.6 m^2/g; the N_2 sorption isotherm is plotted in Figure C.9. Recently, $LiNi_{0.5}Mn_{1.5}O_4$ was synthesized under hydrothermal conditions in LiOH with Ni^{2+} as initial nickel source.[229] However, the reaction was performed at 250 ℃ for 48 h and the final product showed very low crystallinity, In contrast, our material is highly crystalline, showing sharp diffraction features. High resolution TEM imaging shows that the octahedral crystal facets in our LNMO expose the (1 1 1) set of planes to the electrolyte

surface, illustrated in Figure 4.3. From this result, we hypothesize that lithium-ion diffusion will be rapid since lithium insertion occurs along the orthogonal [1 1 0] direction. A view of the spinel crystal structure along [1 1 0] is presented as Figure C.10.

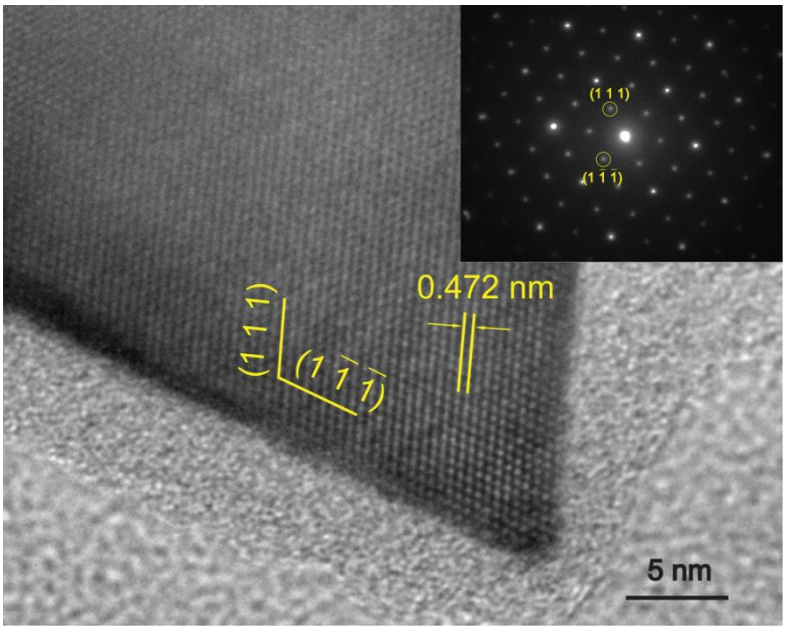

Figure 4.3 HRTEM image of an LNMO crystal. The *d*-spacing matches that of the (111) planes. **Inset**. SAED pattern along [110].

To characterize the surface composition of both the inter-mediate product mixture and the final product, we analyzed the compounds by XP spectroscopy, shown in Figure 4.4. The Ni(2p) spectra are shown in Figure 4.4a,b. Both of these spectra contain a pair of satellite peaks as marked on the higher binding energy of the 2p lines. The spectra of the intermediate mixture is shown in Figure 4.4a, where Ni($2p_{1/2}$) and Ni($2p_{3/2}$) occur at binding energies of 872.7 eV and 855.0 eV, respectively. This is consistent with the Ni^{2+} formal oxidation state. On the other hand, although the 2p regions for the LNMO product are fit to two coupled peaks in Figure 4.4b, the binding energies are lower than those

expected for Ni^{3+} (857 eV) [230]. This hints that all nickel exists as Ni^{2+}. The two peaks could indicated two different chemical environments–perhaps tetrahedral and octahedral sites—or surface nickel that is bound to lattice oxide versus surface hydroxide.

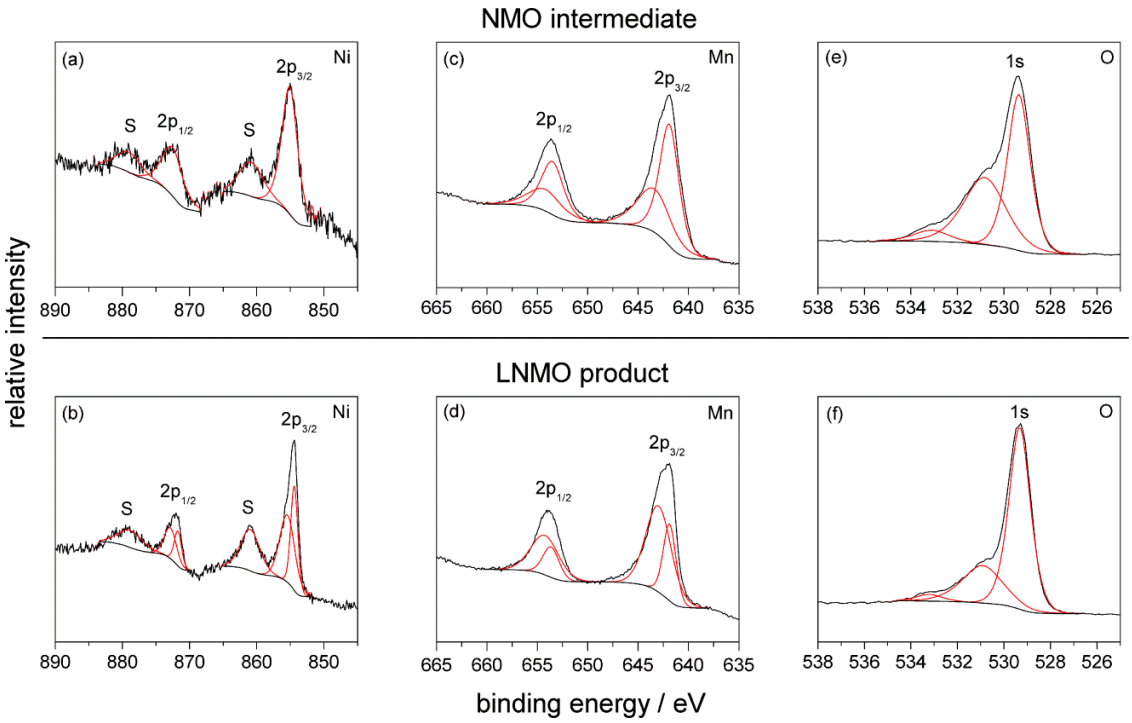

Figure 4.4 XP spectra of NMO and LNMO synthesized by hydrothermal methods.

The set of Mn($2p_{3/2}$) peaks in Figure 4.4c,d show binding energies of 643.0 eV, corresponding to Mn^{4+}, and 641.8 eV, corresponding to Mn^{3+}. By analyzing the XP spectra, it is evident that the initial NMO product contains a larger content of Mn^{3+}; on the contrary, LNMO formed in the subsequent reaction shows Mn^{4+} predominantly.

Finally, the O(1s) region in both of the two compounds, shown in Figure 4.4e,f can be deconvoluted into three Gaussian peaks, all showing the same binding energies: the highest intensity peaks at 529.3 eV represents lattice oxide, the shoulders at 530.9 eV are attributed to surface hydroxide, and adventitious surface water absorbed by the compounds gives rise to the tails observed at 533.1 eV.[231] We note that all XP spectra are

referenced to the adventitious surface C(1s) peak at 284.5 eV. In addition, both NMO and LNMO show surface carbonates, evidenced by peaks at 285.5 eV and 288.4 eV in Fig. S11.† This region is also noteworthy in our study because the K(2p) lines also appear in region. Important is that the K(2p) lines disappear in the final product, and is in accord with our ICP-AES result that no potassium is present in the final LNMO product. That is, ion exchange between K^+ and Li^+ in this second step is complete.

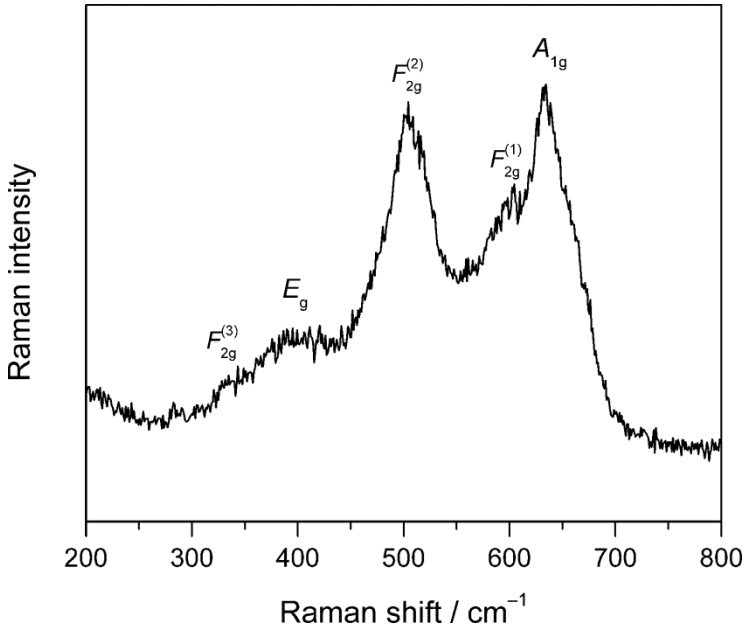

Figure 4.5 Raman spectrum of $Li_{1.02}Ni_{0.5}Mn_{1.5}O_{3.88}$ spinel

With LNMO materials in hand from the reaction sequence provided in Scheme 4.1, we employed Raman scattering as an effective technique to differentiate between the ordered and disordered the structures for $LiNi_{0.5}Mn_{1.5}O_4$.[232–234] A recent study has shown that the symmetries of the normal modes for the cubic disordered ($Fd\bar{3}m$) spinel $LiNi_{0.5}Mn_{1.5}O_4$ transform as:

$$\Gamma(Fd\bar{3}m) = A_g(\text{Raman}) + E_g(\text{Raman}) + 3\,F_{2g}(\text{Raman}) + 4\,F_{1u}(\text{IR}) \quad (2)$$

For these normal modes in cubic symmetry, those symmetric with respect to inversion are Raman active; the four antisymmetric bending modes(F_{1u}) are IR active. The Raman spectrum in Figure 4.5 was obtained for the LNMO final product, and matches the known reported spectrum for the disordered cubic structure. The highest energy A_{1g} band and the $F_{2g}^{(1)}$ shoulder at 632 cm^{-1} and 603 cm^{-1} correspond to Mn–O stretching, and the E_g and $F_{2g}^{(2)}$ modes at 397 cm^{-1} and 500 cm^{-1} respectively correspond to Ni–O stretching.[235–238]

4.3.3 Routine electrochemistry

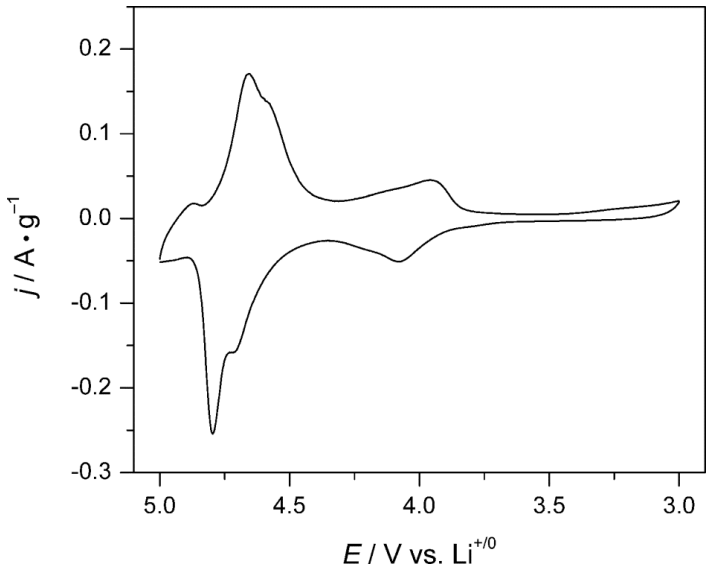

Figure 4.6 Cyclic voltammogram of $Li_{1.02}Ni_{0.5}Mn_{1.5}O_{3.88}$ spinel

The theoretical energy density of $LiNi_{0.5}Mn_{1.5}O_4$ is 691 mWh/g, significantly higher than that of $LiMn_2O_4$ (592 mWh/g). Moreover, the disordered composition is capable of generating additional potential from the $Mn^{4+/3+}$ couple. Figure 4.6 presents the cyclic voltammogram in a voltage window 3.0–5.0 V (*vs.* $Li^{+/0}$) with a 0.1 mV/s scan rate. The lower energy couple at 4.0 V matches that of the $Mn^{4+/3+}$ couple in LMO. Then, the formal $Ni^{4+/2+}$ couple appears as a split wave centered about 4.7 V. This splitting infers

that the oxidation proceeds through discrete one-electron steps with a Ni^{3+} intermediate.[239,240] The higher current and larger area of the higher voltage feature indicate that the majority of the stored energy is in the $Ni^{4+/2+}$ couple. Then, the unresolved peak above 4.8 V can be ascribed to either solvent oxidation or the release of oxygen from the lattice.[241–244]

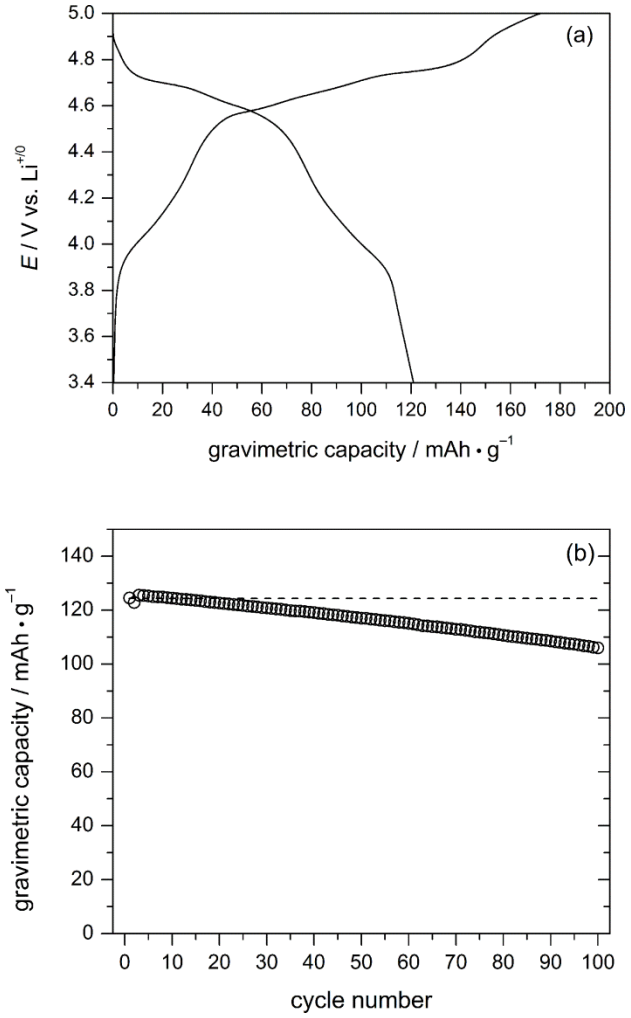

Figure 4.7 a) First charge & discharge cycle of $Li_{1.02}Ni_{0.5}Mn_{1.5}O_{3.88}$ spinel at 0.1 *C* rate;. b) Discharge capacity of $Li_{1.02}Ni_{0.5}Mn_{1.5}O_{3.88}$ spinel at 1 *C* rate.

Next, the first charge/discharge cycle at 0.1 *C* current (the requisite current to charge/discharge the theoretical capacity of the battery in 10 hours) is presented in Figure

4.7a. We note that during the first cycle, there is a large irreversible loss in gravimetric capacity (172 mAh/g charge *vs.* 121 mAh/g dis-charge), which likely stems from the irreversible oxidation of the electrolyte and the cathode material above 4.75 V, as has been described in the literature for LNMO even with higher-voltage titanate anodes[245] Continued cycling at faster current, 1 *C* in Figure 4.7b shows that this capacity is reversible, although it continues to fade at a fairly rapid rate. After 100 cycles, the discharge capacity is ~106 mAh/g, representing a 17.3% fade. To put this into proper perspective, once the capacity fade reaches 20%, a cell is at the end of its usable life.

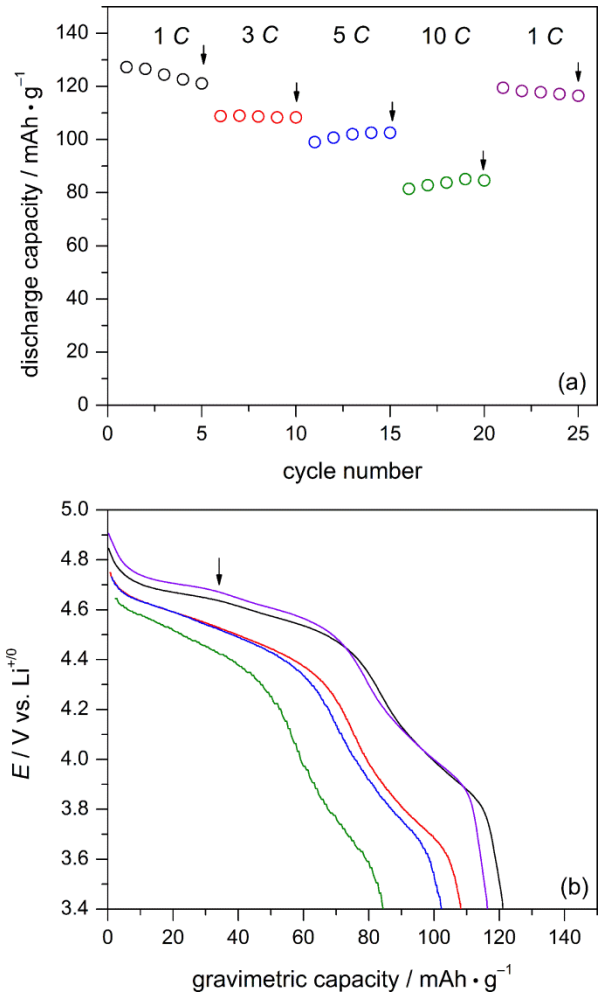

Figure 4.8 a) Rate capability of $Li_{1.02}Ni_{0.5}Mn_{1.5}O_{3.88}$ spinel. Black, red, blue, green, and purple represent 1 *C*, 3 *C*, 5 *C*, 10 *C*, and 1 *C* current respectively; b) voltage profiles of the 5th cycles at each rate.

The high surface area of our material suggests possible high rate capability. Therefore, to examine the rate capability, we varied the current from 1 *C* to 10 *C*, and Figure 4.8 records the discharge capacity retention over first 5 cycles at each current. The cathode shows excellent rate capability, with discharge capacities of 120, 108, 102, and 84 mAh/g at rates 1 *C*, 3 *C*, 5 *C*, and 10 *C* respectively (The corresponding current densities are 0.444, 1.33, 2.22 and 4.44 mA/cm^2). Furthermore, the battery returns to 94% of the initial capacity returned to 1 *C* current after cycling through increasingly faster rate. Figure 4.8b

shows the charge-discharge curves for the fifth cycle at each current. All show two potential plateaus corresponding to Ni^{4+} reduction and Mn^{4+} reduction, corroborated by the voltammetry data. The voltage-capacity curve at 1 *C* shows an inflection point at *ca*. 4.65 V (pointed out by the arrow in Figure 4.8b), inferring a distinct Ni^{4+}/Ni^{3+} and Ni^{3+}/Ni^{2+} couples.[246,247]

High rate capability implies rapid Li^+ diffusion. Therefore, electrochemical impedance spectra were collected. Figure C.12 shows the voltage-dependence of the lithium diffusion constant (D_{Li}) efficient measured from 4–5 V, with the equivalent circuit illustrated in the inset. The data in the Nyquist plots of Figure C.13 were fit to two *RC* circuits in parallel (representing Li-ion migration and charge transfer at high and low frequencies, respectively) and a Warburg impedance, representing solid-state Li-ion diffusion.[248] We estimate that D_{Li} in our two-step hydro-thermally synthesized compound to be 10^{-10} to 10^{-11} cm^2/s, comparable to recently reported carbon-coated samples.[210] The rapid diffusion coefficient here is supported by our microscopy data, in which crystal facets point along the [1 1 0] direction.

4.3.4 Cut-off Voltage and *Ex Situ* Diffraction Studies

In order to understand the capacity fade in this material, we performed our chronopotentiometry cycling experiments using different cut-off voltages. Interestingly, cells cycled from 5.0 to 4.4 V, where the $Mn^{4+/3+}$ couple is not accessed, show excellent chemical stability. Figure 4.9a shows a representative cell in which the first ten cycles are performed in the full voltage window (5.0-3.4 V). However, after cycle 10, the next 50 cycles are performed with a low-voltage cut-off of 4.4 V. Although the capacity is less because we are no longer storing charge in the $Mn^{4+/3+}$ couple, it cycles reversibly with a

capacity of 71 mAh/g. Even more interesting is that a similar experiment in which only the $Mn^{4+/3+}$ couple is accessed (now cycling between 4.4-3.3 V) also results in very stable cycling, albeit with an extremely low capacity of 29 mAh/g, shown in Figure 4.9b.

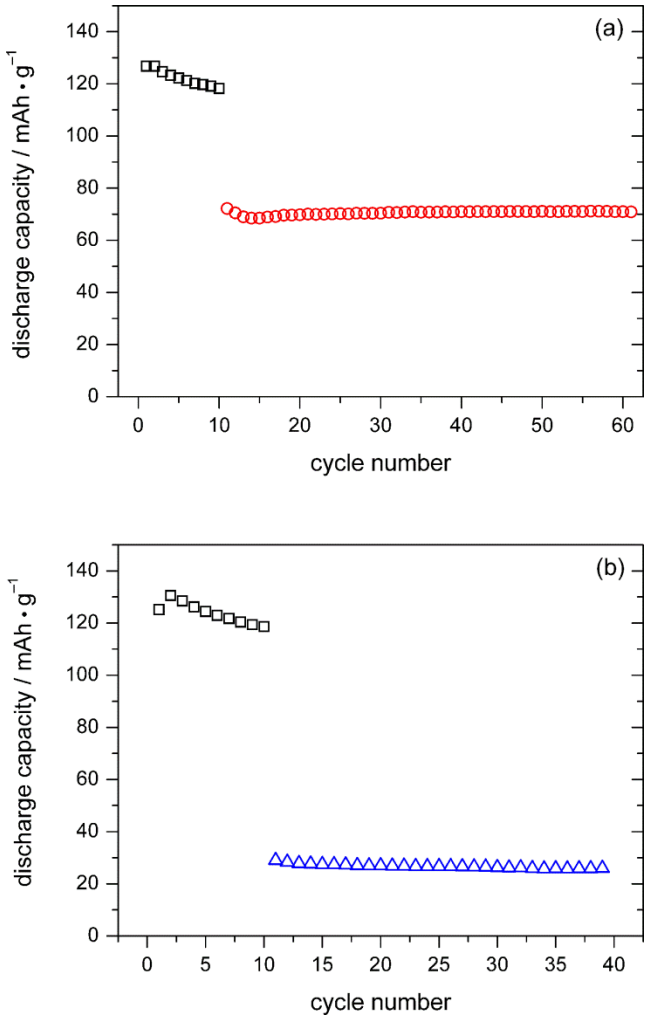

Figure 4.9 Galvanostatic cycling $Li_{1.02}Ni_{0.5}Mn_{1.5}O_{3.88}$ spinel switched between varying cutoff voltages at 1 *C* current. Cycles 1-10 (black squares) are charged and discharged between 3.4 and 5.0 V; cycles 11-121 (red squares) between 4.4 and 5.0 V; cycles 122-622 (blue triangles) between 3.4 and 4.4 V; cycles 623-1123 (green circles) between 4.4 and 5.0 V.

Lastly, we assembled one cell in which the first ten cycles were performed in the full

voltage window (3.4 to 5.0 V), followed by 100 cycles in which 4.4 V is the lower-limit cut-off voltage, then 500 cycles in which 4.4 V is the upper-limit cut-off , and finally 500 cycles in which 4.4 V is the lower-limit cut-off voltage again. This data is presented in Fig. 10, with select voltage profiles presented in Figure C.14. The key observations from this study are:

1. after cycling exclusively through the $Ni^{4+/2+}$ couple, the charge stored in the $Mn^{4+/3+}$ couple is unchanged.
2. after cycling through the $Mn^{4+/3+}$ couple, the charge stored in the $Ni^{4+/2+}$ couple is recovered completely and shows little fade over 500 cycles.
3. The observed energy density of LNMO in the voltage limit 4.4 to 5.0 V is ~320 Wh/kg, comparable to the energy densities observed in other synthesis methods.
4. Although the surface area is large, our nanomaterials demonstrate excellent cyclability during the cut-off voltage studies. Therefore, deleterious side reactions (*e.g.*—electrolyte oxidation, Mn^{2+} dissolution) are not failure mechanisms for our materials.

Interestingly, from Figure 4.9, the sum of the two capacities at cycles 11 performed with 4.4 V low- (9a) and high (9b) cut-off voltages is 100 mAh/g, which is less than the 124 mAh/g observed for cycle 11 of the full voltage range (Figure 4.7). Furthermore, cells cycled between the full voltage range of 3.4 and 5.0 V maintain a capacity of greater than 100 mAh/g through the first 100 cycles. Therefore, we conclude that the chemistry leading to diminished cell performance in the full range is coupled in the two redox events. In constructing a formal oxidation state picture, manganese is fully oxidized to Mn^{4+} at potentials more positive than 4.4 V during the charging process, then continued

extraction of lithium ions requires oxidation of nickel. However, we propose that lithium extraction at potentials greater than 4.4 V requires electronic coupling between nickel and manganese and that the couples are not as simple as $Ni^{4+/2+}$ and $Mn^{4+/3+}$. This assertion is backed up confirmed by a control study in which Ti-substituted LNMO shows a significant decrease in capacity. Ti^{4+} is being d^0, and therefore incapable of strong electronic coupling.[62]

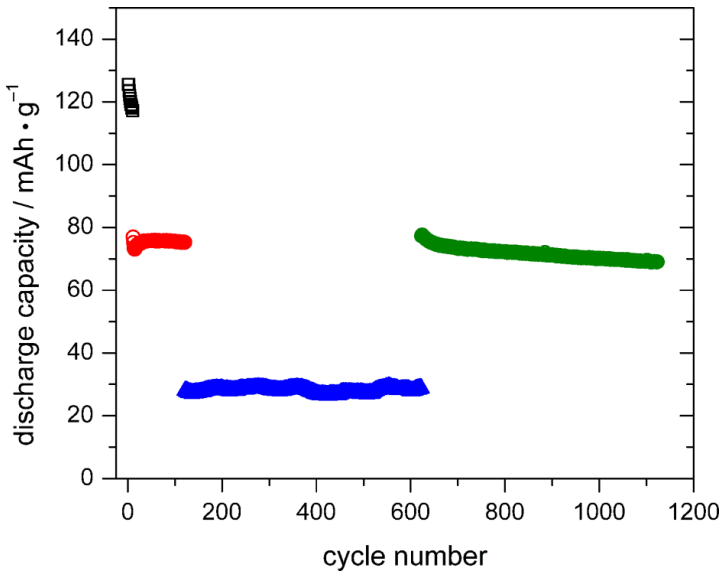

Figure 4.10 Galvanostatic cycling $Li_{1.02}Ni_{0.5}Mn_{1.5}O_{3.88}$ spinel switched between varying cutoff voltages at 1 *C* current. Cycles 1-10 (black squares) are charged and discharged between 3.4 and 5.0 V; cycles 11-121 (red squares) between 4.4 and 5.0 V; cycles 122-622 (blue triangles) between 3.4 and 4.4 V; cycles 623-1123 (green circles) between 4.4 and 5.0 V.

In order to address the capacity behavior uncovered in our cut-off voltage experiments, we performed *ex situ* X-ray diffraction on cells disassembled after cycling. These diffraction samples therefore contain the active spinel-structured material along with carbon black, and poly(vinylidne difluoride) binder, which give a large amorphous background,[249] as well as a strong crystalline signal from the aluminum foil. Therefore, we are limited to a partial refinement that includes the first three Bragg reflections: (111),

(113), and (222). In order to validate our methods, we first collected and refined data for a freshly prepared LNMO electrode, and note that its lattice parameter is 8.185 Å, which is in excellent agreement with the 8.183 Å lattice parameter recorded using the 11 reflections on a pure powder between 15 and 75 º 2θ. (The patterns and refinement parameters for the data in this section are presented as Figure C.15 – 19) A summary of these results is presented in Table 4.2.

After 60 cycles at 1 *C* current between 3.4 and 5.0 V (full range), the lattice parameter after returning the material to 3.4 V is significantly smaller, 8.157 Å. This implies a degradation mechanism for spinel-type cathodes that has been well documented: $2Mn^{3+}$ ions at the surface disproportionate into electrolyte soluble Mn^{2+} and electrochemically inactive Mn^{4+} (in the discharged state), which results in a smaller lattice parameter.

In order to differentiate whether or not the redox events couple to decrease the lattice parameter, we assembled two separate cells. In the first one, the voltage limits were switched to 3.4 – 4.4 V after cycle 10, and we observe that the lattice parameter grows to 8.194 Å after the 60^{th} cycle. This hints that cycling through this redox couple results in an *increase* in Mn^{3+} concentration. Then, in the second cell, the voltage limits are restricted to 4.4 – 5.0 V after cycle 10, and we observe a lattice parameter of 8.189 Å after cycling. This is perhaps slightly larger, but similar to that of the uncycled starting material. This hints that no structural distortions occur during cycling in this higher voltage range. Important is that in neither experiment do we observe a decrease in lattice parameter, and we deduce that the chemistry resulting in the lattice shrinking requires both redox events.

The smaller lattice parameter after full-range cycling suggests a larger Mn^{4+} content and/or fewer oxygen vacancies result. However, we cannot yet say through which couple

this additional capacity is lost, but return to the observation that charge transfer is required for decent cycling. Because of the decrease in lattice parameter after cycling through the full potential window, we hypothesize that electrical energy could be converted to heat in the form of lattice modes through the Ni–O–Mn bridge.[250−252] Current efforts in our lab are focused on further correlating the electrical properties and structure to generate compositions that cycle with greater stability throughout the full voltage window. It is also possible that cation rearrangement on the 16*d* Wyckoff sites occurs during the charging process, which converts electrical energy to lattice energy and gives rapid capacity fade. Transitions between ordered and disordered spinel structures or among varying disordered structures are imperceptible by standard laboratory X-ray diffraction techniques and we have planned neutron diffraction experiments to address these hypotheses.

4.4 Conclusion

In the present study, a low temperature two-step hydrothermal synthesis was used to prepare lithium nickel manganese oxide spinel with a formula $Li_{1.02}Ni_{0.5}Mn_{1.5}O_{3.875}$ without any NiO or $LiNiO_2$ impurities identified. A reaction intermediate was isolated with a mixed α-MnO_2 and MnOOH phase. A reaction mechanism is proposed to interpret the two step synthesis: redox chemistry only occurs on manganese, with nickel remaining in the +2 oxidation state throughout the reaction. The XRD pattern and Raman spectrum corroborates this formulation; the final product processes cubic symmetry, implying a disordered arrangement of manganese and nickel, along with a smaller lattice parameter, which is indicative of oxygen vacancies. LNMO synthesized in this manner crystallize as well-defined octahedral with an edge length of ~200 nm and a surface area of 45.6 m^2/g. Electron diffraction shows that the (111) set of planes is exposed to the surface. Cyclic

voltammetry shows two redox processes related to $Mn^{4+/3+}$ and $Ni^{4+/2+}$ formal couples at 4.0 and 4.7 V, respectively. The Jahn-Teller active Mn^{3+} ion supports the disordered structure and possible oxygen vacancies as previously reported. The final product exhibits good rate capability: the material can be cycled at 10 *C* with a reversible capacity of 84 mAh/g, attributed to rapid lithium diffusion, on the order of 10^{-10} to 10^{-11} cm^2/s. Capacity retention is excellent when the compound is cycled either between 3.4 and 4.4 V or between 4.4 and 5.0 V where nominally only the $Mn^{4+/3+}$ or $Ni^{4+/2+}$ couples are operative and *ex situ* diffraction shows lattice parameters that are the same or are slightly larger than that of the initial material. This is in stark contrast to the decrease in lattice parameter when cycled through the full 3.4 – 5.0 V window, suggesting that the two couples work in tandem to diminish the capacity. A possible charge transfer between Ni and Mn is proposed to explain the capacity maintaining during the voltage cut-off experiments; meanwhile, the capacity loss and fade could be due to either the change of lattice modes of Ni-O-Mn or a structural rearrangement.

CHAPTER 5

Improving the Electrochemical Stability of the High-Voltage Li-Ion Battery Cathode $LiNi_{0.5}Mn_{1.5}O_4$ by Titanate-based Surafe Modification

Portions of this chapter have been published:

Hao, X.; Bartlett, B. M. *J. Electrochem. Soc.* **2013**, *160*, A3162-A3170.

5.1 Introduction

For the past three decades, lithium-ion battery applications have expanded from energy storage for portable electronics to electric vehicles (EV) due to their high volume- and gravimetric energy densities.[253,254] However, larger energy density materials are still much desired for future generations' energy-storage needs.[12,255] The manganese-based spinel-type cathode material $LiMn_2O_4$ is one of the current workhorse materials because of its relatively low cost and toxicity compared to the archetype cathode material $LiCoO_2$.[184] Previous studies have shown that other transition metals can substitute for manganese in lithium manganospinel to yield potentially higher energy-density materials.[256,257] For example, the nickel-substituted $LiNi_{0.5}Mn_{1.5}O_4$ has a theoretical energy of 690 Wh/kg compared to 440 Wh/kg of the pristine $LiMn_2O_4$ due to its higher operating voltage.[258]

$LiMn_2O_4$ possesses a cubic spinel structure with space group *Fd*-3*m*, in which manganese, lithium, and oxygen atoms are located at 16*d*, 8*a* and 32*e* Wyckoff sites respectively.[259]Oxygen vacancies are easily formed during the conventional synthesis of

this compound ($LiMn_2O_{4-\delta}$), which leads to a higher fraction of Mn^{3+} in the structure.[260,175] The chemical energy stored in the manganese redox couple $Mn^{4+/3+}$ can be cycled by electrochemical insertion/extraction of the lithium ions at 8*a* sites. However, the Jahn-Teller distortion of Mn^{3+} causes serious mechanical stress and its disproportionation results in Mn^{2+} dissolution from the surface. On the other hand, stoichiometric $LiNi_{0.5}Mn_{1.5}O_4$ possesses a primitive cubic structure with space group $P4_332$ due to ordering of the two transition metals. Manganese, nickel, and lithium are located at 12*d*, 4*a*, and 8*c* Wyckoff sites respectively. Oxygen atoms are located at both 24*e* and 8*c* sites. However, oxygen vacancies are also common defects in $LiNi_{0.5}Mn_{1.5}O_{4-\delta}$, in which manganese and nickel are disordered giving rise to the face-centered cubic *Fd*-3*m* lattice. In this structure, manganese and nickel are dispersed randomly on the 16*d* sites. Lithium and oxygen are located at 8*a* and 32*e* sites respectively.[261,262] In the oxygen-deficient structure, energy is not only stored in the $Ni^{4+/3+}$ and $Ni^{3+/2+}$ redox couples which offer a potential ~ 4.7 V *vs.* $Li^{+/0}$, but also in the $Mn^{4+/3+}$ couple at ~ 4.0 V. It is known that the disordered, oxygen-deficient structure ($LiNi_{0.5}Mn_{1.5}O_{4-\delta}$) shows more favorable electrochemical characteristics including improved cyclability and rate capability due to the existence of the Mn^{3+} in the structure.[263,264] However, the high-voltage operation (> 4.7 V) is out of the electrochemical stability window of the presently used lithium hexaflourophosphate electrolyte and alkyl carbonate solvent system. Deleterious side reactions between the oxide surface and the electrolyte occur readily, resulting in a non-conductive inorganic and organic SEI layer forming.[265] This undesirable process is accelerated at elevated temperatures. Meanwhile, due to the commercial electrolyte $LiPF_6$, hydrofluoric acid is produced due to autocatalytic

decomposition in the presence of trace moisture, which is extremely corrosive toward metal oxides.[266] Manganese- and nickel dissolution are therefore possible during cycling and storing the battery, which results in potential energy losses.[267,268] In addition, structural degradation due to these side reactions and aging of the materials are inevitable. For example, monoclinic layered phases such as Li_2MnO_3 have been identified after cycling.[269]

From the perspective of synthesis, different particle sizes can be achieved for $LiNi_{0.5}Mn_{1.5}O_{4-\delta}$. Methods that produce nanoparticles such as hydrothermal[270] and sol-gel combustion[271] give rise to improved lithium-ion transport since the lithium-ion path length is shorter. However, side reactions are more pronounced due to the larger surface-to-volume ratio.Previous studies have focused on doping non-distortive transition metals such as Cr, Co or Ru into the face-centered cubic structure to stabilize LNMO.[272–274] These metals also serve to dilute the surface contact between nickel and electrolyte. Meanwhile, effective surface isolation using inert layers such as AlF_3, ZnO and ZrO_2 seems to be most effective for protecting LNMO from deterioration. Certain examples also include surface protection for $LiNi_{0.5}Mn_{1.5}O_{4-}$, $LiCoO_2$ and some other high voltage cathode with high operation voltage.[275–279] In our group, we have successfully applied a sol-gel method for preparing spinel-phase lithium titanium oxide ($Li_4Ti_5O_{12}$) and anatase (TiO_2) synthesis.[280,281] In the present study, we use conventional solid-state methods to preapre micron-sized $LiNi_{0.5}Mn_{1.5}O_{4-\delta}$. The titanate based surface coating was applied to build a protection layer using sol-gel method to achieve better electrochemical stability of the compound under high voltage operation.

5.2 Experimental

5.2.1 General Consideration

Lithium carbonate (99%), nickel (II) oxide (99%, ~325 mesh) and manganese carbonate (99.9%, trace metal basis) were purchased from Sigma Aldrich. Lithium metal 99.9% (metal basis) was purchased from Alfa Aesar. These reagents were used as received. Titanium isopropoxide (97%) was purchased from Sigma Aldrich, and it was distilled prior to storing in a Vacuum Atomospheres OmniLab glove box under an argon atmosphere. Ethanol (200 proof) was purchased from Decon Labs. HPLC-grade toulene was purchased from EMD Millipore and purified through a VAC solvent purifier unit.

Powder X-ray diffraction patterns were collected on a Bruker D8 Advance diffractometer with a Lynx-Eye detector and parallel beam optics using Cu-Kα radition (λ=1.54184 Å). The patterns were refined using the Bruker TOPAS software. N_2-sorption isotherms for surface area measurements (BET) were completed using a Quantachrome Instruments NOVA 4200e. Scanning electron microscopy (SEM) images and energy dispersive X-ray (EDX) spectra were collected on an FEI Nova Nanolab SEM/FIB at an accelerating voltage of 10 kV. High resolution transmission electron (HR-TEM) microscopy was performed on a JEOL 3011 TEM with a LaB_6 electron source operated at 300 kV. The samples were dispersed in tetrahydrofuran and drop cast onto a copper grid with an ultra-thin holy carbon film (Ted Pella^{TM}). Thermal analyses were obtained with a Q50 TGA Thermogravimetric Analyzer (TA Instrument). Raman spectra were obtained using a Renishaw Ramascope Raman spectrometer equipped with a Leica microscope, a Nikon LU plan 20× objective (numerical aperture = 0.40), and a 1200 lines/mm grating. All spectra were taken under 785 nm Laser excitation with 1.1 mW

incident power. Spectral analysis was performed using the fitting routines included in the WiRE 3.2 software package.

5.2.2 Synthesis

Lithium nickel manganese oxide ($LiNi_{0.5}Mn_{1.5}O_{4-\delta}$) was synthesized by a solid-state method. Li_2CO_3, NiO and $MnCO_3$ were ground for 40 min with molar ratio 1:1:3 using a Thinky^{TM} AR-100 mixer. Acetone and Zirconia balls (2 mm and 5 mm with counts ratio 2:10) were added to assist the mixing process. The mixture was first heated to 600 ℃ for 4 hours, followed by calcination at 950 ℃ for 12 hours. The heating and cooling rates were 10 ℃/min. An intermediate grinding was performed, followed by a second 12-hour annealing treatment at 950 ℃. The final LNMO product (~ 3.98 g, 21.8 mmol) was collected, and phase purity was confirmed by X-ray diffraction.

To prepare the lithium titanium oxide ($Li_4Ti_5O_{12}$) coating agent, lithium metal (typically 27 mmol) was dissolved in 40 mL of ethanol in a Schlenk flask purged with nitrogen gas. Titanium isopropoxide was dissolved in 60 mL of toluene in an argon atmosphere. These two reagents were mixed together with additional solvent such that the final volume of the solution is 200 mL. The lithium to titanium mole ratio of solution was 4:5, and the volumetric ratio of ethanol to toluene was 2:3. In a separate experiment, no lithium reagent was added to a similar mixture, resulting in titanium oxide (TiO_2) as the coating agent.

To perform the coating onto solid state prepared LNMO, typically, 200 mg LNMO was added to a round-bottom flask with 25 mL of an ethanol and toluene mixture (volume ratio 2:3). Two different volumes of $Li_4Ti_5O_{12}$ (LTO) or TiO_2 solution (0.2 mL and 0.5 mL) were added to the mixture for the assembling of coating layers. To minimize

particle aggregation caused by the coating layer, grinding balls were also added, and the flask affixed to a rotary evaporator (Buchii). After two hours at reduced pressure, the initial coating layer was formed. The round-bottom flask was then put into a pre-set 60 ℃ vacuum oven (Fisher Scientific) for 2 hours to eliminate any residual solvent. Finally, the coated LNMO powder was collected and heated in two steps in a muffle furnace (MTI): the powder was heated to 200 ℃ for 4 h, followed by annealing at 500 ℃ for 1 h. As a control experiment, the annealing treatment was also performed on the non-coated LNMO; this sample is denoted as bare LNMO.

5.2.3 Electrochemical measurements

All of the electrochemical tests were performed using two-electrode Swagelok™ PTFE cells. Pure lithium metal was used as the counter- and pseudoreference electrode for the measurements. To prepare the working electrode slurry, the synthesized material, carbon black and poly(vinylidene) difluoride (PVDF) (mass ratio of 75:15:10) were mixed in a Thinky™ AR-100 rotation-revolution mixer. *N*-methyl-2-pyrrolidone (NMP) was added to dissolve the PVDF completely and to maintain an appropriate viscosity of the black slurry. This material was then spread onto a de-greased aluminum foil by the doctor blade method, and the foil was dried in the vacuum oven at 120 ℃ overnight prior to assembling the cell in order to minimize the surface-bound water. The active material loading is approximately 5 mg/cm^2. The electrode masses were measured using a Sartorius™ ME36S microbalance. Glass fiber filter paper (GF/D) was used as separator in the cell. The electrolyte solution was composed of 1 M lithium hexafluorophosphate dissolved in 2:1 (v/v) ethylene carbonate and diethyl carbonate. All the cells were assembled in the argon glove box.

Galvonostatic charge/ discharge experiments were performed on a NEWARE BTS-5V1MA cycler in the voltage window 3.4 to 5.0 V (*vs*. $Li^{+/0}$). Cyclic voltammetry was recorded on a CH Instruments 660C electrochemical workstation. Galvanometric intermittent titration technique (GITT) measurements were carried out using a customized Vencon UBA5 battery analyzer. In GITT, a galvanostatic pulse of 0.2 *C* (where *C* is the current required to discharge the theoretical capacity of the cell in one hour) was applied for 600 s followed by relaxation at open circuit for 2 h. The cut-off voltage is set to 3.4 V. Prior to the GITT test, all cells were galvanostatically charged to 3 V with a cut-off current limit of 10 nA followed by a 2-h rest period at open circuit. Electrical resistivity study was performed by four-point probe measurements with a LUCAS LABS^{TM} resistivity test stand S-302-4 assisted with an Autolab PGSTAT302N. A constant potential of 1 V was applied during the test, and the corresponding *i*-*t* curve was recorded. Pellets were pressed using a Specac^{TM} press with a 10000 kg load and a ¼″ die from MTI with a final thickness of ~0.06 cm. All pellets were annealed at 500 ℃ for 4 hours before the conductivity tests. Pellets densities were measured as ~4.1 g/cm^3, which is close to theoretical density of LNMO, 4.4 g/cm^3.

5.3 Results and discussion

5.3.1 Composition, structure and morphology

In the present study, $LiNi_{0.5}Mn_{1.5}O_{4-\delta}$ was synthesized by a high-temperature solid-state method at 950 ℃. It is known that two different structures can be formed during the synthesis of this compound due to the oxygen content.[13] At high temperature, an oxygen-deficient cubic structure is formed (space group *Fd*–3*m*); in this structure, the transition metals are disordered on the 16*d* Wyckoff sites. Figure D.1 shows the XRD pattern and Rietveld refinement of the high- temperature synthesized LNMO. The reflections marked

with arrows index as the rock-salt impurity phase ($(Li_xMn_{0.66}Ni_{0.34})_yO$), which easily forms during the high-temperature synthesis of LNMO.[282,283] The Rietveld refinement confirms the structure and results in a lattice parameter a = 8.191 Å which matches the former results of oxygen deficient LNMO.[284]

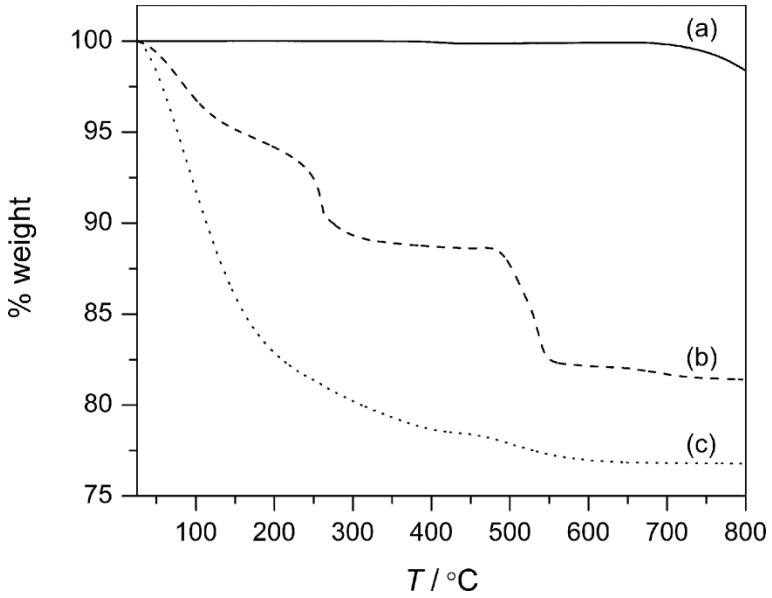

Figure 5.1 TGA trace of solid state synthesized $LiNi_{0.5}Mn_{1.5}O_{4-\delta}$ (a); the TiO_2 precursor solution (b); and the LTO precursor solution (c).

As mentioned in the introduction, at large positive potentials, the electrolyte decomposes and reacts with transition-metal oxides. Those side reactions can cause destructive effects to the electrochemical stability of the high voltage cathodes. Meanwhile, HF arising from trace moisture in the $LiPF_6$ electrolyte leads to the corrosion of the electrode. To maintain the structure integrity of LNMO, we hypothesize that a protective coating can be added at relatively low temperature to maintain stable cycling of the electrode. Based on previous work in our laboratory, LTO can be prepared by a sol-gel process to yield such a coating.[285] Figure 5.1 shows the TGA results for LNMO

and control experiments of LTO/TiO_2 solution. From these results, we select 500 ℃ to perform the heat treatment for the coating process since there is no further mass loss of either the LTO and TiO_2 precursor above this temperature. Meanwhile, there is no obvious mass change of the LNMO sample. Raman spectroscopy (Figure D.2) shows that there is no carbon residue left on the surface of the samples with the performed annealing treatment at 500 ℃. Figure D.3 shows the XRD patterns of the LTO and TiO_2 sol-gel precursor solutions after annealing at 500 ℃. The TiO_2 coating is pure anatase with good crystallinity. However, heating the precursor mixture that we used to prepare LTO to only 500 ℃ results in a mixture of anatase and spinel phases. At 700 ℃, the pure cubic spinel phase can be achieved by annealing the LTO solution. But, heating LNMO to higher temperatures results in further oxygen loss, observed in the TGA.

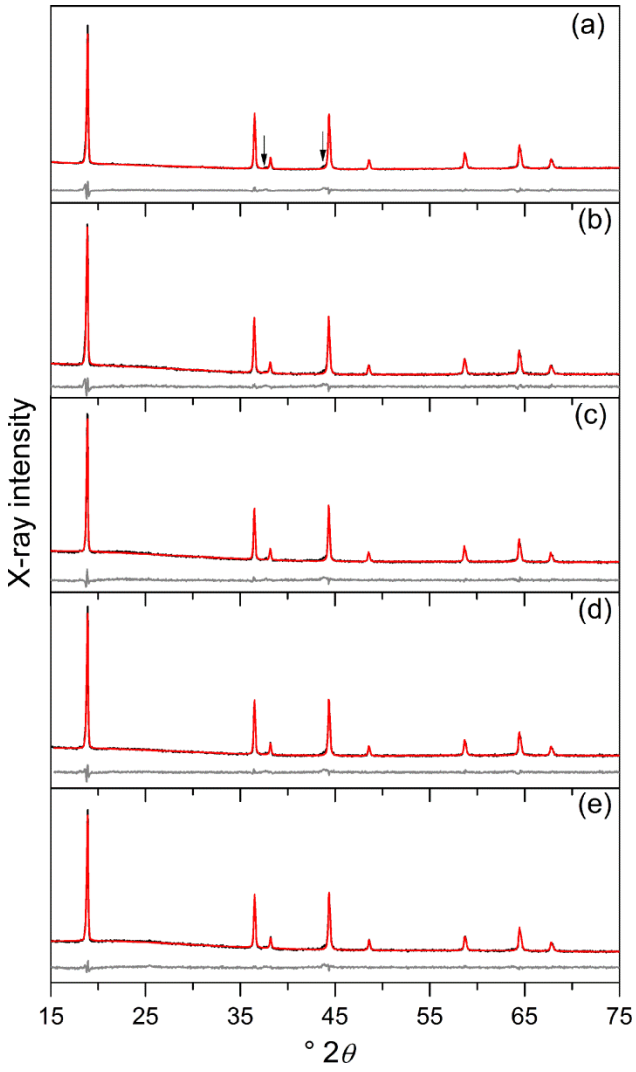

Figure 5.2 Powder X-ray diffraction patterns of solid-state synthesized $LiNi_{0.5}Mn_{1.5}O_{4-\delta}$ (a); 5 – 10 nm LTO-coated LNMO (b); 5 – 10 nm TiO_2-coated LNMO (c); 20 – 30 nm LTO-coated LNMO (d); 20 – 30 nm TiO_2-coated LNMO (e).

Figure 5.2 shows the XRD patterns of the bare LNMO annealed at 500 ℃ and the coated LNMO with their Rietveld refinement results. Notably, the LNMO structure is unaltered after the coating and also after the 500 ℃ annealing treatment. Regardless of the presence of lithium in the precursor solution, the titanate-coated samples show small anatase indexed peaks around 25 ° 2θ. Meanwhile, the rock-salt minor impurity can still be identified from the difference pattern in all five samples. The refinement results are

summarized in Table 5.1. No obvious change occurs during the TGA study for LNMO, after annealing and the lattice parameters are nearly identical after annealing (8.191 to 8.189 Å). The slight decrease after annealing is perhaps indicative of a decrease in the density of oxygen vacancies in the structure,[286] but we note that Rietveld refinement of X-ray data is not sensitive enough to draw a stronger conclusion. Notable is that this phenomenon is not unique; all the coated samples show a slight lattice shrinkage compared to the LNMO sample. The comparison of the materials properties was performed among these five samples to elucidate the composition of the coating layers.

Table 5.1 Rietveld Refinement Results of Electrode Materials used in this Study.

Sample Code	a / Å	V / Å^3	% R_{wp}	% R_{Bragg}
Bare LNMO	8.191(4)	549.6(5)	1.49	0.184
Bare LNMO annealed	8.189(6)	549.2(7)	1.49	8.841
Bare LNMO annealed RT	8.191(9)	549.7(3)	1.25	3.078
Bare LNMO annealed 55 ℃	8.194(1)	550.1(9)	1.02	0.131
5 – 10 nm LTO coating	8.186(2)	548.5(8)	2.15	9.768
5 – 10 LTO coating RT	8.188(8)	549.1(2)	1.67	3.833
5 – 10 LTO coating 55 ℃	8.191(3)	549.6(2)	1.25	0.201
20 – 30 nm LTO coating	8.189(1)	549.1(8)	1.81	5.337
20 – 30 nm LTO coating RT	8.189(2)	549.2(0)	1.66	4.264
20 – 30 nm LTO coating 55 ℃	8.192(8)	549.9(2)	2.04	0.865
5 – 10 TiO_2 coating	8.188(9)	549.1(3)	1.95	6.843
5 – 10 TiO_2 coating RT	8.188(7)	549.1(1)	1.68	0.274
5 – 10 TiO_2 coating 55 ℃	8.189(5)	549.2(5)	1.39	0.519
20 – 30 nm TiO_2coating	8.186(8)	548.7(2)	1.81	5.17
20 – 30 nm TiO_2 coating RT	8.187(8)	548.9(1)	1.27	0.266
20 – 30 nm TiO_2 coating 55 ℃	8.189(4)	549.2(4)	1.34	5.057

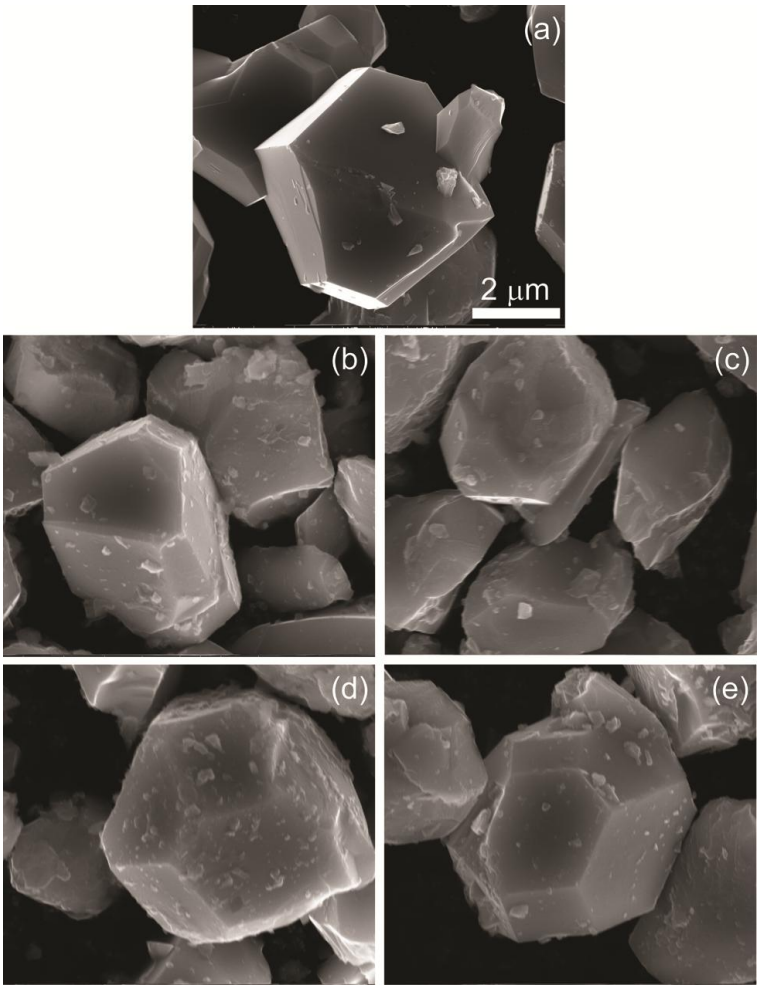

Figure 5.3 SEM images of $LiNi_{0.5}Mn_{1.5}O_{4-\delta}$ (a); 5 – 10 nm LTO-coated LNMO (b); 5 – 10 nm TiO_2-coated LNMO (c); 20 – 30 nm LTO-coated LNMO (d); 20 – 30 nm TiO_2-coated LNMO (e). Note that all images are captured at the same magnification such that the 2 μm scale bar shown in a) is common to all.

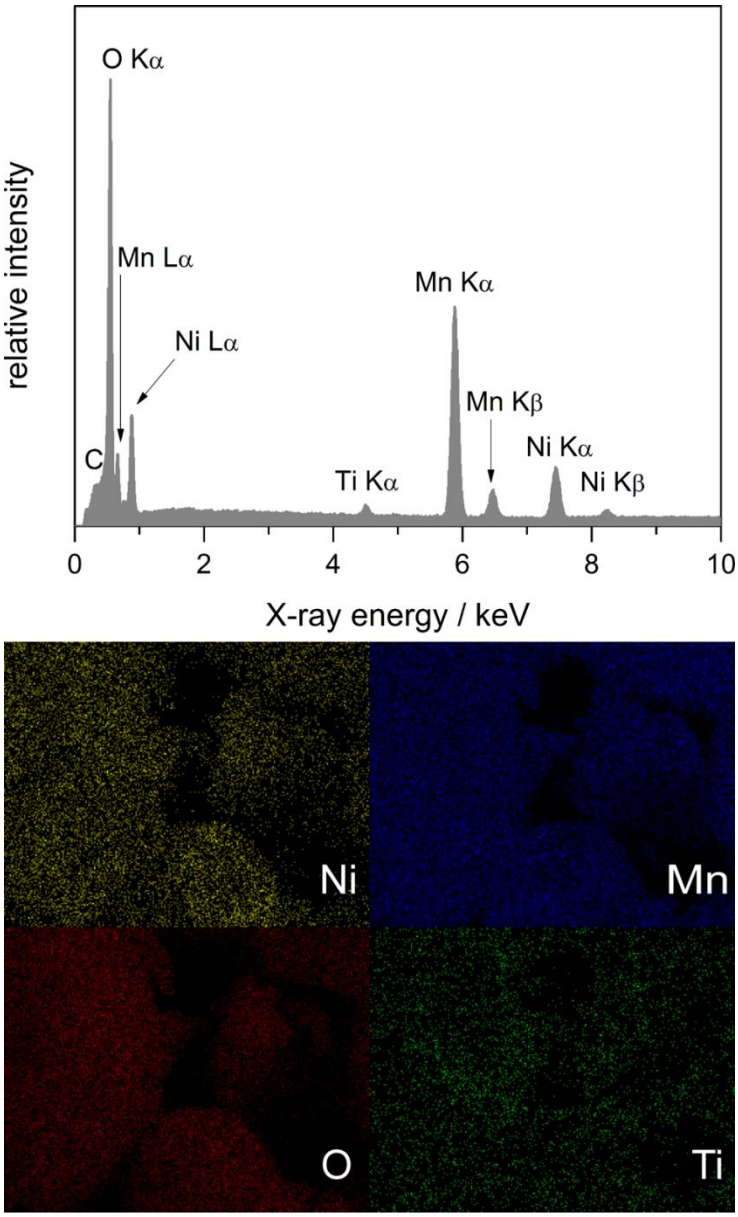

Figure 5.4 EDX spectrum and map of 5 – 10 nm TiO_2-coated LNMO.

Figure 5.3 shows SEM images of the bare LNMO and titania-coated sample. All samples show a particle size of ~5 μm, typical for solid-state synthesized materials. Compared to bare LNMO, the surfaces of the other samples are rougher, indicative of the coating. Small aggregating islands are observable in the coated samples, suggests variation in the thickness of the coating layer. Therefore, to confirm that titania coats the

entire LNMO surface, an energy-dispersive X-ray (EDX) map was constructed; Figure 5.4 shows that titanium and oxygen are evenly dispersed throughout the scale window for one of the anatase-coated LNMO samples, which reveals the effectiveness of the coating method. In addition, a clear titanium signal is observed in the EDX spectrum.

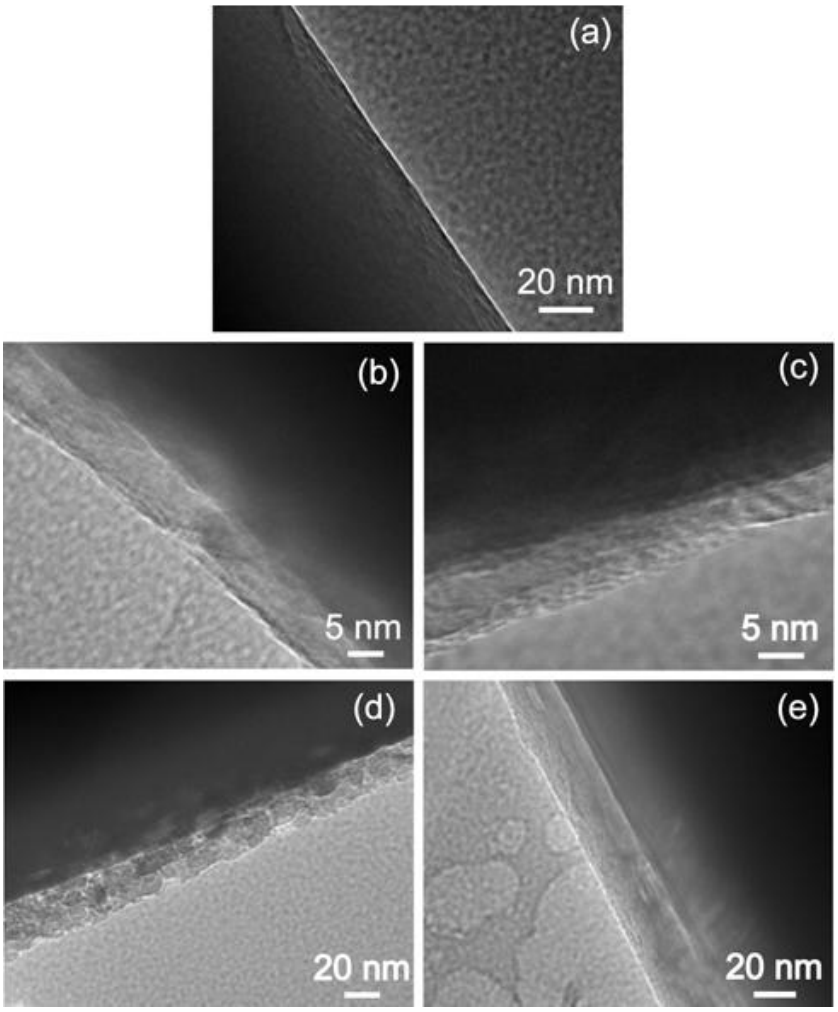

Figure 5.5 HR-TEM images of LNMO (a); 5 – 10 nm LTO-coated LNMO (b); 5 – 10 nm TiO_2-coated LNMO (c); 20 – 30 nm LTO-coated LNMO (d); 20 – 30 nm TiO_2-coated LNMO (e).

To estimate the thickness of the coating layer, high resolution transmission electron microscopy was performed. In the HR-TEM image of Figure 5.5, bare LNMO shows a

flat and clean surface. On the materials that have been coated, there is an additional observable coating that varies in thickness from 5 – 10 nm for 0.2 mL of precursor solution added, and from 20 – 30 nm for 0.5 mL of precursor solution added. That is, the volume of the precursor solution employed is reflected in the thickness of the coating.

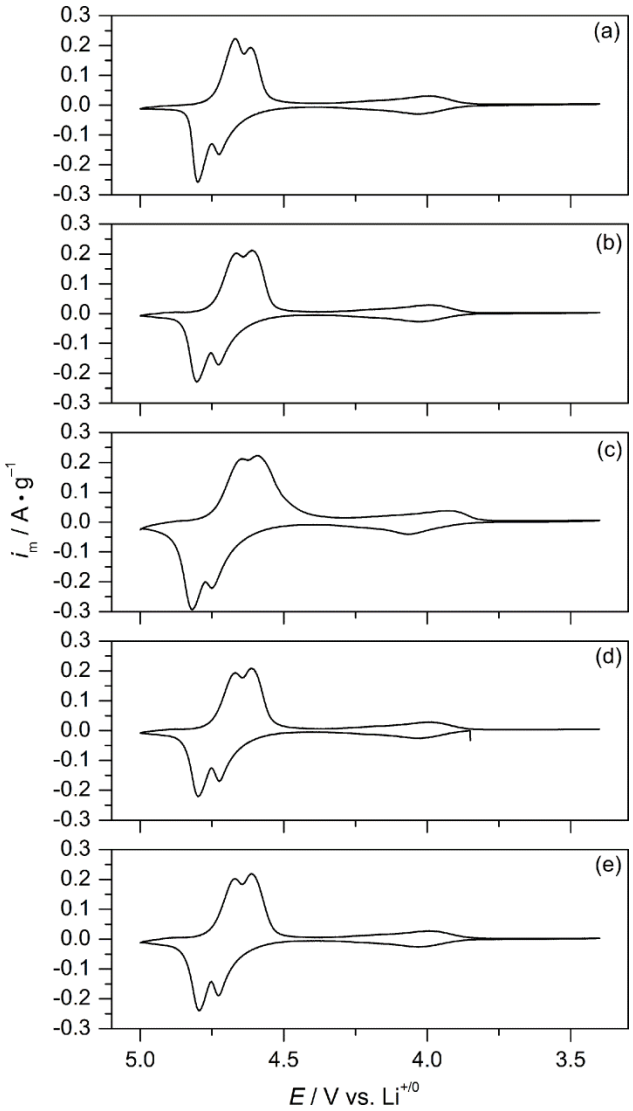

Figure 5.6 Cyclic voltammogram of LNMO (a); 5 – 10 nm LTO-coated LNMO (b); 5 – 10 nm TiO_2-coated LNMO (c); 20 – 30 nm LTO-coated LNMO (d); 20 – 30 nm TiO_2-coated LNMO (e).

Figure 5.6 shows the cyclic voltammetry of all the cathodes discussed in this manuscript. All show the same electrochemical redox reactions at two voltage regions versus lithium metal: Two waves centered about 4.7 V correspond to the $Ni^{4+/3+}$ and $Ni^{3+/2+}$ couples, and a wave centered about 4.0 V corresponds to $Mn^{4+/3+}$. The observation of redox chemistry occurring at 4.0 V confirms the existence of oxygen vacancies in cubic LNMO materials.[287,288] Notable is that the titanium oxide coatings do not add extra features to the voltammogram. In this study, we find that titanate-based coatings are effective for improving the electrochemical stability by separating the direct contact between the LNMO cathode and the electrolyte. One of the main causes of capacity fade is electrolyte decomposition upon charging to high potential (5.0 V).[11] Figure D.4 shows the control voltammograms of the electrolyte on anatase TiO_2 and LTO. Although the current scale is small, undesired oxidation reactions are still identified at potentials more positive than 4.7 – 4.8 V, the typical upper voltage limit for the lithium-ion battery electrolyte. This intrinsic chemistry problem cannot be solved by simply adding a protective layer for the high-voltage cathode, and may be the primary reason for capacity fade for the first few cycles observed in all cathodes. Rather, this points to the need to design electrolytes that are chemically inert at these higher voltages.

5.3.2 Room-temperature Galvanostatic Cycling

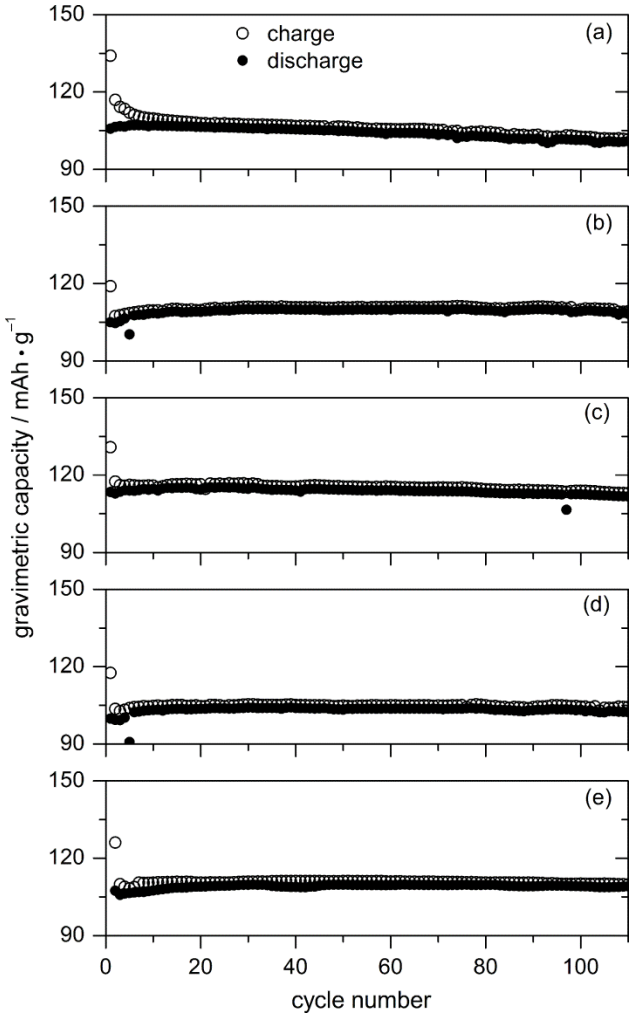

Figure 5.7 Room temperature gravimetric capacity of LNMO (a); 5 – 10 nm LTO-coated LNMO (b); 5 – 10 nm TiO_2-coated LNMO (c); 20 – 30 nm LTO-coated LNMO (d); 20 – 30 nm TiO_2-coated LNMO (e). All cells are cycled galvanostatically at 1 *C*, the filled circles represent discharge capacity, and open circles represent charge capacity.

Electrochemical tests were performed to measure the stability of the coated cathodes. As a control, batteries were also assembled using bare (uncoated) LNMO. Figure 5.7 shows the cyclability of the cathodes versus lithium metal at room temperature for the first 110 cycles at 1 *C* rate (147 mA/g) within the voltage window 3.4 – 5.0 V *vs.* $Li^{+/0}$. Both the charge and discharge capacities were recorded to measure any capacity losses. For bare LNMO, the initial charge capacity is 134 mAh/g, but discharge capacity is 106

mAh/g, meaning that the Columbic efficiency (q_{out} / q_{in}) is only 79%. On the contrary, all the coated samples show Coulombic efficiencies higher than 85% on the first cycle. The irreversible capacity loss at the first few cycles is attributed to SEI layer formation.[289] Then, significant irreversible loss continues through the next five cycles for bare LNMO (85%, 91.0%, 93.4%, 93.9%, 95.5% for cycles 2 – 6). In contrast, the coated samples show efficiencies greater than 97% for the second cycle, suggesting that the coating layer reduces side reactions contributing to SEI layer formation. The titanate layer prohibits direct contact between LNMO and the electrolyte, while allowing Li-ions to diffuse through, and therefore serves as the SEI in the electrochemical system. After 100 cycles, the columbic efficiencies of all materials are greater than 99.0%. Of course, parasitic reactions are still possible at the 5.0 V potential, but we note that after our coating treatment, no obvious changes of discharge capacity were observed compared to bare LNMO material (with a highest discharge capacity as ~107 mAh/g).

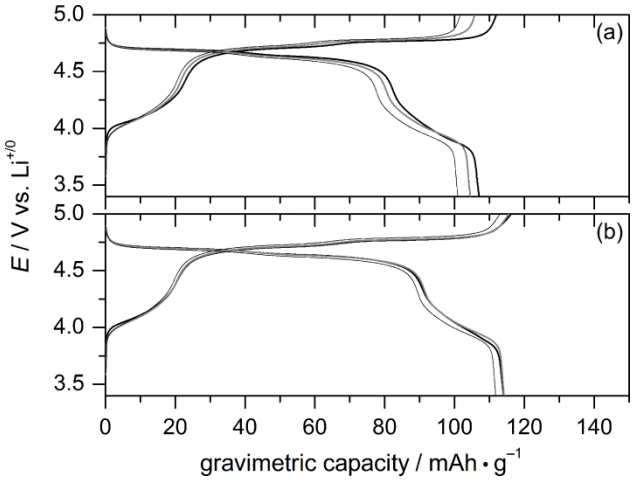

Figure 5.8 5th (thick black), 55th (gray) and 110th (thin black) cycle voltage curves of LNMO (a); 5 – 10 nm TiO_2-coated LNMO (b).

In terms of electrochemical stability, there is a 6.5% discharge capacity fade over the first 110 cycles for the bare LNMO sample. However, no discernible capacity fade is observed for the LTO- and/or TiO_2-coated samples, and the electrochemistry is similar regardless of the coating composition. This verifies that the titanate coating layers are effective to improve the stability of the LNMO cathode. To streamline the discussion, the remainder of the results presented in this manuscript will compare the electrochemistry of bare LNMO to LNMO coated with 5 – 10 nm of anatase TiO_2. First, we note that our results are repeatable from cell to cell. Two additional cells cycled under the same conditions (1 *C* charge and discharge at room temperature) show the exact same galvanostatic profile (data presented in Figure D.5). Our initial hypothesis was the similarity in the crystal structures of LTO and LNMO would result in superior electrochemical performance. However, our results indicate that both coatings are able to stabilize LNMO chemically and that lithium diffusivity is unchanged for either coating at either thickness is added (shown below). Figure 5.8 compares the voltage curves for the 5^{th}, 55^{th} and 110^{th} cycles of bare LNMO and LNMO coated with 5 – 10 nm TiO_2. In these profiles, the high-voltage plateaus near 4.7 V correspond to the $Ni^{4+/3+}$ and $Ni^{3+/2+}$ formal couples in LNMO. As previously mentioned, the cubic structure is commensurate with having oxygen vacancies, which leads to Mn^{3+} in the structure as noted in the cyclic voltammogram; in Figure 5.8, this composition is manifested as a low-voltage plateau observed at ~4.0 V, indicative of the $Mn^{4+/3+}$ couple.

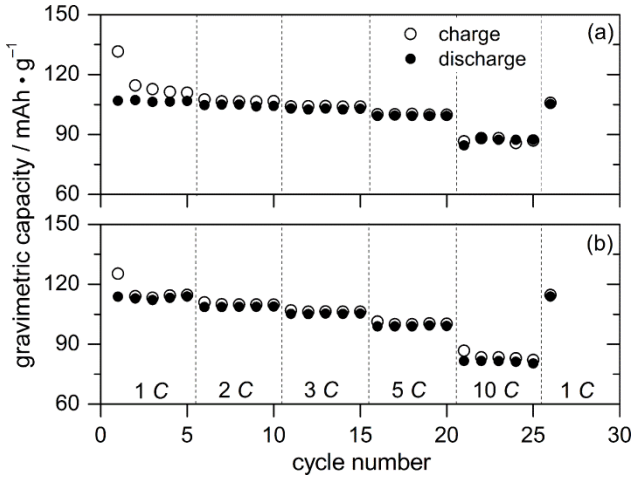

Figure 5.9 Rate capability of LNMO (a); 5 – 10 nm TiO_2-coated LNMO (b).

Next, the rate capability was studied by cycling the cathode materials at different *C* rates; the data are presented in Figure 5.9. LNMO and TiO_2-coated LNMO cells were cycled at 1, 2, 3, 5, and 10 *C* for 5 cycles each at room temperature. The very last cycle returns to 1 *C* current. Bare LNMO shows excellent rate capability with capacity retention with discharge capacities of 106, 104, 102, 99, 87 mAh/g at rates 1, 2, 3, 5 and 10 *C* respectively, which suggests that LNMO is a promising cathode for high power applications. Upon coating with anatase, the battery retains good capacity and rate capability > 80 mAh/g at 10 *C* rate for the coated material. The charge and discharge profiles of the last cycle at each rate (5^{th}, 10^{th}, 15^{th}, 20^{th}, and 25^{th}) are provided in Figure D.6. All the profiles show three voltage plateaus corresponding to the $Ni^{4+/3+}$, $Ni^{3+/2+}$, and $Mn^{4+/3+}$ couples. As the current increases, the polarization gap increases, as is typically observed in batteries.[290] Both cells return to their initial 1 *C* discharge capacity after the rate capability study: 106 mAh/g (bare LNMO) and 114 mAh/g (anatase-coated LNMO).

5.3.3 Elevated-temperature Galvanostatic Cycling

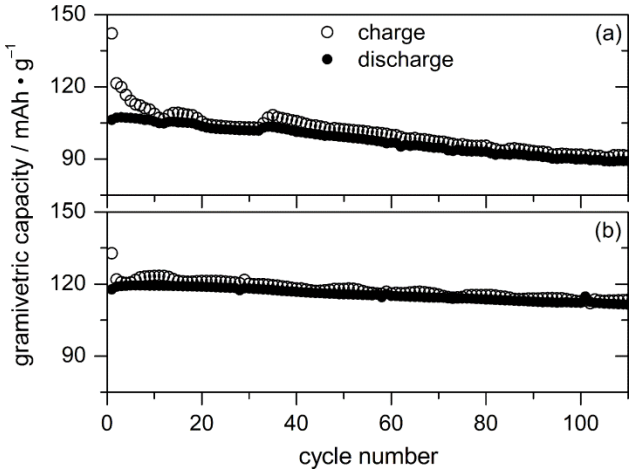

Figure 5.10 55 ℃ gravimetric capacity of LNMO (a), 5 – 10 nm TiO_2-coated LNMO (b). Cells were cycled at 1 *C*.

Galvanostatic cycling at 1 *C* current was also performed at 55 ℃ to determine the electrochemical stability of these compositions at elevated temperature. The cyclablity of bare LNMO and anatase-coated LNMO are recorded in Figure 5.10. At elevated temperatures, the rates of interfacial parasitic reactions between the electrode and the electrolyte increase.[18] Over the first 110 cycles, there is now over 17% discharge capacity loss for the bare LNMO sample. The initial discharge capacity for bare LNMO is still ~107 mAh/g, similar to the capacity at room temperature. On the other hand, the discharge capacity fades to 89 mAh/g at the last recorded (110^{th}) cycle, due to structure collapse and possible metal dissolution at high temperature. The anatase-coated sample shows marked improvement at elevated temperatures. First, even at high temperatures, the irreversible capacity losses are negligible for the second cycle (3 mAh/g) compared to 14 mAh/g for bare LNMO cathode. Then, the capacity is larger: 118 mAh/g initially, dropping to only 111 mAh/g at cycle 110. Notably, all coated samples show improved capacity retention. The discharge capacity retention for the anatase-coated LNMO sample

is 93.2%. Figure S7 shows the voltage profiles at 5th, 55th and 110th cycles at 55 ℃. Clear distinction between formal $Ni^{4+/3+/2+}$ and $Mn^{3+/4+}$ redox processes are maintained.

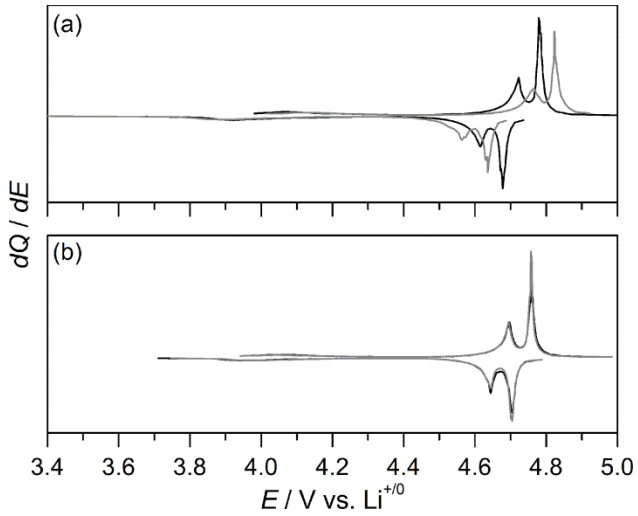

Figure 5.11 Differential capacity-voltage (dQ/dE) curves for the 5th and 55th cycles of LNMO (a); 5 – 10 nm TiO_2-coated LNMO (b) at 55 ℃.

In addition to the capacity, the voltage profile yields polarization resistance by examining the potential difference between the charge and discharge plateaus. Previous work has shown that a thicker SEI layer on the surface of LNMO increases the polarization resistance, resulting in a decrease in useable energy density.[291,292] As shown in Figure D.7, not only does the capacity decrease as LNMO is cycled at elevated temperature, but also the polarization gap between the charge and discharge profiles increases from 5th to 110th cycles. To corroborate this observation, differential capacity-voltage (dQ/dE) curves for 5th and 55th cycles were plotted in Figure 5.11. In the bare LNMO sample, the charge and discharge branches shift apart by ~100 mV after 50 cycles, indicative of increased polarization resistance. On the contrary, in the dQ/dE curves of the anatase-coated sample, the 55th cycle overlaps the 5th cycle, which implies a constant interfacial resistance over time. The polarization gap of the coated samples is

also smaller, only 50 mV. We also note that, at the 5th cycle, the bare LNMO sample's discharge peak is actually shifted ~ 20 mV to more negative potential compared to the peaks observed for the anatase-coated sample. This hints that the surface of the LNMO is more resistive than that of the titanate-coated samples at elevated temperature. This could explain the smaller discharge capacity of the bare LNMO sample.

5.3.4 *Ex situ* Structural Analysis

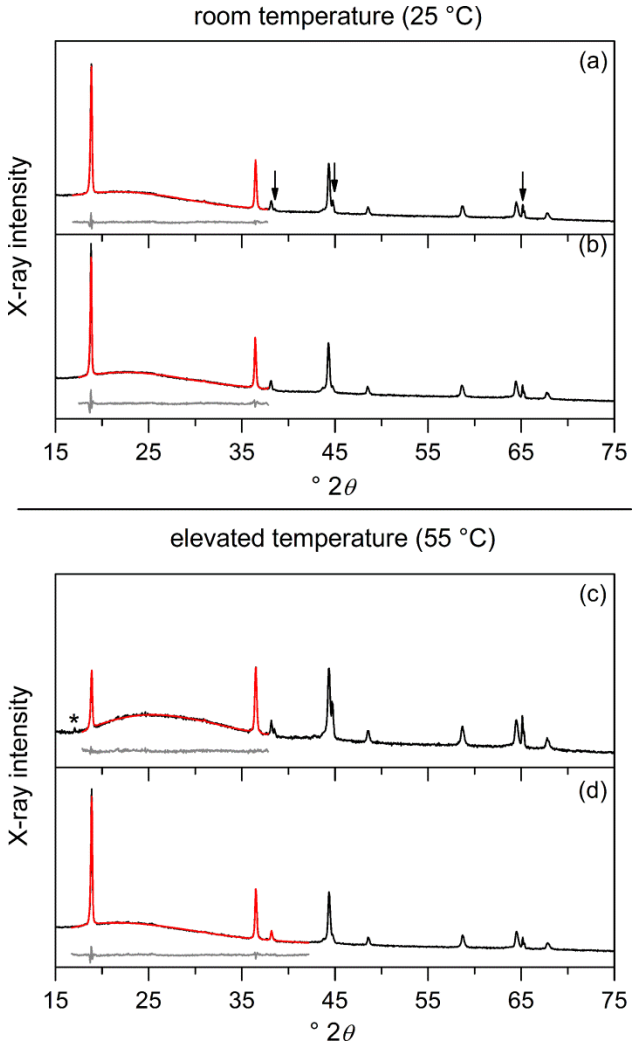

Figure 5.12 XRD patterns of electrodes after 110 cycles at room temperature (LNMO (a) and TiO_2-coated LNMO (b)) and at 55 ℃ (LNMO (c) and TiO_2-coated LNMO (d)). The arrows mark aluminum current collector and the * marks the impurity phase $Li_{2-x}NiO_2$.

Figure 5.12 presents the XRD patterns of the material on the electrodes after 110 cycles at 1 *C* rate at both room temperature and at 55 ℃. To carry out this experiment, the batteries were disassembled after discharging to 3.4 V *vs.* $Li^{+/0}$, then the electrodes were washed with diethylene carbonate, and finally dried in the glove box prior to the structural study. The refinement results are summarized in Table 5.1. Since the XRD patterns were collected with the electrode disks, there are additional reflections due to crystalline aluminum (used as an internal reference, and marked in Figure 5.12a), as well as an increased background due to the amorphous carbon black and binder. All of the XRD patterns can be indexed to cubic spinel after cycling. Rietveld refinement was carried out using the (111) and (113) Bragg reflections, which we showed to be reasonable in our prior work.[21] In comparing the refinement data on the coated electrodes, a common trend shows that after cycling, the lattice parameter increases slightly. And, the lattice parameter after cycling at 55 ℃ is the larger than that obtained after cycling at room temperature. These results are different from the study we reported last year on hydrothermally synthesized LNMO, which shows a decrease in the lattice parameter after cycling cells between 3.4 and 5.0 V. A decrease in the lattice parameter points to manganese disproportionation, which results in an increase in the average manganese valence within the solid. In contrast, previous studies show that high-voltage charging of LNMO can lead to the release of oxygen, which gives rise to an increase in the unit cell volume.[293] This latter observation matches what we observe in this study.

We also note that after 110 cycles at 55 ℃, the (111) peak in the XRD pattern of bare LNMO shows a significant drop in intensity, which suggests dissolution of transition metal layers. Dissolution is supported by the capacity fade observed in Figure 5.10a.

Meanwhile, we notice that a new reflection grows in at 2θ of 17°, which matches the nickel-rich orthorhombic phase $Li_{2-x}NiO_2$.[294, 295] This phase can be denoted as a compositional component of the $LiNi_{0.5}Mn_{1.5}O_4$-MnO_2 phase diagram. In both $Li_{2-x}NiO_2$ and LNMO, the formal oxidation state of nickel is 2+. Isolation of a nickel-rich phase will result in a decrease of the manganese valence. Both of the reasons explain the observed increase in the lattice parameter. More importantly, no $Li_{2-x}NiO_2$ phase can be identified for the surface coated samples, and the X-ray intensity is maintained, indicating that the titanate coating enhances the structural stability of LNMO.

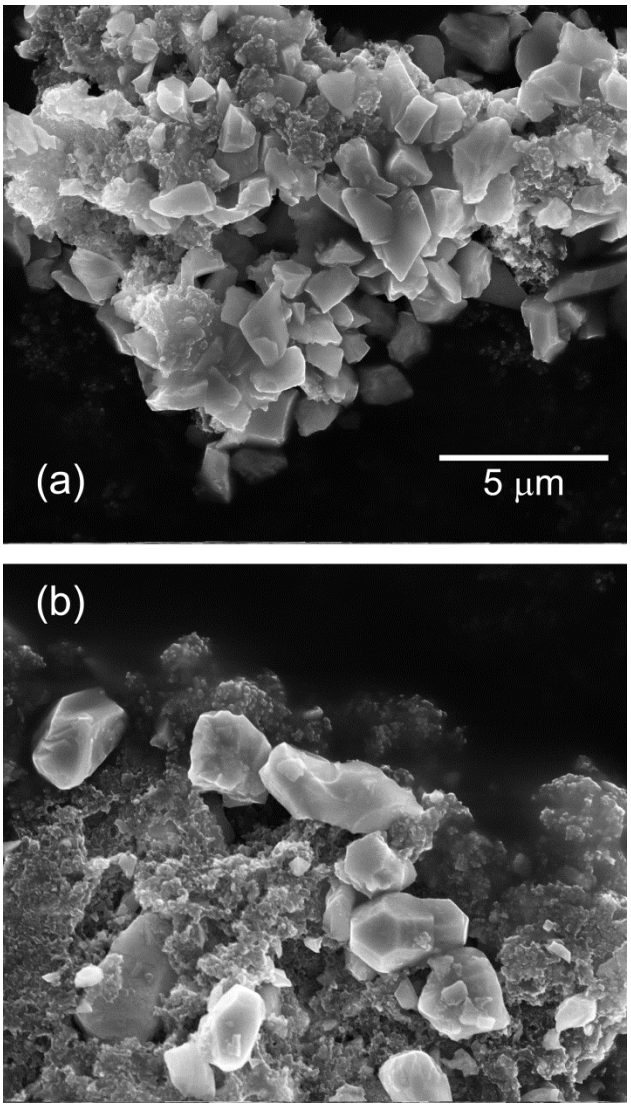

Figure 5.13 SEM images of LNMO (a) and TiO_2-coated LNMO (b) after cycling at 55ºC. Both images are recorded at the same magnification such that the 5 μm scale bar is common.

In Figure 5.13, SEM images of bare-LNMO and 5 – 10 nm TiO_2 coated samples after 55 ℃ long cycling are shown. Particle fracture of the bare-LNMO particles is observed. The cracked particles cause a large resistance and partial electrical isolation of the electrode which leads to capacity fade after many cycles. On the other hand, there is no obvious mechanical degradation of the coated powders, which explains better

cyclability of the coated materials. The mechanism of particle fracture is unclear in this study; it could be ascribed to cycling through the $Mn^{4+/3+}$ couple to give rise to capacity fade or due to changes in oxygen stoichiometry. This is an active area of ongoing research. However, to check the integrity of the titantia coating after cycling, TEM is applied (Figure D.8), which shows that the coating remains intact after cycling.

5.3.5 Li-ion diffusivity and electrode resistivity

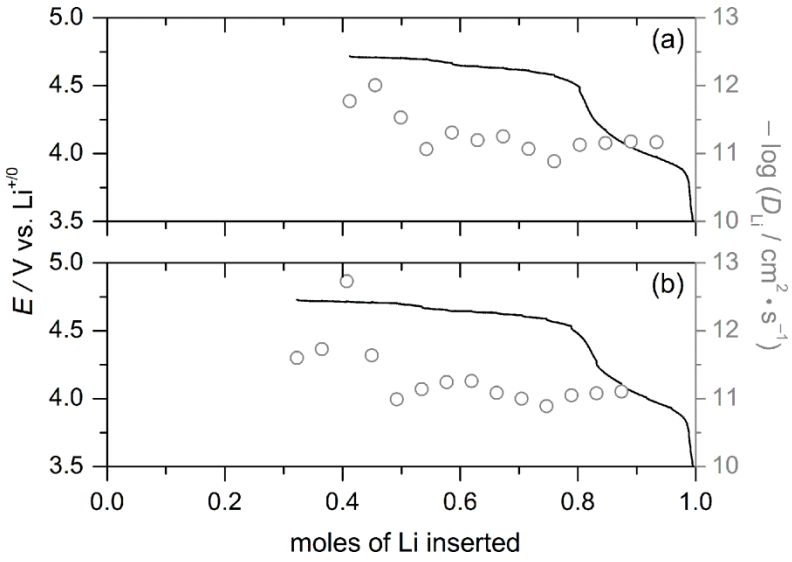

Figure 5.14 GITT curves for LNMO (a); 5 – 10 nm TiO_2-coated LNMO (b).

In the present study, we have successfully coated a titanate and/or titania layer on the surface of LNMO to improve its long-term electrochemical stability at the practical rate of 1 *C*. However, with increasing current, the surface-coated materials show a greater drop in capacity than is observed in the bare LNMO sample. A larger polarization gap results in greater energy density loss. One possibility for higher polarization resistance is that the titanate layer may retard lithium-ion diffusivity. In order to measure the lithium-ion diffusion coefficient, the galvanostatic intermittent titration technique (GITT) was applied for all the cathodes.[296,297] In this experiment, a small current pulse (0.2 $C \approx 147$

μA/cm^2) is applied for 10 min and the cell is then allowed to rest at open circuit for 2 h. Both the initial non-equilibrium voltage and the final equilibrium open circuit voltages are recorded. Then, we calculate the lithium diffusion coefficient according to the equation:

$$D_{Li} = \frac{4}{\pi\tau}\left(\frac{m_B V_M}{M_B S}\right)^2 \left(\frac{\Delta E_s}{\Delta E_t}\right)^2 \quad (\tau \ll L^2/D_{Li})$$

where D_{Li} is the lithium-ion diffusion coefficient; τ is the constant current pulse time; m_{B} is the active material mass on the electrode (5 mg); V_{M} is the molar volume of the compound (330.7 cm^3/mol); M_{B} is the molar mass of the compound (182.69 g/mol); S is the electrode contact area with the electrolyte (150 cm^2, determined by BET analysis of the N_2-sorption isotherms); ΔE_{s} is the difference between the steady potentials; and ΔE_{t} is the total transient voltage change of the cell for an applied galvanostatic current for the time τ. The GITT results are presented for bare LNMO and for thin anatase-coated LNMO in Figure 5.14. In this model, lithium insertion was calibrated using the capacity of manganese redox couple, and complete lithium insertion is assumed at the open circuit potential, 3.4 V. As we observe from the GITT plot, all materials show slower lithium-ion diffusivity at the GITT plateau positions, which corresponds to the two-phase mixture during lithium insertion. Surprisingly, we do not observe a significant difference between the D_{Li} values of bare LNMO and the coated samples. All cathode materials show D_{Li} values of 10^{-11} to 10^{-12} cm^2•s^{-1} throughout the entire range of lithium insertion. Meanwhile, the coating thickness from 5 – 30 nm does not strongly influence the rates of lithium-ion diffusion.

Table **5.2** Electrical Conductivity of LNMO Electrodes used in this Study.

Sample Code	σ / S • cm^{-1}
Bare LNMO	1.12×10^{-5}
5 – 10 nm LTO coating	4.93×10^{-6}
20 – 30 nm LTO coating	2.47×10^{-6}
5 – 10 TiO_2 coating	8.21×10^{-6}
20 – 30 nm TiO_2 coating	7.15×10^{-6}

An alternative hypothesis for the difference in rate capability for bare- and coated LNMO samples is that the electronic conductivity of the cathode materials is lowered upon coating. To test this hypothesis, we carried out four-point probe measurements to determine the electrical resistivity (ρ / Ω • cm). All compounds were pressed into pellets that are ~ 0.06 cm thick. The resistivity can be calculated by:[298]

$$\rho = \frac{V}{I} \cdot CF \cdot W \ (CF = 4.54)$$

where V is the applied voltage (1 V); I is the measured current; CF is a geometric correction factor; W is the thickness of the pellet. The conductivity (σ / S • cm^{-1}) is quoted for each of the electrodes used in this study in Table 5.2 with the *i-t* curves plotted in Figure D.9. Notable is that bare LNMO shows the highest electrical conductivity among all the materials, and corresponds to larger capacity at higher current. In support of this hypothesis, the thicker the coating, the lower the conductivity, and the smaller the capacity at fast rates. Future work will focus on elucidating the cause of greater capacity at high temperatures and exploiting this phenomenon by coupling these coated cathodes with oxide-based anodes to generate a full cell.

5.4 Conclusion

Solid-state synthesized $LiNi_{0.5}Mn_{1.5}O_{4-\delta}$ was successfully coated with titania-based oxide layers by a sol-gel coating method. The electrochemical characteristics of all the coated materials cathodes were carefully studied and compared to bare LNMO. Both of the coatings employed, LTO, and/or anatase-TiO_2 effectively stabilize LNMO during electrochemical cycling. At the elevated temperature 55 ℃, bare LNMO shows significant capacity fade, and the polarization resistance increases. On the contrary, the coated samples show better capacity retention and a smaller polarization gap, ascribed to the suppression of SEI formation. Elevated temperature cycling of bare LNMO yields the formation of an undesirable $Li_{2-x}NiO_2$ phase, and a loss in crystallinity is evident by a decrease in XRD peak intensity. However, coating the sample with LTO or TiO_2 maintains the structural integrity. A greater fraction of oxygen vacancies is found in all samples after electrochemical cycling due to the oxygen loss at high voltages regardless of the presence of a coating. There is no dramatic change in the lithium-ion diffusivity upon coating, and the decrease in capacity retention at faster rates is likely attributed to an increase in surface resistance due to the titania coating; the thicker the coating, the lower the conductivity.

CHAPTER 6

$Li_4Ti_5O_{12}$ Nanocrystals Synthesized by Carbon Templating from Solution Precursors Yield High Performance Thin Film Li-Ion Battery Electrodes

Portions of this chapter have been published:

Hao, X.; Bartlett, B. M. *Adv. Energy Mater.* **2013**, *3*, 753-761.

6.1 Introduction

There is growing interest in alternatives to graphite as the anode material for lithium-ion batteries that improve safety without sacrificing performance. Specifically, the challenge is to find a thermodynamically stable material in which no solid-electrolyte interface (SEI) layer grows.[299,300] The formation and growth of the SEI layer in graphite-containing batteries are well-documented, but remain poorly understood. Meanwhile, recent work has focused on nanomaterials composed of other group 14 elements such as silicon [301] and germanium [302] which show significant higher energy density than carbonaceous anode. However, these materials have the drawback of large volume changes upon lithium insertion, which leads to electrode pulverization on repeated cycling with fast capacity dropping. Pure intercalation oxide-based intercalation materials such as $Li_4Ti_5O_{12}$ (LTO) have the advantage that volume changes in the host lattice is negligible upon lithium insertion.[303 – 305] On the other hand, the low-voltage limit (commonly set at 1.0 V *vs.* $Li^{+/0}$) of oxides is higher, results in a decrease in energy

density. Despite this drawback, LTO remains a promising anode material for Li-ion batteries because of its stability.

To date, no anode material is flawless, and the fundamental limitations to using LTO prepared by existing methods are that the rate of lithium-ion diffusion is too slow (10^{-14} to 10^{-17} cm^2/s)[306] and the compound suffers from poor electrical conductivity < 10^{-13} S/cm.[68] The former problem requires the use of nanoparticles to shorten the path of lithium diffusion in the solid state.[307–309] The latter problem is typically addressed by adding electrically conductive carbon when preparing an electrode slurry,[310–314] but requires low resistance to charge transfer between the LTO nanoparticles and added carbon.

The need to solve both problems simultaneously generates a scientific dilemma. There are many synthesis routes described that result in nanoparticles, including hydrothermal synthesis[315–318] or using a soft template in sol-gel processing methods.[319–321] However, the growing nanoparticles tend to aggregate due to their high surface energies, and as a result, the electrode is composed of micron-sized aggregates. The problem with aggregates is that too many LTO surfaces are in contact with other LTO crystallites, and therefore not available to contact the conducting carbon. Electrodes fabricated from these agglomerates are subject to large polarization losses. Three dimensionally ordered microporous (3DOM) $Li_4Ti_5O_{12}$ and nanoscale porous framework electrode have also been introduced.[322,323] However, high rate capability is not achievable due to the lack of electrical contact with conductive carbon in those electrodes.

To resolve this predicament, we describe in this manuscript for the first time the synthesis of LTO nanocrystals from solution-phase precursors using a carbon-templated

growth process. In this process, crystal growth is complete (all of the nutrients are consumed) and the surfaces are annealed at high temperature at nearly the same rate at which the template burns off. Therefore, the LTO product is composed of regularly shaped octahedra whose crystal facets point along the [011] direction. Advantageously, this direction is the one from which lithium ions insert from the electrolyte, and the electrochemical characteristics far exceed those of typical nanoparticles grown without such a template. When 30 μm thin-film electrodes composed of LTO nanocrystals are cycled against Li-foil, the cells show highly reversible electrical energy storage of over 250 Wh/kg at the slow rate of 1 *C* (the current required to charge/ discharge the battery in one hour, 175 mA/g). Remarkably, the energy density remains large as the power increases: 190 kW/kg, at 100 *C* (charge/ discharge in 36 s).

6.2 Experimental

6.2.1 General consideration

Lithium metal 99.9% (metal basis) was purchased from Alfa Aesar. Titanium isopropoxide 97% was purchased from Sigma Aldrich, and it was distilled prior to storing in a Vacuum Atmospheres OmniLab glove box under an argon atmosphere. Ethanol (200 proof) was purchased from Decon Labs. Toluene was purchased from EMD milipore and purified through a VAC solvent purifier unit. Acetylene black (carbon black, /CB) was purchased from Strem Chemicals. CB was kept in a Fisher Scientific^{TM} oven at 150°C prior to use. Deuterated toulene (99.5%) and ethanol (99.5%) were purchased from Cambridge Isotope Laboratories.

Powder X-ray diffraction patterns were collected on a Bruker D8 Advance diffractometer with a Lynx-Eye detector and parallel beam optics using Cu-Kα radiation (λ= 1.54184 Å). The patterns were indexed and refined using the Bruker TOPAS

software. Scanning electron microscopy images were obtained on an FEI Nova Nanolab SEM/FIB at an accelerating voltage of 10 kV. High resolution transmission electron microscopy was performed on a JEOL 3011 TEM with a LaB_6 electron source operated at 300 kV. The samples were prepared by sonicating a dispersion of powdered sample in tetrahydrofuran and drop casting the resulting suspension onto a Cu grid with an ultra-thin holy carbon film (Ted Pella^{TM}). The samples were heated to 60 °C in a Fisherbrand vacuum oven prior to the measurement. X-ray photoelectron spectra were collected with a Krato Axis Ultra spectrometer with a monochromatic Al Kα source and a charge neutralizer system was used for all the analyses. The data collected were fit using Casa^{TM} XPS software package 2.3.15. Electron paramagnetic resonance spectra were recorded on a Bruker X-band (9.3 GHz) EMX spectrometer at 6 K. The microwave power and frequency were 20.51 mW and 9.28 GHz respectively, with a modulation amplitude of 1.00 G at 100 kHz. Thermal analyses were obtained with a TGA7 Thermogravimetric Analyzer (Perkin Elmer^{TM}) at a heating rate of 10 °C / min. under a flow of air. Raman spectra were obtained using a Renishaw Ramascope Raman Spectrometer. All spectra were taken under 785 nm laster excitation with 1.1 mW incident power. NMR spectra were recorded on a Varian MR400 400 MHz spectrometer using toluene-d_8 and ethanol-d_6 solvents.

6.2.2 Synthesis

Lithium metal (typically 27 mmol) was dissolved in 40 mL of ethanol in a Schlenk flask charged with nitrogen. Titanium isopropoxide was dissolved in 60 mL of dry toluene in an argon atmosphere glove box. These two reagents were mixed together by cannula transfer to give a transparent solution containing both lithium and titanium

synthons (200 mL total, lithium to titanium molar ratio is 4:5 and the volumetric ratio of ethanol to toluene was adjusted to 2:3). This precursor solution is stable under ambient room atmosphere, as evidenced by an unchanged NMR spectrum.

To prepare the lithium titanate directly from this precursor solution (S-LTO), a 15 mL aliquot of the precursor stock solution was poured into a 23 mL scintillation vial and placed in the vacuum oven at 60 °C for 2 h in order to remove excess solvent. The resulting white residue was transferred to an alumina boat and annealed in an MTI muffle furnace at 700 °C for 1 h with both heating and cooling rates of 10 °C /min. From this reaction, ~ 100 mg of product is isolated.

To prepare lithium titanate using a carbon black templating method (C-LTO), typically, 1 g of carbon black was added to 50 mL of the precursor solution. This mixture was stirred overnight and then sonocated for 2 h to form a well dispersed suspension. Then, the resulting thick slurry was centrifuged to give a residue coated with carbon black. This residue was dried in the vacuum oven at 60 °C for 2 h, then annealed at 700 °C for 1 h as described above. To study the growth mechanism of C-LTO nanocrystals, other annealing temperatures (400 °C and 450 °C) were employed, where carbon is not completely oxidized.

6.2.3 Electrochemical measurements

Thin-film electrodes were prepared by mixing the synthesized material, carbon black and poly(vinylidene) difluoride (PVDF, purchased from Alfa Aesar) (mass ratio of 75:15:10) with a Thinky AR-100 rotation/revolution super mixer. *N*-methyl-2-pyrrolidone (NMP, 99+%, purchased from Alfa Aesar) was added to dissolve the PVDF completely and to maintain an appropriate viscosity of the resulting black slurry. This

material was then coated onto a de-greased copper foil using the doctor blade method, and the foil was dried in the vacuum oven at 120 °C overnight prior to assembling the cell in order to minimize surface-bound water. The working electrode and glass fiber separator (GF/D) were cut and fit into a Swagelok^{TM} PTFE union in the argon glove box. The active material loading is approximately 1 mg/cm^2 or 4 mg/cm^2. The electrode masses were measured using a Sartorius^{TM} ME36S microbalance. In all cells, the electrolyte solution was composed of 1 M lithium hexafluorophosphate (99.99+%, Sigma Aldrich) dissolved in 2:1 (v/v) ethylene carbonate (99%, anhydrous, Sigma Aldrich) and diethyl carbonate (99+%, anhydrous, Sigma Aldrich), and lithium foil was used as both the auxiliary and reference electrode in a 2-electrode configuration.

Galvanostatic charge/ discharge curves were recorded on a CH Instruments 660C electrochemical workstation with a voltage window of 1 to 3 V (*vs.* $Li^{+/0}$). The polarization gaps due to hysteresis in the charge and discharge profiles are reported at one half the gravimetric capacity values. Galvanometric intermittent titration technique (GITT) measurements were collected using a customized Vencon UBA5 battery analyzer. In GITT measurements, a galvanostatic pulse of 0.2 *C* was applied for 600 s followed by relaxation at open circuit 2 h. The cut-off voltage is set to 1 V. Prior to the GITT test, all cells were galvanostatically charged to 3 V with a cut-off current limit of 10 nA followed by a 2 h rest period at open circuit. Electrochemical impedance spectra (EIS) were collected using an Autolab PGSTAT302N with a FRA (frequency reponse analysis) module. Batteries were cycled ten times between 1.0 and 3.0 V at 1 *C* current before the measurements. The cycling behavior was stopped at half the charging capacity on the last cycle, at which point all of the cells were stored in an argon glovebox

overnight such that the spectra start at the open circuit potential, 1.55 V. The EIS were recorded in a frequency range from 10^5 to 10^{-2} Hz with AC perturbation was ± 10 mV. Zview™ software package was used for the data fitting.

6.3 Results

6.3.1 Synthesis and characterization of LTO nanocrystals

In the present study, a solution-based method starting from alkoxide precursors of lithium and titanium was applied in order to obtain atomic-level mixing from which to synthesize $Li_4Ti_5O_{12}$ (LTO). The synthon lithium ethoxide is the first prepared on a Schlenk line by reacting metallic lithium with absolute ethanol, liberating hydrogen in the process. The other synthon, titanium isopropoxide is prepared as a 0.48 M solution in toluene, and the two reactants are mixed—4 parts LiOEt to 5 parts $Ti(O^iPr)_4$. We then add additional toluene such that the precursor mixture is 2:3 EtOH:PhMe; this combination slows solvolysis. ^{1}H-NMR spectroscopy (Figure E.1) shows that the as-synthesized precursor is composed of isopropoxide and ethoxide, and the solution is stable for several days under ambient room conditions, noted by the unchanged spectrum after storage.

Isolated LTO nanocrystals form from a templated synthesis using this precursor solution and carbon (acetylene) black. In a typical synthesis, we add 1 g of carbon black per 50 mL of precursor solution prior to removing the solvents. Carbon black is a form of amorphous carbon whose role is to prevent aggregation of the growing nanocrystals during annealing. In order to achieve the minimum carbon loading and to maximize interparticle contact, we centrifuged the samples to eliminate as much excess solvent as possible prior to annealing. The annealing scheme was determined from the results of thermogravimetric analysis (Figure E.2). Solvent evaporation continues as the

temperature is ramped to ~ 200 °C, irrespective of the presence of carbon black. The two syntheses are distinguished above 500 °C, where an abrupt change in mass occurs for the material containing carbon black. This mass change corresponds to the ignition of carbon black; the sample glows bright red, commensurate with burning carbon. No further mass loss is observed above 600 °C. Above this temperature, there is no carbon remaining, further supported by Raman spectroscopy (Figure E.3).

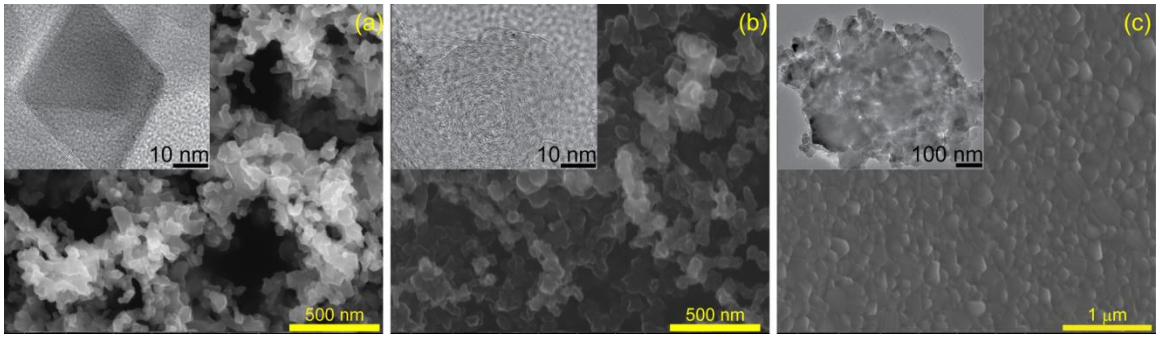

Figure 6.1 (a) SEM and HR-TEM images of C-LTO nanocrystals; (b) the carbon template; (c) and the S-LTO aggregates.

Figure 6.1a shows SEM and HR-TEM images of the resulting nanocrystals from the carbon-templated synthesis (C-LTO). The material is composed of 67 ± 17 nm crystallites with distinct octahedral facets, with a histogram of the particle size distribution shown in Figure E.4. Images of the carbon template in Figure 6.1b show that it too is composed of ~70 nm particles, thus dictating the particle size of the product. Most important, the particles resulting from annealing the precursor solution (S-LTO) without adding the carbon template are illustrated in Figure 6.1c. Here, we observe micron-sized aggregates.

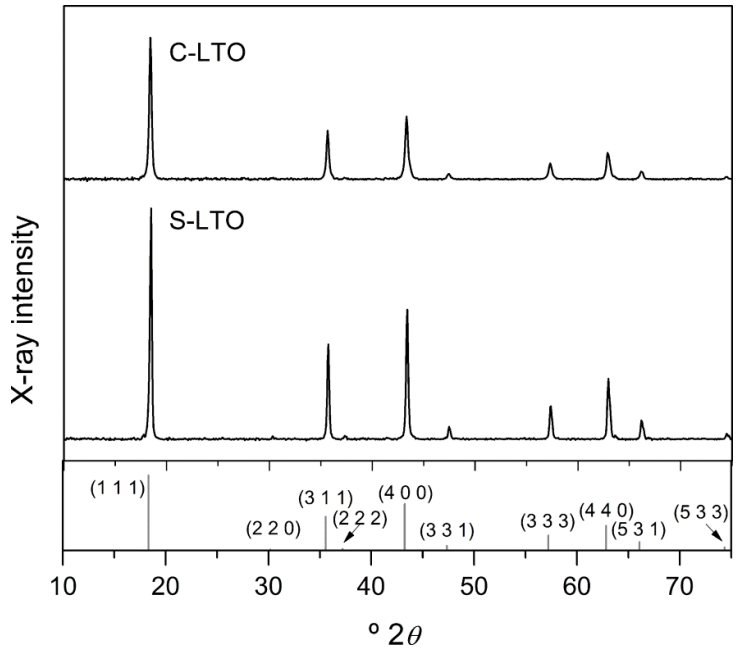

Figure 6.2 (a) XRD patterns for C-LTO (top) and S-LTO (bottom). The indexed pattern for LTO is presented in gray underneath.

The powder X-ray diffraction pattern in Figure 6.2 confirms that the crystalline products obtained are spinel regardless of the presence or absence of the template. Rietveld analysis of the diffraction patterns (Figures E.5 and E.6 with associated Tables E.1–4) give nearly identical lattice parameters, 8.362 and 8.363 Å for C-LTO and S-LTO respectively in agreement to what has been reported.[324] The only notable difference is in the intensities of the reflections of the two samples, which is due to the smaller particles resulting from the C-LTO preparation; defining the crystalline domain size by the Scherrer equation[184] in our Rietveld refinement corroborates our SEM findings: 58 nm suggests nearly single crystals of C-LTO; the domain size of S-LTO is much larger, 201 nm. The selected area electron diffraction pattern (Figure E.7) of the individual C-LTO nanocrystal in the inset of Figure 1a shows exposed facets that point along [0 1 1], the direction along which Li-ion channels are organized, also illustrated in Figure E.7. This

result is similar to what we recently report for $LiNi_{0.5}Mn_{1.5}O_4$ spinel materials synthesized by low temperature hydrothermal methods.[325]

Finally, the surface area of C-LTO is slightly larger, 27 m^2/g, compared to 20 m^2/g for S-LTO as determined by BET analysis of N_2 sorption isotherms (Figure E.8). The high surface area of these LTO samples will result in high rate capability (i.e.—high power) electrodes. However, the negligible aggregation in C-LTO nanocrystals helps to retain a large energy density as well. The lack of aggregation is demonstrated in the section 2.3 of the results.

6.3.2 Details of the crystal growth mechanism

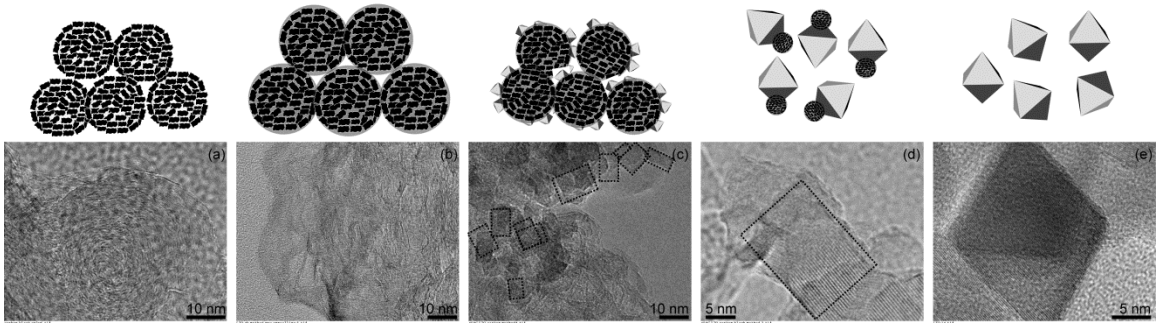

Figure 6.3 TEM images highlighting the growth mechanism of C-LTO nanocrystals from a carbon black template.

In order to elucidate the crystal growth mechanism, we performed temperature-dependent studies of the C-LTO synthesis, returning to our TGA trace (Figure E.2). There are two plateaus of stability—one between 200 and 500 °C, and the second above 600 °C. TEM images shown in Figure 6.3 give the account of nanocrystal growth. First, in Figure 6.3a, we observe only the carbon template at room temperature; it is composed of 50 nm spheres, as was highlighted above. Figure 6.3b shows the image of the precursor solution loaded with the carbon template. Not surprisingly, there is no order

since this material has not yet been annealed. During the synthesis, carbon is completely soaked with the precursor solution, and lithium and titanium are evenly dispersed on the surface as evidenced by the energy dispersive X-ray spectra and map in Figure E.9.

After annealing the sample to 450 °C (within the first plateau of stability) for 1 h, order emerges. Figure 6.3c shows crystalline domains that are ~10 nm in diameter growing off of the carbon black template. Curiously, the image in Figure 6.3d is also captured after annealing at 450 °C for 1 h. Here, much larger crystalline domains are observed with residual carbon attached, which suggests that particle growth is concomitant with template removal (carbon is oxidized to carbon dioxide). Figure 6.3e shows the final product to be regular octahedra after annealing to 700 °C. By controlling the annealing temperature and time, we conclude that crystal size is ultimately limited by the size of the template. And, since crystal growth consumes nutrients localized on the carbon black template surface, minimal aggregation results.

6.3.3 Electrochemistry

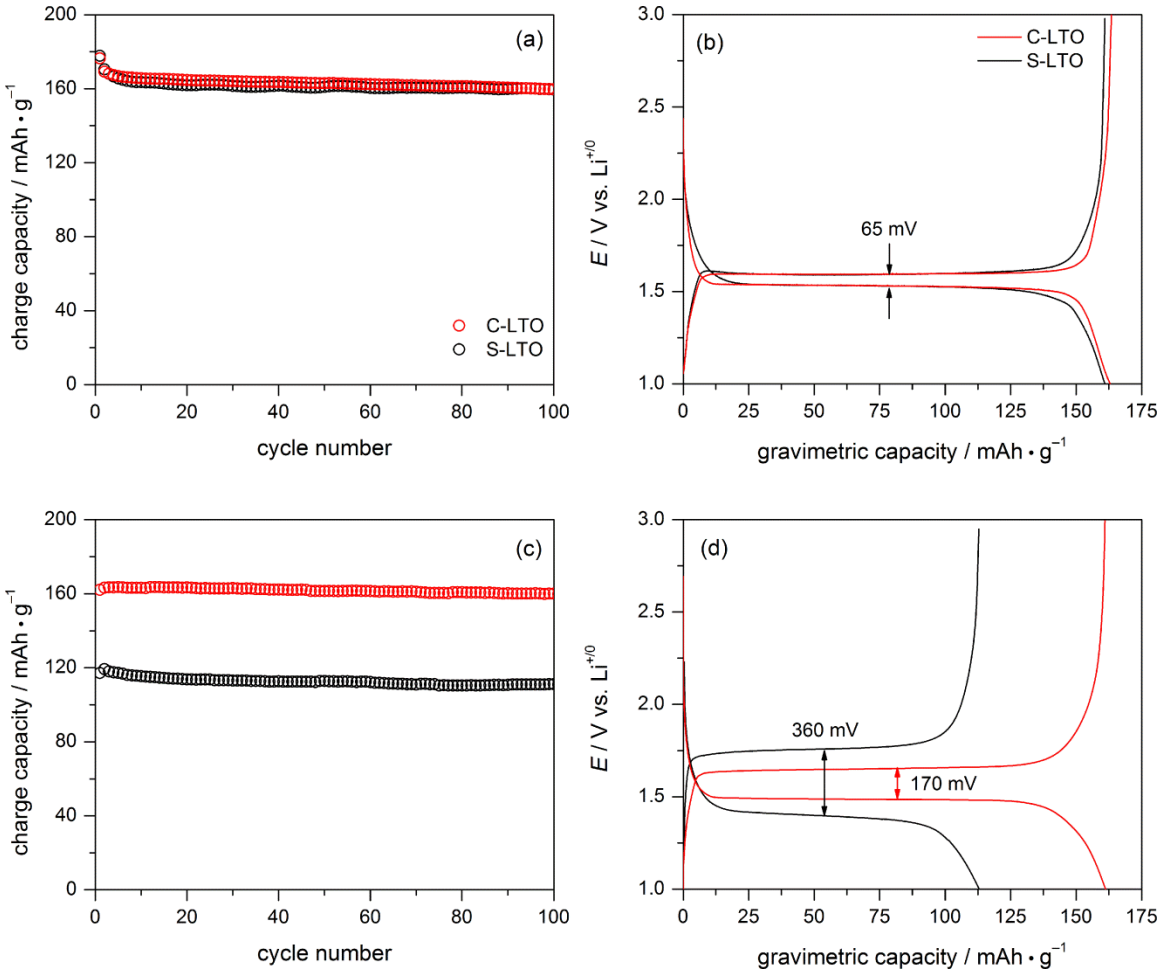

Figure 6.4 (a) Gravimetric charge capacity of C-LTO (black) and S-LTO (gray) cycled galvanostatically at 1 *C;* (b) individual charge and discharge curves for cycle 50 at 1 *C*; (c) galvanostatic cycling at 10 *C*; (d) charge discharge curves for cycle 50 at 10 *C*.

$Li_4Ti_5O_{12}$ can uptake three lithium ions during the charging process, corresponding to a theoretical energy storage capacity of 175 mAh/g.[264,326] Figure 6.4a shows the gravimetric capacity of thin-film electrodes composed of either C-LTO or S-LTO materials cycled at 1 *C* current. In the *C*-rate convention, *n* C current represents the load required to charge/ discharge the theoretcial capacity in 1/*n* hours. For an electrode composed of 1 mg LTO, 1 *C* corresponds to a current density of 175 μA/cm^2. Lithium insertion and extraction

occur as a two-phase mixture of $Li_4Ti_5O_{12}$ and $Li_7Ti_5O_{12}$, leading to a flat, constant voltage plateau (a consequence of the Gibbs's phase rule) at 1.55 V *vs.* $Li^{+/0}$.[327] However, slow Li^+ diffusion and charge transfer tend to lower the capacity and also cause hysteresis between the charge and discharge profiles. Both materials show similarly excellent capacity retention for the first 100 cycles, with an intial capacity of 167 mAh/g (at cycle 4) and 160 mAh/g (97.6% retention) at the end of the test. The initial charge capacity of the material nearly reaches the theoretical capacity value. Voltage curves for the 50th charge and discharge cycles are higlighted in Figure 6.4b. Regardless of the preparation method, LTO shows a polarization voltage gap (hysteresis) of 65 mV; the charging plateau potentials were 1.53 V in both cases. This observation suggests that neither charge transfer nor Li^+ diffusion within LTO are limited by the difference in particle size or by aggregation at low current.

Next, C-LTO and S-LTO materials were cycled at a rate of 10 *C* (1.75 mA/cm^2), shown in Figure 6.4c. Both electrodes still show excellent capacity retention after 100 cycles at 10 *C*: 97.6% for C-LTO and 94.1% for S-LTO. However, two key differences arise as we plot the voltage curve for the 50th cycle in Figure 6.4d. First, C-LTO shows a much larger capacity (161 mAh/g compared to 113 mAh/g for S-LTO). Second, C-LTO shows a smaller polarization–170 mV, which is *less than half* that observed for S-LTO, 360 mV. To demonstrate the repeatability of our cell fabrication, we assembled two additional cells; Figure E.10 plots the charge capacity for three of each cell C-LTO and S-LTO cycled at both 1 *C* and 10 *C* current. All cells show virtually the same performance, and we conclude that isolated nanocrystals prepared by templated crystal

growth not only retard the rate of deliterious side reactions that lead to capacity fade, but also result in a decrase in the charge-transfer resistance in the material.

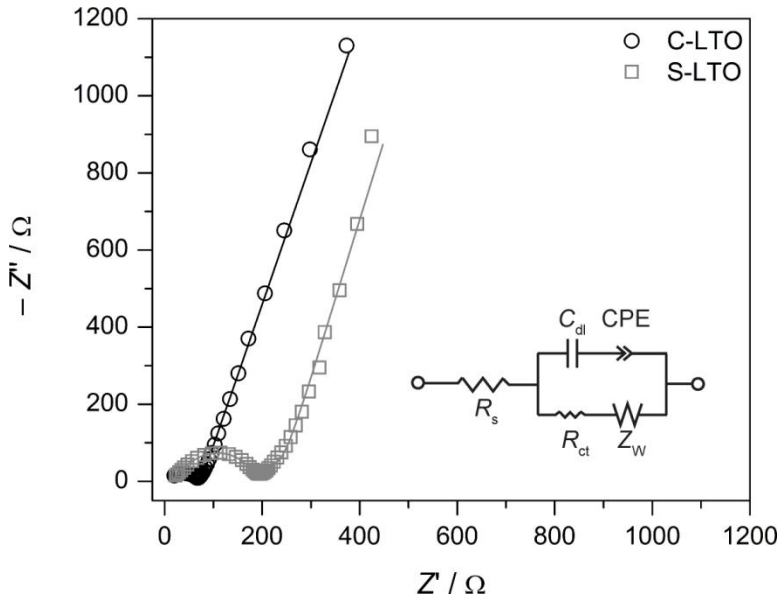

Figure 6.5 Nyquist plots for EIS data recorded for C-LTO (black) and S-LTO (gray). The **inset** shows the equivalent circuit used to obtain the fits (solid lines).

Table 6.1 EIS fit parameters for C-LTO and S-LTO

Compound	R_s [Ω]	R_{ct} [Ω]	Z_W-R [Ω]	Z_W-T [s]	Z_W-P	C_{dl} [10^{-6} F]	CPE-T [10^{-4} s]	CPE-P
C-LTO	19.9	62.72	53.45	0.3375	0.4152	1.67	5.06	0.303
S-LTO	23.2	197.8	224.5	0.3194	0.401	2.31	3.62	0.364

R-resistance, *T*-time constant or capacitance, *P*-an exponent

$Z_{CPE} = 1/[T(i \cdot \omega)^P]$

$Z_W = R \cdot ctnh[(i \cdot T \cdot \omega)^P]/(i \cdot T \cdot \omega)^P$

To corroborate this result, we have measured the electrochemical impedance of the thin-film electrode and fit the data to include solution resistance, an *RC* circuit representing

charge transfer, and a Warburg impedance representing ion diffusion. The resulting Nyqust plot and the equivalent circuit are shown together in Figure 6.5. R_{ct}, the charge-transfer resistance, is the diameter of the semicircle. Table 6.1 shows the best fit parameters for the EIS spectra. The chief result is that the cell composed of C-LTO has a signficantly smaller R_{ct}, 62.7 Ω vs. 197.8 Ω for S-LTO.

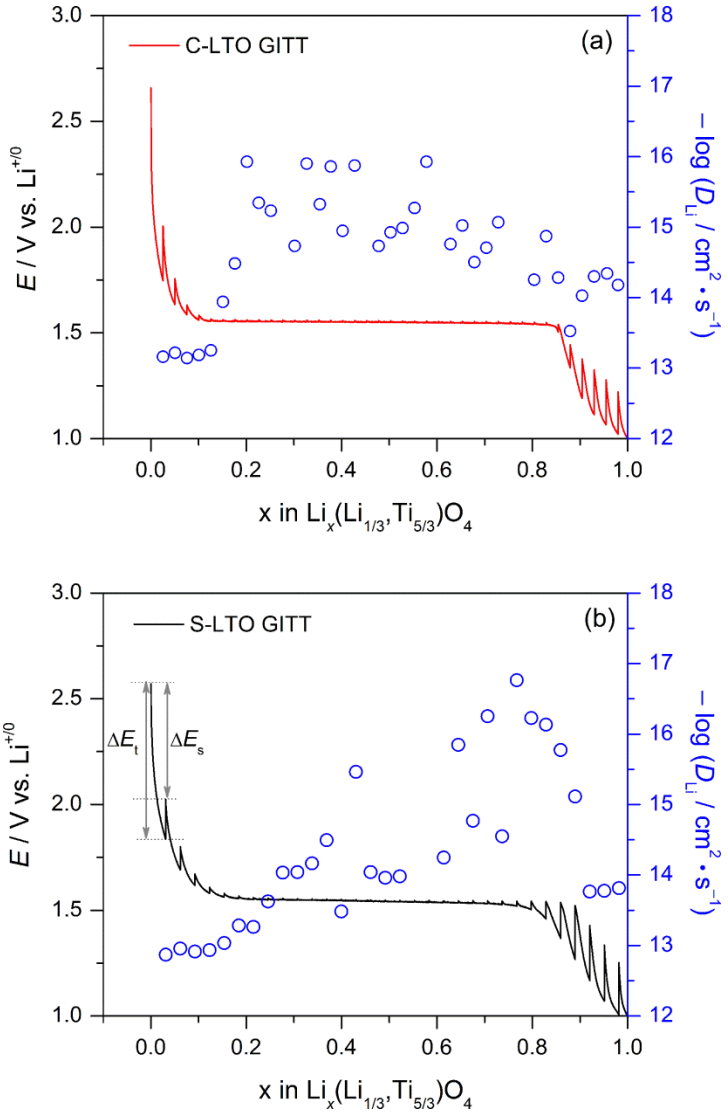

Figure 6.6 GITT curves for C-LTO, (a) and S-LTO (b). The gray circles in each plot represent the diffusion constant calculated from equation 1, as described in the text.

Although the fit to EIS data can give an estimate of the lithium-ion diffusion constant (D_{Li}), this method has the servere limation that it assumes the a perfectly homogeneous, planar electrode. Therefore, we turn to galvanostatic intermittent titration technique[328,329] (GITT) measurements to provide estimates of the lithium-ion diffusion coefficient for both LTO samples. In this experiment, a small current pulse (0.2 C = 35 μA/cm^2) is applied for 10 min and the cell is then allowed to rest at open circuit for 2 h. Both the initial non-equilibrium voltage and the final equilibrium open circuit voltages are recored. Then, we calculate the lithium diffusion coefficient according to:

$$D_{Li} = \frac{4}{\pi\tau}\left(\frac{m_B V_M}{M_B S}\right)^2 \left(\frac{\Delta E_s}{\Delta E_t}\right)^2 \quad (\tau \ll L^2/D_{Li}) \qquad (1)$$

where D_{Li} is the lithium-ion diffusion coefficient; τ is the constant current pulse time; m_B is the active material mass on the electrode (1 mg); V_M is the molar volume of the compound (987 cm^3/mol); M_B is the molar mass of the compound (459.09 g/mol); S is the electrode contact area with the electrolyte (85.4 cm^2 for C-LTO and 63.3 cm^2 for S-LTO, determined by BET surface-area measurements); ΔE_s is the difference between the steady potentials; and ΔE_t is the total transient voltage change of the cell for an applied galvanostatic current for the time τ. ΔE_s and the ΔE_t are determined in the experiment, and are marked in the Figure 6b as an example.

The GITT results and the calcuated diffusion constants for both C-LTO and S-LTO are ploted in Figure 6. The chemical formula of $Li_4Ti_5O_{12}$ can been re-written to represent the atomic positions in the standard spinel AB_2O_4 notation, $(Li)_{8a}[Li_{1/3},Ti_{5/3}]_{16d}(O_4)_{32e}$, where the subscripts outside of the parentheses represent the Wyckoff positions in the unit cell. This shorthand is simply ⅓ the stoichiometric formula, so in this notation, one mole of lithium inserts. Upon insertion, Li^+ residing on the 8*a* tetrahedral sites migrate to the

previously vacant 16*c* octahedral sites (see Figure E.7), and the product can be expressed as $[Li_2]_{16c}[Li_{1/3},Ti_{5/3}]_{16d}(O_4)_{32e}$.[330] In Figure 6.6, the curves are plotted showing one mole of lithium being added per mole of spinel on the *x* axis. The charging plateaus as determined by the open circuit potentials are greater than 1.55 V, showing that a 2 h rest period at open circuit is sufficient for the cell to reach equilibrium. The magnitude of D_{Li} ranges from 10^{-13} to 10^{-16} $cm^2 \cdot s^{-1}$ throughout the insertion process, regardless of the synthesis method employed. This behavior shows that lithium-diffusion is not limited by particle aggregation in the S-LTO material. Also notable is that for both materials, the beginning and ending steps show diffusion that is ~ 10^3 faster than what is observed in the two-phase region.[331,332]

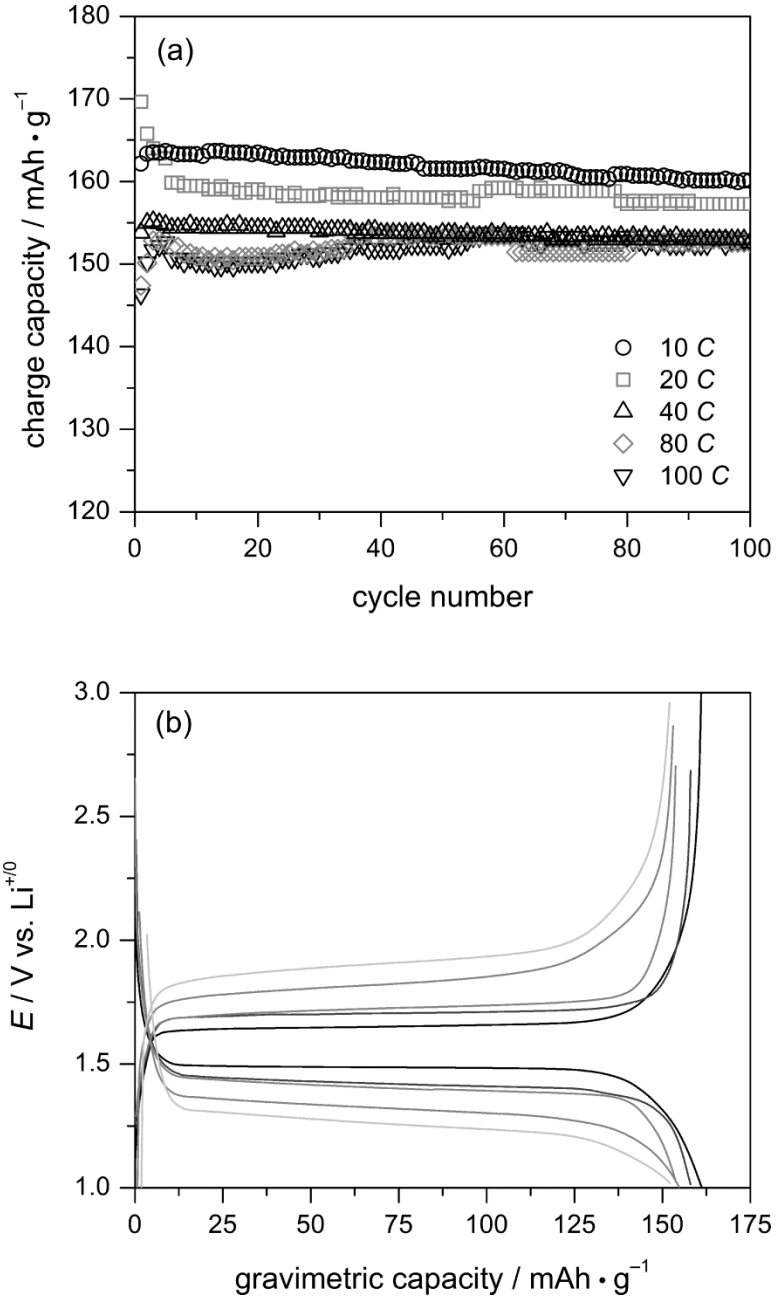

Figure 6.7 (a) Rate capability of C-LTO cycled at varying current; (b) individual charge and discharge curves for the 50th cycle at each current. Note that polarization increases as *C* rate increases.

Despite the similarity in lithium-ion diffusion rates, the smaller charge-transfer resistance between nanocrystals and carbon black in C-LTO electrodes allows for better rate capability. To determine the rate capability of the C-LTO material, we cycled cells at

10 *C*, 20 *C*, 40 *C*, 80 *C* and 100 *C* current. The observed capacities and retention over the first 100 cycles are provided in Figure 6.7a. Capacity retention is excellent for all rates; even at 100 *C* current, 100 % of the capacity at cycle 3 is retained after cycle 100. At this rate, the battery is capable of storing and releasing *all* of its charge in 36 s. In Figure 6.7b, the voltage profiles for the 50th cycle at each rate are plotted together.

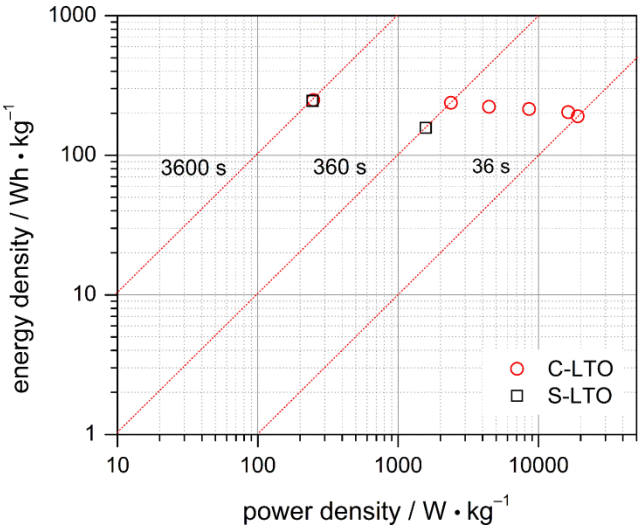

Figure 6.8 Ragone plot for C-LTO (red) and S-LTO (black).

Although the total energy stored in C-LTO and S-LTO is the same, 250 Wh/kg, for thin-film cells operated at low current (1 *C*), the energy density drops dramatically for S-LTO as the load increases. C-LTO stores 238 Wh/kg of energy even when cycled at 10 *C*, whereas the energy density of S-LTO decreases to 157 Wh/kg. Notably, C-LTO stores more energy (190 Wh/kg) at ten times the load (100 *C* current) compared to S-LTO at 10 *C*, shown in the Ragone plot of Figure 6.8. This result best highlights the electrochemical advantage of our carbon-templated nanocrystal growth.

We note that practical battery use in electric vehicles requires greater density of the active material on the working electrode. Therefore, we assembled three additional cells using C-LTO with an active material mass loading of 4 mg/cm^2, and cycled the cells at 1 *C* current. As observed in Figure E.11, all three cells show similar capacity retention for the first 100 cycles compared to those cells with only 1 mg/cm^2 C-LTO cells. We note that the polarization gap is ever so slightly larger (72 mV *vs*. 65 mV). As a result, our work provides material that shows real promise in the search for safe, high power, high energy density lithium-ion battery anodes—ones competent enough to replace graphite.

6.4 Discussion

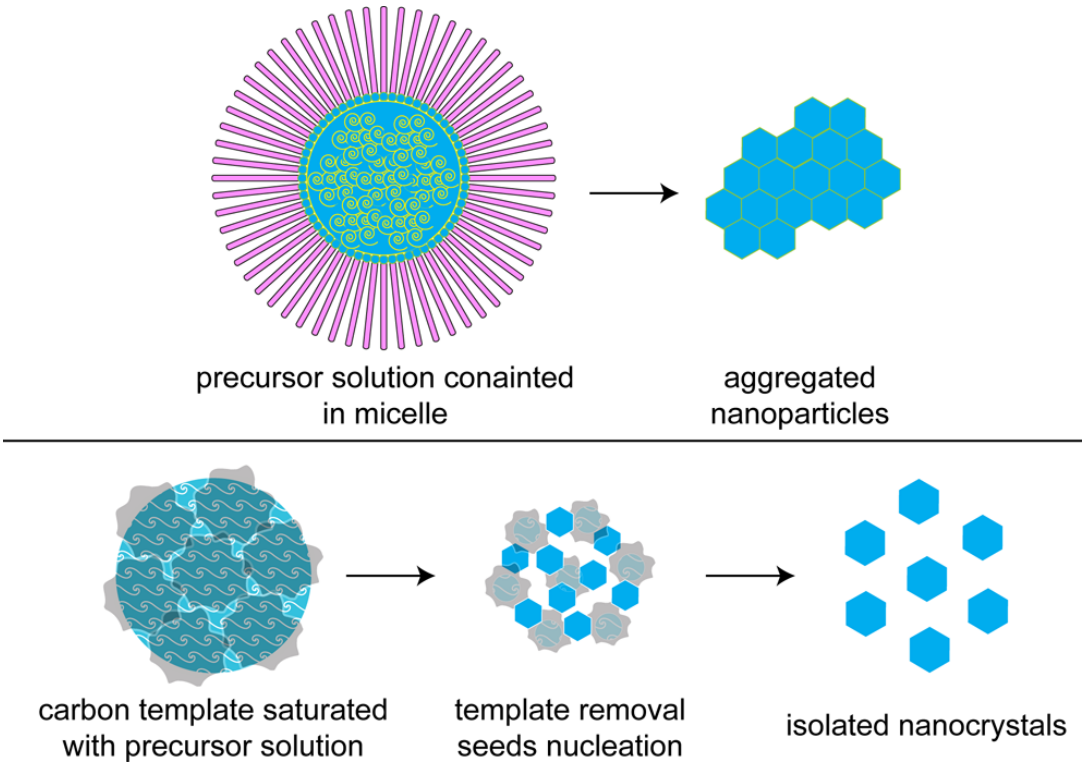

Scheme 6.1 Comparison between soft-templating methods (top) and carbon templating (bottom) for LTO crystal growth.

Although there are other examples of employing a template during the synthesis of LTO to reduce particle size, our work improves upon the use of a template to reduce particle size *without* subsequent aggregation of nanoparticles. The typical approach is to use a soft template and surfactant such as cetyltrimethylammonium bromide (CTAB)[333] or copoly-mers.[334,335] However, this strategy results in all of the nutrients residing in a hydrophilic core. Then, nucleation and growth also occur within this small core and the particles aggregate as crystallite surfaces come into contact. Alternatively, the carbon template that we use keeps all of the nutrients contained without allowing as many of the growing nanocrystals on the surface to come into close contact. Burning off the template seeds nucleation, and growth is limited as the solvent is removed. This growth method gives well isolated C-LTO nanocrystals. The chemistry differences between these two approaches toward growing nanomaterials using a template are illustrated in Scheme 6.1. In our method, minimizing particle aggregation within nanoscale materials has important consequences in the energy density and power of the resulting thin-film electrodes, as we now explain.

First, we consider the three elementary steps in the charge and discharge of a titanium-based lithium-ion battery: 1) lithium-ion diffusion in bulk; 2) charge-transfer from the ion-conducting oxide to the electron-conducting carbon; and 3) ion diffusion in the electrolyte. [336] Not surprisingly, the lithium-ion diffusion constants of C-LTO nanocrystals and S-LTO aggregates are the same, and match those reported for bulk samples. The key conclusion is that rate of lithium-ion diffusion in LTO is extremely slow regardless of morphology or use of a template to prepare nanoparticles. Therefore, in a Li-ion battery, LTO nanomaterials are vital because they shorten the lithium path.

Next, we note that since lithium-ion diffusion is slow, the observation of high rate capability requires that charge transfer between the oxide nanocrystals and the conductive carbon be extremely rapid. Indeed, C-LTO electrodes demonstrate R_{ct} that is 3 times smaller than that observed in S-LTO electrodes, and represents the hallmark of our work. We propose that the superior rate capability arises because there is less aggregation within nanocrystals grown using a carbon template. Therefore, there is greater surface contact between the nanocrystals and the conductive carbon added to the thin-film electrode slurry. In nanoparticle aggregates, charge transfer is limited because too many LTO crystallites adhere only to other non-conductive LTO crystallites in a percolated network rather than contacting the conducting carbon black in the slurry. Scheme 6.2 illustrates this proposition.

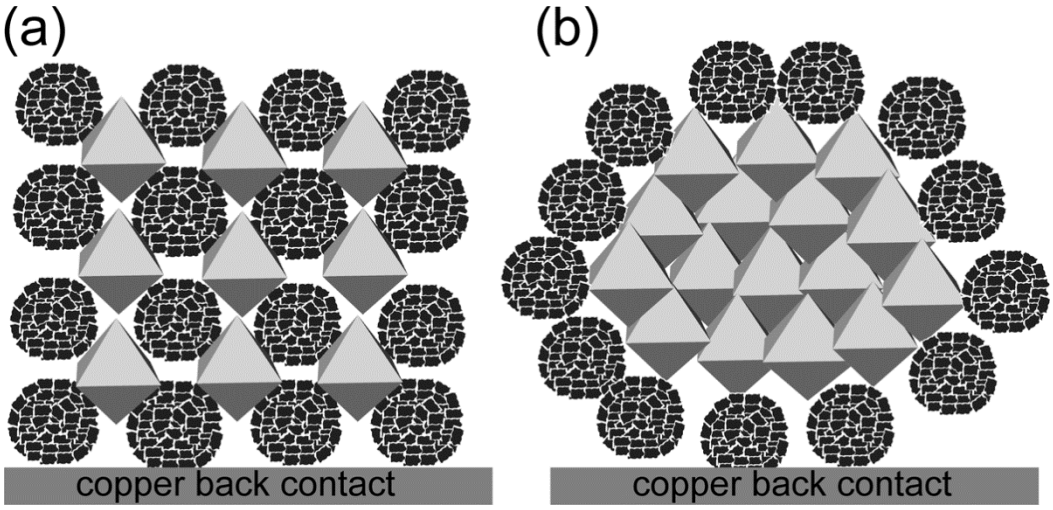

Scheme 6.2 Greater conducting carbon-LTO nanocrystal contact in C-LTO (a), compared to S-LTO aggregates (b).

Then, it has been proposed in the literature that the presence of Ti^{3+} in the prepared compound enhances the surface conductivity, and therefore accelerates the rate of charge

transfer.[337,338] We performed low-temperature EPR spectroscopy and XPS measurments on our C-LTO and S-LTO materials. The data are presented in Figure E.12; no evidence of Ti^{3+} either in bulk or on the surface of our synthesized material is detected by these methods. In the XP spectrum, two different chemical environments are identified ($^2P_{3/2}$ peaks at 458.0 eV and 459.2 eV), both of which correspond to Ti^{4+}.[339,340] The observation of two environments is likely ascribed to surface-bound carbonate or hydroxide;[341] surface Ti^{3+} would show its $^2P_{3/2}$ peak at lower binding energy. Of course, Ti^{3+} is formally present as lithium inserts, with the average oxidation state of titanium in $Li_7Ti_5O_{12}$ being +3.4.

Finally, we bolster this hypothesis by examining the electrochemistry of other LTO samples in Table 6.2. We compare our LTO nanocrystals against bulk LTO, nanoparticle agglomerates of LTO prepared without templating, and aggregates prepared with CTAB templating. We note that the *charge* storage capacity of LTO is similar to what other researchers report. It should be; it is an inherent property of the material. At the reversible limit (i.e.—cycled sufficiently slowly), all LTO materials would show a gravimetric capacity of 175 mAh/g. In functional materials, however, two new factors come into play. We have highlighted the first factor in the preceding paragraphs. The capacity is smaller because the end user has no time to wait for Li^+ to insert throughout the entire material to store charge. The second is that the sheer amount of charge stored in a material is irrelevant if that charge has little stored *energy*. The hysteresis losses in nanomaterials prepared by classic methods render high rate cycling impractical; with a voltage difference between charge and discharge of > 250 mV, over 30% of the energy is lost as heat (determined by integrating the difference in areas under the charge and

discharge curves). Thin-film electrodes composed of our nanocrystals show marked improvement, with an energy density retention of 90 % at 1 *C* current, and 100 % at 100 *C*.

Table 6.2 Electrochemical Comparison of LTO Synthesized by Varying Methods

Compound	Capacity [mAh•g^{-1}]	Polarization [mV]	Reference
CTAB-LTO[(a)]	~135 at 1000 mA/g	>250	321
3DOM-LTO[(b)]	~145 at 0.625 mA/g (~10 *C*)	N/A	317
Hollow sphere-LTO[(c)]	~100 at 10 *C*	>250	335
carbon coated LTO sphere[(d)]	~110 at 10 *C*	>250	336,337
S-LTO[(e)]	113 at 10 *C*	360	this work
C-LTO[(f)]	161 at 10 *C*	170	this work

(a) porous structrue with surface area 219.2 m^2/g

(b) macroporous structure; No conductive agent in electrode

(c) using micron sized carbon sphere as a hard template

(d) using pitch as a carbon coating agent (5.2 wt%); 70 μm

(e) 1 mg/cm^2 loading(30 μm); carbon black template employed

(f) 1 mg/cm^2 loading(30 μm); direct solution method

6.5 Conclusion

We have pioneered a crystal growth process for oxide nanocrystals that relies on templating with amorphous carbon. The template serves two purposes—decreasing the particle size and preventing aggregative growth. As a result, thin-film electrodes comprising $Li_4Ti_5O_{12}$, a sought after material for lithium-ion battery anodes, show

dramatically improved energy density retention when cycled at high *C* rates. We demonstrate that this improvement arises because charge transfer between isolated nanocrystals and the conducting carbon in the electrode is rapid, unlike to the larger charge transfer resistance observed in a percolated network of nanoparticle aggregates.

CHAPTER 7
Conclusion and Future Work

7.1 Introduction

This thesis focused on development of complex transition metal oxide electrodes for lithium ion batteries. Detailed synthesis, characterization and analysis are described in Chapters 2 to 5. Experiments on both cathodes and anodes studies are included in this work. To achieve a stable battery system, the two electrochemical terminals need to meet the stability window the electrolyte; this includes careful selections of the electrode materials based on the potential of the redox active couple, and also further reinforcement of the electrode surface. In addition, long term electrochemical cycling life requires improved structural stability of the electrode hosts for lithium-ion intercalation chemistry. Current and future efforts emphasize the fundamental understanding of the electrode material properties, in order to develop next generation batteries.

7.2 Microstructural analysis of oxygen defects in $LiMn_2O_4$

Based on the cathode material studies in this work, oxygen defects play a significant role influencing the electrochemical characteristics of the material. The cathode research starts from $LiMn_2O_4$ incorporated with possible oxygen vacancies incorporated into the structure. We have learned from Chapters 2 and 3 that increasing oxygen content level improves the long term cycling stability of the cathode. The issue of oxygen defects translate to manganese oxidation state control. The existing correlation between structural stability and manganese valence was revealed by careful elemental analysis and neutron

diffraction. One of the major challenges is to uncover the detailed structure transformation mechanism of oxygen deficient $LiMn_2O_4$. A spinel to double hexagonal transition model originally was proposed by Tarascon was substantiated by electron microscopy work in this. In Chapter 3, structural failure is shown to corrolate directly to capacity fade and an increase in the internal resistance of the battery. Future efforts should focus on careful structure analysis by (*in-situ*) microscopy and advanced diffraction techniques with electrodes at various SOCs. In addition, the distribution of oxygen defects, particularly at the surface, requires additional study.

7.3 Charge transfer consideration in $LiNi_{0.5}Mn_{1.5}O_4$

Similar to $LiMn_2O_4$, oxygen defects also occur in $LiNi_{0.5}Mn_{1.5}O_4$ as discussed in Chapters 4 and 5. It has been proved the capacity and cylability a better electrochemical property of $LiNi_{0.5}Mn_{1.5}O_{4-\delta}$ improve with oxygen vacancies at 32*e* sites. However, this material's gravimetric energy density is decreased due to higher Mn^{3+} content and its low redox potential in oxygen deficient $LiNi_{0.5}Mn_{1.5}O_{4-\delta}$. It's important to understand the structural properties of $LiNi_{0.5}Mn_{1.5}O_4$ with various levels of oxygen defects for stability optimization. In Chapter 4, for the first time, cut-off potentials, 3.4 - 4.4 and 4.4 -5.0 V regions, related cyclibility is observed with long term-electrochemical stability of the material. It has been noticed that the compounds with oxygen defects show much better capacity retention upon hundreds of cycles with purely high voltage "Ni region" (4.4 - 5.0 V) or "Mn region" (3.4 - 4.4 V). On the contrary, constant capacity decay occurs when the electrochemical potential window covers both regimes (3.4 - 5.0 V). This phenomenon suggests a possible charge transfer mechanism between formal $Ni^{2+/4+}$ and $Mn^{3+/4+}$ redox couples through the Ni-O-Mn bridge. Since the electronic structure of the

bridge is directly related to the oxygen level in the compound, optical and magnetic measurements can elucidate the mechanism of charge transfer in this material.

7.4 Electrode surface structure and improvement of the SEI layer

Other than the bulk materials' properties, the surface plays a significant role influencing the material stability. There have been many reports on the surface vacancies in catalysis, which could provide fruitful suggestions on additional characterization routes.

In Chapter 5, it was demonstrated that adding an artificial titanate SEI layer on the surface of the Ni based high voltage spinel cathode increases the electrochemical stability. For future work, post-cycling analysis of the electrode surfaces by high resolution electron microscopy will provide better understanding of the failure mechanism and inform artificial SEI designs. As shown in Chapter 5, although the titanate layer offered valid protection to the cathode material, the low conductivity , a serious drawback, was obvious as well. It is necessary to explore new coating layers with higher electrical conductivity with respect to the rate capability. Meanwhile, the lithium-ion pathway through the layer is also unclear. Future efforts should also take the ionic diffusion mechanism into considerations. How does the intrinsically formed SEI layer change based on different surface structures? Building correlations between the SEI layer stability and the defects chemistry will assist future spinel cathodes developments.

7.5 Full cell development and future work about the anode

$Li_4Ti_5O_{12}$ has been developed with a super high rate capability as described in Chapter 6. Although the material's morphology has been engineered successfully to support fast rates, the lithium diffusion coefficient and surface electrical conductivity are still poor.

Future modification of the composition is required to improve these characteristics. There have been reports of cation or anion doping intending to improve the conductivity and charge transfer resistance in the battery. However, little research has focused on incorporating both cation and anion dopants to the system in order to improve the charge transfer, which has been well practiced in our lab for photocatalytic dye degradation.

All the electrochemical studies for this thesis were performed in half-cells format for the purpose of better monitoring of the electrochemical characteristics of one material at a time. However, the ultimate goal is to couple novel cathodes and anodes in a full cell system. For this purpose, it's necessary to further study the coupled material chemistry and possible capacity fading mechanism in a full cell format with the developed materials.

7.6 Conclusion

High energy, high power, and long-term stability electrode materials and batteries are in great demand for modern society developments. As a practical research topic, safety and cost are both considered during the most current efforts. Lithium-ion batteries have taken the dominant market share of energy storage devices, which have been around for more than two decades. One of the major challenges remains maintaining structural stability within the active electrodes during the long term operation of the batteries. Our work on spinel-structured cathodes and anodes provides a better understanding the correlations between the structural defects, surface and electrochemical properties. Further fundamental researches on the defects control, charge transfer mechanism, and modifying composition of the electrode materials will continuously provide experimentally demonstrated suggestions for future battery optimization.

APPENDIX A

SUPPORTING DATA FOR CHAPTER 2

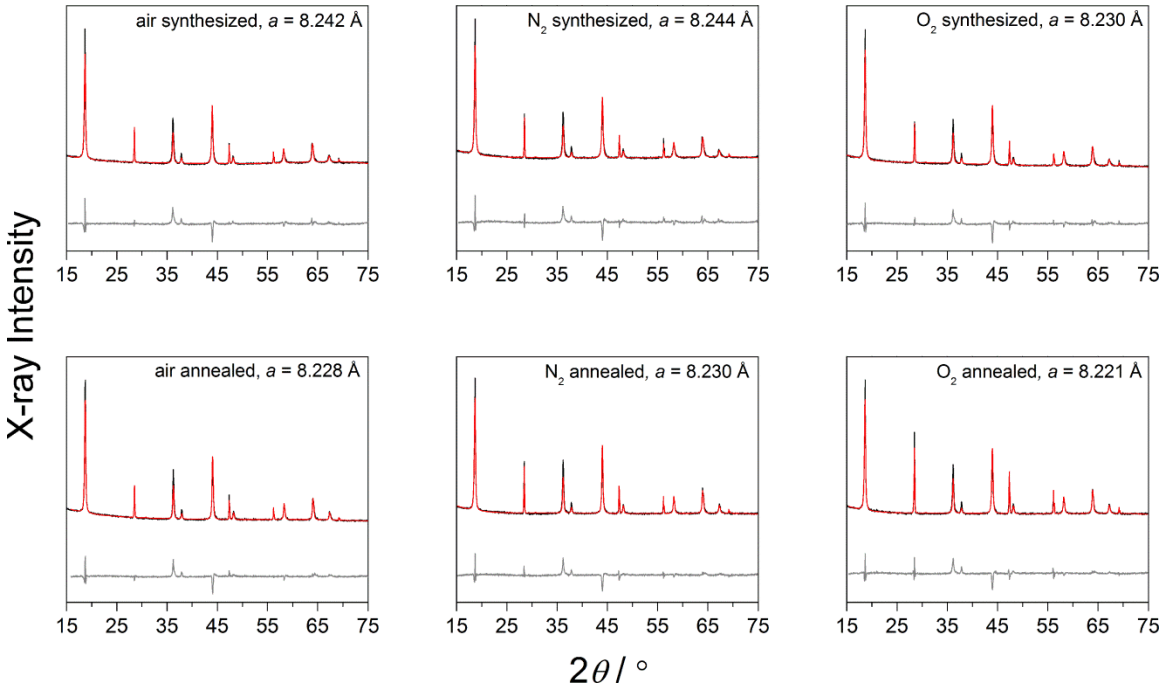

Figure A.1 XRD patterns of hydrothermally synthesized lithium manganospinels.

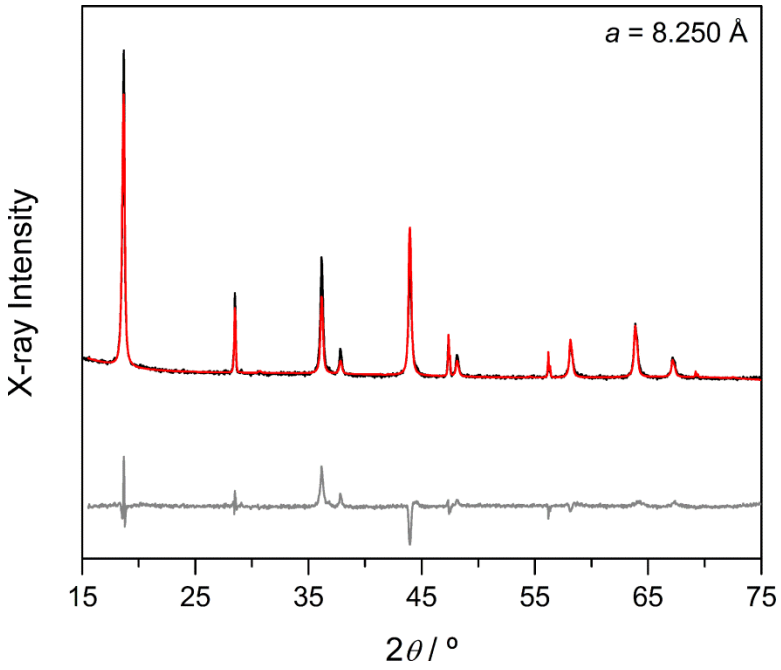

Figure A.2 XRD pattern of lithium manganospinel synthesized hydrothermal in air followed by annealing under N_2.

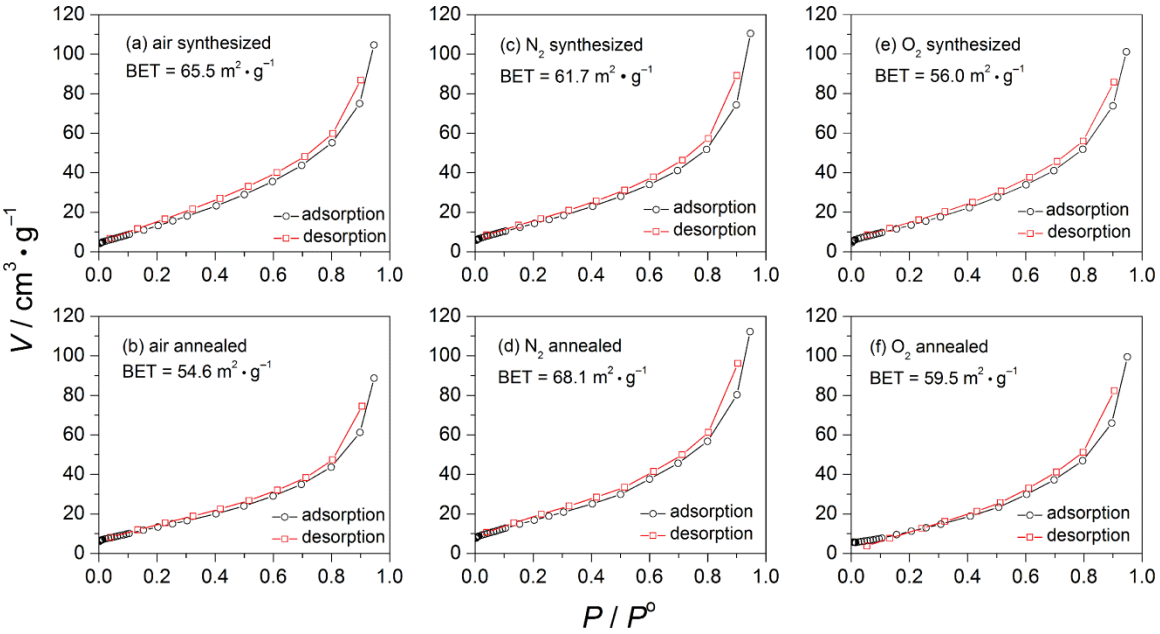

Figure A.3 N_2 sorption isotherms for lithium manganospinels prepared hydrothermally. The top panels represent the synthesized samples and the bottom panels represent the annealed samples. All compounds type II isotherms with surface areas of ~60 m^2/g as determined from the Brunauer-Emmett-Teller (BET) method.

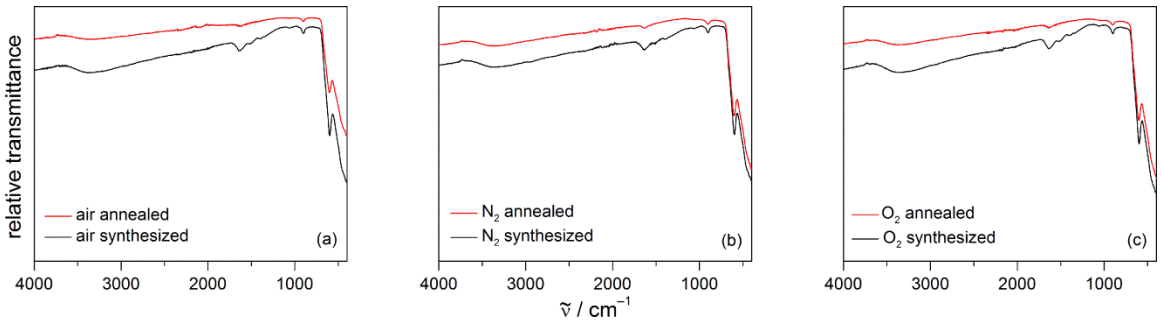

Figure A.4 FTIR spectra of hydrothermally synthesized lithium manganospinels. Black and red traces represent the synthesized and annealed spectra for compounds prepared in a) air; b) N_2; c) O_2, respectively. ν(O–H) and δ(H–O–H) modes at 3300 and 1630 cm^{-1} respectively indicate surface-bound water.

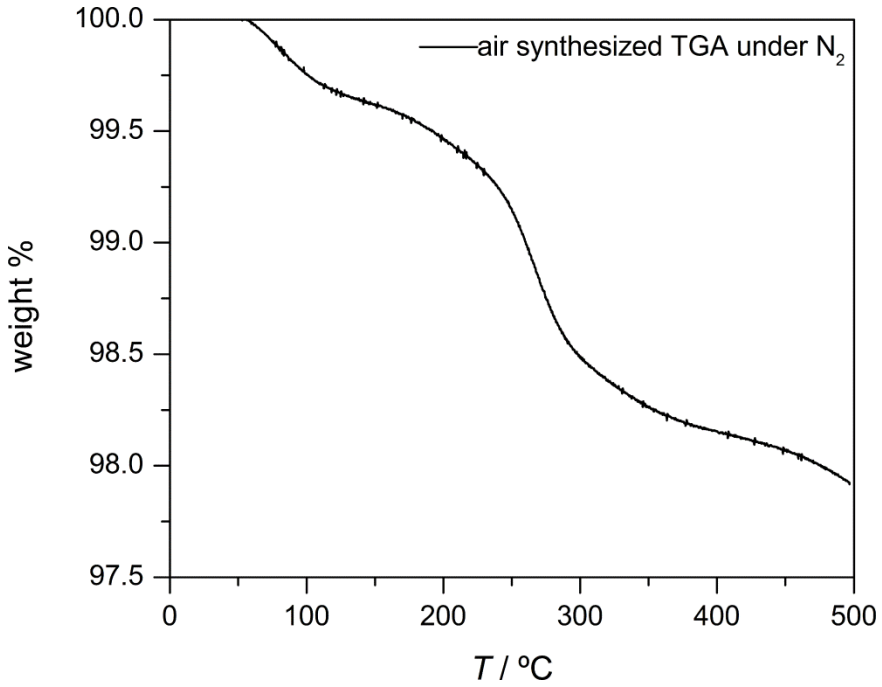

Figure A.5 TGA of the air synthesized sample performed under N_2 purge. No mass gain associated with oxygen uptake between 250–350 ℃ is observed.

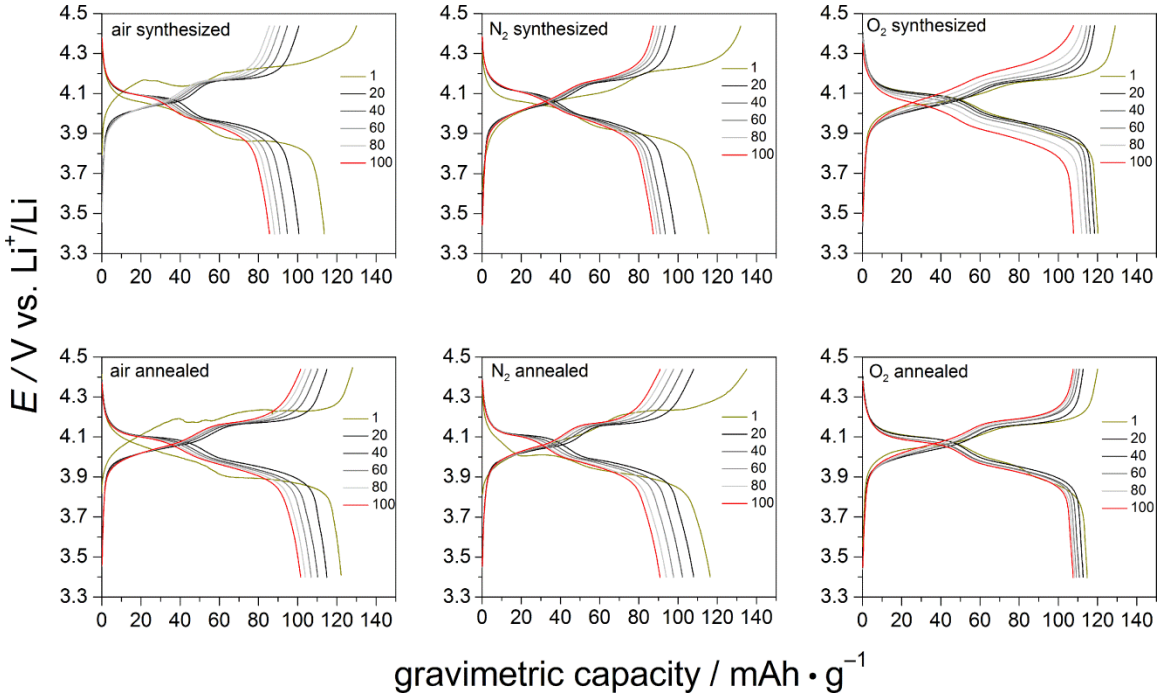

Figure A.6 Individual chronopotentiometry profiles for *C*/3cycling experiments. The first charge-discharge cycle is in gold and the 100th cycle is in red.

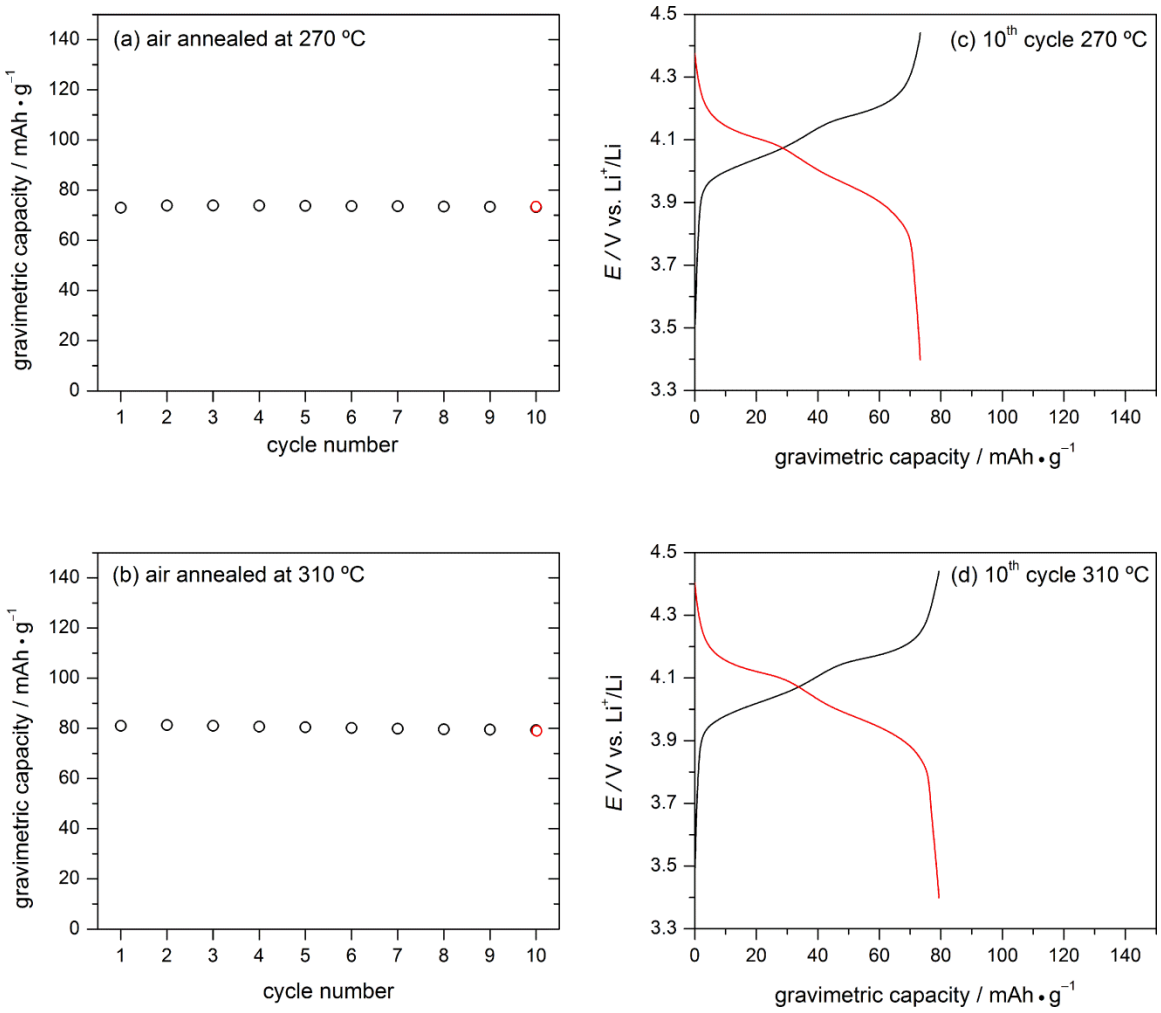

Figure A.7 Cycling behavior of lithium manganospinel synthesized in air and annealed at (a) 270 ℃ and (b) 310 ℃ respectively. Panels (c) and (d) show the charge and discharge curves for the 10th cycles of each.

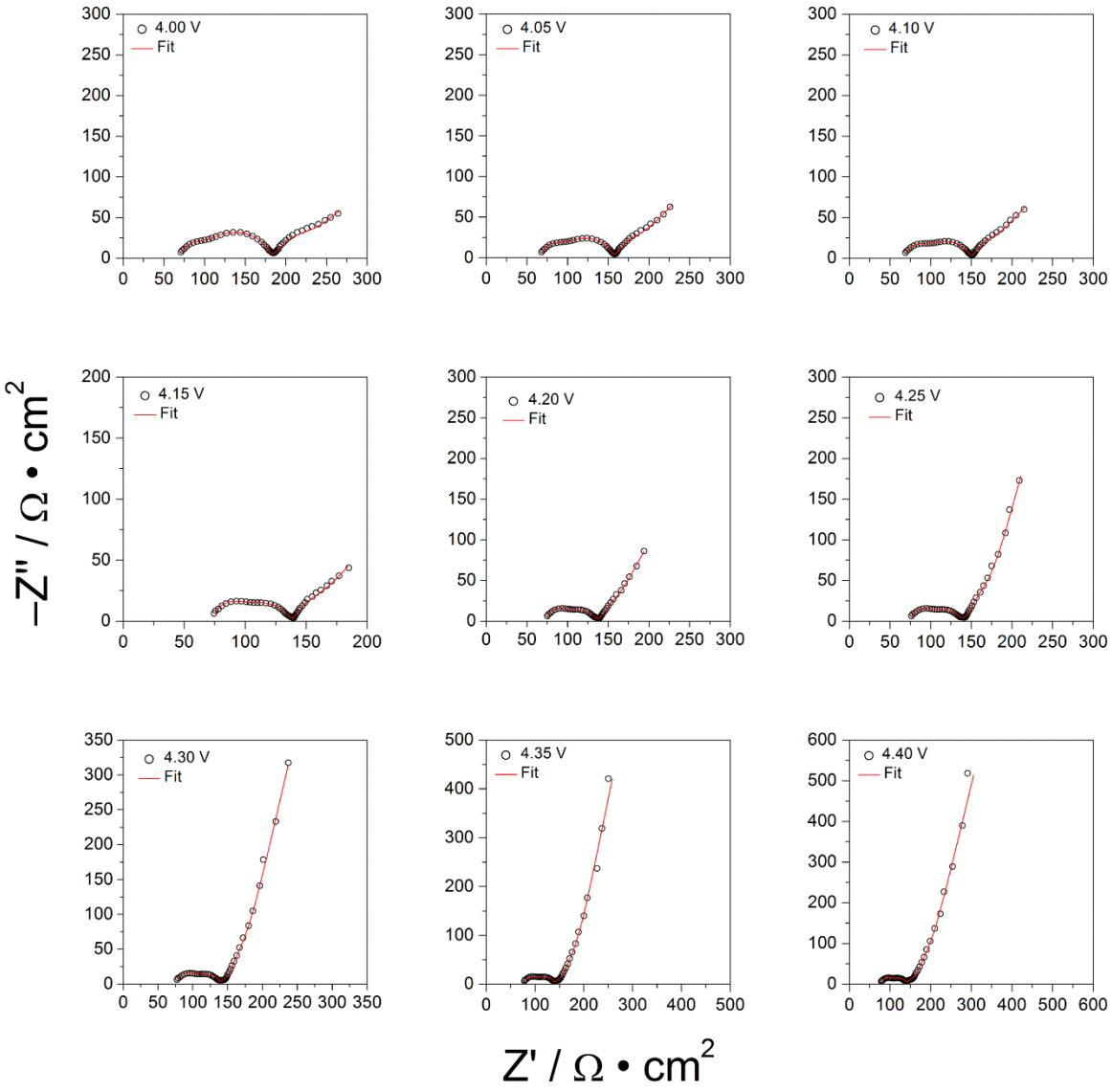

Figure A.8 Nyquist plots for O_2 annealed sample at varying potential.

APPENDIX B

SUPPORTING DATA FOR CHAPTER 3

Table B.1 Refinement parameters for C-LMO. (The experimental XRD pattern is shown as Fig. 1 in the text).

Space Group	$Fd\bar{3}m$
Scale	4.240×10^{-3}
Lattice parameter, *a* (Å)	8.254
Unit Cell Mass (g•mol^{-1})	1435.250
Unit Cell Volume (Å^3)	560.630
Crystallite Size, Lorentzian (nm)	128.1
Crystal Density (g•cm^3), calculated	4.251
Crystal Linear Absorption Coefficient (cm^{-1})	721.343
Wt%-Rietveld	100.000
R_{exp}/ R_{exp}' [(*a*)]	0.27/0.55
R_{wp}/ R_{wp}'	1.92/3.85
R_p/ R_p'	0.92/1.94
R_{Bragg}	1.044
GoF	6.97
DW_d	0.19

(*a*)-Primed parameters are background corrected.

Table B.2 Atomic coordinates and isotropic thermal parameters for C-LMO

Atom	Wyckoff Site	*x*	*y*	*z*	SOF	B_{eq}
Li	8*a*	0	0	0	1	-0.6825
Mn	16*d*	0.6250	0.6250	0.6250	1	2.023
O	32*e*	0.38928	0.38924	0.38928	1	2.138

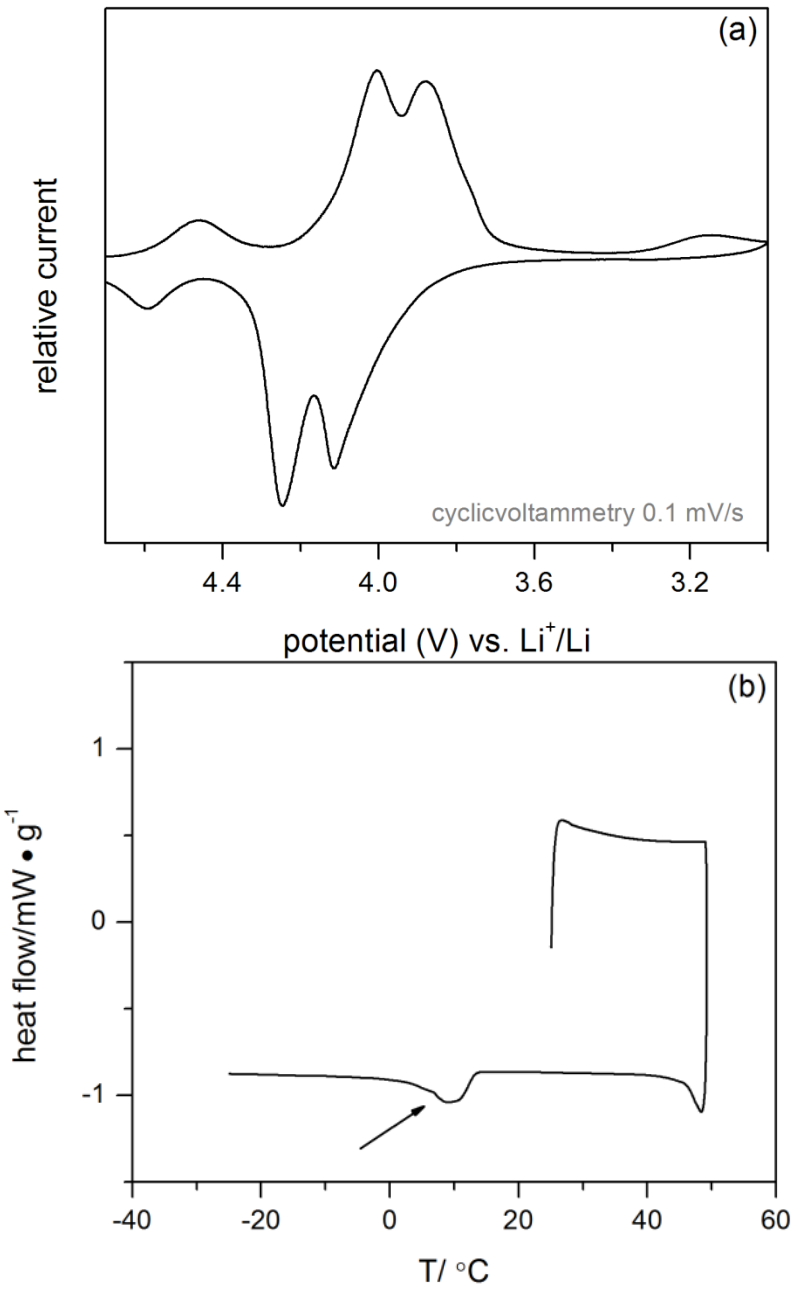

Figure B.1 Cyclic voltammetry (CV) and differential scanning calorimetry (DSC) of C-LMO

Table B.3 Elemental analysis of compounds presented in this study

Compound	ppm Li	ppm Mn	Z_{Mn}	Sample mass per mg	Composition
C-LMO	0.409(3.87%)	6.451(61.42%)	3.38	10.5	$LiMn_2O_{3.88}$
S-LMO	0.514(3.82%)	8.12(60.60%)	3.53	13.4	$LiMn_2O_{4.03}$
D-LMO	0.485(3.88%)	7.686(61.47%)	3.37	12.5	$LiMn_2O_{3.87}$

Table B.4 Atomic parameters, occupancies and equivalent displacement parameters ($Å^2$) of C-LMO

Atom	Wyckoff site	x	y	z	Occ.	Uiso
Li	8*a*	0.125	0.125	0.125	1	0.0117
Mn	16*d*	0.5	0.5	0.5	1	0.01144
O	32*e*	0.2634(7)	0.2634(7)	0.2634(7)	0.97(1)	0.01647

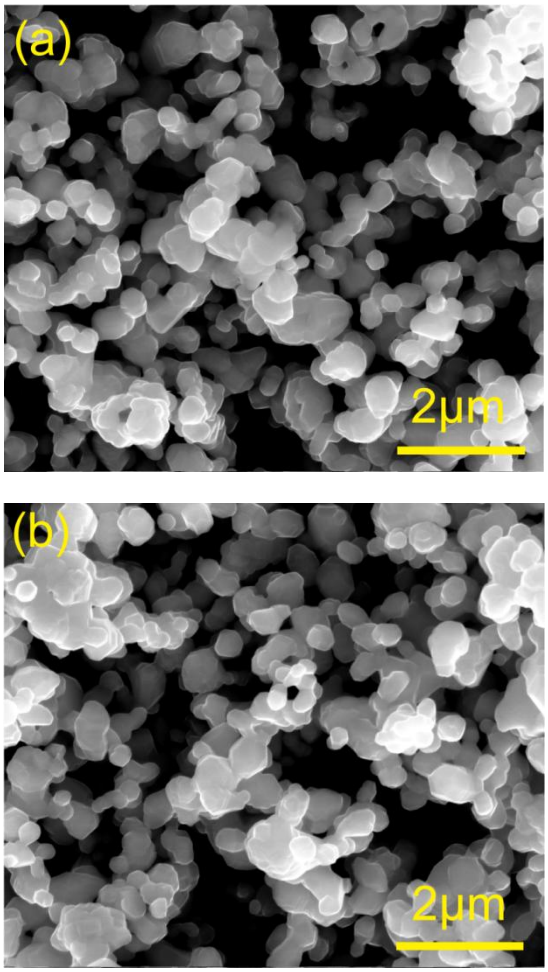

Figure B.2 SEM image of S-LMO (a) and D-LMO (b)

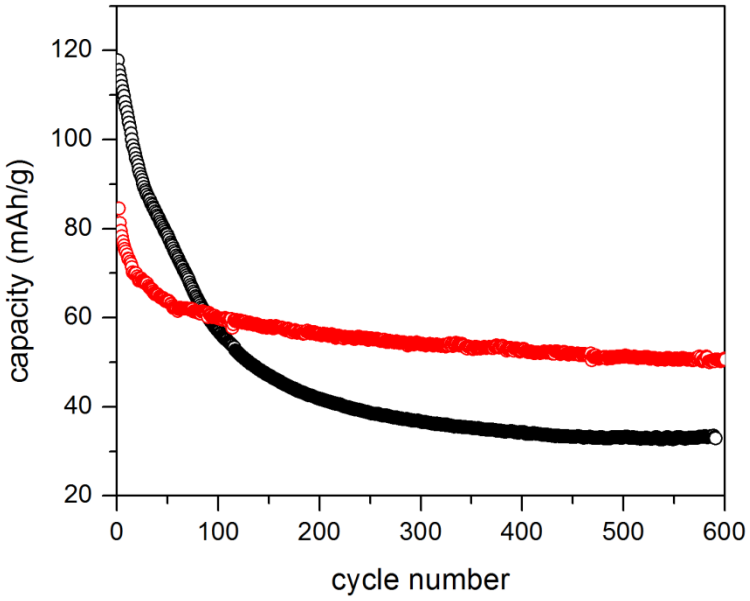

Figure B.3 Capacity retention comparison of C-LMO and D-LMO at 0.2 C between 3.40 ~ 4.45 V

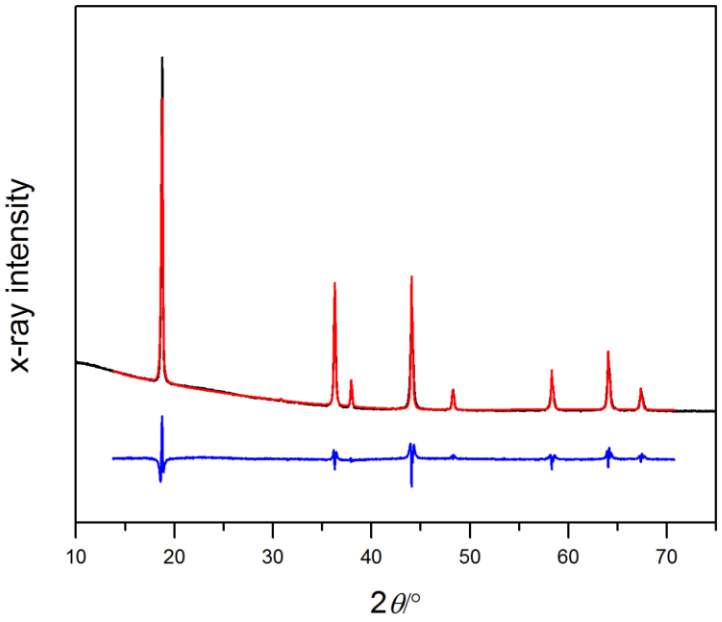

Figure B.4 XRD and refinement results of S-LMO

Table B.5 Refinement parameters for S-LMO

Space Group	$Fd\,\bar{3}m$
Scale	3.786×10^{-3}
Lattice parameter, *a* (Å)	8.233
Unit Cell Mass (g•mol^{-1})	1435.250
Unit Cell Volume (Å^3)	558.108
Crystallite Size, Lorentzian (nm)	102.4
Crystal Density (g•cm^3), calculated	4.270
Crystal Linear Absorption Coefficient (cm^{-1})	724.603
Wt%-Rietveld	100
R_{exp}/ R_{exp}' $^{(a)}$	1.13/1.04
R_{wp}/ R_{wp}'	1.05/6.34
R_p/ R_p'	1.67/2.40
R_{Bragg}	0.874
GoF	1.92
DW_d	0.73

(*a*)-Primed parameters are background corrected.

Table B.6 Atomic coordinates and isotropic thermal parameters for S-LMO

Atom	Wyckoff Site	*x*	*y*	*z*	SOF	B_{eq}
Li	8*a*	0	0	0	1	0.7086
Mn	16*d*	0.6250	0.6250	0.6250	1	1.667
O	32*e*	0.38876	0.38876	0.38876	1	1.098

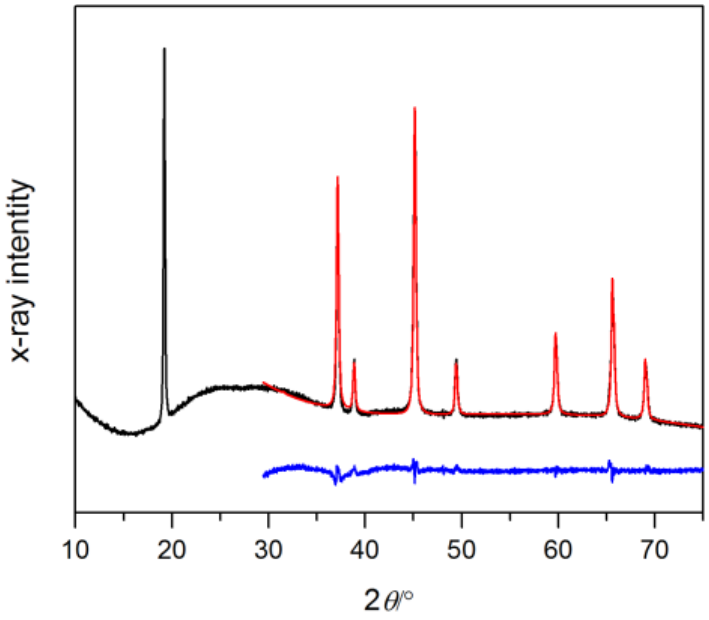

Figure B.5 XRD and refinement results of S-LMO at SOC of 4.45 V

Table B.7 Refinement parameters for S-LMO at SOC of 4.45 V

Space Group	$Fd\,\bar{3}m$
Scale	3.973×10^{-3}
Lattice parameter, *a* (Å)	8.072
Unit Cell Mass (g•mol^{-1})	1435.250
Unit Cell Volume (Å^3)	526.013
Crystallite Size, Lorentzian (nm)	51.9
Crystal Density (g•cm^3), calculated	4.531
Crystal Linear Absorption Coefficient (cm^{-1})	768.816
Wt%-Rietveld	100
R_{exp}/ R_{exp}' $^{(a)}$	0.36/0.85
R_{wp}/ R_{wp}'	0.78/1.82
R_p/ R_p'	0.55/1.34
R_{Bragg}	6.698
GoF	2.14
DW_d	0.49

(*a*)-Primed parameters are background corrected.

Table B.8 Atomic coordinates and isotropic thermal parameters for S-LMO at SOC of 4.45 V

Atom	Wyckoff Site	*x*	*y*	*z*	SOF	B_{eq}
Li	8*a*	0	0	0	1	1.976
Mn	16*d*	0.6250	0.6250	0.6250	1	1.712
O	32*e*	0.38760	0.38760	0.38760	1	0.1722

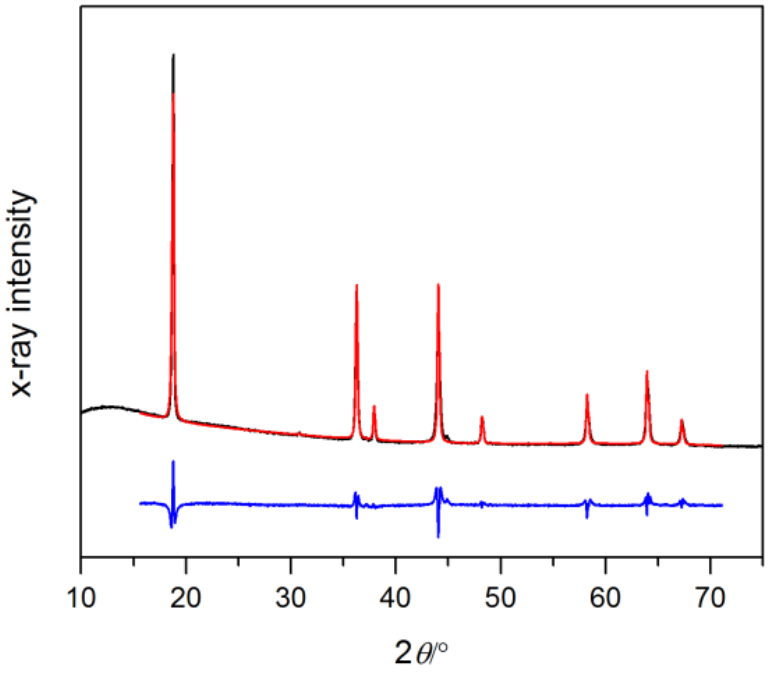

Figure B.6 XRD and refinement results of D-LMO

Table B.9 Refinement parameters for D-LMO

Space Group	$Fd\,\bar{3}m$
Scale	7.119×10^{-3}
Lattice parameter, *a* (Å)	8.253
Unit Cell Mass (g•mol^{-1})	1435.250
Unit Cell Volume (Å^3)	562.300
Crystallite Size, Lorentzian (nm)	85.5
Crystal Density (g•cm^3), calculated	4.238
Crystal Linear Absorption Coefficient (cm^{-1})	719.201
Wt%-Rietveld	100.000
R_{exp}/ R_{exp}' $^{(a)}$	0.28/0.60
R_{wp}/ R_{wp}'	1.62/3.44
R_p/ R_p'	0.84/1.92
R_{Bragg}	0.814
GoF	5.74
DW_d	0.14

(*a*)-Primed parameters are background corrected.

Table B.10 Atomic coordinates and isotropic thermal parameters for D-LMO

Atom	Wyckoff Site	*x*	*y*	*z*	SOF	B_{eq}
Li	8*a*	0	0	0	1	-0.1554
Mn	16*d*	0.6250	0.6250	0.6250	1	3.432
O	32*e*	0.39103	0.37998	0.39103	1	3.498

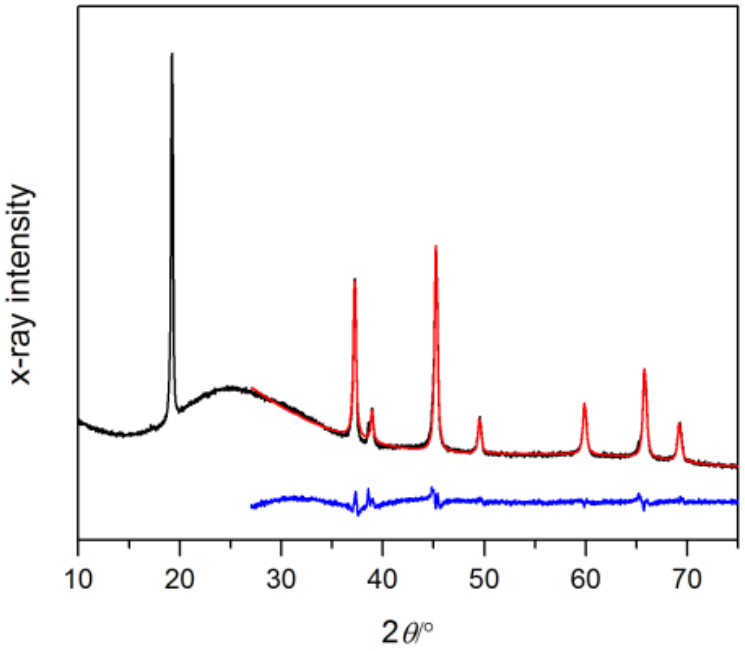

Figure B.7 XRD and refinement results of D-LMO at SOC of 4.45 V

Table B.11 Refinement parameters for D-LMO at SOC of 4.45 V

Space Group	$Fd\,\bar{3}m$
Scale	2.491×10^{-3}
Lattice parameter, *a* (Å)	8.050
Unit Cell Mass (g•mol^{-1})	1435.250
Unit Cell Volume (Å^3)	521.660
Crystallite Size, Lorentzian (nm)	36.0
Crystal Density (g•cm^3), calculated	4.569
Crystal Linear Absorption Coefficient (cm^{-1})	775.231
Wt%-Rietveld	100.000
R_{exp}/ R_{exp}' $^{(a)}$	0.36/0.83
R_{wp}/ R_{wp}'	0.92/2.12
R_p/ R_p'	0.65/1.54
R_{Bragg}	2.452
GoF	2.55
DW_d	0.33

(*a*)-Primed parameters are background corrected.

Table B.12 Atomic coordinates and isotropic thermal parameters for D-LMO at SOC of 4.45 V

Atom	Wyckoff Site	*x*	*y*	*z*	SOF	B_{eq}
Li	8*a*	0	0	0	1	2.020
Mn	16*d*	0.6250	0.6250	0.6250	1	0.6991
O	32*e*	0.38695	0.38695	0.38695	1	-0.9988

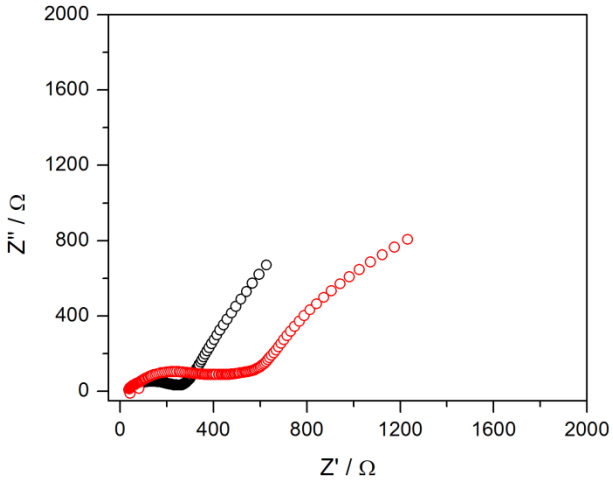

Figure B.8 EIS result of S-LMO (black) and D-LMO (red) at open circuit potential after 100 cycles at 1*C*.

APPENDIX C
SUPPORTING DATA FOR CHAPTER 4

Table C.1 Refinement parameters for LNMO synthesized in air

Space Group	$Fd\,\bar{3}m$
Scale	5.460×10^{-4}
Lattice parameter, *a* (Å)	8.183
Unit Cell Mass (g•mol^{-1})	1450.260
Unit Cell Volume (Å^3)	548.141
Crystallite Size, Lorentzian (nm)	120.8
Crystal Density (g•cm^3), calculated	4.393
Crystal Linear Absorption Coefficient (cm^{-1})	592.397
Wt%-Rietveld	86.398
R_{exp}/ R_{exp}' $^{(a)}$	0.93/1.69
R_{wp}/ R_{wp}'	1.85/3.34
R_p/ R_p'	1.23/2.40
R_{Bragg}	3.607
GoF	1.98
DW_d	0.76

(*a*)-Primed parameters are background corrected.

Table C.2 Atomic coordinates and isotropic thermal parameters for LNMO synthesized in air.

Atom	Wyckoff Site	*x*	*y*	*z*	SOF	B_{eq}
Li	8*a*	0	0	0	1	2.924
Mn	16*d*	0.6250	0.6250	0.6250	0.75	1.758
Ni	16*d*	0.6250	0.6250	0.6250	0.25	0.9867
O	32*e*	0.38723	0.38723	0.38723	1	-0.06318

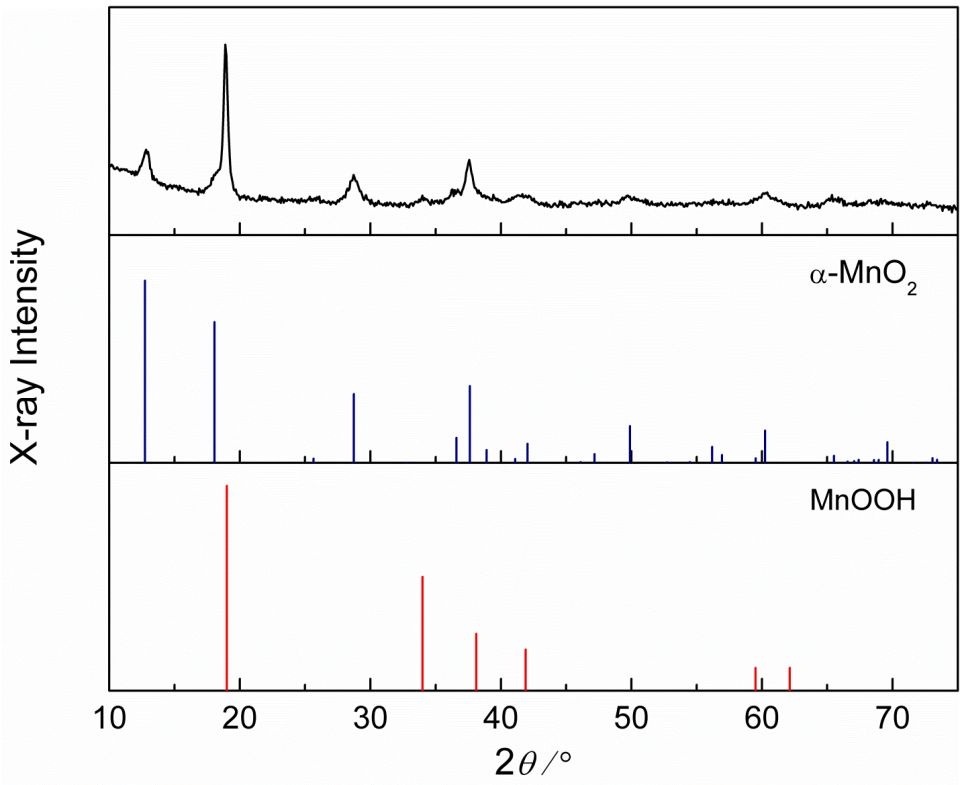

Figure C.1 Indexed XRD pattern of the NMO intermediate ($H_{0.4}K_{0.08}Ni_{0.5}Mn_{1.5}O_{3.305}$)

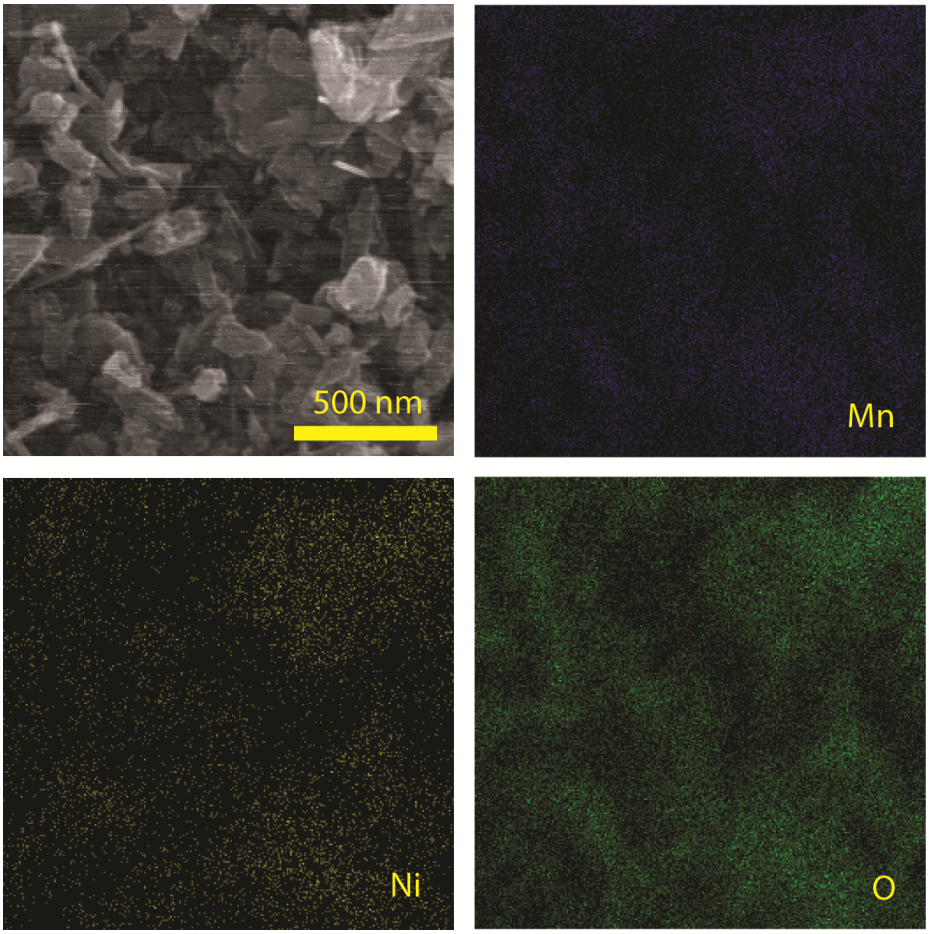

Figure C.2 EDX elemental map of the NMO intermediate

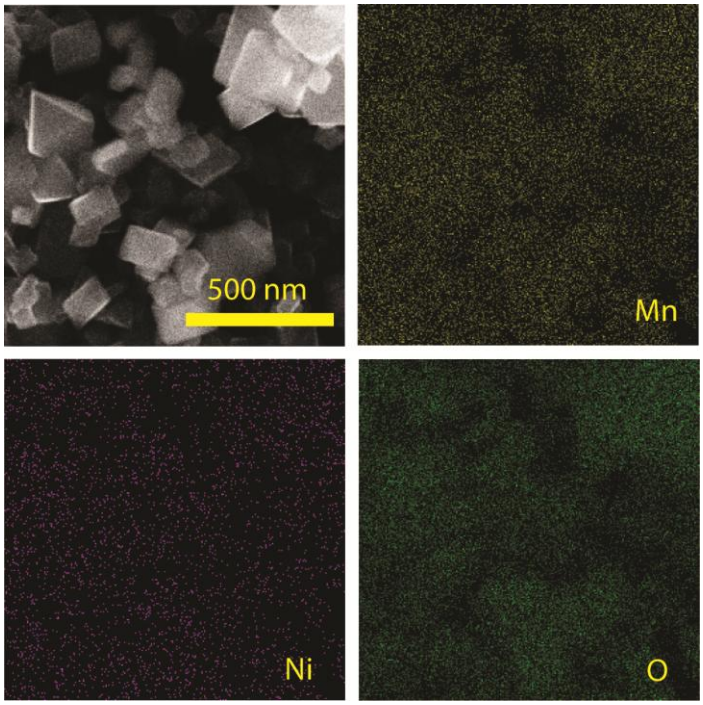

Figure C.3 EDX elemental map of the LNMO product

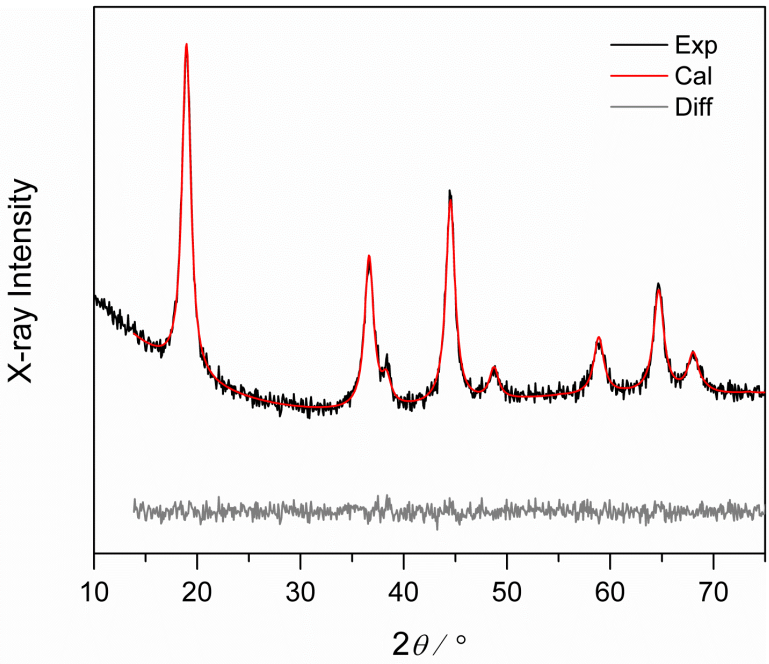

Figure C.4 XRD pattern of the one-pot synthesis LNMO product.

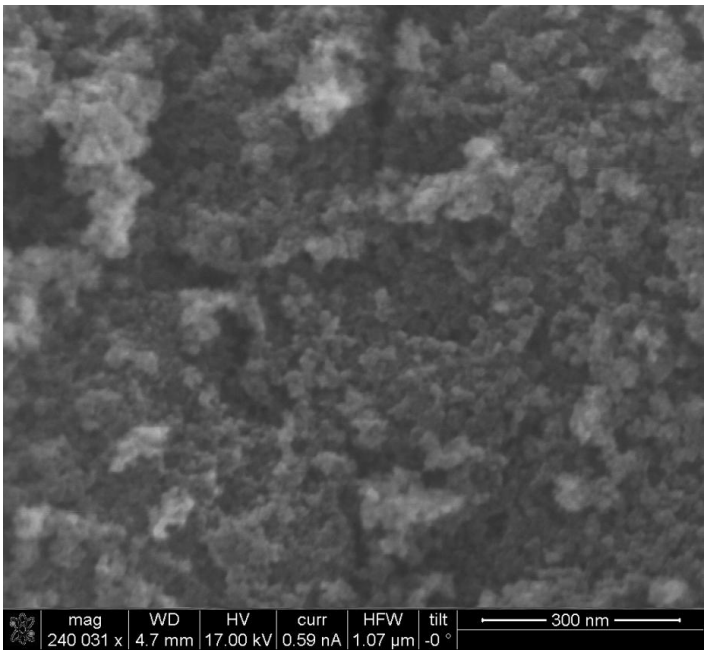

Figure C.5 SEM image of the one-pot synthesis LNMO product.

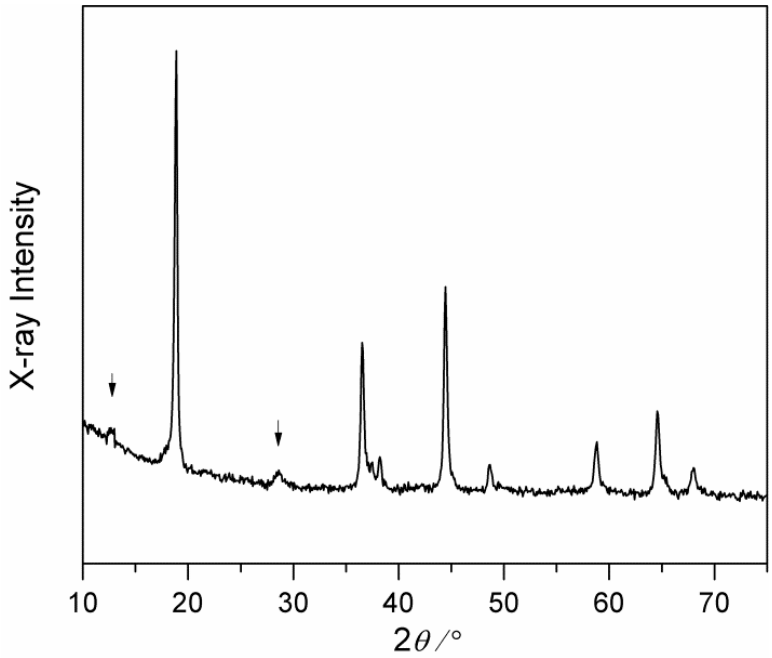

Figure C.6 XRD pattern of the products of the LNMO reaction performed under O_2. The arrows point out reflections for the α-MnO_2 impurity phase. Since the reaction product is not phase-pure, no Rietveld refinement was carried out.

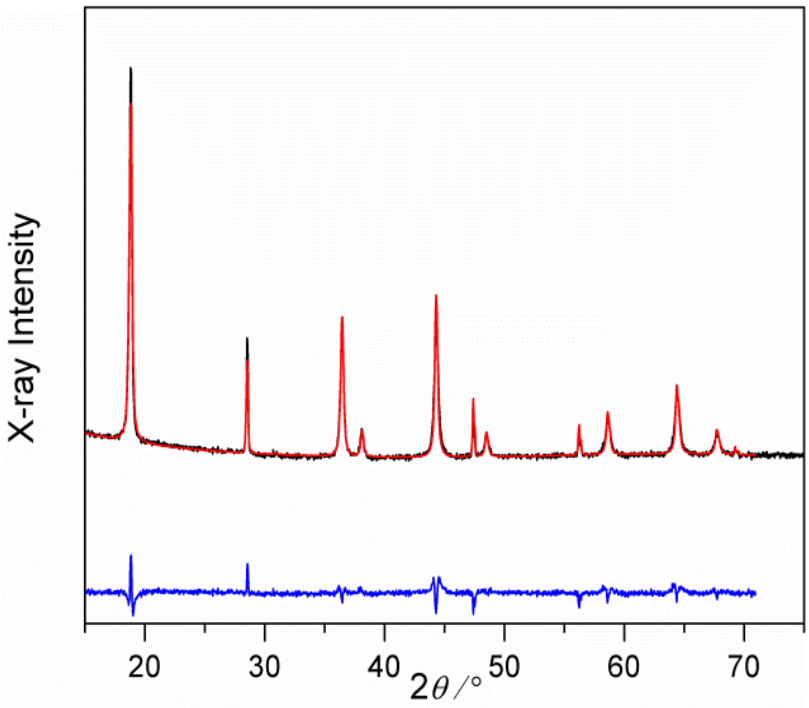

Figure C.7 XRD data (black), calculated Rietveld refinement (red), and difference pattern (blue) for LNMO with second step prepared in N_2.

Table S3. Refinement parameters for LNMO synthesized under N_2

Space Group	$Fd\,\bar{3}m$
Scale	5.328×10^{-4}
Lattice parameter, *a* (Å)	8.196
Unit Cell Mass ($g \bullet mol^{-1}$)	1450.260
Unit Cell Volume ($Å^3$)	549.649
Crystallite Size, Lorentzian (nm)	111.9
Crystal Density ($g \bullet cm^3$), calculated	4.381
Crystal Linear Absorption Coefficient (cm^{-1})	590.771
Wt%-Rietveld	86.675
R_{exp}/ R_{exp}' [(a)]	0.91/3.04
R_{wp}/ R_{wp}'	1.94/6.49
R_p/ R_p'	1.26/4.70
R_{Bragg}	0.413
GoF	2.14
DW_d	0.69

(*a*)-Primed parameters are background corrected.

Table C.3 Refinement parameters for LNMO synthesized under N_2

Space Group	$Fd\,\bar{3}m$
Scale	5.328×10^{-4}
Lattice parameter, *a* (Å)	8.196
Unit Cell Mass (g•mol^{-1})	1450.260
Unit Cell Volume (Å^3)	549.649
Crystallite Size, Lorentzian (nm)	111.9
Crystal Density (g•cm^3), calculated	4.381
Crystal Linear Absorption Coefficient (cm^{-1})	590.771
Wt%-Rietveld	86.675
R_{exp}/ R_{exp}' [(*a*)]	0.91/3.04
R_{wp}/ R_{wp}'	1.94/6.49
R_p/ R_p'	1.26/4.70
R_{Bragg}	0.413
GoF	2.14
DW_d	0.69

(*a*)-Primed parameters are background corrected.

Table C.4 Atomic coordinates and isotropic thermal parameters for LNMO synthesized under N_2

Atom	Wyckoff Site	*x*	*y*	*z*	SOF	B_{eq}
Li	8*a*	0	0	0	1	2.916
Mn	16*d*	0.6250	0.6250	0.6250	0.75	1.962
Ni	16*d*	0.6250	0.6250	0.6250	0.25	0.9938
O	32*e*	0. 38749	0. 38749	0. 38749	1	-5.697×10^{-5}

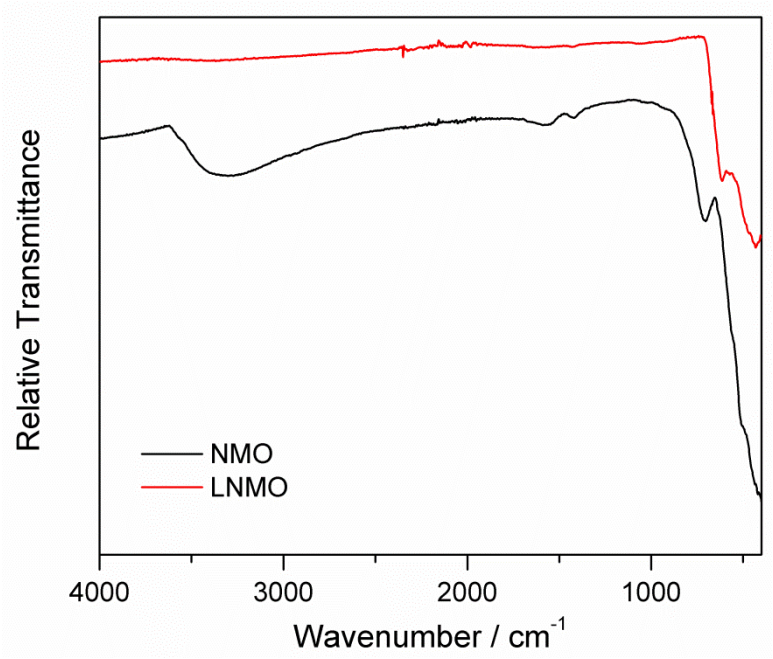

Figure C.8 FTIR spectra of the NMO intermediate and LNMO product.

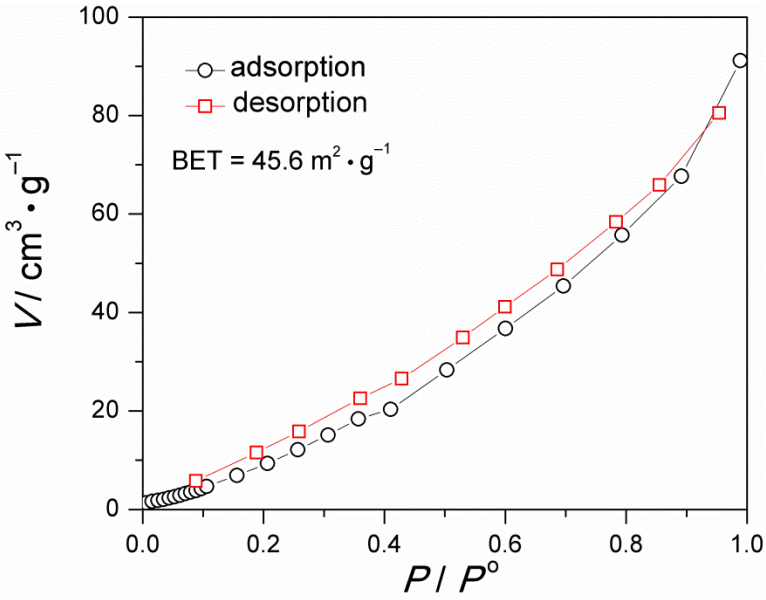

Figure C.9 N_2 sorption isotherm for the final LNMO product synthesized in the two-step hydrothermal method in air.

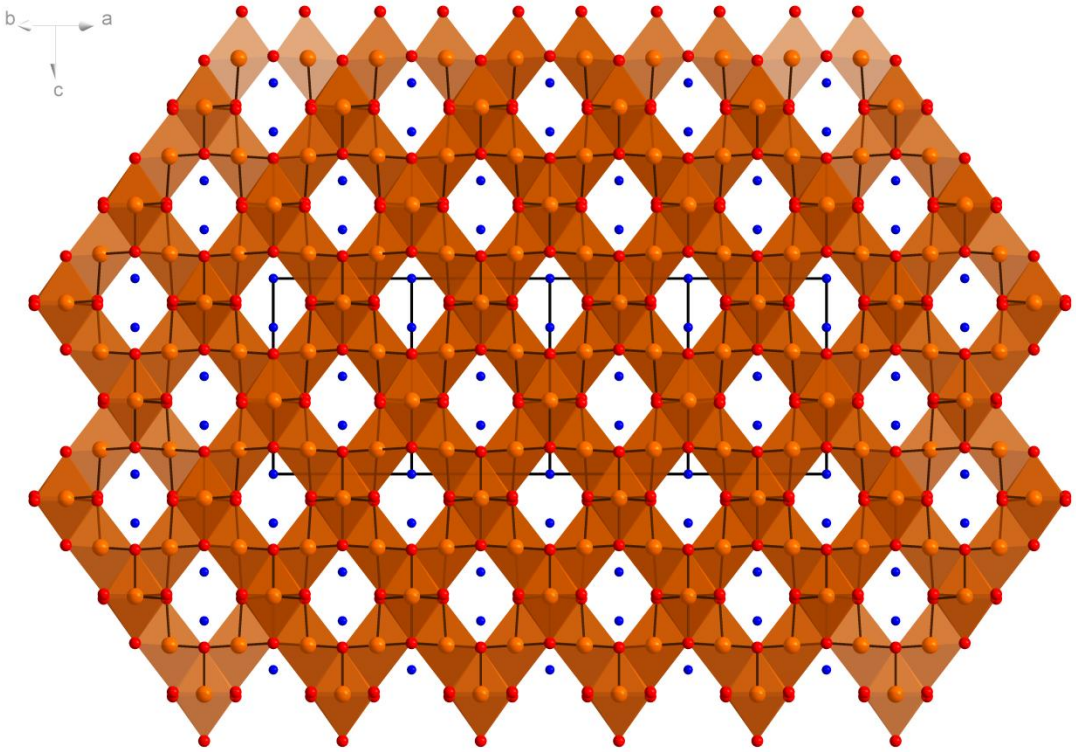

Figure C.10 View of the spinel crystal structure along the [1 1 0] direction. Blue, orange, and red spheres represent lithium, manganese/nickel, and oxygen atoms respectively.

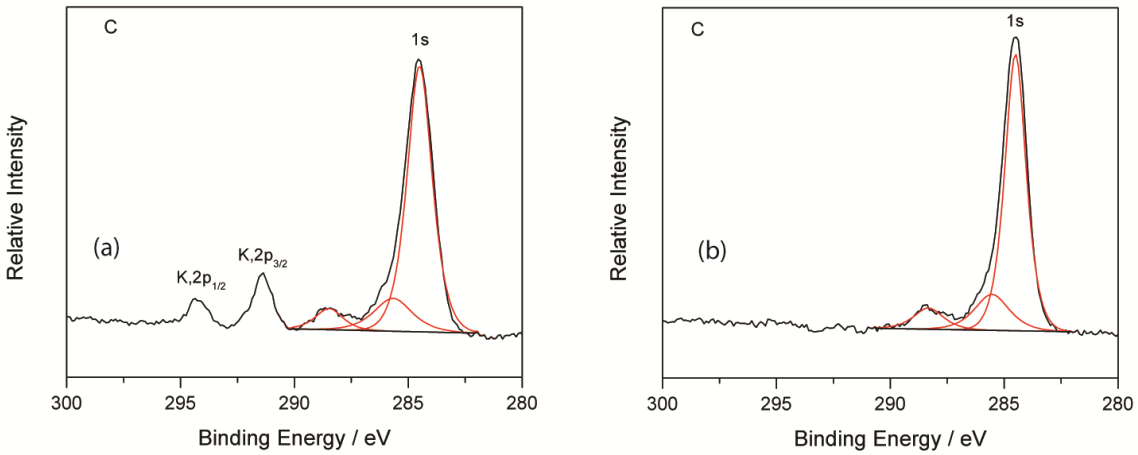

Figure C.11 C(1s) XP spectra for NMO (a) and LNMO (b). NMO also shows K(2p) features.

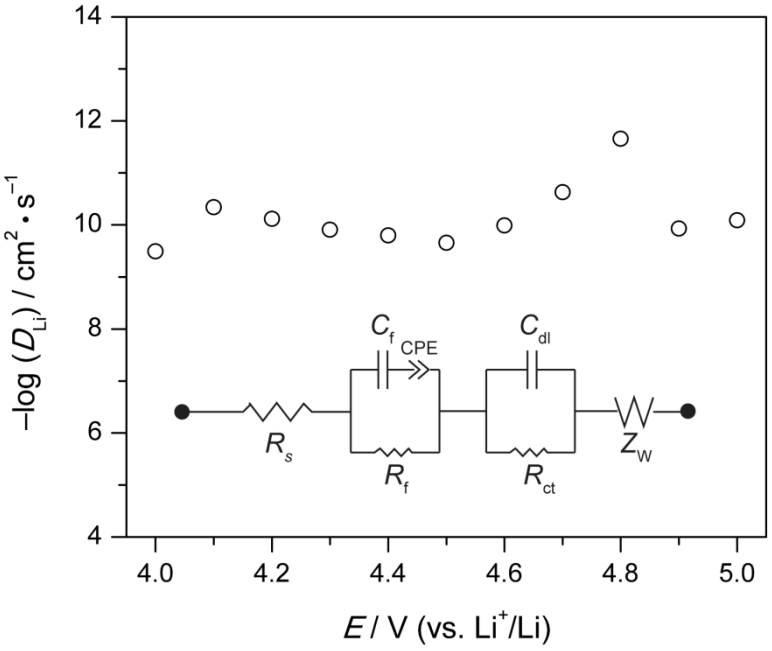

Figure C.12 Voltage-dependence of the Li^+ diffusion constant (D_{Li}) determined from electrochemical impedance spectroscopy. The data are fit to the equivalent circuit illustrated in the inset.

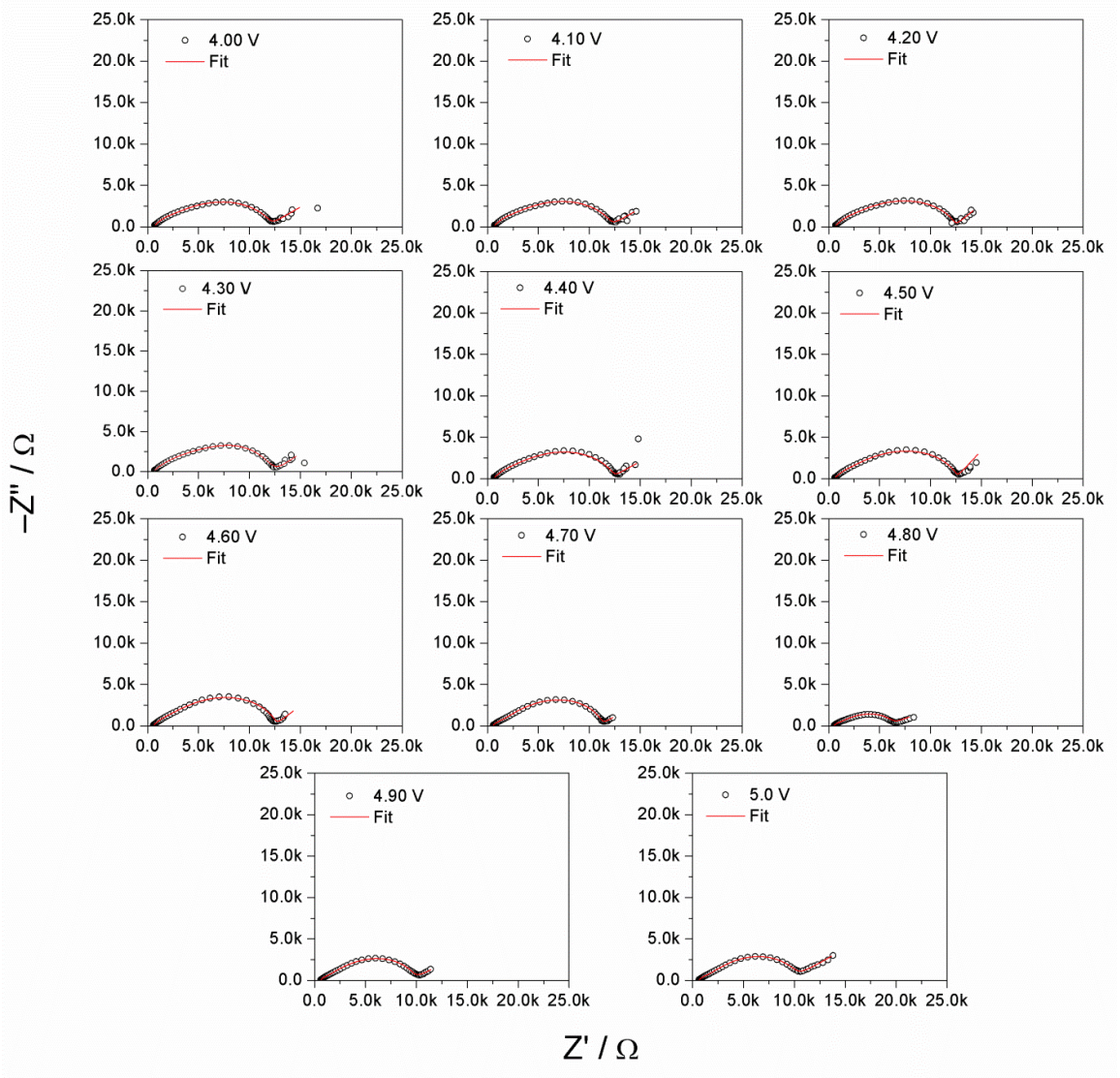

Figure C.13 Nyquist plots for determining D_{Li} of LNMO as a function of potential.

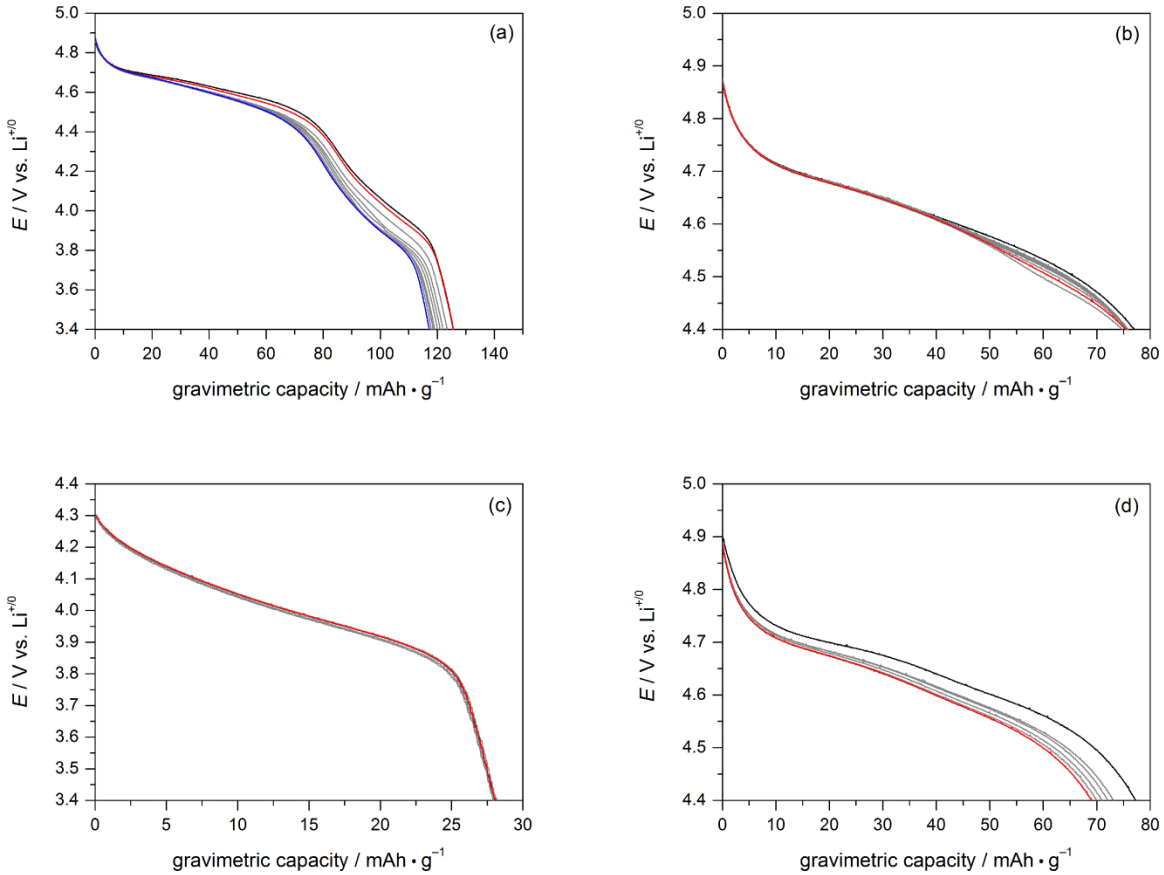

Figure C.14 Voltage profiles for the 1000 cycle LNMO cell. a) Cycles 1 – 10 performed between the voltage limits 3.4 – 5.0 V. Black, red, and blue represent cycles one, two, and ten respectively. Others are shown in gray. b) Cycles 11 – 121 performed between the voltage limits 4.4 – 5.0 V. Black and red represent cycles 11 and 121 respectively. Every 10th cycle in between is shown in gray. c) Cycles 122 – 622 performed between the voltage limits 3.4 – 4.4 V. Black and red present cycles 122 and 622 respectively with every 100th cycle in between shown in gray. d) Cycles 623 – 1123 performed between the voltage limits 4.4 – 5.0 V. Black and red represent cycles 623 and 1123 respectively with every 100th cycle in between shown in gray.

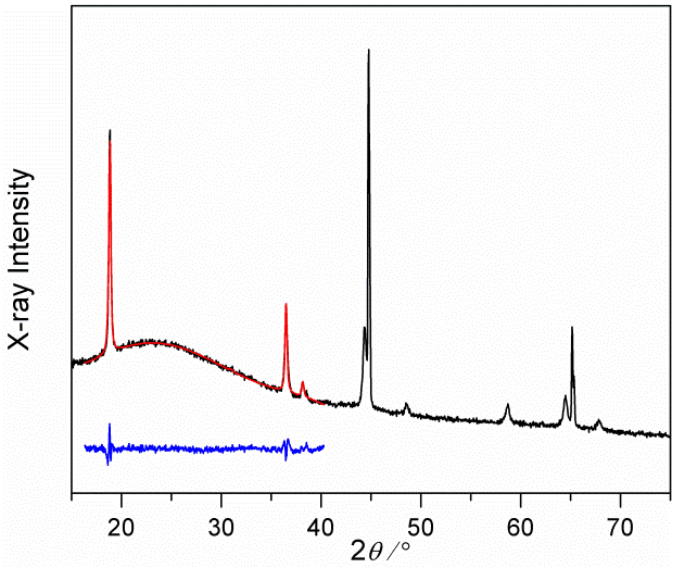

Figure C.15 XRD data (black), calculated Rietveld refinement (red), and difference pattern (blue) for a freshly prepared LNMO electrode.

Table C.5 Refinement parameters for a freshly prepared LNMO electrode.

Space Group	$Fd\,\bar{3}m$
Scale	4.603×10^{-5}
Lattice parameter, *a* (Å)	8.185
Unit Cell Mass (g•mol^{-1})	1450.260
Unit Cell Volume (Å^3)	548.485
Crystallite Size, Lorentzian (nm)	68.8
Crystal Density (g•cm^3), calculated	4.391
Crystal Linear Absorption Coefficient (cm^{-1})	592.025
Wt%-Rietveld	100
R_{exp}/ R_{exp}' $^{(a)}$	1.28/2.50
R_{wp}/ R_{wp}'	1.93/3.78
R_p/ R_p'	1.39/2.79
R_{Bragg}	0.166
GoF	1.51
DW_d	1.01

(*a*)-Primed parameters are background corrected.

Table C.6 Atomic coordinates and isotropic thermal parameters for a freshly prepared LNMO electrode.

Atom	Wyckoff Site	*x*	*y*	*z*	SOF	B_{eq}
Li	8*a*	0	0	0	1	-3.857
Mn	16*d*	0.6250	0.6250	0.6250	0.75	16.04
Ni	16*d*	0.6250	0.6250	0.6250	0.25	6.058
O	32*e*	0. 37415	0. 37415	0. 37415	1	13.79

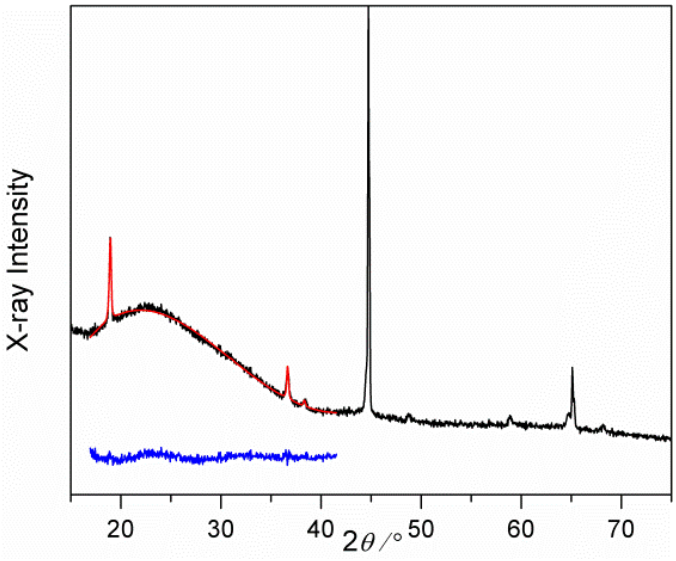

Figure C.16 XRD data (black), calculated Rietveld refinement (red), and difference pattern (blue) for an LNMO electrode after 60 cycles between 3.4 – 5.0 V.

Table C.7 Refinement parameters an LNMO electrode after 60 cycles between 3.4 – 5.0 V.

Space Group	$Fd\,\bar{3}m$
Scale	1.187×10^{-4}
Lattice parameter, *a* (Å)	8.157
Unit Cell Mass (g•mol^{-1})	1450.260
Unit Cell Volume (Å^3)	542.886
Crystallite Size, Lorentzian (nm)	102.6
Crystal Density (g•cm^3), calculated	4.436
Crystal Linear Absorption Coefficient (cm^{-1})	598.131
Wt%-Rietveld	100
R_{exp}/ R_{exp}' $^{(a)}$	1.60/3.15
R_{wp}/ R_{wp}'	2.02/3.97
R_p/ R_p'	1.62/3.22
R_{Bragg}	0.058
GoF	1.26
DW_d	1.31

(*a*)-Primed parameters are background corrected.

Table C.8 Atomic coordinates and isotropic thermal parameters for an LNMO electrode after 60 cycles between 3.4 – 5.0 V.

Atom	Wyckoff Site	*x*	*y*	*z*	SOF	B_{eq}
Li	8*a*	0	0	0	1	7.31
Mn	16*d*	0.6250	0.6250	0.6250	0.75	18.71
Ni	16*d*	0.6250	0.6250	0.6250	0.25	17.79
O	32*e*	0.36358	0. 36358	0. 36358	1	20

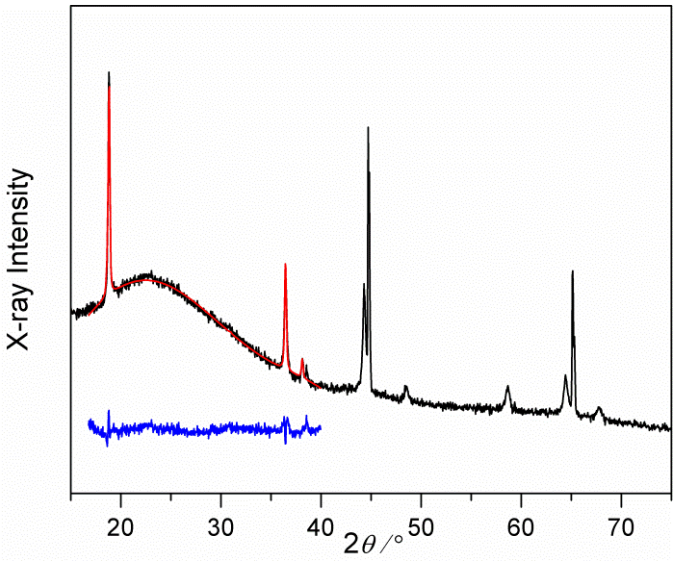

Figure C.17 XRD data (black), calculated Rietveld refinement (red), and difference pattern (blue) for an LNMO electrode after 10 cycles 3.4 – 5.0 V and 50 cycles 3.4 - 4.4 V charge/discharge.

Table C.9 Refinement parameters for LNMO after 10 cycles 3.4 – 5.0 V and 50 cycles 3.4 - 4.4 V charge/discharge.

Space Group	$Fd\,\bar{3}m$
Scale	2.687×10^{-4}
Lattice parameter, *a* (Å)	8.194
Unit Cell Mass (g•mol^{-1})	1450.260
Unit Cell Volume (Å^3)	550.261
Crystallite Size, Lorentzian (nm)	110.0
Crystal Density (g•cm^3), calculated	4.376
Crystal Linear Absorption Coefficient (cm^{-1})	590.114
Wt%-Rietveld	100
R_{exp}/ R_{exp}' [(*a*)]	1.45/2.85
R_{wp}/ R_{wp}'	2.01/3.95
R_p/ R_p'	1.55/3.10
R_{Bragg}	1.459
GoF	1.38
DW_d	1.21

(*a*)-Primed parameters are background corrected.

Table C.10 Atomic coordinates and isotropic thermal parameters for LNMO after 10 cycles 3.4 – 5.0 V and 50 cycles 3.4 - 4.4 V charge/discharge.

Atom	Wyckoff Site	*x*	*y*	*z*	SOF	B_{eq}
Li	8*a*	0	0	0	1	13.38
Mn	16*d*	0.6250	0.6250	0.6250	0.75	19.53
Ni	16*d*	0.6250	0.6250	0.6250	0.25	1
O	32*e*	0. 36880	0. 36880	0. 36880	1	-7.117

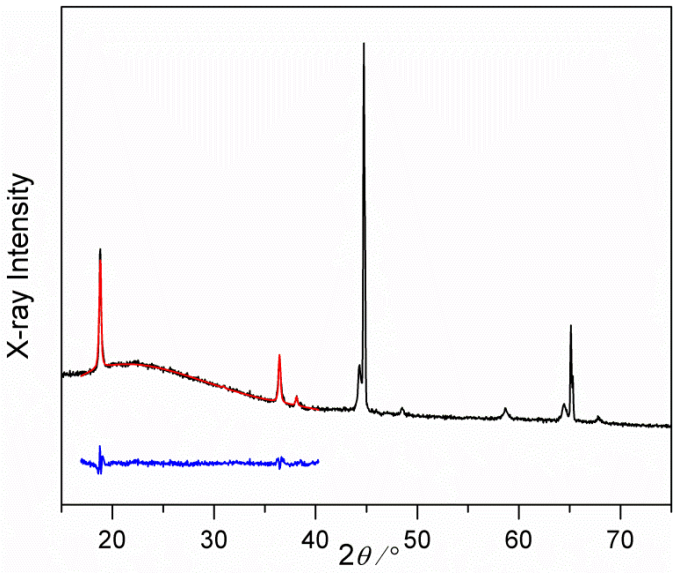

Figure C.18 XRD data (black), calculated Rietveld refinement (red), and difference pattern (blue) for an LNMO electrode after 10 cycles 3.4 - 5 V and 50 cycles 4.4 - 5 V charge/discharge.

Table C.11 Refinement parameters for an LNMO electrode after 10 cycles 3.4 - 5 V and 50 cycles 4.4 - 5 V charge/discharge.

Space Group	$Fd\,\bar{3}m$
Scale	3.976×10^{-4}
Lattice parameter, *a* (Å)	8.189
Unit Cell Mass (g•mol^{-1})	1450.260
Unit Cell Volume (Å^3)	549.322
Crystallite Size, Lorentzian (nm)	83.3
Crystal Density (g•cm^3), calculated	4.384
Crystal Linear Absorption Coefficient (cm^{-1})	591.123
Wt%-Rietveld	100
R_{exp}/ R_{exp}' [(*a*)]	1.39/2.70
R_{wp}/ R_{wp}'	2.25/4.36
R_p/ R_p'	1.64/3.21
R_{Bragg}	0.529
GoF	1.62
DW_d	1.06

(*a*)-Primed parameters are background corrected.

Table C.12 Atomic coordinates and isotropic thermal parameters for an LNMO electrode after 10 cycles 3.4 - 5 V and 50 cycles 4.4 - 5 V charge/discharge.

Atom	Wyckoff Site	*x*	*y*	*z*	SOF	B_{eq}
Li	8*a*	0	0	0	1	-9.146
Mn	16*d*	0.6250	0.6250	0.6250	0.75	16.04
Ni	16*d*	0.6250	0.6250	0.6250	0.25	19.59
O	32*e*	0. 37019	0. 37019	0. 37019	1	19.93

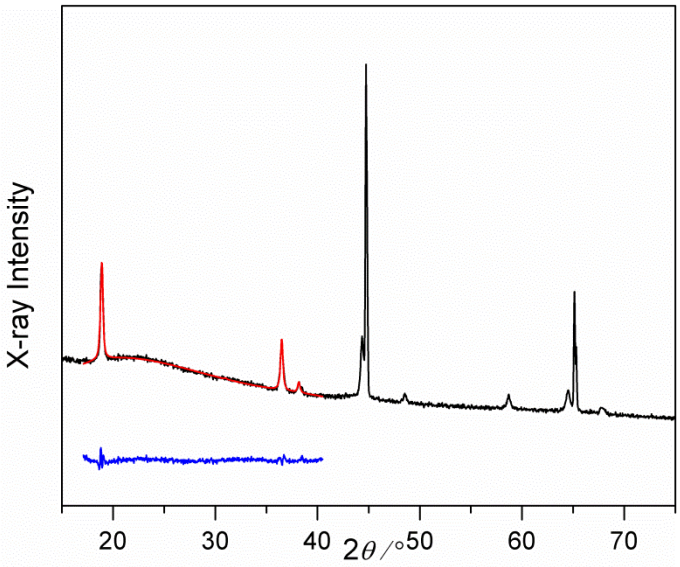

Figure C.19 XRD data (black), calculated Rietveld refinement (red), and difference pattern (blue) for an LNMO electrode after 1000 cycles with different electrochemical windows.

Table C.13 Refinement parameters for an LNMO electrode after 1000 cycles with different electrochemical windows.

Space Group	$Fd\,\bar{3}m$
Scale	1.281×10^{-4}
Lattice parameter, *a* (Å)	8.209
Unit Cell Mass (g•mol^{-1})	2347.295
Unit Cell Volume (Å^3)	553.229
Crystallite Size, Lorentzian (nm)	92.5
Crystal Density (g•cm^3), calculated	4.396
Crystal Linear Absorption Coefficient (cm^{-1})	680.508
Wt%-Rietveld	100
R_{exp}/ R_{exp}' $^{(a)}$	1.41/2.71
R_{wp}/ R_{wp}'	1.98/3.80
R_p/ R_p'	1.51/2.95
R_{Bragg}	1.158
GoF	1.40
DW_d	1.06

(*a*)-Primed parameters are background corrected.

Table C.14 Atomic coordinates and isotropic thermal parameters for an LNMO electrode after 1000 cycles with different electrochemical windows.

Atom	Wyckoff Site	*x*	*y*	*z*	SOF	B_{eq}
Li	8*a*	0	0	0	1	19.92
Mn	16*d*	0.6250	0.6250	0.6250	0.75	19.68
Ni	16*d*	0.6250	0.6250	0.6250	0.25	12.18
O	32*e*	0.34704	0.34704	0.34704	1	-0.8975

APPENDIX D

SUPPORTING DATA FOR CHAPTER 5

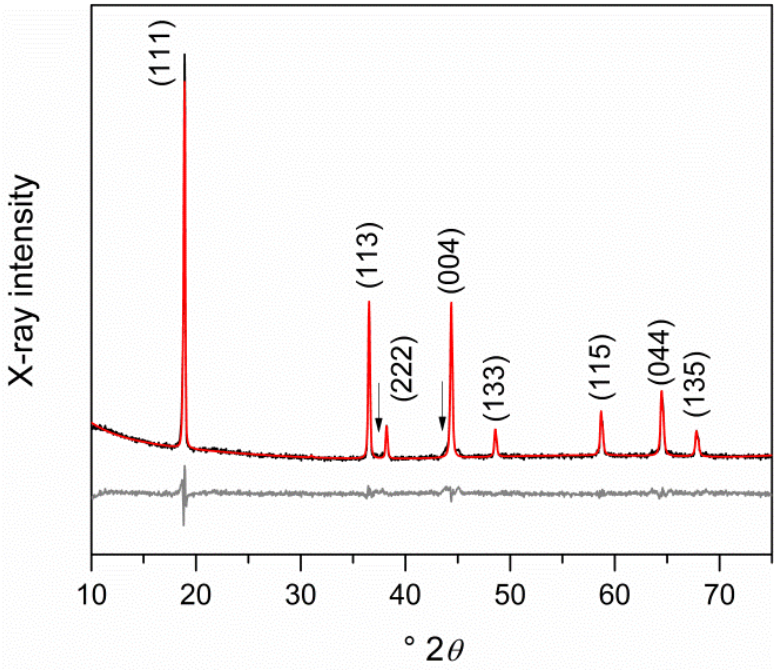

Figure D.1 XRD Pattern of $LiNi_{0.5}Mn_{1.5}O_{4-\delta}$.

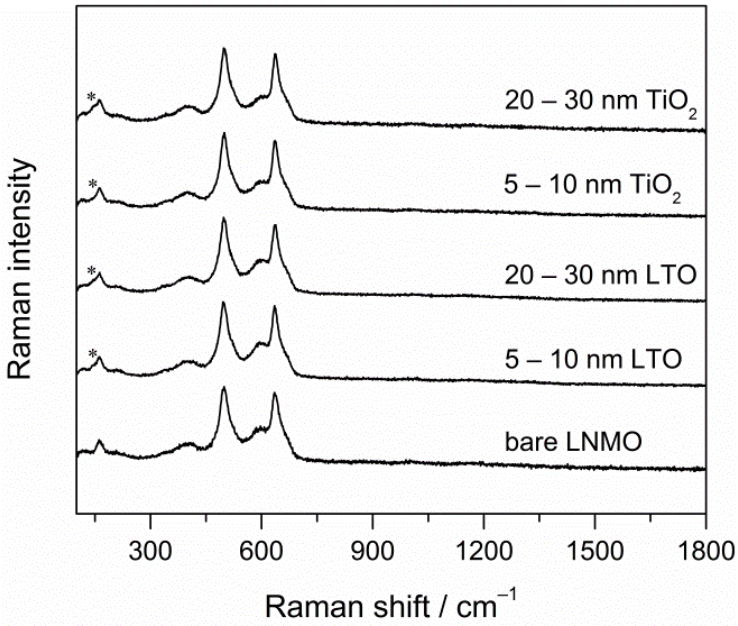

Figure D.2 Raman spectra of LNMO samples.

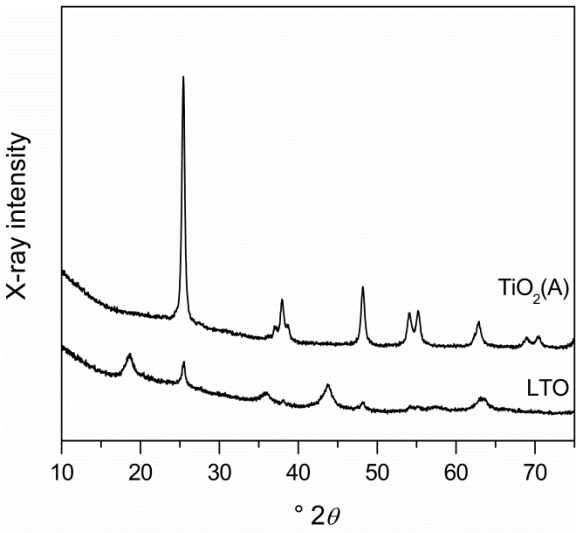

Figure D.3 XRD Patterns of anatase-TiO_2 and spinel LTO coatings.

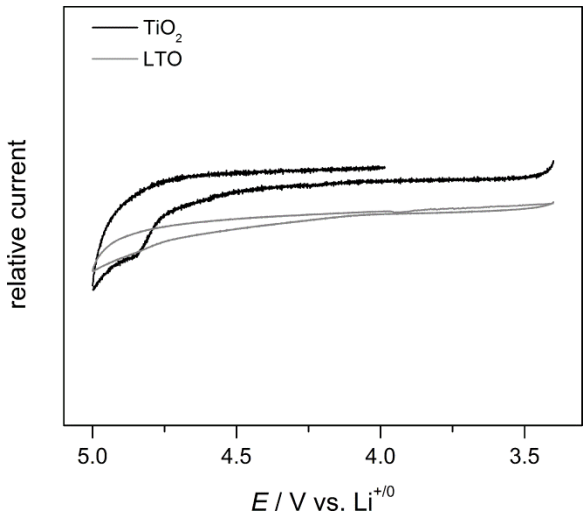

Figure D.4 CVs of anatase-TiO_2 and LTO. Scan rate is 0.1 mV/s.

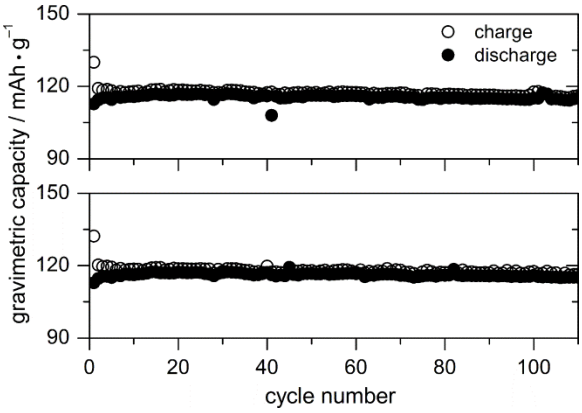

Figure D.5 Room-temperature 1 *C* cycling data for two additional 5 – 10 nm TiO_2-coated LNMO cells.

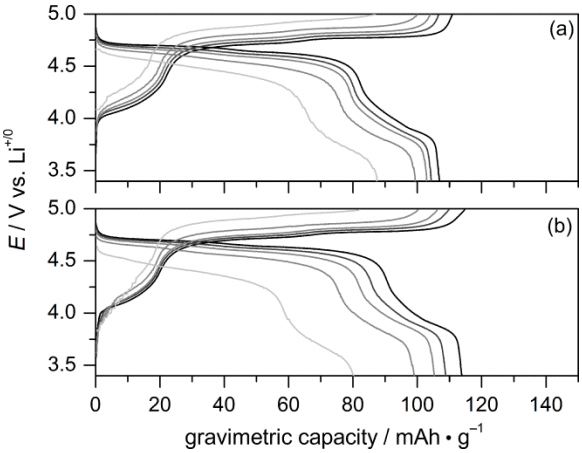

Figure D.6 Profiles of last cycle at each rate of the rate capability study for (a) a bare LNMO electrode; (b) TiO_2-coated LNMO. From right to left, rates are 1, 2, 3, 5, and 10 *C*.

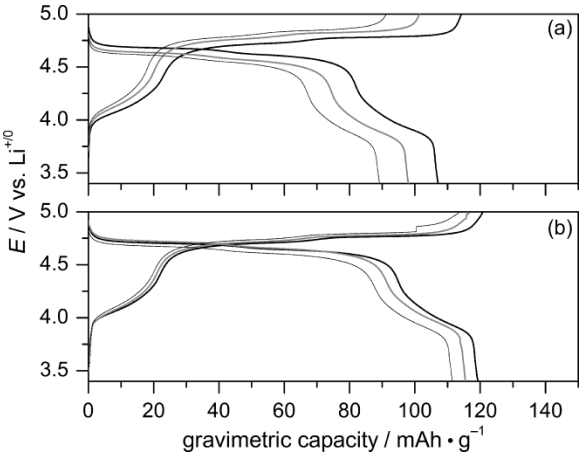

Figure D.7 Profiles of the 5th, 55th, and 110th cycles at 55 ℃ for (a) a bare LNMO electrode; (b) TiO_2-coated LNMO. Cells are charged and discharged at 1 *C* rate.

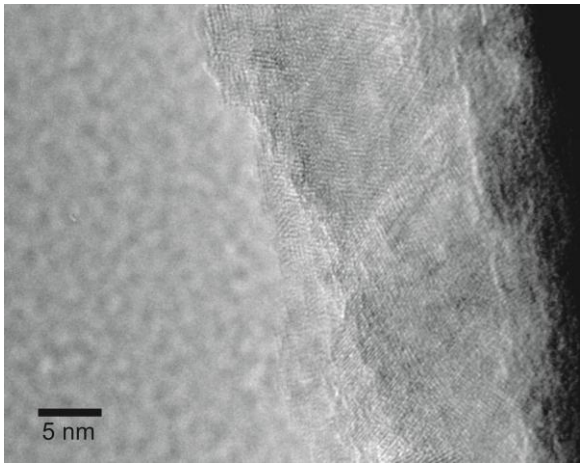

Figure D.8 HR-TEM image of TiO_2-coated LTO after 110 cycles at 55 ℃ (1 *C* charge and discharge).

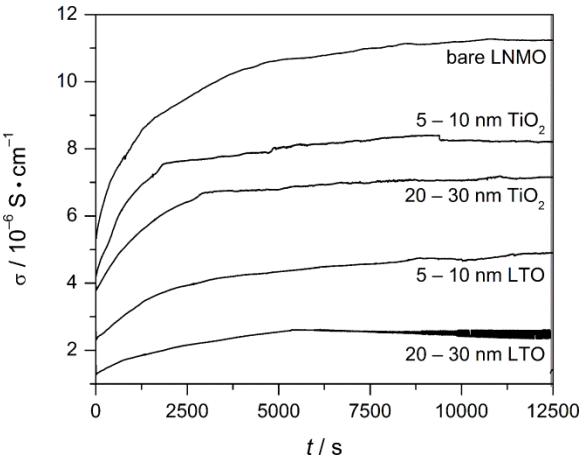

Figure D.9 Conductivity of LNMO pellets.

APPENDIX E

SUPPORTING DATA FOR CHAPTER 6

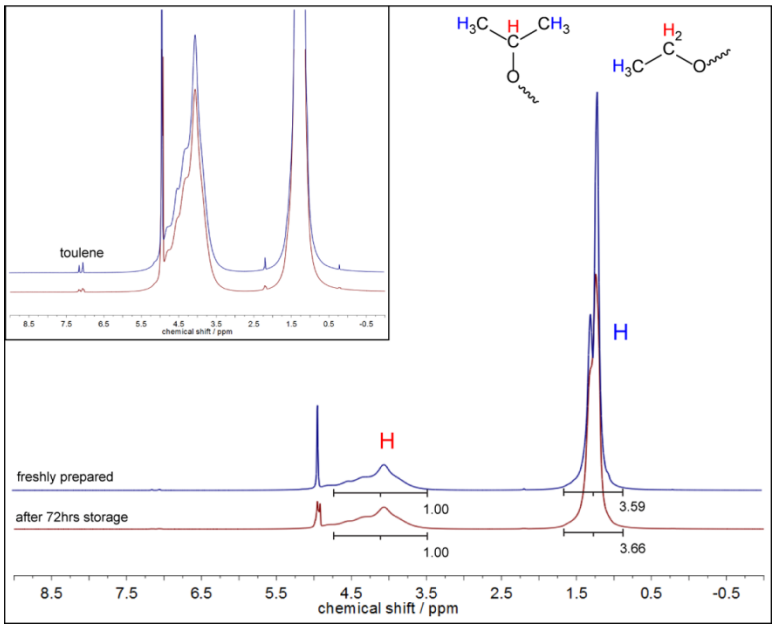

Figure E.1 ^{1}H-NMR spectra of fresh precursor solution of LiOEt and Ti(O^{i}Pr)$_4$ in toluene-d_8 (blue) and after storing for 72 h under ambient conditions (red).

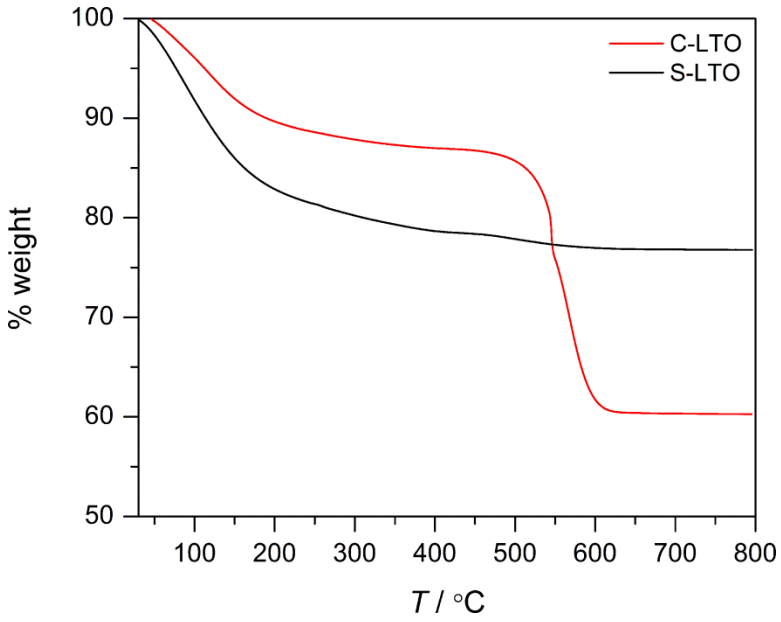

Figure E.2 TGA traces of C-LTO nanocrystals and S-LTO aggregates.

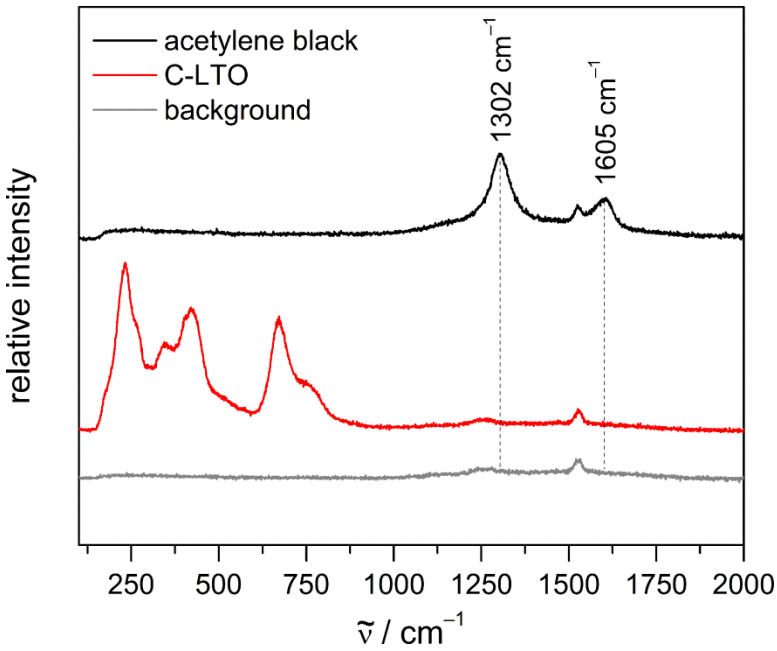

Figure E.3 Raman spectrum of C-LTO showing that no carbon black remains on the surface after annealing. Raman features at *ca.* 1250 and 1520 cm^{-1} arise from the background.

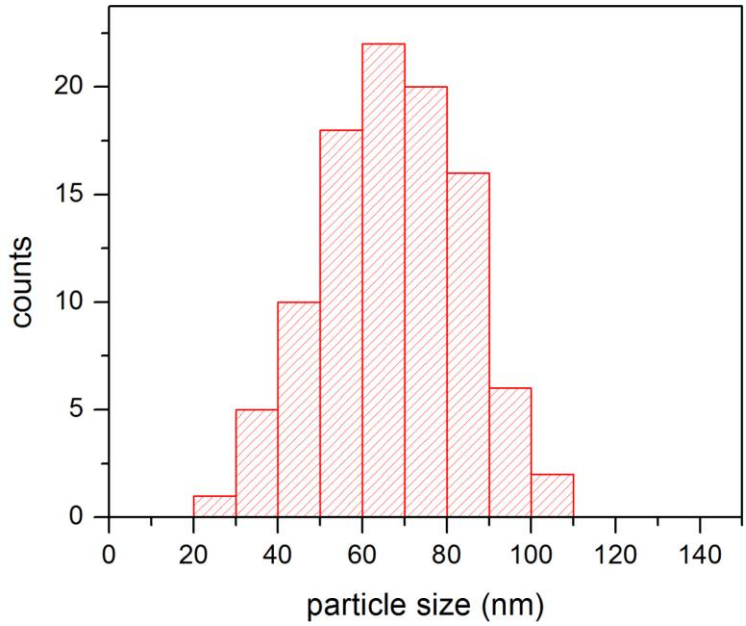

Figure E.4 Particle size distribution histogram of C-LTO.

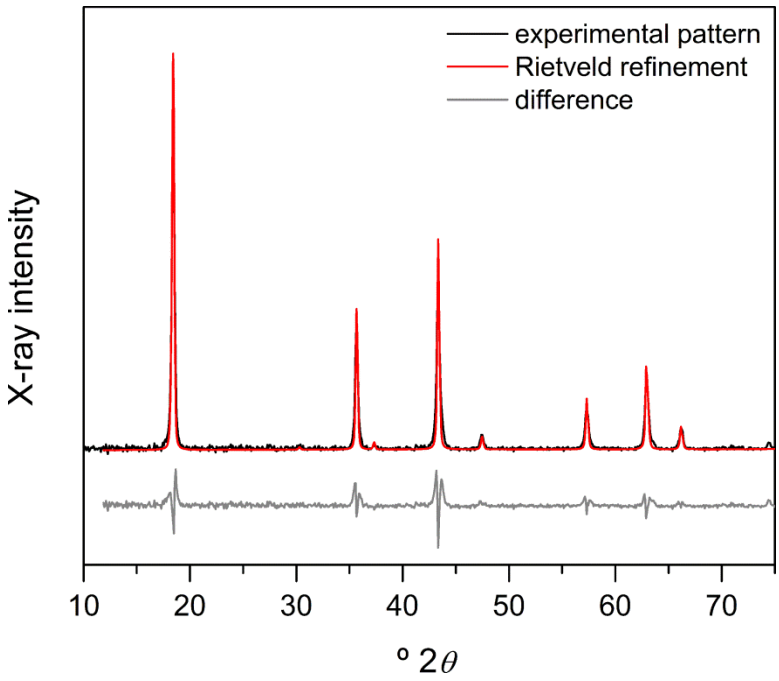

Figure E.5 X-ray diffraction pattern and Rietveld refinement of C-LTO nanocrystals.

Table E.1 Refinement parameters for C-LTO nanocrystals

Space Group	$Fd\bar{3}m$
Scale	4.896×10^{-4}
Lattice parameter, *a* (Å)	8.362
Unit Cell Mass (g•mol^{-1})	1439.529
Unit Cell Volume (Å^3)	584.654
Crystallite Size, Lorentzian (nm)	58.01
Crystal Density (g•cm^3), calculated	4.089
Crystal Linear Absorption Coefficient (cm^{-1})	452.192
Wt%-Rietveld	100.00
R_{exp}/ R_{exp}' (*a*)	2.81/3.69
R_{wp}/ R_{wp}'	2.94/1.49
R_p/ R_p'	2.26/1.70
R_{Bragg}	0.521
GoF	2.48
DW_d	0.78

(*a*)-Primed parameters are background corrected.

Table E.2 Atomic coordinates and isotropic thermal parameters for C-LTO nanocrystals

Atom	Wyckoff Site	*x*	*y*	*z*	SOF	B_{eq}
Li	8*a*	0	0	0	1	6.131
Li	16*d*	0.6250	0.6250	0.6250	0.167	3.319×10^{-4}
Ti	16*d*	0.6250	0.6250	0.6250	0.833	7.082
O	32*e*	0. 38867	0. 38867	0. 38867	1	–0.9752

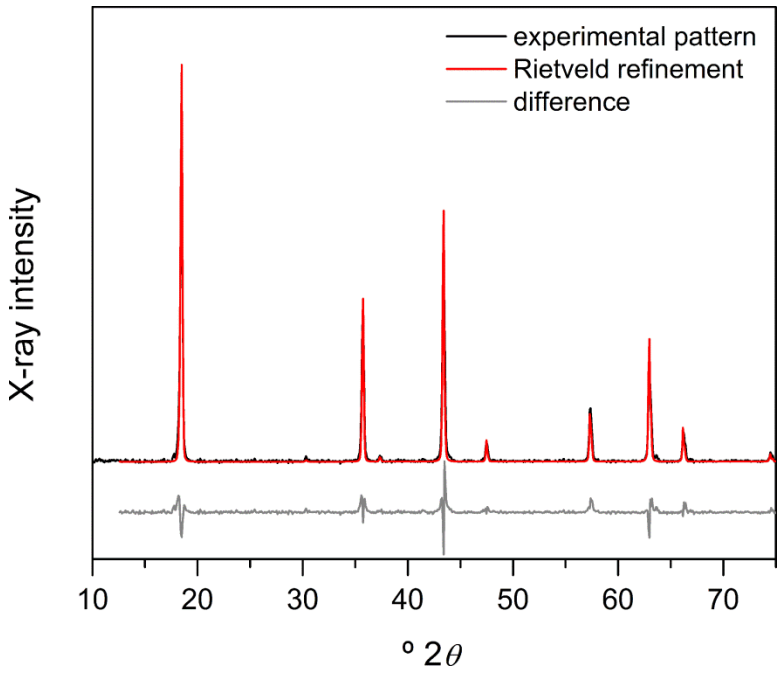

Figure E.6 X-ray diffraction pattern and Rietveld refinement of S-LTO aggregates.

Table E.3 Refinement parameters for C-LTO nanocrystals

Space Group	$Fd\bar{3}m$
Scale	4.315×10^{-4}
Lattice parameter, *a* (Å)	8.363
Unit Cell Mass (g•mol^{-1})	1439.529
Unit Cell Volume (Å^3)	585.458
Crystallite Size, Lorentzian (nm)	201.3
Crystal Density (g•cm^3), calculated	4.083
Crystal Linear Absorption Coefficient (cm^{-1})	451.571
Wt%-Rietveld	100.00
R_{exp}/ R_{exp}' (*a*)	1.34/2.07
R_{wp}/ R_{wp}'	1.54/2.49
R_p/ R_p'	3.16/2.67
R_{Bragg}	0.775
GoF	2.15
DW_d	0.83

(*a*)-Primed parameters are background corrected.

Table E.4 Atomic coordinates and isotropic thermal parameters for C-LTO nanocrystals

Atom	Wyckoff Site	*x*	*y*	*z*	SOF	B_{eq}
Li	8*a*	0	0	0	1	4.016
Li/Ti	16*d*	0.6250	0.6250	0.6250	0.167	-8.246
Ti	16*d*	0.6250	0.6250	0.6250	0.833	7.082
O	32*e*	0. 38587	0. 38587	0. 38587	1	–3.645

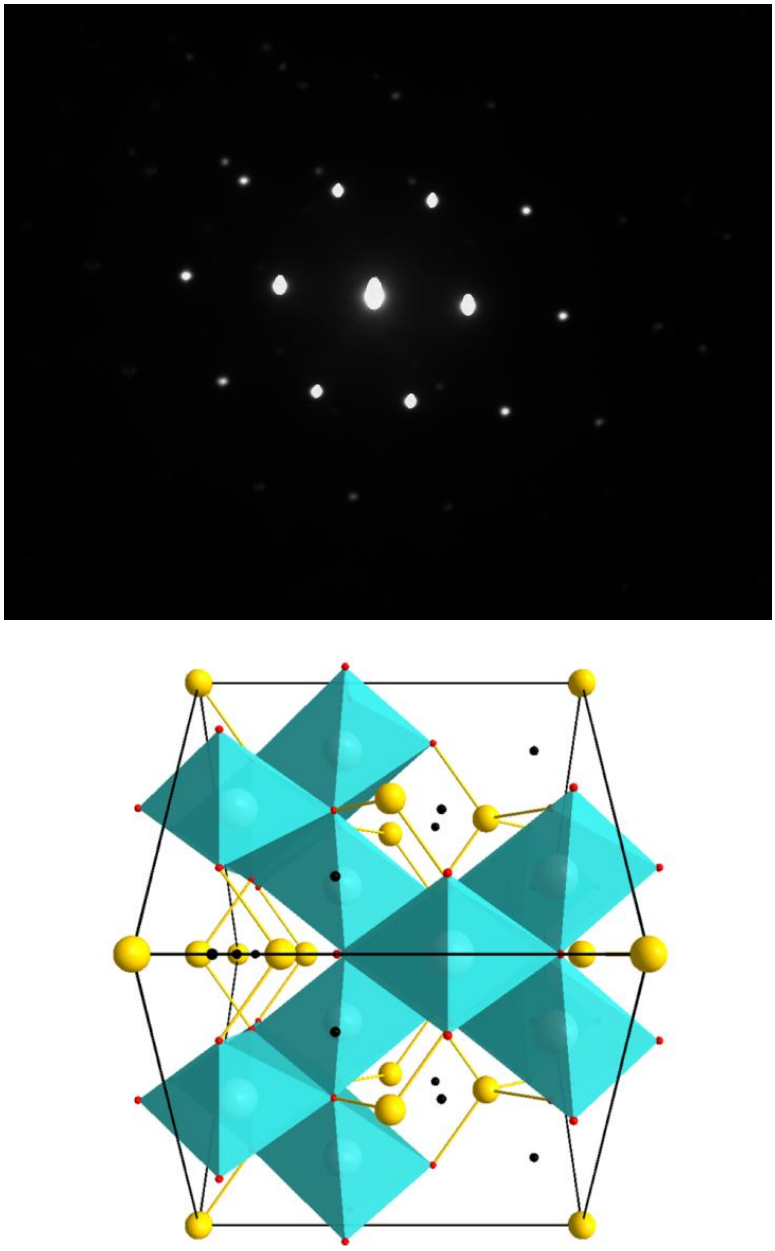

Figure E.7 SAED pattern of C-LTO nanocrystals (top). The view is along [011], and diffraction spots correspond to the {111} family of planes. Unit cell of $Li_4Ti_5O_{12}$ viewed along [011] (bottom). Yellow spheres represent Li on 8*a* tetrahedral Wyckoff sites, light blue polyhedra represent $(Li/Ti)O_6$ octahedra on 16*d* sites, and black spheres represent the 16*c* octahedral sites. These sites are empty in $Li_4Ti_5O_{12}$, but occupied in the fully lithiated material $Li_7Ti_5O_{12}$.

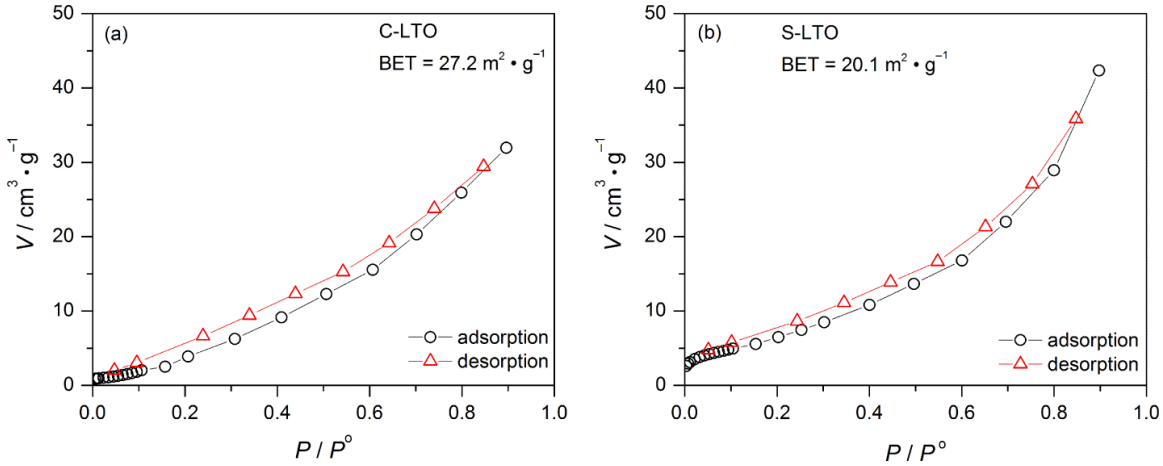

Figure E.8 N_2 sorption isotherms for C-LTO (a) and S-LTO (b).

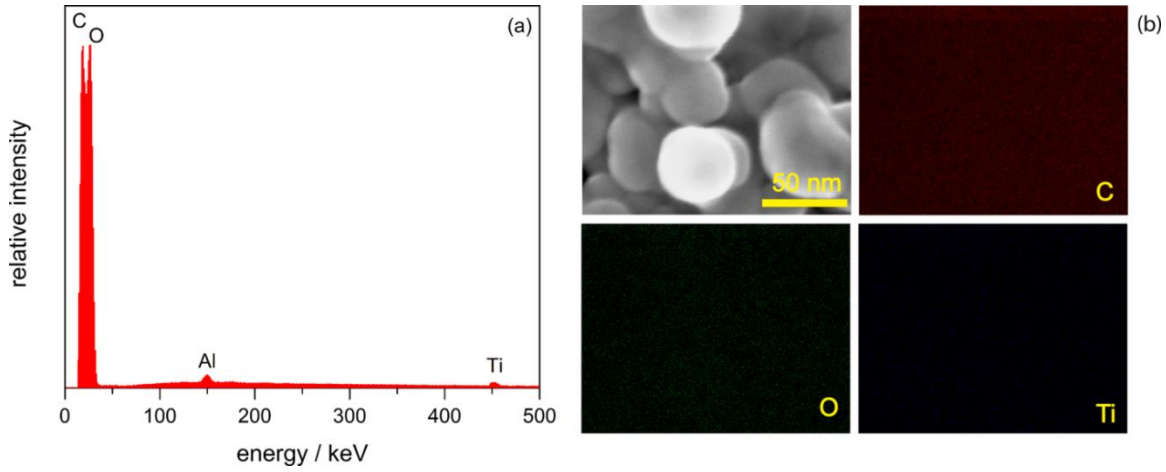

Figure E.9 EDX spectrum (a) and map (b) of C-LTO nanocrystals.

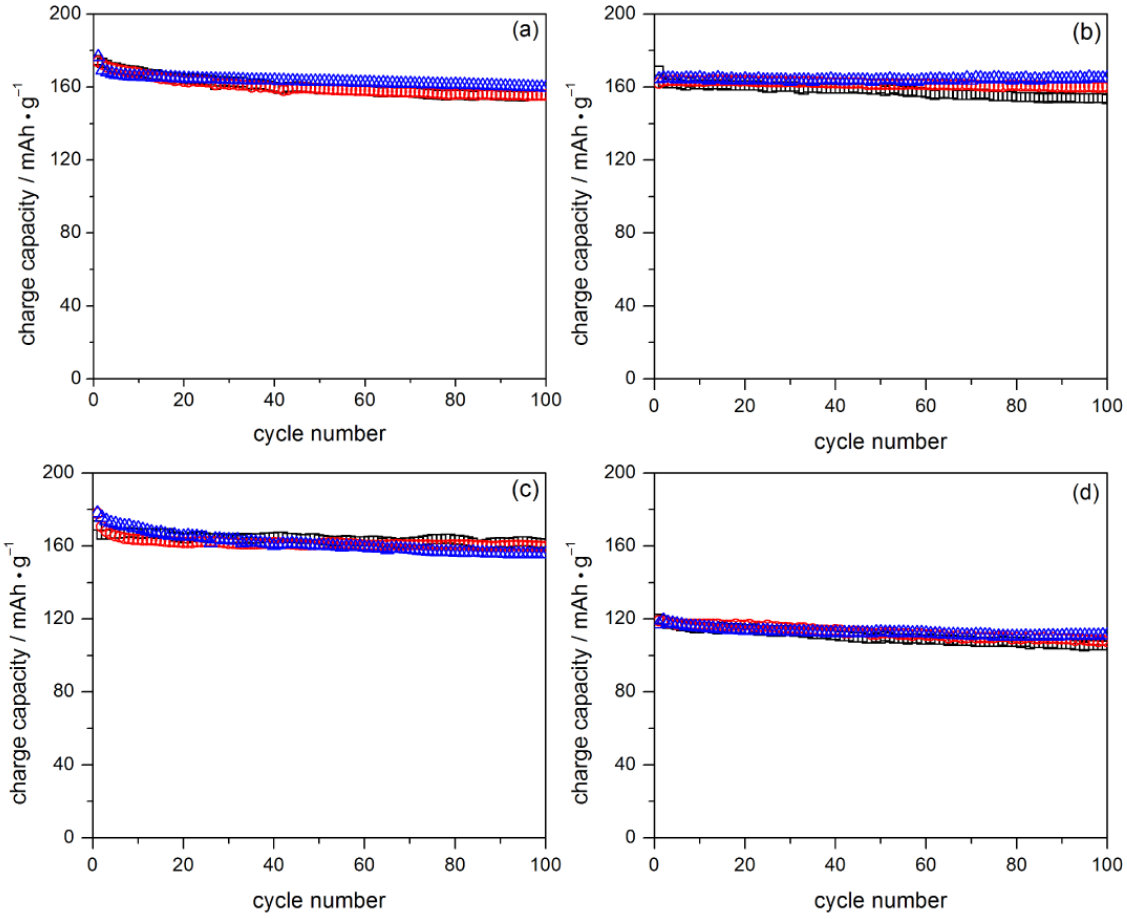

Figure E.10 (a) Gravimetric charge capacity of C-LTO cells cycled galvanostatically at 1 *C;* (b) Gravimetric charge capacity of C-LTO cells cycled galvanostatically at 10 *C;* (c) Gravimetric charge capacity of S-LTO cells cycled galvanostatically at 1 *C;* (d) Gravimetric charge capacity of C-LTO cells cycled galvanostatically at 10 *C.*

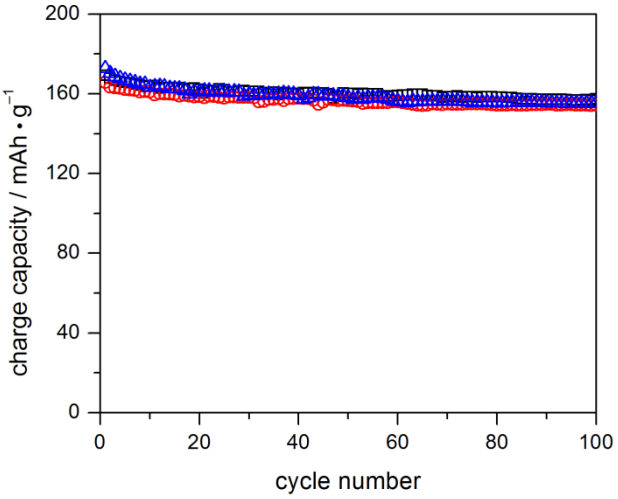

Figure E.11 Gravimetric charge capacity of C-LTO cells (4mg/cm^2 active material loading) cycled galvanostatically at 1 *C*.

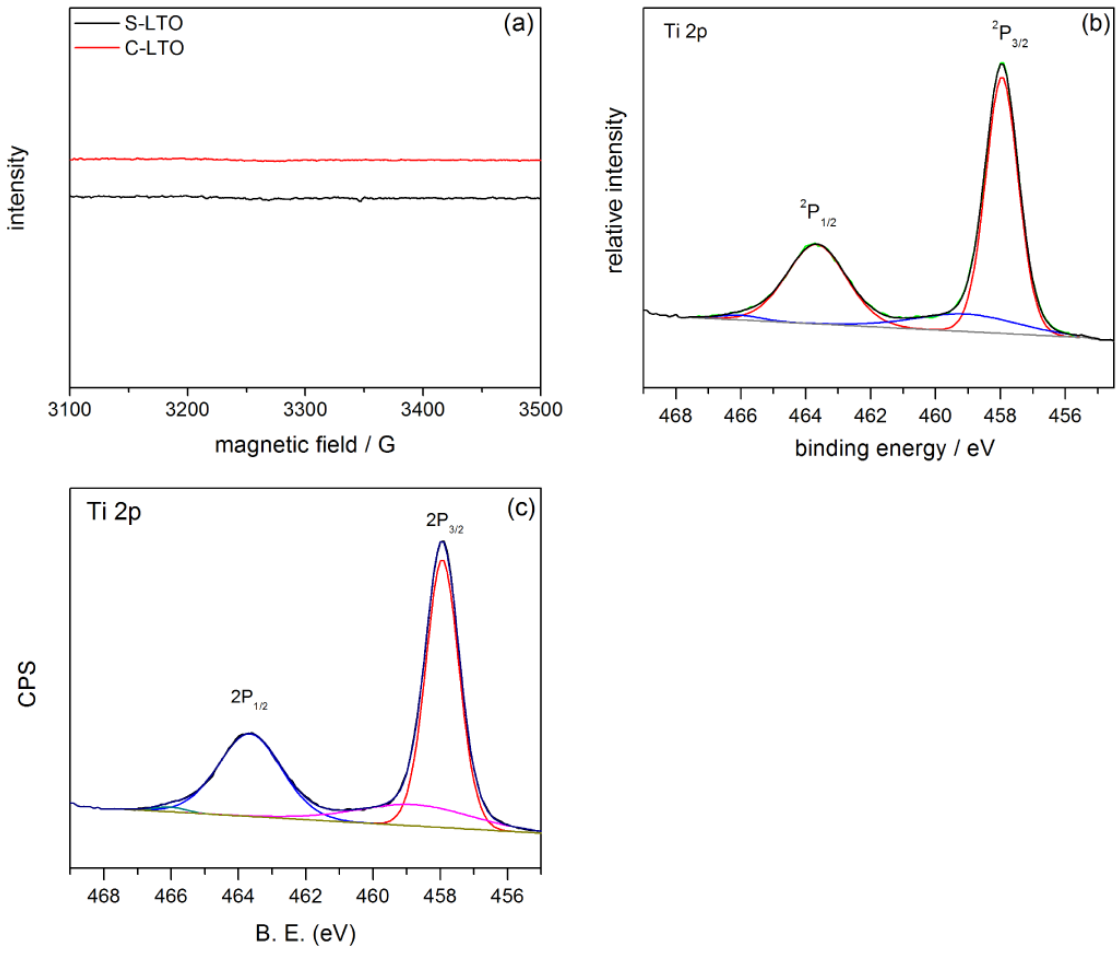

Figure E.12 EPR spectrum (a) , Ti 2p XP spectrum of C-LTO nanocrystals (b) Ti 2p XP xpectrum of S-LTO nanocrystals (c).

Reference

1 Key World Energy Statics, International Energy Agency, www.iea.org, 2013.
2 Lewis, N. L.; Nocera, D. G. Proc. Natl. Acad. Sci. U.S.A **2006**, *103*, 15729.
3 Dollars from Sense: The Economic Benefits of Renewable Energy, produced for the U. S. Department of Energy by the National Renewable Energy Laboratory, **1997**.
4 Armand, M.; Tarascon, J.-M. *Nature*, **2008**, *451*, 652.
5 Winter, M.; Brodd, R. J. *Chem. Rev*. **2004**, *104*, 4245.
6 Dunn, B.; Kamath, H.; Tarascon, J.-M. *Science*, **2011**, *334*, 928.
7 Palac ń, M. R. *Chem. Soc. Rev*. **2009**, *38*, 2565.
8 Whittingham, M. S. *Chem. Rev*. **2004**, *104*, 4271.
9 Cairns, E. J.; Shimotake, H. *Science*, **1969**, *164*, 1347.
10 Olsen, R. B.; Bruno, D. A.; Briscoe, J. M. *J. App. Phys.* **1985**, *58*, 4709.
11 Xu, K. *Chem. Rev.* **2004**, *104*, 4303.
12 Goodenough, J. B and Kim, Y. *Chem. Mater*. **2010**, *22*, 587.
13 Bernardi, D.; Pawlikowski, E. and Newman, J. *J. Electrochem. Soc.* **1985**, *132*, 5.
14 Gibbard, H. F. *J. Electrochem. Soc*. **1978**, *125*, 353.
15 Meyer, B. M.; Leifer, N.; Sakamoto, S.; Greenbaum, S. G. and Grey, C. P. *Electrochem. Solid-State Lett.* **2005**, *8*, A145.
16 Chan, C. K.; Peng, H.; Liu, G.; McIlwrath, K.; Zhang, X. F.; Huggins, R. A.; Cui, Y. *Nat. Nano.* **2008**, *3*, 31.
17 Aric ò, A. S.; Bruce, P.; Scrosati, B.; Tarascon, J.-M.; Schalkwijk, W. van, *Nat. Mater.*, **2005**, *4*, 366.
18 Kang, B.; Ceder, G. *Nature*, **2007**, *458*, 190.
19 Jacobson, A. J.; Chianelli, R. R.; Rich, S. M.; Whittingham, M. S. *Mater. Res. Bull.* **1979**, *14*, 1437.
20 Whittingham, M. S. *J. Solid State Chem*. **1979**, *29*, 303.
21 Watanabe, H.; Nakane, I.; Saito, T.; Furukawa, S. *Jpn. Kokai Tokkyo Koho*, **1988**, JP 1987-120801.
22 Flandrois, S.; Simon, B. *Carbon*, **1999**, *37*, 165.
23 Kanamura, K.; Shiraishi, S.; Takehara, Z.-i. *J. Electrochem. Soc*. **1996**, *143*, 2187.
24 Nagaura, T.; Tozawa, K. Prog. Batt. *Solar Cells*, **1990**, *9*, 209.
25 Di Pietro, B.; Patriarca, M.; Scrosati, B. *J. Power Sources*, **1982**, *8*, 2.
26 Mizushima, K.; Jones, P. C.; Wiseman, P. J.; Goodenough, J. B. *Mater. Res. Bull*., **1980**, *15*, 783.
27 Dunning, J. S.; iedemann, W. H.; Hsueh, L.; Bennion, D. N. *J. Electrochem. Soc*., **1971**, *11*, 1886.
28 Hunger, H. F.; Heymach, G. J., *U. S. Nat. Tech. Inform. Serv. AD Rep*. **1972**, 33.
29 Pistoia, G.; De Rossi, M.; Scrosati, B., *J. Electrochem. Soc.*, **1970**, *117*, 500.
30 Besenhard, J.; Fritz, H. P., *J. Electrochem. Soc.*, **1972**, *119*, 1679.
31 Arora, P.; Zhang, Z. J., *Chem. Rev*., **2004**, *104*, 4419.
32 Armstrong, A. R.; Bruce, P. G., *Nature*, **1996**, *381*, 499.
33 Hunter, J. C., *J. Solid State Chem.*, **1981**, *39*, 142.
34 Thackeray, M. M.; Johnson, P. J.; De Picciotto, L. A.; Bruce, P. G.; Goodenough, J. B., *Mater. Res. Bull.* **1984**, *19*, 179.

35 Kemp, J. P.; Cox, P. A., *J. Phys. Conden. Mat.*, **1990**, *2*, 9653.
36 Van Elp, J.; Wieland, J. L.; Eskes, H.; Kuiper, P.; Sawatzky, G. A.; De Groot, F. M. F.; Turner, T. S., *Phys Rev B: Conden. Mat. Mater. Phys.*, **1991**, *44*, 6090.
37 Czyzyk, M. T.; Potze, R.; Sawatzky, G. A., *Phys Rev B: Conden. Mat. Mater. Phys.*,**1992**, *46*, 3729.
38 Aydinol, M. K.; Ceder, G.; Kohan, A. F., *Mater. Res. Soc. Sym. Proc.*, **1997**, *453*, 233.
39 Godshall, N. A.; Raistrick, I. D.; Huggins, R. A., *J. Electrochem. Soc.*, **1984**, *131*, 543.
40 Orsini, F.; du Pasquier, A.; Beaudouin, B.; Tarason, J.-M.; Trentin, M.; Langenhuizen, N.; de Beer, E.; Notten, P., *J. Power Sources*, **1999**, *81*, 918.
41 Yamaguchi, S.; Asahina, H.; Hirasawa, K. A.; Sato, T.; Mori, S., *Mol. Crys. Liquid Crys. Sci. Tech*, A, **1998**, *322*, 239.
42 Schuette, L.; Colsmann, G.; Reuter, B., *J. Solid State Chem.*, **1979**, *27*, 227.
43 Lenglet, M.; Lopitaux, J.; Guillamet, R.; Duerr. J., *Mater. Chem. Phys.*, **1986**, *14*, 199.
44 Masquelier, C.; Tabuchi, M.; Ado, K.; Kanno, R.; Kobayashi, Y.; Maki, Y.; Nakamura, O.; Goodenough, J. B., *J. Solid State Chem.*, **1996**, *123*, 255.
45 Mosbah, A.; Verbaere, A.; Tournoux, M., *Mater. Res. Bull.*, **1983**, *18*, 1375.
46 Kang, S.-H.; Goodenough, J. B., *J. Electrochem. Soc.*, **2000**, *147*, 3621.
47 Yamada, A., *J. Solid State Chem.*, **1996**, *122*, 160.
48 Yamada, A.; Miura, K.; Hinokuma, K.; Tanaka, M., *J. Electrochem. Soc.*, **1995**, *142*, 2149.
49 Gummow, R. J.; de Kock, A.; Thackeray, M. M.; *Solid State Ionics*, **1994**, *69*, 59.
50 Bergstein, A.; Kleinert, P., *Phys. Chem. Solids*, **1965**, *26*, 181.
51 W. Lu, I. Belharouak, S. H. Park, Y. K. Sun, K. Amine, *Electrochim. Acta*, 2007, **52**, 5837.
52 L. Dupont, M. Hervieu, G. Rousse, C. Masquelier, M. R. Palacin, Y. Chabre, J. M. Tarason, *J. Solid State Chem*., 2000, **155**, 394.
53 Q. Zhong, A. Banakdarpour, M. Zhang, Y. Gao, J. R. Dahn, *J. Electrochem. Soc*., 1997, **144**, 205.
54 D. Gryffroy, R. E. Vandenberghe, *J. Phys. Chem. Solids*, 1992, **53**, 777.
55 D. Gryffroy, R. E. Vandenerghe, E. Legrand, *Mater. Sci. Forum*, 1991, **79-82**, 785.
56 S.-T. Myung, S. Komaba, N. Kumagai, H. Naoaki, H.-T. Chung, T.-H. Cho, *Electrochim. Acta*, 2002, **47**, 2543.
57 J. Li, R. Yao, C. Cao, *ACS App. Mater. Inter.*, 2014.
58 J. H. Kim, S. T. Myung, C. S. Yoon, S. G. Kang, Y. K. Sun, *Chem. Mater*., 2004, **16**, 906.
59 Y.-K. Sun, Y.-S. Lee, M. Yoshio, K. Amine, Electrochem. *Solid State Lett*., 2002, **5**, A99.
60 Y. Kobayashi, H. Miyashiro, K. Takei, H. Shigemura, M. Tabuchi, H. Kageyama, T. Iwahori, *J. Electrochem. Soc.*, 2003, **150**, A1577.
61 W. J. Macklin, R. J. Neat, *Solid State Ionics*, 1992, **53-56**, 694.
62 S. Y. Huang, L. Kavan, I. Exnar, M. Graetzel, *J. Electrochem. Soc.*, 1995, **142**, L142.

63 A. R. Armstrong, G. Armstrong, J. Canales, P. G. Bruce, *Angew. Chem*., 2004, **43**, 2286.
64 V. Etachaeri, A. Van der Ven, B. M. Bartlett, *J. Mater. Chem.* A 2013, **1**, 12028.
65 Y.-Y. Hu, Z. Liu, K.-W. Nam, O. J. Borkiewicz, J. Cheng, X. Hua, M. Dunstan, T. Mattew, X. Yu, K. M. Wiaderek, L.-S. Du, K. W. Chapman, P. J. Chupas, X.-Q. Yang, C. P. Grey, *Nat. Mater*., 2013, **12**, 1130.
66 E. Ferg, R. J. Gummow, A. de Kock, M. M. Thackeray, *J. Electrochem. Soc.*, 1994, **141**, L147.
67 A. Deschanvres, B. Raveau, Z. Sekkal, *Mater. Res. Bull*., 1971, **6**, 699.
68 C. H. Chen, J. T. Vaughey, A. N. Jansen, D. W. Dees, A. J. Kahaian, T. Goacher, M. M. Thackeray, *J. Electrochem. Soc*., 2001, **148**, A102.
69 L. Zhao, Y.-S. Hu, H. Li, Z. Wang, L. Chen, *Adv. Mater.*, 2011, **23**, 1385.
70 S. Huang, Z. Wen, X. Zhu, Z. Gu, *Electrochem. Comm*., 2004, **6**, 1093.
71 L. Cheng, J. Yan, G.-N. Zhu, J.-Y. Luo, C.-X. Wang, Y.-Y. Xia, *J. Mater. Chem*., 2010, **20**, 595.
72 G. J. Wang, J. Gao, L. J. Fu, N. H. Zhao, Y. P. Wu, T. Takamura, *J. Power Sources*, 2007, **174**, 1109.
73 A. S. Prakash, P. Manikandan, K. Ramesha, M. Sathiya, J.-M. Tarascon, A. K. Shukla, *Chem. Mater*., 2010, **22**, 2857.
74 W. J. H. Borghols, M. Wagemaker, U. Lafont, E. M. Kelder, F. M. Mulder, *J. Am. Chem. Soc*., 2009, **131**, 17786.
75 Yoshio, M.; Noguchi, H. A Review of Positive Electrode Materials for Lithium-Ion Batteries. In *Lithium-Ion Batteries: Science and Technology*; Yoshi, M.; Brodd, R. J.; Kozawa, A., Eds.; Springer: New York, 2010; pp 17-30.
76 M. M. Thackeray, A. de Kock, H. Rossouwm, D. Liles, R. Bittihn and D. Hoge, *J. Electrochem. Soc.*, 1992, **139**, 363.
77 D. G. Wickham and W. J. Croft, *J. Phys. Chem. Solids*, 1958, **7**, 351.
78 M. M. Thackeray, W. I. F. David, P. G. Bruce and J. B. Goodenough, *Mater. Res. Bull.*, 1983, **18**, 461.
79 M. M. Thackeray, P. J. Johnson, L. A. de Picciotto, P. G. Bruce and J. B. Goodenough, *Mater. Res. Bull.*, 1984, **19**, 179.
80 R. J. Gummow, A. de Kock and M. M. Thackeray, *Solid State Ionics*, 1994, **69**, 59.
81 A. Manthiram, A. V. Murugan, A. Sarkar and T. Muraliganth, *Energy Environ. Sci.,* 2008, **1**, 621.
82 J. M. Tarascon, W. R. McKinnon, F. Coowar, T. N. Bowmer, G. Amatucci and D. Guyomard, *J. Electrochem. Soc.*, 1994, **141**, 1421.
83 A. Momchilov, V. Manev and A. Nassalevska, *J. Power Sources*, 1993, **41**, 305.
84 Y. Xia, H. Takeshige, H. Noguchi and M. Yoshio, *J. Power Sources*, 1995, **56**, 61.
85 Y. Xia and M. Yoshio, *J. Power Sources*, 1995, **57**, 125.
86 Y. Xia, Y. Zhou and M. Yoshio, *J. Electrochem. Soc.*, 1997, **144**, 2593.
87 A. S. Aricò, Bruce, P. Bruce, B. Scrosati, J.-M. Tarascon and W. van Schalkwijk, *Nat. Mater.*, 2005, **4**, 366.
88 Q. Feng, H. Kanoh, Y. Miyai and K. Ooi, Chem. Mater., 1995, **7**, 1226.
89 T. Kanasaku, K. Amezawa and N. Yamamoto, *Solid State Ionics*, 2000, **133**, 51.

90 Q. Feng, Y. Higashimoto, K. Kajiyoshi and K. Yanagisawa, *J. Mater. Sci. Lett.*, 2001, **20**, 269.
91 Y. C. Zhang, H. Wang, H. Y. Xu, B. Wang, H. Yan, A. Ahniyaz and M. Yoshimura, *Solid State Ionics*, 2003, **158**, 113.
92 Liu, Z.; Wang, W.-L.; Liu, X.; Wu, M.; Zeng, Z.; Li, D. *Inorg. Chem. Commun.* **2004**, *7*, 308.
93 Y. Lu, M. Wei, Z. Wang, D. G. Evans and X. Duan, *Electrochim. Acta*, 2004, **49**, 2361.
94 Z. Liu, W.-L. Wang, X. Liu, M. Wu, D. Li and Z. Zeng, *J. Solid State Chem.,* 2004, **177**, 1585.
95 K. Kanamura, K. Dokko and T. Kaizawa, *J. Electrochem. Soc.*, 2005, **152**, A391.
96 Y.-Y. Liang, S.-J. Bao, B.-L. He, W.-J. Zhou and H.-L. Li, *J. Electrochem. Soc.*, 2005, **152**, A2030.
97 C. H. Jiang, S. X. Dou, H. K. Liu, M. Ichihara and H. S. Zhou, *J. Power Sources*, 2007, **172**, 410.
98 X. Li, R. Xiang, T. Su and Y. Qian, *Mater. Lett.*, 2007, **61**, 3597.
99 D. K. Kim, P. Maualidharan, H.-W. Lee, R. Ruffo, Y. Yang, C. K. Chan, H. Peng, R. A. Huggins and Y. Cui, *Nano Lett.*, 2008, **8**, 3948.
100 H. Fang, L. Li, Y. Yang, G. Yan and L. Guangshe, *J. Power Sources*, 2008, **184**, 494.
101 P. Ragupathy, H. N. Vasan and N. Munichandraiah, Mater. *Chem. Phys.*, 2010, **124**, 870.
102 J.-W. Lee, J.-I. Kim and S. H. Min, J. *Power Sources*, 2011, **196**, 1488.
103 M. H. Rossouw, A. de Kock, L. A. de Picciotto and M. M. Thackeray, *Mater. Res. Bull.*, 1990, **25**, 173.
104 D. Guyomard and J. M. Tarascon, *Solid State Ionics*, 1994, **69**, 222.
105 M. N. Richard, E. W. Fuller and J. R. Dahn, *Solid State Ionics*, 1994, **73**, 81.
106 Y. Gao and J. R. Dahn, J. *Electrochem. Soc.*, 1996, **143**, 100.
107 Y. Chida, H. Wada and K. Shizuka, *J. Power Sources*, 1999, **81–82**, 454.
108 A. Yamada, K. Miura, K. Hinokuma and M. Tanaka, *J. Electrochem. Soc*., 1995, **142**, 2149.
109 S. Ma, H. Noguchi and M. Yoshio, *J. Power Sources*, 2004, **126**, 144.
110 B. J. Liddle, S. M. Collins and B. M. Bartlett, *Energy Environ. Sci.*, 2010, **3**, 1339.
111 Janssen, T. *Crystallographic Groups;* North Holland: Amsterdam, 1973.
112 Van Smaalen, S. *Incommensurate Crystallography;* Oxford University Press, Inc.: New York, 2007.
113 H. Björk, T. Gustafsson, J. O. Thomas, S. Lidin, V. *J.* Petříček, *Mater. Chem.* 2003, **13**, 585.
114 X. Q. Yang, X. Sun, M. Balasubramanian, J. McBreen, Y. Xia, T. Sakai and M. Yoshio, *Electrochem. Solid-State Lett.*, 2001, **4**, A117.
115 J. M. Amarilla and R. M. Rojas, *J. Therm. Anal. Calorim.*, 2003, **73**, 191.
116 A. Yamada and M. Tanaka, *Mater. Res. Bull.*, 1995, **30**, 715.
117 K. Oikawa, T. Kamiyama, F. Izumi, B. C. Chakoumakos, H. Ikuta, M. Wakihara, J. Li and Y. Matsui, *Solid State Ionics*, 1998, **109**, 35.

118 J. Rodr ǵuez-Carvajal, G. Rousse, C. Masquelier and M. Herview, *Phys. Rev. Lett.*, 1998, **81**, 4660.
119 C. Masquelier, M. Tabuchi, K. Ado, R. Kanno, Y. Kobayashi, Y. Maki, O. Nakamura and J. B. Goodenough, *J. Solid State Chem.*, 1996, **123**, 255.
120 Y. Gao and J. R. Dahn, *Solid State Ionics*, 1996, **84**, 33.
121 T. Ohzuku, M. Kitagawa and T. Hirai, *J. Electrochem. Soc.*, 1990, **137**, 769.
122 B. Deng, H. Nakamura and M. Yoshio, *J. Power Sources*, 2008, **180**, 864.
123 D. Lu, W. Li, X. Zuo, Z. Yan and Q. Huang, *J. Phys. Chem.* C, 2007, **111**, 12067.
124 Q.-C. Zhuang, T. Wei, L.-L. Du, Y.-L. Cui, L. Fang and S.-G. Sun, *J. Phys. Chem.* C, 2010, **114**, 8614.
125 C. Ho, I. D. Raistrick and R. A. Higgins, *J. Electrochem. Soc.*, 1980, **127**, 343.
126 S. Bach, J. Farcy and J. P. Pereira-Ramos, *Solid State Ionics*, 1998, **110**, 193.
127 A. Bergstein and P. Kleinert, *J. Phys. Chem. Solids*, 1965, **26**, 1181.
128 J. Sugiyama, T. Atsumi, T. Hioki, S. Noda and N. Kamegashira, *J. Alloys Compd*., 1996, **235**, 163.
129 J. Sugiyama, T. Atsumi, T. Hioki, S. Noda and N. Kamegashira, *J. Power Sources*, 1997, **68**, 641.
130 M. Wang and A. Navrotsky, *J. Solid State Chem*., 2005, **178**, 1182.
131 M. M. Thackeray, M. F. Mansuetto, D. W. Dees and D. R. Vissers, *Mater. Res. Bull.*, 1996, **31**, 133.
132 D. B. Rogers, R. W. Germann and R. J. Arnott, *J. Appl. Phys.*, 1965, **36**, 2338.
133 G. Amatucci and J.-M. Tarascon, *J. Electrochem. Soc.*, 2002, **149**, K31.
134 G. Rousse, C. Masquelier, J. Rodrıguez-Carvajal and M. Herview, *Electrochem. Solid-State Lett.*, 1999, **2**, 6.
135 R. Kanno, M. Yonemura, T. Kohigashi, Y. Kawamoto, M. Tabuchi and T. Kamiyama, *J. Power Sources*, 2001, **97–98**, 423.
136 R. Kanno, A. Kondo, M. Yonemura, R. Gover, Y. Kawamoto, M. Tabuchi, T. Kamiyama, F. Izumi, C. Masquelier and G. Rousse, *J. Power Sources,* 1999, **81–82**, 542.
137 Y. Xia and M. Yoshio, *J. Electrochem. Soc.*, 1997, **144**, 4186.
138 J. M. Paulsen and J. R. Dahn, *Chem. Mater.*, 1999, **11**, 3065.
139 M. Yonemura, A. Yamada, H. Kobayashi, M. Tabuchi, T. Kamiyama, Y. Kawamoto and R. Kanno, *J. Mater. Chem.*, 2004, **14**, 1948.
140 R. Benedek,M.M. Thackeray and A. van de Walle, *J. Mater. Chem.*, 2010, **20**, 369.
141 B. Deng, H. Nakamura and M. Yoshio, Electrochem. *Solid-State Lett.*, 2005, **8**, A171.
142 G. G. Amatucci, C. N. Schmutz, A. Blyr, C. Sigala, A. S. Gozdz, D. Larcher and J. M. Tarascon, *J. Power Sources*, 1997, **69**, 11.
143 H. Suzuki and Y. Nakayama, *Prog. Batt. Solar Cells*, 1984, **5**, 151.
144 X. M. He, J. J. Li, Y. Cai, Y. Wang, J. Ying, C. Jing and C. Wan, *J. Solid State Electrochem.*, 2005, **9**, 438.
145 Z. Jiang and K. M. Abraham, *J. Electrochem. Soc.*, 1996, **143**, 1591.
146 J.–M. Tarascon and M. Armand, *Nature,* 2001, **414**, 359.

147 K. Mizushima, P. C. Jones, P. J. Wiseman and J. B. Goodenough, *Mater. Res. Bull.*, 1980, **15**, 783.
148 T. Ohzuku, A. Ueda and M. Nagayama, *J. Electrochem. Soc.*, 1993, **140**, 1862.
149 A. K. Padhi, K. S. Nanjundaswamy and J. B. Goodenough, *J. Electrochem. Soc.*, 1997, **144**, 1188.
150 J. C. Hunter, *J. Solid State Chem.*, 1981, **39**, 142.
151 Q. Zhong, A. Bonakdarpour, M. Zhang, Y. Gao and J. R. Dahn, *J. Electrochem. Soc.*, 1997, **144**, 205.
152 R. Yazami and Ph. Touzain, *J. Power Sources*, 1983, **9**, 365.
153 G. G. Amatucci, J. M. Tarascon and L. C. Klein, *Solid State Ionics*, 1996, **83**, 167.
154 K. Huang, M. Feng, J. Goodenough and M. Schmerling, *J. Electrochem. Soc.*, 1996, **143**, 3630.
155 H. Wang, Y.-I. Jang, B. Huang, D. R. Sadoway and Y.-M. Chiang, *J. Power Sources*, 1999, **81–82**, 594.
156 H. Wang, Y.-I. Jang,; B. Huang, D. R. Sadoway and Y.-M. Chiang, *J. Electrochem. Soc.*, 1999, **146**, 473.
157 D. Wang, X. Wu, Z. Wang and L. Chen, *J. Power Sources*, 2005, **140**, 125.
158 K. Dokko, M. Nishizawa, S. Horikoshi, T. Itoh, M. Mohamedi and Uchida, I. *Electrochem. Solid-State Lett.*, 2000, **3**, 125.
159 W. H. Woodford, W. C. Carter and Y.-M Chiang, *Energy Environ. Sci.*, 2012, **5**, 8014.
160 T. Ohzuku, H. Tomura and K. Sawai, *J. Electrochem. Soc.*, 1997, **144**, 3496.
161 J. R. Wilson, J. S. Cronin, S. A. Barnett and S. J. Harris, *J. Power Sources*, 2011, **196**, 3443.
162 Y. Chen, K. Chen-Wiegart, Z. Liu, K. T. Faber, S. A. Barnett and J. Wang, *Electrochem. Comm.*, 2013, **28**, 127.
163 E. Prada, D. Di Domenico, Y. Creff, J. Bernard, V. Sauvant-Moynot and F. Huet, *J. Electrochem. Soc.*, 2013, **160**, A616.
164 Z. Ma, T. Li, Y. L. Huang, J. Liu, Y. Zhou and D. Xue, *RSC Advances*, 2013, **3**, 7398.
165 M. Pharr, Z. Suo and J. J. Vlassak, *Nano Lett.*, 2013, **13**, 5570–5577.
166 W. Liang, L. Hong, H. Yang, F. Fan, Y. Liu, H. Li, J. Li, J. Y. Huang, L.-Q. Chen, T. Zhu and S. Zhang, *Nano Lett.*, 2013, **13**, 5212.
167 M. T. McDowell, S. W. Lee, W. D. Nix and Y. Cui, *Adv Mat.*, 2013, **25**, 4966–4984.
168 X. H. Liu, L. Zhong, S. Huang, S. X. Mao, T. Zhu and J. Y. Huang, *ACS Nano*, 2012, **6**, 1522–1531.
169 S. Bhattacharya, A. R. Riahi and A. T. Alpas, *J. Power Sources*, 2011, **196**, 8719.
170 Y. Qi, Q. Xu and A. Van der Ven, *J. Electrochem. Soc.*, 2012, **159**, A1838.
171 J. Christensen and J. Newman, *J. Electrochem. Soc.*, 2006, **153**, A1019.
172 K. E. Aifantis and J. P. Dempsey, *J. Power Sources*, 2005, **143**, 203.
173 M. Zhu, J. Park, and A. M. Sastry, *J. Electrochem. Soc.*, 2012, **159**, A492.
174 X. Hao, O. Gourdon, B. J. Liddle and B. M. Bartlett, *J. Mater. Chem.*, 2012, **22**, 1578.

175. M. Yonemura, A. Yamada, H. Kobayashi, M. Tabuchi, T. Kamiyama, Y. Kawamoto and R. Kanno, *J. Mater. Chem.*, 2004, **14**, 1948–1958.
176. M. R. Palacin, Y. Chabre, L. Dupont, M. Hervieu, P. Strobel, G. Rousse, C. Masquelier, M. Anne, G. G. Amatucci and J. M. Tarascon, *J. Electrochem. Soc.*, 2000, **147**, 845–853.
177. A. Yamada and M. Tanaka, *Mater. Res. Bull.*, 1995, **30**, 715.
178. K. Oikawa, T. Kamiyama, F. Izumi, B. C. Chakoumakos, H. Ikuta, M. Wakihara, J. Li and Y. Matsui, *Solid State Ionics*, 1998, **109**, 35–41.
179. J. Hun, M. Chung, M. Park, S.Woo, X. Zhang, A. M. Sastry, *J. Electrochem. Soc.* 2011, **158**, A434.
180. D. Aurbach, M. D. Levi, E. Levi, B. Markovsky, G. Salitra, H. Teller, U. Heider and L. Heider, *MRS Proc.*, 1998, **496**, 435.
181. T. R. Thurston, N. M. Jisrawi, S. Mukerjee, X. Q. Yang, J. McBreen, M. L. Daroux, X. K. Xing, *App. Phys. Lett.* 1996, **69**, 194.
182. S. Mukerjee, T. R. Thurston, N. M. Jisrawi, X. Q. Yang, J. McBreen, M. L. Daroux, X. K. Xing, *J. Electrochem. Soc.* 1998, **145**, 466.
183. J. H. Kim, C. S.Yoon, S. T. Myung, J. Prakash, and Y. K. Sun, *Solid-State Lett.* 2004, **7**, A216.
184. M. Wagemaker, W. J. H. Borghols, and F. M. Mulder, *J. Am. Chem. Soc*. 2007, **129**, 4323.
185. M. Jo, Y.-S. Hong, J. Choo and J. Cho, *J. Electrochem. Soc*., 2009, **156**, A430–A434.
186. D. Kovacheva, B. Markovsky, G. Salitra, Y. Talyosef, M. Gorova, E. Levi, M. Riboch, H.-J. Kim and D. Aurbach, *Electrochim. Acta*, 2005, **50**, 5553.
187. A. Karim, S. Fosse, K. A. Persson, *Phys. Rev. B* 2013, **87**, 075322.
188. J. S. Kim, K. S. Kim, W. H. Cho, R. Kanno, J. W. Choi, *Nano Lett.* 2012, **12**, 6358.
189. K. R. Chemelewski, E. S. Lee, W. Li, A. Manthiram, *Chem. Mater.* 2013, **25**, 2890.
190 M. M. Thackeray, *J. Am. Ceram. Soc*., 2004, **82**, 3347.
191 D. Guyomard and J. M. Tarascon, *Solid State Ionics*, 1994, **69**, 222.
192 M. M. Thackeray, W. I. F.. David, P. G. Bruce and J. B. Goodenough, *Mater. Res. Bull.*, 1983, **18**, 461.
193 Y. Ein-Eli, J. T. Vaughey, M. M. Thackeray, S. Mukerjee, X. Q. Yang, J. McBreen, *J. Electrochem. Soc.*, 1999, **146,** 908.
194 T. Ohzuku, S. Takeda, M. Iwanaga, *J. Power Sources*, 1999, **81-82**, 90.
195 J. M. Amarialla, R. M. Rojas, F. Pico, L. Pascual, K. Petrov, D. Kovacheva, M. G. Lazarraga, I. Lejona, J. M. Rojo, *J. Power Sources*, 2007, **174**, 1212.
196 K. Amine, H. Tukamoto, H. Yaduda, Y. Fujita, *J. Electrochem. Soc,* 1996, **143**, 1607.
197 J. Shu, T.-F. Yi, M. Shui, Y. Wang, R.-S. Zhu, X.-F. Chu, F. Huang, D. Xu, L. Hou, *Comput. Mater. Sci.*, 2010, **50**, 776.
198 M. Okada, Y.-S. Lee, M. Yoshio, *J. Power Sources*, 2000, **90**, 196.
199 H. F. Xiang, X. Zhang, Q. Y. Jin, C. P. Zhang, C. H. Chen, X. W. Ge, *J. Power Sources,* 2008, **183**, 355.

200 F. Zhou, X. Zhao, A. Bommel, X. Xia, J. R. Dahn, *J. Electrochem. Soc*, 2011, **158**, A187.
201 P. Reale, S. Panero, B. Scrosati, *J. Electrochem. Soc*., 2005, **152**, A1949.
202 G. Armstrong, A. R. Armstrong, P. G. Bruce, P. Reale, B. Scrosati, *Adv. Mater*., 2006, **18**, 2597.
203 X. F. Xiang, Q. Y. Jin, R. Wang, C. H. Chen, X. W. Ge, *J. Power. Sources*, 2008, **179**, 351.
204 A. Abouimrane, I. Belharouak, K. Amine, *Electrochem. Commun*., 2009, **11**, 1073.
205 J. M. Tarascon, E. Wang, F. K. Shokoohi, W. R. McKinnon, S. Colson, *J. Electrochem. Soc.*, 1991, **138**, 2859.
206 Y.-K. Sun, K. -J. Hong, J. Prakash, K. Amine, *Electrochem. Commun.*, 2002, **4**, 344.
207 X. Wu, S. B. Kim, *J. Power Sources*, 2002, **109**, 53.
208 Y. -K. Sun, C. S. Yoon, I. -H. Oh, *Electrochim. Acta*, 2003, **48**, 503.
209 K. M. Shaju and P. G. Bruce, *Dalton Trans*., 2008, 5471.
210 T. Yang, N. Zhang, Y. Lang, K. Sun, *Electrochim. Acta*, 2011, **56**, 4058.
211 L. Wang, H. Li, X. Huang, E. Baudrin, *Solid State Ionics*, 2011, **193**, 32.
212 G. Q. Liu, L. Wen, Y. M. Liu, *J. Solid State Electrochem*., 2010, **14**, 2191.
213 R. Santhanam, B. Rambabu, *J. Power Sources*, 2010, **195**, 5442.
214 J.-H. Kim, S.-T. Myung, C. S. Yoon, S. G. Kang, and Y.-K. Sun, *Chem. Mater*., 2004, **16**, 906.
215 M. Kunduraci, J. F. Al-Sharab, G. G. Amatucci, *Chem. Mater*. 2006, **18**, 3585.
216 Q. Zhong, A. Bonakdarpour, M. Zhang, Y. Gao, J. R. Dahn, *J. Electrochem. Soc*., 1997, **144**, 205.
217 M. Zhang, J. Wang, Y. Xia, Z. Liu, *J. Alloys Compd*. 2012, **518**, 68.
218 G. Q. Liu, L. Wen, X. Wang, B. Y. Ma, *J. Alloys Compd*, 2011, **509**, 9377.
219 X. Huang, D. Lv, Q. Zhang, H. Chang, J. Gan, Y. Yang, *Electrochim. Acta*., 2010, **55**, 4915.
220 W. Xiao, D. Wang, X. W. Lou, *J. Phys. Chem. C*, 2010, **114**, 1694.
221 Z. Liu and K. Ooi, *Chem. Mater*., 2003, **15**, 3696.
222 H. Fang, L. Li, Y. Yang, G. Yan, G. Li, *J. Power Sources*, 2008, **184**, 494.
223 T. Kanasaku, K. Amezawa, N. Yamamoto, *Solid State Ionics*, 2000, **133**, 51.
224 Q. Feng, Y. Higashimoto, K. Kajiyoshi, K. Yanagisawa, *J. Mater. Sci. Lett*., 2001, **20**, 269.
225 D. Liu, J. Han, J. B. Goodenough, *J. Power Sources*, 2010, **195**, 2918-2923.
226 G. Du, Y. NuLi, J. Yang, J. Wang, *Mater. Res. Bull*., 2008, **43**, 3607.
227 B. J. Liddle, S. M. Collins, B. M. Bartlett, *Energy Environ. Sci.*, 2010, **3**, 1339.
228 Y. Xu, Q. Feng, K. Kajiyoshi, K. Yanagisawa, *Chem. Mater.*, 2002, **14**, 697.
229 X. Huang, Q. Zhang, J. Gan, H. Chang and Y. Yang, *J. Electrochem. Soc*., 2011, **158**, A139.
230 J. C. Arrebola, Ă. Caballero, L. Hernán, M. Melero, J. Morales and E. R. Castellón, *J. Power Sources*, 2006, **162**, 606.
231 T. Choudhury, S. O. Saied, J. L. Sullivan and A. M. Abbot, *J. Phys. D: Appl. Phys*., 1989, **22,** 1185.
232 R. Baddour-Hadjean and J.-P. Pereira-Ramos, *Chem. Rev.*, 2010, **110**, 1278.

233 M. Kunduraci and G. G. Amatucci, *J. Electrochem. Soc*, 2006, **153**, A1345.
234 S. H. Oh, K. Y. Chung, S. H. Jeon, C. S. Kim, W. I. Cho and B. W. Cho, *J. Alloys Compd*., 2009, **469**, 244.
235 N. Amdouni, K. Zaghib, F. Gendron, A. Mauger and C. M. Julien, *J. Magn.Magn. Mater*., 2007, **309**, 100.
236 Y. J. Wei, L. Y. Yan, C. Z. Wang, X. G. Xu, F. Wu and G. Chen, *J. Phys, Chem. B*, 2004, **108**, 18547.
237 N. Amdouni, K. Zaghib, F. Gendron, A. Mauger and C. M. Julien, *Ionics*, 2006, **12**, 117.
238 Y. Wei, K. -B. Kim and G. Chen, *Electrochim. Acta*, 2006, **51**, 3365.
239 R. Alcántara, M. Jaraba, P. Lavela,J. L. Tirado, Ph. Biensan, A. de Guibert, C. Jordy, J. P. Peres, *Chem. Mater*., 2003, **15**, 2376.
240 L. Yu, Y. Cao, H. Yang and X. Ai, *J. Solid State Electrochem.*, 2006, **10**, 283.
241 J. C. Arrebola, A. Caballero, M. Cruz, L. Hernán, J. Morales and E. R. Castellón, *Adv. Funct. Mater*., 2006, **16**, 1904.
242 J. Li, Y. Zhang, J. Li and L. Wang, *Ionics*, 2011, **17**, 671.
243 S. Brutti, V. Gentili, P. Reale, L. Carbone and S. Panero, *J. Power Sources*, 2011, **196**, 9792.
244 L. Yang, B. Ravdel and B. L. Lucht, *Elecrochem. Solid-State Lett*., 2010, **13**, A95.
245 J.-T. Han and J. B. Goodenough, *Chem. Mater*., 2011, **23**, 3404.
246 J. B. Goodenough, *Advances in Lithium-Ion Batteries*, W. Van Schalkwijk and B. Scrosati, Editors, Kluwer Adademic, Norwell, MA/Plenum Publishers, New York, 2002.
247 S. Mukerjee, X. Q. Yang, X. Sun, S. J. Lee, J. McBreen and Y. Ein-Eli, *Electrochim. Acta*., 2004, **49**, 3373.
248 D. Aurbach, K. Gamolsky, B. Markovsky, G. Salitra, Y. Gofer, U. Heider, R. Oesten and M. *J.* Schmidt, *Electrochem. Soc.*, 2000, **147**, 1322.
249 D. Liu, Y. Lu and J. B. Goodenough, *J. Electrochem. Soc.*, 2010, **157**, A1269.
250 Y. J. Lee, C. Eng and C. P. Grey, *J. Electrochem. Soc.*, 2001, **148**, A249.
251 J. -H. Kim, S.-T. Myung, C.S. Yoon, I. -H. Oh and Y. -K. Sun, *J. Electrochem. Soc.*, 2004, **151**, A1911.
252 R. Alcántara, M. Jaraba, P. Lavela and J. L. Tirado, *Chem. Mater*., 2004**, 16**, 1573.
253 J. B. Goodenough and Y. Kim, *J. Power Sources*, **196**, 6688 (2011).
254 R. Marom, S. F. Amalraj, N. Leifer, D. Jacob and D. Aurbach, *J. Mater. Chem*., 2011, **21**, 9938.
255 M. S. Whittingham, *Chem. Rev*., 2004, **104**, 4271.
256 Q. Zhong, A. Bonakdarpour, M. Zhang, Y. Gao and J. R. Dahn, *J. Electrochem. Soc*., 1997, **144**, 205.
257 T. Ohzuku, S. Takeda, M. Iwanaga, *J. Power Sources*, 1999, **81-82**, 90.
258 G. Q. Liu, L. Wen, Y. M. Liu, *J. Solid State Electrochem*., 2010, **14**, 2191.
259 D. G. Wickham and W. J. Croft, *J. Phys. Chem. Solids*, 1958, **7**, 351.
260 R. J. Gummow, A. de Kock and M. M. Thackeray, *Solid State Ionics*, 1994, **69**, 59.
261 M. Wagemaker, F. G. B. Ooms, E. M. Kelder, J. Schoonman, G. J. Kearley and F. M. Mulder, *J. Am. Chem. Soc*., 2004, **126**, 13526.

262 D. Pasero, N. Reeves, V. Pralong and A. R. West, *J. Electrochem. Soc*., 2008, **155**, A282.
263 J. -H. Kim, S.-T. Myung, C. S. Yoon, S. G. Kang and Y.-K. Sun, *Chem. Mater*., 2004, **16**, 906.
264 J.-H. Kim, C. S. Yoon, S.-T. Myung, J. Prakash and Y.-K. Sun, *Electrochem. Solid-State Lett*., 2004, **7**, A216.
265 L. Yang, B. Ravdel and B. L. Lucht, *Electrochem. Solid-State Lett*., 2010, **13**, A95.
266 G. G. Amatucci, N. Pereira, T. Zheng and J. -M. Tarascon, *J. Electrochem. Soc*., 2001, **148**, A171.
267 B. Markovsky, Y. Talyossef, G. Salitra, D. Aurbach, H.-J. Kim, S. Choi, *Electrochem. Comm*., 2004, **6**, 821.
268 D. Aurbach, B. Markovsky, Y. Talyossef, G. Salitra, H.-J. Kim, S. Choi, J. Power Sources, 2006, **162**, 780.
269 Y.-K. Sun, Y.-S. Lee, M. Yoshio and K. Amine, *Electrochem. Solid-State Lett.*, 2002, **5**, A99.
270 X. Hao, M. H. Austin and B. M. Bartlett, *Dalton Trans*., 2012, **41**, 8067.
271 K. M. Shaju and P. G. Bruce, *Dalton Trans*., 2008, 5471.
272 D. Liu, Y. Lu and J. B. Goodenough, *J. Electrochem. Soc*., 2010, **157**, A1269.
273 J. Hassoun, K.-S. Lee, Y.-K Sun and B. Scrosati, *J. Am. Chem. Soc*., 2011, **133**, 3139.
274 H. Wang, T. A. Tai, P. Yang, M. O. Lai and L. Lu, *J. Phys. Chem. C*, 2011, **115**, 6102.
275 Y.-K. Sun, C. S. Yoon, I.-H. Oh, *Electrochim. Acta*, 2003, **48**, 503.
276 Y. Kobayashi, H. Miyashiro, K. Takei, H. Shigemura, M. Tabuchi, H. Kageyama and T. Iwahori, *J. Electrochem. Soc*., 2003, **150**, A1577.
277 H. Miyashiro, A. Yamanaka, M. Tabuchi, S. Seki, M. Nakayama, Y. Ohno, Y. Kobayashi, Y. Mita, A. Usami and M. Wakihara, *J. Electrochem. Soc*., 2006, **153**, A348.
278 J. M. Zheng, Z. R. Zhang, X. B. Wu, Z. X. Dong, Z. Zhu and Y. Yang, *J. Electrochem. Soc*., 2008, **155**, A775.
279 J. Cho, Y. J. Kim and B.Park, *Chem. Mater*., 2000, **12**, 3788.
280 X. Hao and B. M. Bartlett, *Submitted*.
281 T. M. Breault, B. M. Bartlett, *J. Phys. Chem. C*, 2012, **116**, 5986.
282 J. Cabana, M. Casas-Cabanas, F. O. Omenya, N. A. Chernova, D. Zeng, M. S. Whittingham and C. P. Grey, *Chem. Mater*., 2012, **24**, 2952.
283 N. Reeves, C. A. Kirk and A. R. West, *J. Mater. Chem*., 2001, **11**, 249.
284 J. Cabana, H. Zheng, A. K. Shukla, C. Kim, V. S. Battaglia and M. Kunduraci, *J. Electrochem. Soc*., 2011, **158**, A997.
285 X. Hao and B. M. Bartlett, *Adv. Energy Mater*., 2013, **3**, 753.
286 J. Xiao, X. Chen, P. V. Sushko, M. L. Sushko, L. Kovarik, J. Feng, Z. Deng, J. Zheng, G. L. Graff, Z. Nie, D. Choi, J. Liu, J.-G. Zhang and M. S. Whittingham, *Adv. Mater*., 2012, **24**, 2109.
287 R. Alcántara, M. Jaraba, P. Lavela, J. L. Tirado, Ph. Biensan, A. de Guibert, C. Jordy and J. P. Peres, *Chem. Mater*., 2003, **15**, 2376.

288 L. Yu, Y. Cao, H. Yang and X. Ai, *J. Solid State Electrochem*., 2005, **10**, 283.
289 H. M. Wu, I. Belharouak, A. Abouimrane, Y.-K. Sun, K. Amine, *J. Power Sources*, 2010, **195**, 2909.
290 S.-Y. Chung, J.T. Bloking and Y.-M. Chiang, *Nature Mater.* 2002, **1**, 123.
291 Y. Fan, J. Wang, Z. Tang, W. He, J. Zhang, *Electrochim. Acta*, 2007, **52**, 3870.
292 J. Mun, T. Yim, K. Park, J. H. Ryu, Y. G. Kim and S. M. Oh, *J. Electrochem. Soc.*, 2011, **158**, A453.
293 J.-T. Han and J. B. Goodenough, *Chem. Mater.*, 2011, **23**, 3404.
294 J. R. Dahn, U. von Sacken and C. A. Michal, *Solid State Ionics*, 1990, **44**, 87.
295 K. Kang, C.-H. Chen, B. J. Hwang and G. Ceder, *Chem. Mater*., 2004, **16**, 2685.
296 M. Wagemaker, D. R. Simon, E. M. Kelder, J. Schoonman, C. Ringpfeil, U. Haake, D. Lützenkirchen-Hecht, R. Frahm, and F. M. Mulder, Adv. Mater., 2006, 18, 3169.
297 W. Weppner and R. Huggins, *J. Electrochem. Soc*., 1977, **124**, 1569.
298 W. E. Beadle, J. C. C. Tsai and R. D. Plummer, Eds., *Quick Reference Manual for Silicon Integrated Circuit Technology*, Wiley, 1985, New York.
299 G.-N. Zhu, Y.-G. Wang and Y.-Y. Xia, *Energy Environ. Sci.*, 2012, **5**, 6652.
300 J. Jiang, and J. R. Dahn, *J. Electrochem. Soc*., 2006, **153**, A310.
301 L.-F. Cui, R. Ruffo, C. K. Chan, H. Peng and Y. Cui, *Nano Lett*., 2009, **9**, 491.
302 J. Gu, S. M. Collins, A. I. Carim, X. Hao, B. M. Bartlett and S. Maldonado, *Nano Lett*., 2012, **12**, 4617.
303 K. M. Colbow, J. R. Dahn and R. R. Haering, *J. Power Sources*, 1989, **26**, 397.
304 M. M. Thackeray, *J. Electrochem. Soc*., 1995, **142**, 2558.
305 F. Ronci, P. Peale, B. Scrosati, S. Panero, V. Rossi Albertini, P. Perfetti, M.di Michiel and J. M. Merino, *J. Phys, Chem. B*, 2002, **106**, 3082.
306 L. Kavan, J. Rathousky, M. Grätzel, V. Shklover and A. Zukal, *J. Phys. Chem. B.* 2000, **104**, 12012.
307 L. Kavan, J. Procházka, T. M. Spitler, M. Kalbáč, M. Zukalová, T. Drezen and M. Grätzel, *J. Electrochem. Soc*., 2003, **150**, A1000
308 J. Li, Z. Tang and Z. Zhang, *Electrochem. Commun*., 2005, **7**, 894.
309 A. S. Aricò, P. Bruce, B. Scrosati, J.-M. Tarascon and W. van Schalkwijk, *Nature Mater*., 2005, **4**, 366-377.
310 K. Naoi, W. Naoi, S. Aoyagi, J. Miyamoto, and T. Kamino, *Acc. Chem. Res*. **2012**, DOI: 10.1021/ar200308.
311 K. Naoi, S. Ishimoto, Y. Isobe and S. Aoyagi, *J. Power Sources*, 2010, **195**, 6250.
312 Y. Tang, F. Huang, W. Zhao, Z. Liu and D. Wan, *J. Mater. Chem*., 2012, **22**, 11257.
313 B. Zhang, Y. Liu, Z. Huang, S. Oh, Y. Yu, Y.-W. Mai and J.-K. Kim, *J. Mater. Chem*., 2012, **22**, 12133.
314 H.-K. Kim, S.-M. Bak and K.-B. Kim, *Electrochem. Commun*., 2010, **12**, 1768.
315 Y.-Q. Wang, L. Gu, Y.-G. Guo, H. Li, X.-Q. He, S. Tsukimoto, Y. Ikuhara and L.-J. Wan, *J. Am. Chem. Soc.*, 2012, **134**, 7874.
316 Y. F. Tang, L. Yang, Z. Qiu and J. S. Huang, *Electrochem. Commun*., 2008, **10**, 1513.
317 J. Kim and J. Cho, *Solid-State Lett*., 2007, **10**, A81.

318 S.-L. Chou, J.-Z. Wang, H.-K. Liu and S.-X. Dou, *J. Phys. Chem. C*. 2011, **115**, 16220.
319 D. H. Kim, Y. S. Ahn and J. Kim, *Electrochem. Commun*., 2005, **7**, 1340.
320 Y. Hao, Q. Lai, Z. Xu, X. Liu and X. Ji, *Solid State Ionics*, 2005, **176**, 1201.
321 Y. H. Rho and K. Kanamura, *J. Solid State Chem*., 2004, **177**, 2094.
322 K. Kanamura, N. Akutagawa and K. Dokko, *J. Power Sources*, 2005, **146**, 86.
323 J. M. Feckl, K. Fominykh, M. Döblinger, D. F.-Rohlfing and T. Bein, *Angew. Chem. Int. Ed.*, 2012, **51**, 7459.
324 C. M. Julien, M. Massot and K. Zaghib, *J. Power Sources*, 2004, **136**, 72.
325 P. Scherrer, *Göttinger Nachrichtern Gesell*., 1918, **2**, 98.
326 K. Zaghib, M. Simoneau, M. Armand and M. Gauthier, *J. Power Sources*, 1999, **81-82**, 300.
327 L. Kavan and M. Grätzel, *Electrochem. Solid-State Lett*., 2002, **5**, A39.
328 M. Wagemaker, D. R. Simon, E. M. Kelder, J. Schoonman, C. Ringpfeil, U. Haake, D. Lützenkirchen-Hecht, R. Frahm and F. M. Mulder, *Adv. Mater*., 2006, **18**, 3169.
329 W. Weppner and R. Huggins, *J. Electrochem. Soc*., 1977, **124**, 1569.
330 J. R. Macdonald and L. D. Potter, Jr. *Solid State Ionics*, 1987, **23**, 61.
331 E. M. Sorensen, S. J. Barry, H.-K. Jung, J. R. Rondinelli, J. T. Vaughey and K. R. Poeppelmeier, *Chem. Mater*., 2006, **18,** 482.
332 M. Wilkening, R. Amade, W. Iwaniak and P. Heitjans, *Phys. Chem. Chem. Phys*., 2007, **9**, 1239.
333 M. Wagemaker, E. R. H. van Eck, A. P. M. Kentgens and F. M. Mulder, *J. Phys. Chem. B*., 2009, **113**, 224.
334 J. Chen, L. Yang, S. Fang, S. I. Hirano and K. Tachibana, *J. Power Sources*, 2012, **200**, 59.
335 J. Huang and Z. Jiang, *Solid-State Lett.*, 2008, **11**, A116.
336 B. Smarsly, D. Grosso, T. Brezesinski, N. Pinna, C. Boissière, M. Antonietti and C. Sanchez, *Chem. Mater*., 2004, **16**, 2948.
337 L. Cheng, X. L. Li, Liu, J. H. H. M. Xiong, P. W. Zhang and Y. Y. Xia, 2007, **154**, A692.
338 X. Chen, X. Guan, L. Li and G. Li, *J. Power Sources*, 2012, **210**, 297.
339 Y. Wang, H. Liu, K. Wang, H. Eiji, Y. Wang and H. Zhou, *J. Mater. Chem*., 2009, **19**, 6789.
340 D. Gonbeau, C. Guimon and G. Pfister-Guillouzo. *Sur. Sci*., 1991, **254**, 81.
341 R.P. Vasquez, *J. Electron Spectrosc. Relat. Phemon*., 1991, **56**, 217.
335 N. He, B. Wang, J. Huang, *J. Solid State Electrochem*. 2010, **14,** 1241.
336 H.-G. Jung, M. W. Jang, J. Hassoun, Y.-K. Sun, and B. Scrosati, *Nature Commun*. 2011, **2**, 1.
337 H.-G. Jung, S.-T. Myung, C. S. Yoon, S.-B. Son, K. H. Oh, K. Amine, B. Scrosati, Y.-K. Sun, *Energy Environ. Sci*. 2011, **4**, 1345.